Critical cobalt and where to find it: distribution of cobalt in the Dolostone Ore Formation deposit, Namibia

Viktor Bertrandsson Erlandsson[1], Rainer Ellmies[2], Phillip Gopon[1], Helene Waldl[3], David Misch[1], Frank Melcher[1]
[1]Department of Applied Geosciences and Geophysics, University of Leoben, Austria
[2]Gecko Namibia, Swakopmund, Namibia
[3]Christian Doppler Laboratory for Advanced Coated Cutting Tools, University of Leoben, Austria

Abstract. In the pursuit of new sources of the critical metal Co, we investigate the sediment-hosted Cu-Co-Zn Dolostone Ore Formation (DOF) deposit in Namibia. Besides the stoichiometric Co-phase linnaeite, all sulfides associated with the main Co-forming ore stage (pyrite, sphalerite, and chalcopyrite) are enriched in Co, with significant concentrations found in sphalerite and pyrite. Sphalerite was measured to contain up to 1.5 wt% Co, which is the highest Co concentration reported in sphalerite. Atom probe tomography measurements of the Co-rich sphalerite demonstrates that these high Co concentrations occur homogeneously distributed. Petrographic evidence suggests that the Co was originally hosted in the pyrite, which was later remobilized during metamorphism to get incorporated into sulfides that formed during later ore stages. The Co finally got incorporated into the Co-rich sphalerite and to a lesser extend chalcopyrite. This study showcases the potential of secondary Co-bearing minerals as a source for the future of exploration and production of the critical metal Co.

1 Introduction

Cobalt is one of the many metals now classified as “critical” (European Commission 2020; USGS 2022) largely due to its use large demand in high-tech and green technologies, in particular high capacity batteries for electric cars (e.g. Alves Dias et al. 2018). Around 68 % of the global Co production comes from the Central African Copperbelt, in particular from the sediment-hosted Cu-Co deposits in the Democratic Republic of Congo (European Commission 2020; USGS 2020).

This study focuses on a recently discovered Co mineralization outside the Central African Copper Belt, the Dolostone Ore Formation (DOF) Cu-Co-Zn deposit in northwestern Namibia. To better define the distribution and mode of occurrence of Co in the sulfides of the DOF deposit, we use a correlative approach. Alongside with petrographic work with reflective light microscopy and scanning electron microscopy (SEM), we used laser ablation inductively coupled plasma mass spectrometry (LA-ICP-MS) to quantify the trace element composition of the various sulfides of the DOF deposit.

Electron probe micro analyzer (EPMA), electron backscattered diffraction (EBSD), and atom probe tomography (APT) were used to comprehend and visualize the Co distribution in Co-rich sphalerite. By applying all of these methods, we hope to better understand the occurrence and processes required to form Co-bearing phases in sediment-hosted deposits.

2 Geological setting

2.1 Regional geology

The DOF deposit is hosted in the Neoproterozoic Ombombo Subgroup of the Damara Supergroup (Allen 2016). The Damara Supergroup contains a sediment succession derived from the break-up of Rodinia with initial rifting with sandstones and conglomerates into carbonate platform environment with interlayered shales, siltstones and carbonates (Hoffman & Halverson 2008; Miller 2008; Porada 1989; Guj 1970). The Abenab Subgroup overlays the Ombombo Subgroup in the DOF area, containing the Chuos Formation diamictite and Rasthof Formation cap-carbonates (Allen 2016; Hoffman 2011; Hoffman & Prave 1996). The DOF deposit is located within the Eastern Foreland of the Kaoko Belt, the northern branch of the Damara orogen (Goscombe et al. 2005). The Eastern Foreland Zone experienced low-grade greenschist facies metamorphism (300 – 400 °C) during two stages of the Damara orogeny: the Kaoko Phase (590 – 535 Ma) and Damara Phase (555 – 505 Ma; Goscombe et al. 2017, 2003; Foster et al. 2009; Guj 1970).

2.2 Geology of the DOF deposit

The DOF Cu-Co-Zn mineralized horizon has been traced for at least 43 km E-W extension, dipping to the north, and is hosted in siltstones, shales, and carbonates within the Ombazu Trough in the Kunene region of northwestern Namibia (Figure 1). The mineralization has been subdivided into the main Cu-Co-Zn stage, expressed as sulfides disseminated in the host rock along with mineralized nodules and polysulfide aggregates. The second Cu-Zn stage occurs primarily within veins and pressure shadow mineralization. The main sulfides are pyrite, pyrrhotite, chalcopyrite, sphalerite, and linnaeite with lesser amounts of cobaltpentlandite, galena, and cobaltite. Linnaeite is restricted to the main stage mineralization (Bertrandsson Erlandsson 2022). The Ge-Ga-In-Mn-Fe (GGIMF) in sphalerite geothermometer (Frenzel 2016) indicates formation temperatures of all sphalerite to be above 310 ± 50 °C (Bertrandsson Erlandsson 2022).

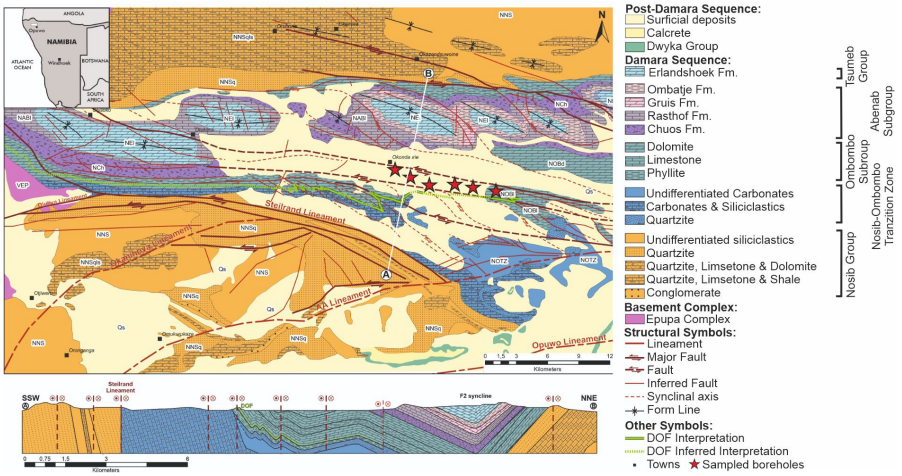

Figure 1. Geological map of the DOF deposit (green line) with sampled boreholes marked by stars. With schematic profile through the Ombazu Trough (white line). Modified after Bertrandsson Erlandsson (2022).

3 Methods

3.1 Sampling and petrographic methods

Polished mounts were made from sampling of six different exploration boreholes drilled by Celsius Resources (Figure 1), along the E-W extent of the DOF horizon. Boreholes are located approximately 2 km apart from each other. Mineral identification and textural observations were primarily done using reflective light microscopy and a Zeiss EVO MA 10 (SEM) coupled with a Bruker Quantax EDX detector.

3.2 LA-ICP-MS trace element analyses

An ESI Nd:YAG NWR213 laser ablation system coupled to an Agilent 8800 QQQ ICP-MS was used for in-situ trace element analyses of sphalerite, chalcopyrite, pyrite, and pyrrhotite. Masses analyzed were: ^{34}S, ^{51}V, ^{52}Cr, ^{55}Mn, ^{57}Fe, ^{59}Co, ^{60}Ni, ^{63}Cu, ^{67}Zn, ^{71}Ga, ^{74}Ge, ^{75}As, ^{82}Se, ^{95}Mo, ^{107}Ag, ^{111}Cd, ^{115}In, ^{118}Sn, ^{121}Sb, ^{125}Te, ^{197}Au, ^{201}Hg, ^{205}Tl, ^{208}Pb, and ^{209}Bi. Element concentrations were calculated using Iolite 4 (Paton et al. 2011), using two reference materials: the sphalerite standard MUL-ZnS1 (Onuk et al. 2017) and the polysulfide standard MASS-1 (Wilson et al. 2002).

3.3 EPMA mapping

Element maps of linnaeite, Co-rich sphalerite and pyrite were done using a JEOL Superprobe JXA 8200 EPMA equipped with five wavelength-dispersive spectrometers and one energy dispersive spectrometer. Maps were made with a 15 keV and 100 nA beam in stage scan mode.

3.4 EBSD mapping

A FEI Versa 3D Dual Focused Ion Beam FE-SEM was utilized to carry out EBSD mapping. Measurements were carried out with 20 keV electron-beam, with phase cubic scan parameters and a 500 nm step size in beam scanning mode.

3.5 APT measurements

Sphalerite APT analyses were carried out in laser mode with a 355 nm UV laser using a CAMECA LEAP 5000 XR. The measurements were done at a stage temperature of 50 K with 125 Hz pulse rate and laser pulse energy between 40 – 80 pJ. These parameters were adapted after the successful APT analyses of pyrite by Gopon et al. (2022). Sample preparation was done after Thompson et al. (2007) using a FEI Versa 3D Dual Focused Ion Beam FE-SEM equipped with a focused ion beam (FIB). Data reconstructions and peak ranging were done in IVAS 3.8.

4 Results

4.1 Mineralization styles of the DOF

Disseminated sulfides in the DOF deposit occur in several mineralization styles: disseminated, clusters, nodules, veins and in pressure shadows. There are also the locally termed “Events” that are vein-like but show both brittle and ductile deformation. Petrography of the sulfides from the main Cu-Co-Zn mineralization shows sphalerite overgrowing, and chalcopyrite forming rims around linnaeite and iron sulfides, indicating a more complex genesis of the main stage. The linnaeite is almost exclusively enveloped in pyrite and often appears partially altered. Main stage mineralization is associated with host rock alteration containing stilpnomelane and euhedral siderite, both which crosscut the pyrite. Disseminated sulfides occur oriented along the schistosity and mineralization styles such as the polysulfide cluster seems to be ripped apart in the orientation of the schistosity. See Bertrandsson Erlandsson (2022) for more details.

4.2 Sulfide trace element composition

Trace element LA-ICP-MS analyses revealed two main groups between the different mineralization styles. Group 1 is primarily recognized by the

elevated concentrations of Co in sphalerite (Figure 2), chalcopyrite, and pyrite. Other trace elements also differ significantly between the two groups, e.g. Ni and Se in sphalerite and chalcopyrite. Sphalerite contains up to 1.5 wt% Co.

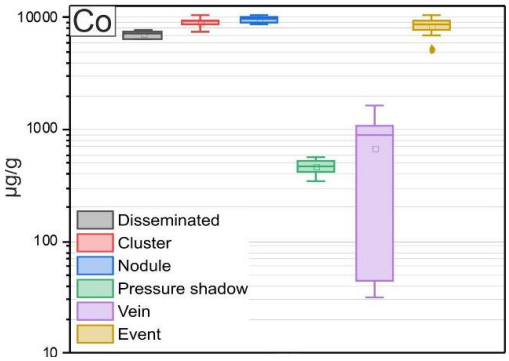

Figure 2. Cobalt concentrations in sphalerite showing distinct grouping between Co-rich and Co-poor sphalerite. Mineralization styles in legend are briefly explained in section 4.1.

4.3 EPMA and EBSD mapping of Co-sphalerite

EPMA mapping shows homogeneous distribution of Co within the Co-rich sphalerite, but also revealed a Co-poor and Zn-rich network (Figure 3). EBSD mapping shows subgrains within sphalerite that seem to correlate with the network feature identified by the EPMA. EPMA mapping shows oscillatory Co-zoning in the pyrites from the main Cu-Co-Zn stage mineralization, where the innermost zones show higher Co concentrations (Figure 4).

4.1 APT data reconstruction

3D reconstructions of the APT needle shaped sample reveal that Co occur homogenously within the Co-rich sphalerite, with no evidence for nano-inclusions (Figure 5).

5 Discussion

Based off the LA-ICP-MS analyses, all sulfides that occur are associated with the stoichiometric Co-mineral linnaeite have elevated Co contents. Both the Co-rich sphalerite and chalcopyrite crosscut the linnaeite and pyrite of the main Cu-Co-Zn mineralization, suggesting a relatively later formation of these phases. As linnaeite contains Co^{3+} and pyrite, which envelops the linnaeite, should only include 2+ cations, it is assumed that different physiochemical changes were involved in the remobilization of Co in the DOF deposit (Bertrandsson Erlandsson et al. 2023). The sphalerite and chalcopyrite formation would also imply an additional source of Zn and Cu, as these elements are not significantly elevated in the earlier pyrite (Bertrandsson Erlandsson et al. 2022).

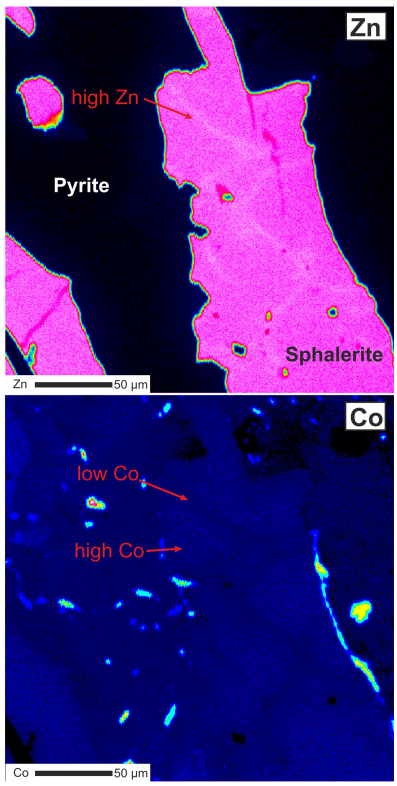

Figure 3. EPMA element maps of Zn and Co from Co-rich sphalerite. Cobaltpentlandite inclusions in pyrite are visible as spots of high Co. Note that the high Co on the right-side of the sphalerite-pyrite contact is an edge artifact from holes in the sample, and not trustworthy data.

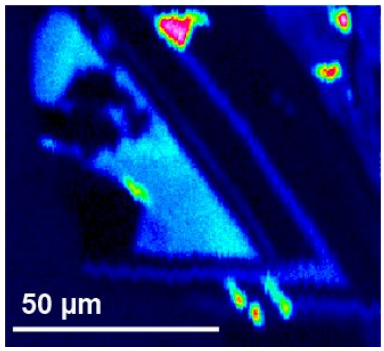

Figure 4. EPMA map of cobalt zonation within pyrite from another part of the cluster mineralization style, with crosscutting cobaltpentlandite inclusions (high Co in map).

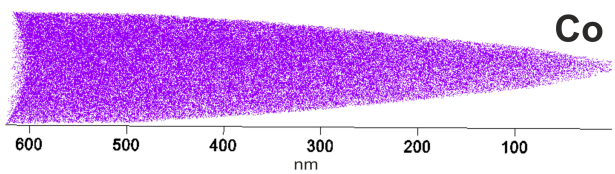

Figure 5. Tip reconstructions of homogenously distributed Co ions from the APT data. X-axis showing scale of the APT tip.

The observation of Cu-Co-Zn stage sulfides being aligned with the host rock schistosity and the GGIMF in sphalerite geothermometer yielding formation temperatures 310 ± 50 °C (in agreement with regional metamorphic temperatures) strongly suggests that the DOF mineralization formed during the Damara orogeny. The vein-hosted Cu-Zn

mineralization is believed to have formed later and is thus related to a late orogenic stage. It is worth noting that the network feature, identified by EPMA in the Co-rich sphalerite (Figure 3), has lower Co concentrations than the rest of the sphalerite, as the later Cu-Zn mineralization sulfides were also shown to also contain significantly lower Co concentrations by LA-ICP-MS (Figure 2). This later Cu-Zn mineralization occurs predominantly within veins and is believed to have formed later than the Co-mineralization (Bertrandsson Erlandsson et al. 2022). Attempts of dating have so far been unsuccessful and therefore these mineralization stages cannot be attributed to the different Damara orogenic phases.

6 Conclusions

This study highlights the widespread Co-enrichment in all sulfides associated with the main Cu-Co-Zn mineralization stage (pyrite, sphalerite, and chalcopyrite) of the DOF deposit. Whilst the later vein-hosted Cu-Zn mineralization lacks stochiometric Co-phases and has low Co trace element concentrations. APT analyses of sphalerite containing up to 1 wt% Co, shows homogenous distribution of Co. The petrographic evidence suggests that the Co in the sphalerite is the result of Co remobilization through several stages related to metamorphism and physiochemical changes. The presence of additional Co-rich minerals (e.g. sphalerite and pyrite) may be important as additional sources of Co in future exploration as the demand of critical metals increases.

Acknowledgments

The authors would like to acknowledge funding and support from the Gecko Namibia exploration team, M. Zimmermann for his assistance with the EPMA, and G. Hawranek for assistance with EBSD analyses.

References

Allen NK (2016) Structurally controlled Cu-Zn-(Co-Pb) mineralization in the Neoproterozoic Ombombo Subgroup, Kaokoland, Namibia. Colorado School Mines.

Alves Dias P., Blagoeva D, Pavel C, Arvanitidis N (2018) Cobalt: demand-supply balances in the transition to electric mobility. Publications Office of the European Union 10:97710.

Bertrandsson Erlandsson V, Gopon P, Waldl H, Misch D, Ellmies R, Melcher F (2023) Sphalerite as a non-traditional critical metal source: correlative microscopy (EPMA, EBSD, APT) of cobalt-enriched sulfides from the sediment-hosted copper-cobalt Dolostone Ore Formation deposit, Namibia. Front Earth Sci 11:543. doi: 10.3389/feart.2023.1171859

Bertrandsson Erlandsson V, Wallner D, Ellmies R, Raith JG, Melcher F (2022) Trace element composition of base metal sulfides from the sediment-hosted Dolostone Ore. Formation (DOF) Cu-Co deposit in northwestern Namibia: Implications for ore genesis. J Geochem Explo: 107105.

European Commission (2020) Communication from the Commission to the European Parliament, the Council, the Economic and Social Committee and the Committee of the Regions. Critical Raw Materials Resilience: Charting a Path towards greater Security and Sustainability. Online: https://eur-lex.europa.eu/legal-content/EN/TXT/?uri=CELEX%3A52020DC0474.

Foster DA, Goscombe BD, Gray DR (2009) Rapid exhumation of deep crust in an obliquely convergent orogen: The Kaoko Belt of the Damara Orogen. Tectonics 28:1–24.

Frenzel M, Hirsch T, & Gutzmer J (2016) Gallium, germanium, indium, and other trace and minor elements in sphalerite as a function of deposit type—A meta-analysis. OGR:52–78.

Gopon P, Douglas JO, Meisenkothen F, Singh J, London AJ, Moody MP (2022) Atom probe tomography for isotopic analysis: development of the 34S/32S system in sulfides. Microsc Microanal 28:1127–1140.

Goscombe BD, Foster DA, Gray DR, Wade B (2017) Metamorphic response and crustal architecture in a classic collisional orogen: The Damara Belt, Namibia. Gondwana Res 52:80–124.

Goscombe BD, Gray DR, Hand M (2005) Extrusional Tectonics in the Core of a Transpressional Orogen; the Kaoko Belt, Namibia. J Petro 46: 1203–1241.

Goscombe BD, Hand M, Gray DR (2003) Structure of the Kaoko Belt, Namibia: progressive evolution of a classic transpressional orogen. J Struc Geo 25:1049–1081.

Guj P (1970): The Damara Mobile Belt in the south-western Kaokoveld South West Africa (PhD Thesis). Uni Cape Town / Precambrian Research Unit, Cape Town, South Africa.

Haley D (2018) 3Depict: Valued Point Cloud Visualization and Analysis Software. Retrieved from http://threedepict.sourceforge.net/

Hoffman PF, Halverson GP (2008) Otavi Group of the western Northern Platform, the Eastern Kaoko Zone and the western Northern Margin Zone. In R. M. Miller (Ed.), The Geology of Namibia: Neoproterozoic to Lower Palaeozoic (2nd ed., 13-69–13-136). Windhoek, Namibia: Geo Survey.

Hoffmann KH, Prave AR (1996) A preliminary note on a revised subdivision and regional correlation of the Otavi Group based on glaciogenic diamictites and associated cap dolostones. Com Geo Survey Namibia 77–82.

Onuk, P, Melcher F, Mertz-Kraus R, Gäbler HE, Goldmann S (2017) Development of a matrix-matched sphalerite reference material (MUL-ZnS-1) for calibration of in situ trace element measurements by laser ablation-inductively coupled plasma-mass spectrometry. Geost Geoanal Res 41:263-272.

Paton C, Hellstrom J, Paul B, Woodhead J, Hergt J (2011) Iolite: Freeware for the visualisation and processing of mass spectrometric data. J Ana Atomic Spectrometry 26:2508-2518.

Porada H (1989) Pan-African rifting and orogenesis in southern to equatorial Africa and eastern Brazil. Precambrian Research:103–136.

Thompson K, Lawrence D, Larson DJ, Olson JD, Kelly TF, Gorman B (2007) In situ site-specific specimen preparation for atom probe tomography. Ultramicroscopy 107:131–139.

Wilson SA, Ridley W I, Koenig AE (2002) Development of sulfide calibration standards for the laser ablation inductively-coupled plasma mass spectrometry technique. J Analy Atomic Spectrometry 17:406–409.

USGS (2020) Mineral commodity summaries 2020. Advance online publication. https://doi.org/10.3133/mcs2020

USGS (2022) 2022 Final List of Critical Minerals. Notices. https://www.usgs.gov/news/national-news-release/us-geological-survey-releases-2022-list-critical-minerals.

Geostatistical and geometallurgical investigation of Co in the Rocklands tailings deposit, Queensland, Australia

Rosie Blannin[1], Laura Jackson[1], Anita Parbhakar-Fox[1]
[1]WH Bryan Mining Geology Research Centre, Sustainable Minerals Institute, University of Queensland, QLD, 4072, Australia

Abstract. Historical mining and processing operations did not always target critical minerals, and typically had lower efficiencies than present day. As a result, mine wastes have the potential to become unconventional resources of critical minerals. To assess this potential, the contents and mode of occurrence of critical minerals in the mine wastes must be investigated through sampling, characterisation and modelling. This study applied several analytical methods to identify critical minerals in the Rocklands tailings deposit in Queensland, Australia, and characterise their deportment. The Co and Cu grades of the tailings deposit were modelled with co-kriging, a geostatistical method. The results were assessed in combination with mineralogical, textural and mineral chemistry data to investigate the resource potential of the Rocklands tailings. Cobalt and Cu are found to be hosted by a range of both primary and secondary sulphide and oxide minerals. Due to the complex nature of the materials, recovery of the critical minerals from the Rocklands tailings may require a range of processing technologies.

1 Introduction

Critical minerals are those of high importance for the economy and green energy transition, often with supply chain risks, e.g., Co, In, REEs, Sn, Ge, Ga and W. Many deposits in Queensland, Australia, are known to be endowed in critical minerals alongside the main commodities (Fig. 1). There is great potential to explore mine wastes in Australia and elsewhere as unconventional resources for critical minerals. In order to assess resource potential of mine wastes, the contents and mode of occurrence of critical minerals must be investigated through sampling, characterisation and modelling.

The Rocklands mine is one example of a deposit hosting critical minerals in Queensland (Fig. 1). The main commodity at Rocklands is Cu, but the deposit also hosts Au and Co, the latter of which is critical. The mineralisation at Rocklands comprises an enriched supergene oxide zone overlying a hypogene copper sulphide zone. The supergene zone reaches depths of up to 100 m, with variable development of chalcocite and secondary native copper and chalcocite. Surface outcrops comprise siliceous breccias with minor malachite and azurite. Primary copper sulphide mineralisation comprises coarse intergrowths of chalcopyrite as breccia infill, with pyrite, calcite, actinolite, magnetite and quartz. Cobalt grades range from 500 to 1,800 g/t and up to 3,390 g/t in the hypogene zones (Beams, 2009).

Rocklands was mined as an open pit operation between 2012 and 2018, targeting Cu, Co, Au and Fe. Native copper was recovered with gravity separation (jigs, gravity spirals, tables), while separate copper sulphide and pyrite concentrates were recovered with flotation. Magnetic separation of the flotation tailings was performed to recover magnetite. CuDeco (2018) reported that 2.3 Mt of ore was processed between 2015 and 2017, with a Cu recovery of 78 % (CuDeco 2017). As a result, significant volumes of tailings, possibly enriched in Co and Cu, were produced and stored in the Rocklands tailings facility.

This study aimed to sample, analyse and spatially model tailings deposit at Rocklands in order to assess the resource potential of Co, as well as Cu. Geostatistical modelling was implemented in 3D to model the Co and Cu grades in the tailings. Previous studies have successfully applied geostatistical modelling to tailings deposits (e.g., Parviainen et al. 2020; Wilson et al. 2021; Blannin et al. 2022, 2023). Furthermore, mineralogical and textural properties related to the recoverability of Co were investigated to evaluate the potential for re-processing of the Rocklands tailings.

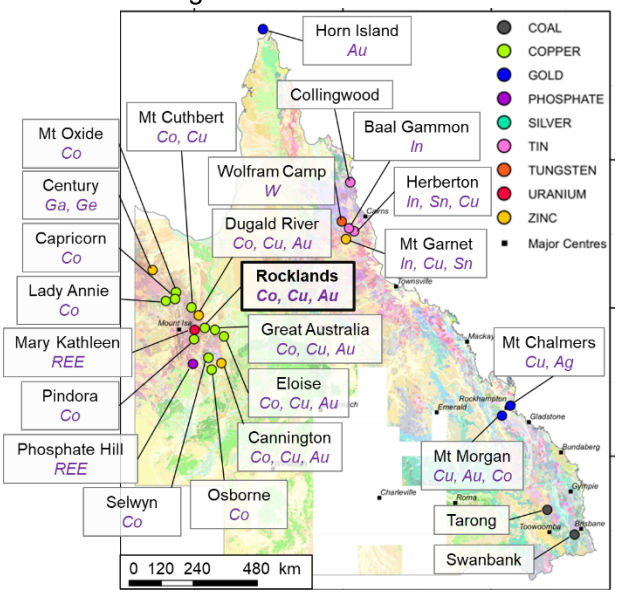

Figure 1. Map of critical minerals, alongside the main commodities, at operating mines and major deposits in Queensland, Australia. The Rocklands mine, the tailings of which are the focus of this study, is highlighted.

2 Methodology

2.1 Sampling and analysis

The tailings facility at the Rocklands mine was sampled with an auger at 24 locations (Fig. 2). A total of 139 samples were taken up to a maximum depth of 7 m. The base of the tailings was not intersected as to not damage the basal lining.

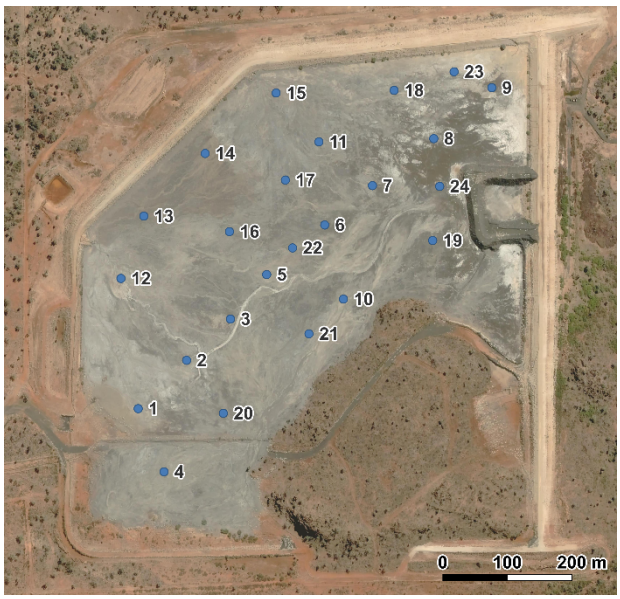

Figure 2. Map of the sample locations at the Rocklands tailings facility in Queensland, Australia.

The samples were sent to Australian Laboratory Services in Brisbane for sample preparation and geochemical analysis with inductively coupled plasma atomic emission spectroscopy or mass spectroscopy (ICP-AES/MS). The thirty samples with the highest Co assays were selected for mineralogical studies to determine the dominant modes of occurrence of Co, as well as Cu. Bulk mineralogy was measured by X-ray Diffractometry (XRD) at Queensland University of Technology, using a PANalytical X'Pert Pro powder diffractometer and cobalt Kα. The mineral liberation analyser (MLA), an automated mineralogy tool, was used to collect mineralogical and textural data on the potentially Co-bearing sulphide minerals, namely pyrite. The MLA measurements were performed at the Sustainable Minerals Institute, University of Queensland with the XBSE measurement mode. Laser ablation analyses were carried out to investigate the trace element distributions in the sulphide minerals. The analyses were performed at CODES Analytical Laboratories, University of Tasmania, using a RESOlution laser platform, equipped with a Coherent COMPex Pro 193 nm excimer laser and Lauren Technic S155 large format sample cell, coupled to an Agilent 7700 quadrupole ICP-MS.

2.2 Geostatistical modelling of chemistry

In order to investigate the spatial variability of critical minerals in the Rocklands tailings facility and estimate their average grades, geostatistical modelling was performed. Specifically, Co and Cu grades were interpolated using co-kriging, (Wackernagel 1995; Goovaerts 1997). The modelling was performed in R studio (R Core Team 2021), making use of the "gstat" package (Pebesma 2004; Gräler et al. 2016).

First, the Co and Cu grades were log-transformed. Variograms and cross-variograms were computed for the log-transformed variables with the following parameters: horizontal lag distance of 25 m; maximum horizontal distance of 375 m; vertical lag distance of 0.25 m; maximum vertical distance of 3.75 m; vertical angle tolerance of 2°. The variogram and cross-variogram models were automatically fitted by the "gstat" program, using exponential models and a range of 100 m. The sedimentary-style deposition of tailings forms a horizontally layered structure, resulting in a greater continuity in the horizontal direction than the vertical direction. An anisotropy factor of 0.00625 was calculated for fitting the variogram models, based on the horizontal and vertical ranges of the variograms.

Leave-one-out cross validation was performed to validate the geostatistical model (e.g., Goovaerts, 1997). This involves sequentially removing each sample from the dataset and using the geostatistical model to predict the value at that location. By comparing the original (observed) and predicted values, the quality of the modelling results can be evaluated. Following this, the Co and Cu grades were interpolated into a 3D grid across the tailings using co-kriging with the geostatistical model. The 3D grid had a horizontal spacing of 15 m and a vertical spacing of 1.5 m. The grid extended to a depth of 7.5 m, based on the available samples.

3 Results and discussion

3.1 Geochemistry

Geochemical analysis revealed that the Co grade varies from 200 to 1,275 g/t (average: 570 g/t) whilst Cu ranges from 304 g/t to 6,960 g/t (average: 2,021 g/t). Cobalt is strongly correlated with both S and Fe. However, there is a bimodal association pattern of Co and S, suggesting that Co is hosted in both sulphide and Fe oxides phases, and potentially a secondary sulphate or jarosite. The Cu remaining in the Rocklands tailings is potentially economically significant, with an average grade of 0.2 %. Positive Cu associations are seen with Zn, Ni and Au while a negative correlation is observed with S, suggesting that little Cu is sequestered in sulphides.

3.2 3D grade models

The cross-validation of the geostatistical model showed that there is an excellent correspondence between the observed (assay) values and those predicted by the geostatistical model, as seen by the observed-predicted (Obs-Pred) R^2 values of 89 % for Co and 75 % for Cu (Table 1, Fig. 4). The mean errors (ME) and correlations between the predicted and residual values (Pred-Res R^2) are low, showing that the geostatistical model is unbiased (Table 1). Therefore, co-kriging is shown to be an appropriate method for geostatistical modelling of the Rocklands tailings and should be applicable to other studies.

Table 1. Cross validation results for co-kriging.

	ME	Obs-Pred R^2	Pred-Res R^2
Co	7.0×10^{-5}	0.89	0.01
Cu	0.004	0.75	0.07

The summary statistics of the predicted Co and Cu grades are shown in Table 2. The mean grades of Co and Cu are around 535 and 1,631 g/t, respectively. This demonstrates that there are potentially economic grades of critical minerals in the Rocklands tailings. The Cu grade is more variable than the Co grade, with a relative standard deviation (standard deviation divided by mean) of ~ 40 % compared to ~ 15 % for Co.

Table 2. Summary statistics of the predicted Co and Cu grades (g/t). SD = standard deviation.

	2.5th perc.	Median	97.5th perc.	Mean	SD
Co	334	538	680	535	82
Cu	820	1,493	3,371	1,631	686

The spatial distribution of the critical minerals throughout the tailings is also of importance when investigating resource potential, as it may influence appropriate mining methods and re-processing routes. As such, horizontal maps of Co and Cu grades at 1.5 m depth intervals are plotted in Fig. 4.

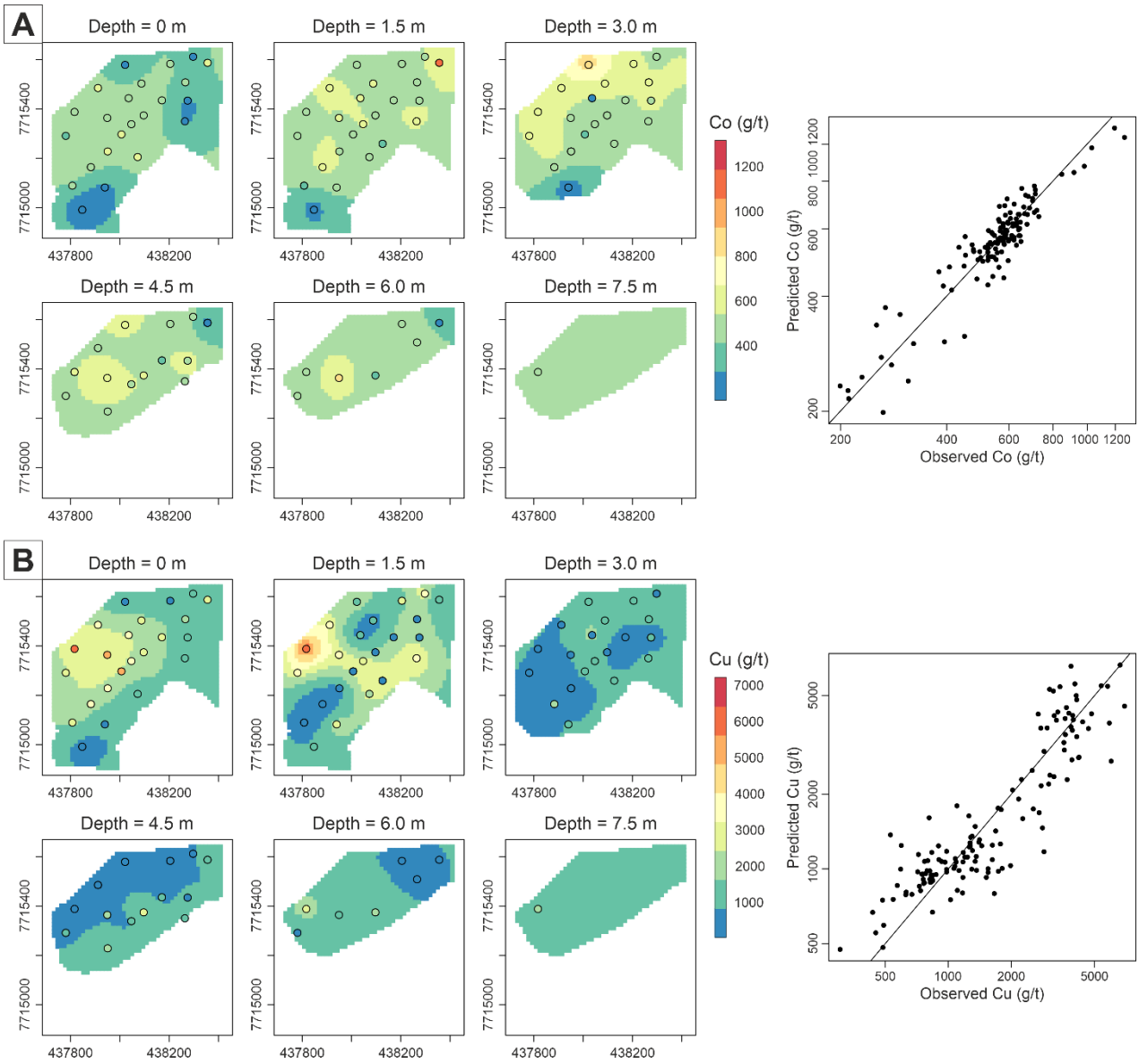

Figure 4. Heatmaps of the interpolated Co (A) and Cu (B) grades at 1.5 m depth intervals are shown on the left. The color-coded points show the sample locations and assay values. Cross-validation plot for the co-kriging of the Co and Cu grades are shown on the right, with the 1:1 line to show the good correspondence between the observed and predicted values.

Cobalt and Cu follow rather different spatial distribution trends (Fig. 4), suggesting that they are not (always) hosted by the same mineral(s) and may be concentrated in different tailings facies. Higher Co grades are concentrated in the central-north zone of the tailings, particularly at a depth of 3 m. In contrast, copper grades are higher at the surface, in the north-west and central zones. This may be in relation to the oxidised zone in the near surface of the tailings.

3.3 Mineralogy and textural properties

A total of 38 minerals were identified by MLA. The modal mineralogy of the tailings is dominated by quartz (~ 13.5 wt. %), plagioclase (~ 16 wt. %), Ca-amphibole (~ 15.3 wt. %), chlorite (~ 8.9 wt. %) and Fe oxide / magnetite (~ 12.8 wt. %). Pyrite was present in all samples (~ 3.1 wt. %) with two notably high samples (9.1 and 8.6 wt. %). Minor amounts of carrollite (up to 0.04 wt. %), a Cu-Co-bearing sulphide, were identified but cobaltite was not. A wide range of Cu sulphides (chalcopyrite, bornite, chalcocite, covellite) and Cu oxide or silicate minerals (cuprite, malachite/ azurite, chrysocolla) are present at varying concentrations. Jarosite was identified in all samples at < 1 wt. %. Notably, calcite contents of around 14.7 wt. % indicate that intrinsic neutralising potential is available within the tailings, reducing the potential for acid mine drainage.

Overall, there are likely to be at least three hosts of Co in the tailings: pyrite, pyrite weathering products and Fe oxide. The p80 of the pyrite grains ranges from ~ 75 to 180 µm. The abundance of fully liberated pyrite varies between ~ 44 and 75 %. Lower pyrite grades generally coincide with higher oxidisation and therefore poorer liberation of pyrite due to the formation of surface coatings. Pyrite also exhibits minor associations with pyrrhotite, jarosite and amphibole. Similarly, Fe oxide particles have mineral associations with plagioclase, chlorite and amphibole and similar liberation degrees to pyrite (between 32 and 78 % fully liberated).

Cobalt occurs in pyrite in the form of micro-inclusions and larger inclusions, leading to an average Co concentration of 10,412 ppm, and up to 51,815 ppm. For Cu, an average and maximum of 2,331 and 277,167 ppm occur, respectively, suggesting that pyrite contains intercalations of chalcopyrite. Corresponding to these Co and Cu concentrations in pyrite, and assuming an average pyrite grade of 3.1 wt. % in the tailings, around 60 % of the Co content in the Rocklands tailings is hosted by pyrite compared to only 5 % of the Cu content. The remainder of the Co may be (partially) hosted by Fe oxides. Copper appears to be dominantly hosted by Cu oxide minerals. Overall, Co and Cu are present in different mineral phases and their recovery from the range of sulphide and oxide phases present, both primary and secondary, will require different processing methods.

Whitworth et al. (2022) reviewed re-processing methods for mine wastes and found that different challenges are faced for the recovery of critical minerals when compared to primary deposits. For instance, the pyrite particle sizes observed would be amenable to flotation. However, the relatively poor liberation of pyrite, combined with weathering and surface coatings, would require additional processing steps to produce fresh surfaces prior to flotation. Additionally, the abundance of secondary phases may impact flotation responses. As a result, leaching or bioleaching may be preferable to recover Co and Cu from the Rocklands tailings.

4 Conclusions

This work aimed to demonstrate the importance of mine wastes as sources of critical minerals. By characterising the Rocklands tailings with a range of analytical methods, the critical minerals and the opportunities and challenges for their recovery were identified. Additionally, 3D models of Co and Cu in the Rocklands tailings deposit were produced as a first step to assessing the resource potential. Metallurgical test work should be performed to optimise the recovery of the critical minerals present in the Rocklands tailings.

Acknowledgements

The authors would like to thank the Department of Resources, Queensland, for providing funding (NEMI-UQ-06) to enable completion of this work.

References

Beams SD (2009) Geology and mineralisation at the Rocklands Copper-Cobalt deposits, Cloncurry District, Northwest Queensland, Australia. Proc 10th Bienn SGA Meet, Townsville, 17-20th August 2009.

Blannin R, Frenzel M, Tolosana-Delgado R, et al (2023) 3D geostatistical modelling of a tailings storage facility: resource potential and environmental implications. Ore Geol Rev 154. https://doi.org/10.1016/j.oregeorev.2023.105337

Blannin R, Frenzel M, Tolosana-Delgado R, Gutzmer J (2022) Towards a sampling protocol for the resource assessment of critical raw materials in tailings storage facilities. J Geochem Explor 236. https://doi.org/10.1016/j.gexplo.2022.106974

CuDeco (2017) Annual Report, CuDeco Ltd, pp 45.

CuDeco (2018) Rocklands Ore Reserve Update. Market release dated 22 March 2018, pp 45.

Goovaerts P (1997) Geostatistics for Natural Resources Evaluation. Oxford University Press, New York

Gräler B, Pebesma E, Heuvelink G (2016) Spatio-Temporal Interpolation using gstat. R J 8:204–218. https://doi.org/10.32614/RJ-2016-014

Parviainen A, Soto F, Caraballo MA (2020) Revalorization of Haveri Au-Cu mine tailings (SW Finland) for potential reprocessing. J Geochem Explor 218. https://doi.org/10.1016/j.gexplo.2020.106614

Pebesma EJ (2004) Multivariable geostatistics in S: the gstat package. Comput Geosci 30:683–691

R Core Team (2021) R: A language and environment for statistical computing. R Foundation for Statistical Computing, Vienna, Austria

Wackernagel H (1995) Ordinary Kriging. In: Multivariate Geostatistics. Springer Berlin Heidelberg, pp 74–81

Whitworth AJ, Forbes E, Verster I, et al (2022) Review on advances in mineral processing technologies suitable for critical metal recovery from mining and processing wastes. Clean Eng Technol 7. https://doi.org/10.1016/j.clet.2022.100451

Wilson R, Toro N, Naranjo O, et al (2021) Integration of geostatistical modeling into discrete event simulation for development of tailings dam retreatment applications. Miner Eng 164. https://doi.org/10.1016/j.mineng.2021.106814re

Copper in Onshore New Zealand: Mineral Deposit Types, Occurrences and Potential for this Critical Metal

Anthony (Tony) B. Christie
[1]GNS Science, Lower Hutt, New Zealand

Abstract. New Zealand has intermittently produced small quantities of Cu ore between 1846 and 1972. Most of the known Cu deposits are classified into four main types:

1.) Porphyry Cu deposits that consist of stockwork quartz veins deposited from hydrothermal fluids generated by Miocene stocks and dikes of diorite to granodiorite composition (e.g. Coppermine Island, Miners Head, Paritu, Ohio Creek);

2.) VMS hydrothermal deposits related to submarine volcanic activity, including Mesozoic deposits associated with chert and pillow lava in greywacke sequences (e.g. Kawau Island, Te Kumi, Maharahara, Moke Creek, Waitahuna), and Cretaceous deposits associated with marine basalts (e.g. Pupuke, Pakotai, Parakao, Lottin Point) and the Pounamu Ultramafics;

3.) Serpentine-hosted Fe-Cu deposits that are shear-controlled massive sulfide lenses in serpentinised ultramafic rocks of the Permian Dun Mountain Ophiolite Belt (e.g. D'Urville Island, Dun Mountain, Red Mountain); and

4.) Gabbroid-associated Ni-Cu/Cu-Ni deposits formed by magmatic crystallization in mafic magma chambers or conduits (e.g. Riwaka, Blue Mountain, Otama and Longwood igneous complexes).

Porphyry Cu deposits represent the best exploration target in terms of size potential, but higher Cu grades of the other deposit types may enable production from smaller deposits or as a by-product.

1 Introduction

Copper is a critical element required for electricity generation and transmission in the carbon neutral future and therefore it is timely to review New Zealand's Cu deposits and their exploration potential. A little more than 7500 t of Cu ore has been mined in New Zealand since the country's first underground mine was opened on Kawau Island in 1846. This production was mainly from porphyry Cu (Miners Head, Great Barrier Island), volcanogenic massive sulfide (Kawau Island, Pakotai, Pupuke, Parakao, Te Kumi, Maharahara, Moke Creek, Waitahuna), serpentine-hosted (D'Urville Island, Dun Mountain), and epithermal vein (Tui) deposits (Fig. 1 and Table 1). Occurrences of other types of Cu-bearing deposits include: porphyry Mo-Cu, gabbroid associated Ni-Cu and Cu-Ni, and skarn Cu deposits (Table 1). This study reviews available information on New Zealand Cu deposits to highlight their exploration potential.

Some small quartz vein and disseminated stratabound/stratiform Cu-bearing deposits, particularly in Fiordland National Park, are not described here because of their apparent small size and insufficient information available to determine their deposit type and genesis. See Williams (1974), Brathwaite and Pirajno (1993), and Christie and Brathwaite (1994) for additional information.

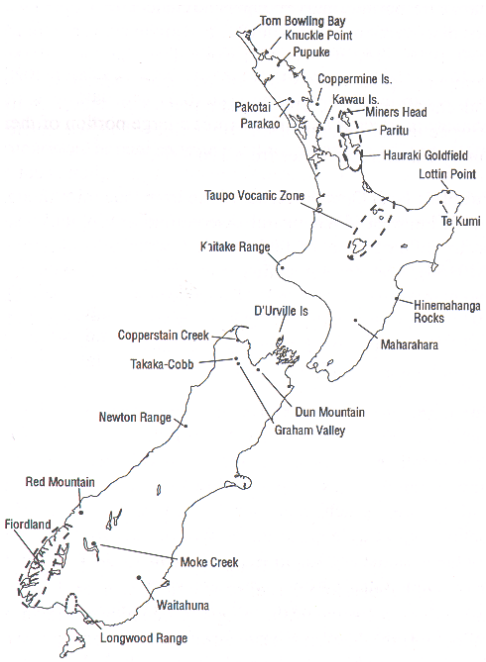

Figure 1. Location of Cu occurrences in New Zealand.

2 Porphyry Cu deposits

Porphyry Cu style mineralization occurs associated with the intrusion of Miocene quartz diorite, diorite and granodiorite stocks and dikes into Permian-Jurassic greywacke metasedimentary rocks and Miocene andesite in Northland (Knuckle Point, Coppermine Island) and the Hauraki Goldfield - Coromandel Volcanic Zone (Miners Head of Great Barrier Island, Paritu, Manaia, and Ohio Creek).

Exploration from the 1960s to 1980s included geochemical and geophysical surveys, and drilling of diamond drill holes (DDH) at Coppermine Island (4 DDH; Wodzicki and Thompson 1970), Paritu (3 DDH totalling 357 m; Bates 1980) and Ohio Creek (6 DDH totalling 2530 m; Brathwaite et al. 2001).

At Paritu, Cu mineralization is associated with a pluton (Paritu Plutonics) predominantly of quartz diorite to granodiorite composition. Exploration in the 1970s identified anomalous Cu geochemistry in Ongohi and Stony Bay streams (Bates 1980). Three DDH totalling 357 m were drilled in the Ongohi zone and intersected disseminated chalcopyrite, magnetite and pyrite in biotite quartz diorite, averaging 0.16% Cu. At Ohio Creek, a dacite stock and surrounding intrusion breccia host a quartz vein stockwork containing pyrite-chalcopyrite and returning an average grade of 0.18% Cu (Brathwaite et al. 2001). Some of the mineralization contains significant concentrations of gold, e.g. a 2.1 m interval of 17.3 g/t Au was intersected in drillhole OC6.

Table 1. New Zealand Cu deposit types and occurrences (source: Williams 1974; Brathwaite and Pirajno 1993; Christie and Brathwaite 1994).

	Form	Setting	Age	Minerals	Examples	Production (ore or conc)
Porphyry Cu	stockwork vn, dissem, breccia	stocks and dikes of diorite, quartz diorite, granodiorite, and dacite intruded into Jurassic metasediments	Miocene (~17-10 Ma)	py, cp (po, mo)	Knuckle Point, Coppermine Is, Miners Head, Paritu, Ohio Ck	Miners Head, Otea mine (2325 t, 1857-1867)
VMS, Ophiolite-hosted (Cyprus) type	stratiform lens, dissem	basalt, dolerite, chert	Cretaceous-Tertiary	py, cp, (mc, sp, gn, mt, hm)	Pupuke, Pakotai, Parakao, Purua, Lottin Point	Pupuke (30 t, 1892-1912 & 1964-1968), Pakotai(1400 t, 1947-1951), Parakao (1040 t, 1961-1966)
VMS associated with chert and pillow lava in greywacke	stratiform lens, dissem	chert and basalt in greywacke sequences	Permian-Jurassic	py, mc, cp, (po, sp, mt)	Kawau Is, Te Kumi, Maharahara, Moke Ck, Waitahuna	Kawau Is (2500 t, 1846-1860), Maharahara (50 t. 2% Cu, 1881-1891 & 1930), Moke Ck (1880s, 1917 &1968), Waitahuna (minor, late 1800s)
VMS in the Pounamu Ultramafics	stratiform lens, dissem	greenschist (metabasalt) and metaserpentinite	Permian-Triassic	py, cp	Newton, Diedrich, Meta, Bowen & Wilberg ranges, Whitcombe R	None
Serpentine-hosted Fe-Cu	lenses in shear zones	serpentinized ultramafic rocks of the Dun Mt Ophiolite Belt	Permian	py, cp, po, (mt)	D'Urville Is, Dun Mt	D'Urville Is (minor, 1879-1880), Dun Mt (930 t, 1886 & 1908-1909)
Gabbroid-associated Ni-Cu and Cu	dissem, lenses	gabbro, peridotite, trondhjemite, diorite, anorthosite, troctolite	Devonian-Permian (ca. 364 Ma for Riwaka)	po, cp, pent, py, mt (il, PGE)	Riwaka, Cobb Valley, Blue Mt, Mt Tapuaenuku, Otama IC, Longwood IC	None
Epithermal quartz vein	vn	andesite and dacite	Miocene	py, sp, gn, cp, Ag, Au	Monowai, Tui, Waiorongomai	Tui (404 t, 1967-1974)
Porphyry Mo	vn, stockwork vn, dissem	stocks of granite, granite geniss, quartz monzonite, granodiorite intruded into metasediments	Cretaceous (most between 100 and 120 Ma; ca. 122.5 Ma for Copperstain Ck)	py, mo, cp, (mt, gn, sp, Bi-min)	Eliot Ck, Copperstain Ck, Burgoo Stm, Karamea Bend, Mt Radiant, Taipo Spur, Bald Hill, McConnochie Ck	None
Skarn	dissem	skarn, schist, marble, granodiorite porphyry	Cretaceous (ca. 122.5 Ma)	py, cp, mo	Copperstain Ck	None

Ck = Creek, conc = concentrate, dissem = disseminated, IC = Igneous Complex, Is = Island, Mt = Mountain, R = River, Stm = stream, vn = vein. Minerals: Bi-min = Bi-minerals, cp = chalcopyrite, gn = galena, hm = hematite, il = ilmenite, mc = marcasite, mo = molybdenite, mt = magnetite, PGE = platinum group elements, po = pyrrhotite, py = pyrite, sp = sphalerite, () = minor metallic minerals

3 Volcanogenic massive sulfide deposits

Volcanogenic massive sulfide (VMS) hydrothermal deposits are formed in association with submarine volcanic activity. The first metalliferous mining in New Zealand was production of Cu ore from a VMS deposit on Kawau Island from 1846 to 1860. The known VMS deposits in New Zealand consist of small sulfide lenses composed mainly of pyrite and chalcopyrite that are associated with: (a) marine basalts of Cretaceous-Tertiary age in Northland and East Cape

(mafic-ultramafic or Cyprus type VMS; Shanks and Thurston 2010), (b) chert and pillow lava in greywacke sequences of Permian-Jurassic age, and their metamorphic equivalents (siliclastic-mafic or Besshi type VMS: Shanks and Thurston 2010), and (c) greenschists (metabasalts) and metaserpentinite of the Cretaceous Pounamu Ultramafics in Westland (Brathwaite and Pirajno 1993).

3.1 Mafic-ultramafic (Cyprus type) VMS deposits in Northland and East Cape

Previously mined Cu deposits at Pupuke, Pakotai and Parakao, and several other Cu deposits in Northland and at Lottin Point in East Cape are associated with allocthonous ophiolite sequences of Cretaceous-Tertiary age: the Tangihua Complex in Northland (Brathwaite et al. 2012) and Matakoa Volcanics in East Cape (Brathwaite et al. 2008). Geochemical trace and rare earth element studies (e.g. Whattam et al. 2004, 2005) have indicated that they contain island arc tholeiites, in addition to mid-ocean ridge basalts, and were formed in a suprasubduction zone setting close to their Late Oligocene obduction site. Exploration in East Cape from the 1980s, including reconnaissance and detailed geochemical, and airborne and ground based geophysical surveys, and 5 DDH at the Lottin Point prospect have so far failed to locate significant Cu resources.

3.2 Siliclastic-mafic or Besshi type VMS deposits associated with chert and pillow lava in greywacke

In both the North and South islands, several small siliclastic-mafic or Besshi type Cu deposits occur in Torlesse Supergroup and Waipapa Group greywacke, and Haast Schist associated with cherts and/or spilitic pillow lavas (Brathwaite and Pirajno 1993; Christie and Brathwaite 1994). The mineralization forms single or multiple stratiform bands, layers and lenses up to 6.7 m thick (Te Kumi) and 46 m long (Maharahara). Modern exploration has been limited to reconnaissance geochemical sampling.

3.3 Massive sulfide lenses in the Pounamu Ultramafics

Small massive sulfide lenses are present in Cretaceous greenschist metavolcanics and metaserpentinite of the Pounamu Ultramafics on the western side of the Southern Alps in Westland. The Pounamau Ultramafics are interpreted as ophiolite (ocean crust) basement to the Torlesse terrane (Cooper and Reay 1983). The sulfide lenses in the Wilberg Range appear to be the largest, with a 3 m to 9 m wide and 1500 m long mineralized zone containing numerous pyrite-chalcopyrite lenses (30 cm to 90 cm wide) (McPherson et al. 1970). Later exploration in the same area (Coleman 1980) identified a more extensive zone of mineralization comprising many small pods of massive sulfide within greenschist, with grades between 0.5 and 2.0% Cu. Higher grades, up to 5.1% Cu and 3.9 ppm Ag, were reported from sulfide lenses in the Diedrich Range.

4 Serpentine-hosted Fe-Cu

Small shear-controlled lenses of Cu mineralization are present in serpentinised ultramafic rocks of the Permian Dun Mountain Ophiolite Belt in the Nelson region (D'Urville Island and Dun Mountain) and in Southland (Red Mountain) (Williams 1994; Brathwaite and Pirajno 1993). Dun Mountain is the largest lens group, although even here the lenses are discontinuous and of small extent, with maximum dimensions of less than 150 m in length by 4 m in width. Primary ore was typically in the range of 1-1.5% Cu.

5 Gabbroid-associated Ni-Cu, Cu-Ni and Cu

In the South Island, several Paleozoic and Mesozoic mafic and ultramafic intrusive complexes, stocks and dikes have associated Ni-Cu, Cu-Ni or Cu mineralization formed from magmatic crystallization. The most significant occurrence is the Riwaka Complex in Northwest Nelson. The complex is a Late Devonian (ca. 364 Ma), SSW-NNE striking, elongate intermediate-mafic-ultramafic intrusive body 50 km long and ≤6 km wide representing a vertically sheeted conduit emplaced in an extensional back-arc post-orogenic setting (Turnbull et al. 2017). It intrudes metasedimentary rocks of Ordovician to Devonian age. The Ni-Cu mineralization occurs mainly in a 12 km long section of gabbro and pyroxenite between the Graham Valley and Prices Creek, where sulfide content ranges from 1-50%, characteristically with Ni>Cu. Drilling of 33 DDH between 1968 and 1976 gave best intersections of 0.60% Cu and 2.2% Ni over 1.4 m, 0.22% Cu and 1.52% Ni over 2.5 m, and 0.42% Cu and 1.42% Ni over 3.6 m (Christie and Turnbull 2016)

Nickel-Cu, Cu-Ni and Cu sulfide mineralization is also associated with mafic-ultramafic rocks in other areas (Table 1), some of which have received exploration attention for PGE, e.g. The Longwood Complex in Southland (Ashley et al. 2012).

6 Epithermal quartz veins

Chalcopyrite is present in several epithermal Au-Ag-base metal quartz vein deposits hosted in Miocene andesite and dacite of the Coromandel Group (Christie et al. 2007). The most Cu-rich veins are in the former gold mines between Tapu and Thames (e.g. Zeehan, Paroquet, Monowai, Comstock and Sylvia), and in the former base metal and gold mines at Tui and Waiorongomai respectively. Mining on the Champion and Ruakaka veins at Tui between 1967 and 1974, produced a concentrate containing 404 t of Cu, along with Zn, Pb, Ag, Au (Christie et al. 2007).

7 Porphyry Mo

Exploration in the late 1960s to early 1980s discovered a number of porphyry Mo deposits in the northwestern part of the South Island (Table 1). They are related to the emplacement of Late Cretaceous (120-106 Ma) I-type Separation Point suite granitoids into the Paleozoic S-type granites of the Karamea suite (e.g. Karamea Batholith) or quartzose metasedimentary rocks, mostly of the Aorere Group and Greenland Group (Eggers and Adams 1979; Brathwaite and Pirajno 1993). Most of the deposits are hosted by the metasedimentary rocks or by the intrusive Cretaceous granitic stocks, with a few hosted in Paleozoic Karamea suite granite (e.g. Taipo Spur). The geochemistry of the Mo-bearing granitoids is characterised by low K_2O, Rb, and F, and high Sr and Ti, confirming the classification of the deposits as Mo end members of the porphyry Cu-Mo family (Tulloch and Rabone 1993).

A slightly older (133.5 Ma) porphyry Mo deposit at Copperstain Creek occurs where granodiorite stocks and sills intrude lower Paleozoic Mount Arthur Marble and Onekaka Schist (Brathwaite et al. 2004). Skarn Cu mineralization is also present (see below). Exploration, including 14 DDH, outlined a Cu-bearing zone about 60 m wide and 760 m long, dipping steeply to the west and grading 0.06-0.6% Cu.

8 Skarn deposits

Copper occurrences with a skarn association include: Copperstain Creek, Mount Arthur, Arthur Range and Leslie River (Christie and Brathwaite 1994). At Copperstain Creek, skarns are developed in the calcareous rocks and exhibit a zonal pattern from an outer tremolite-actinolite-epidote±talc zone, through an intermediate diopside zone, to an inner garnet-magnetite±hedenbergite zone. Lateral zonation ranges from Mo in the granodiorite, out through Cu, to Pb-Zn in peripheral locations.

9 Conclusions

New Zealand has intermittently produced small quantities of Cu ore between 1846 and 1972, from several deposit types including porphyry Cu, VMS, serpentine-hosted Fe-Cu, and epithermal vein deposits. Although the known Cu deposits are all small, the varied geology and number of Cu occurrences offers exploration potential for future Cu production, possibly as a by-product of mining other metals (e.g. Au, Ni, PGE). Based on international examples, the porphyry Cu deposits are likely to yield the largest resources of Cu although other types may provide higher grades of Cu.

References

Ashley P, Craw D, MacKenzie D, Rombouts M, Reay A (2012) Mafic and ultramafic rocks, and platinum mineralization potential, in the Longwood Range, Southland, New Zealand. NZ J Geol Geophys 55:3–19

Bates TE (1980) Final report on EL 33-066 Paritu area, Coromandel Peninsula: Otter Mineral Exploration Ltd. NZ Petroleum & Minerals, MBIE unpublished report MR0378

Brathwaite RL, Christie AB, Lukovic B (2012) Desktop study documenting the occurrence and geological characteristics of known VMS deposits associated with Northland's Tangihua Complex. GNS Science Report 2012/08. 43 p

Brathwaite RL, Kamo SL, Faure K (2004) U-Pb geochronology and geochemistry of molybdenum-bearing granodiorite porphyry at Copperstain Creek, west Nelson, New Zealand. NZ J Geol & Geophys 47:219-225

Brathwaite RL, Pirajno F (1993) Metallogenic map of New Zealand. Institute of Geological and Nuclear Sciences Monograph 3.

Brathwaite RL, Sewell RJ, Christie AB (2008) Nature and tectonic setting of massive sulfide mineralization and associated sediments and volcanics in the Matakaoa Volcanics, Raukumara Peninsula, New Zealand. NZ J Geol Geophys 51:349-366

Brathwaite RL, Simpson MP, Faure K, Skinner DNB (2001) Telescoped porphyry Cu-Mo-Au, advanced argillic alteration and polymetallic quartz-sulfide-gold-anhydrite veins in the Thames District, New Zealand. Mineral Deposita 36:623-640

Christie AB, Brathwaite RL (1994) Mineral commodity report 4 - copper. New Zealand Mining 14:32-42

Christie AB, Simpson MP, Brathwaite RL, Mauk JL, Simmons SF (2007) Epithermal Au-Ag and related deposits of the Hauraki Goldfield, Coromandel Volcanic Zone, New Zealand. Econ Geol 102:785-816

Christie AB, Turnbull RE (2016) Exploration of nickel–copper mineralization in mafic and ultramafic rocks of the Riwaka Complex, West Nelson, South Island. AusIMM Monograph 31:453-462

Coleman AC (1980) Final report on the Wilberg area (PL 31527) Westland, New Zealand. Amoco Minerals NZ Ltd. NZ Petroleum & Minerals, MBIE unpublished report MR1664

Cooper AF, Reay A (1983) Lithology, field relationships, and structure of the Pounamu Ultramafics from the Whitcombe and Hokitika Rivers, Westland, New Zealand. NZ J Geol Geophys 26:359-380

Eggers AJ, Adams CJ (1979) Potassium-argon ages of molybdenum mineralization and associated granites of Bald Hill and correlation with other molybdenum occurrences in the South Island, New Zealand. Econ Geol 74:628-637

McPherson RI, Babcock RC, Howitt, G (1970) Final report on MPWs 8502, 8504 Wilberg Range, Westland. Kennecott Exploration Aust Pty Ltd. NZ Petroleum & Minerals, MBIE unpublished report MR1622

Shanks WCP, Thurston R eds (2012) Volcanogenic massive sulfide occurrence model.. U.S. Geological Survey Scientific Investigations Report 2010–5070–C, 345 p.

Tulloch AJ, Rabone SDC (1993) Mo-bearing granodiorite porphyry plutons of the Early Cretaceous Separation Point Suite, west Nelson, New Zealand. NZ J Geol Geophys 36:401–408, DOI: 10.1080/00288306.1993.9514586

Turnbull RE, Size WB, Tulloch AJ, Christie AB (2017) Theultramafic–intermediate Riwaka Complex, New Zealand: summary of the petrology, geochemistryand related Ni–Cu–PGE mineralization. NZ J Geol Geophys 60:270–295, DOI: 10.1080/00288306.2017.1316747

Whattam SA, Malpas JG, Ali JR, Smith IEM, Lo Ching-hua (2004). Origin of the Northland Ophiolite, northern New Zealand: discussion of new data and reassessment of the model. NZ Jour Geol & Geophys 47:383-389

Whattam SA, Malpas JG, Ali JR, Lo Ching-hua, Smith IEM. 2005. Formation and emplacement of the Northland Ophiolite, northern New Zealand: SW Pacific tectonic implications. Journal of the Geological Society, London 162:225-241.

Williams GJ (1974) Economic geology of New Zealand. AusIMM Monograph 4

Wodzicki A, Thompson BN (1970) The geology and mineralization of Coppermine Island. NZ J Geol Geophys 13:631-646, DOI: 10.1080/00288306.1970.10431334

New paradigms on phosphate mining in the Colombian industry: Crystallochemistry and geochemistry of phosphorites from the Lidita Superior Formation of Quebrada Talora, Colombia

Juan F. Correa-Briceño[1], Juan F. Galán-Palacios[1], Thomas Cramer[1]
[1]Departamento de Geociencias, Universidad Nacional de Colombia, Sede Bogotá

Abstract. X-ray-fluorescence (XRF) analysis and X-ray diffraction (XRD) techniques reveal rare earth elements (REEs) enrichment in granular sedimentary phosphorite rocks near the town of Piedras, Tolima, Colombia. These phosphorites are part of the Lidita Superior Formation, which is a Campanian-aged lithostratigraphic unit located in the Upper Magdalena Valley**.** High radiation levels of up to 0.6 µSv/h in these phosphorus strata stem from uranium found in concentrations of 65 ppm. Additionally, these intervals are rich in benthic foraminifera and bone remains and have shown an enrichment of up to 800 ppm of the sum of Rare Earth Elements and yttrium (ΣRE-Y). Based on a combined petrographic study that incorporates both X-ray diffraction (XRD) and X-ray fluorescence (XRF) analyses, we present a discussion on the potential of using radioactivity as an indicator of REEs enrichment. Furthermore, we propose that this approach can be utilized as an exploratory tool to optimize beneficiation processes and maximize the exploitation of these elements. Ultimately, our proposal aims to promote a transition towards a circular mining model.

1 Introduction

In Colombia, studies about the distribution of phosphatic deposits mainly in sedimentary rocks, phosphate prospecting techniques, and mining as well as fertiliser development were carried out since the 1960s by the Colombian Geological Survey (SGC, former Ingeominas) and other authors (Burgl et al. 1967; McKelvey 1967; Cathcart et al. 1967; Irving E 1967). About 90% of phosphatic rocks are used as raw material for producing fertilizers. Colombia is currently the fifth largest producer of phosphates on the continent, after the United States, Brazil, Peru and Mexico. In the last 5 years, approximately 65 thousand tonnes of phosphate have been produced on average per year in Colombia, and total World market demand is estimated to grow from 250 Mt in 2024 to 263 Mt in 2035, driven by the need to feed a growing world population and by the constraints of arable land expansion, which will require higher fertiliser application rates (UPME 2018).

Marine phosphorites may be interesting because of their potential to enrich rare earth elements and yttrium (RE-Y) (e.g. Hein et al. 2016) as well as U, Th and other incompatible elements, mainly incorporating them in different crystallographic sites of apatite-series minerals [$Ca_5(PO_4)_3(Cl,F,OH)$]. Global REE demand is increasing by 8-12% per year and is expected to double from 300,000 tonnes in 2022 to 600,000 tonnes in 2030 (World Energy Trade Platform 2022). So, obtaining REEs as a by-product of phosphorite mining becomes increasingly attractive and necessary. About this, the systematic exploration and extraction of REEs in Colombia is still in its beginnings and focus more on associated magmatic-hydrothermally formed minerals like monazite, coltan, cassiterite or uranium phases in the NW-Amazonian Craton region, with informal mining, if any.

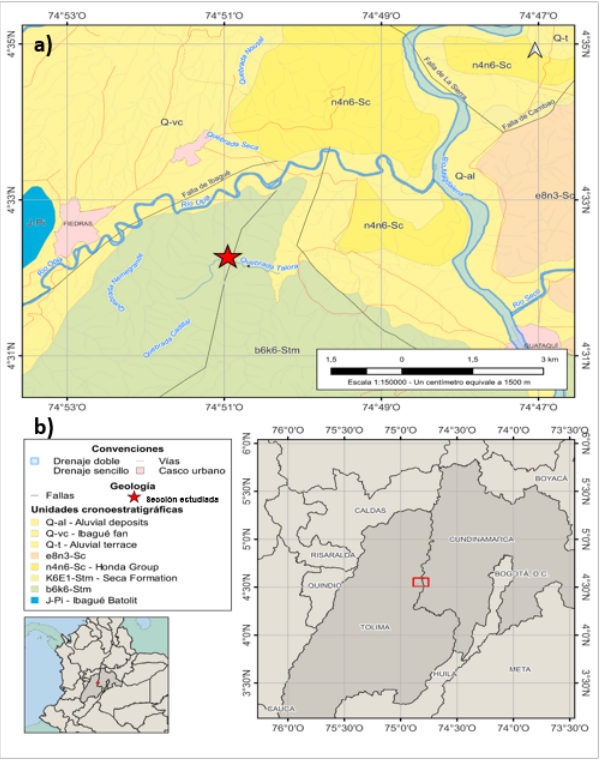

Figure 1. a Simplified geological map of the study area at scale 1:100,000, modified from the cartographic base of Girardot plate 245 of Acosta et al. (1999). See the lithostratigraphic unit studied, the Lidita Superior Formation, and the location of the Quebrada Talora. **b.** Location of the section studied. Physiographically, it is the northernmost part of the Upper Magdalena Valley, 40 km east of Ibague and 75 km west of Bogotá.

Much less is known in Colombia about REEs distributions in marine phosphorite deposits formed in different Cretaceous sedimentary rocks. Therefore, this study tries to fill partly this gap by determining whether phosphorite layers in the Cretaceous Upper Lidita Formation deposited in the

Upper Magdalena River Valley (Fig 1a) host economically interesting REEs concentrations.

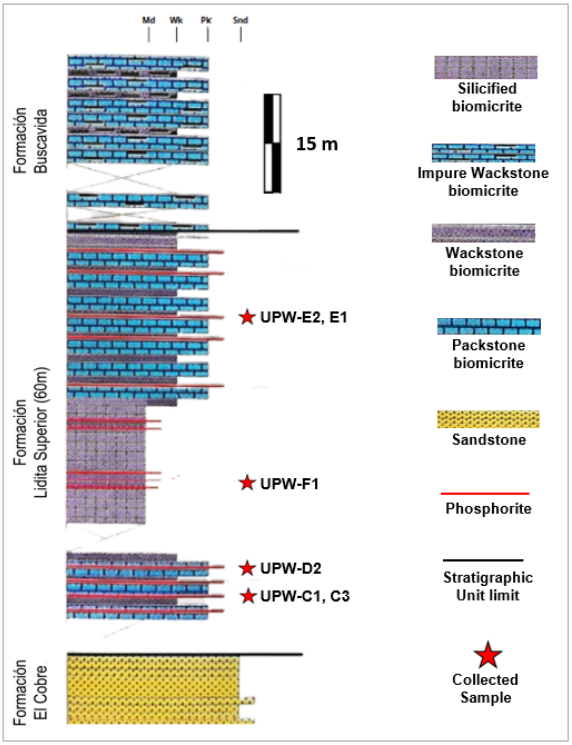

Figure 2. Stratigraphic column with the studied Upper Lidita Formation, showing, as red lines, the phosphorus-rich levels, and as red stars, the sampling sites. Modified from Guerrero et al. (2000).

2 Methodology

2.1 Sample collection and petrography

Two field trips to Quebrada (=Creek) Talora, east of Piedras town, in the Tolima Department, allowed field descriptions and collecting of 30 samples of the phosphorus-rich levels (Fig 2) previously reported by Guerrero et al. (2000) in the Lidita Superior Formation. From the 10 most significant samples, considering their texture, facial changes and distribution in the stratigraphic column, ten polished thin sections were prepared in the MinerLab laboratory.

2.2 X-ray fluorescence geochemistry

Phosphorite samples UPW-E2 and UPW-C3 were analysed at the X-ray spectroscopy laboratory of the Universidad Nacional de Colombia using a MagixPro PW 2440 Philips (WDXRF) X-ray fluorescence spectrometer, equipped with a rhodium tube, a maximum power of 4 kW and a sensitivity of 100 ppm for heavy metallic elements. Samples were powdered and dried at 105°C for 12 hours, then mixed with Merck spectrometric wax in a 10:1 ratio, homogenized by stirring, and compacted in a hydraulic press at 120 kN for one minute, to produce two pellets of 37 mm diameter. The measurement applying 11 scans was performed using the Semio5 software, in order to detect all the elements present in the sample, excluding H, Li, Be, B, N, C, O, noble gases and transuranic elements.

2.3 X-ray diffraction and γ-ray spectroscopy

Seven samples (UPW-C1, UPW-C3B, UPW-D1, UPW-E1, UPW-C3TF, UPW-E2 and UPW-C3TL) were analysed by means of a Bruker D2-Phaser diffractometer using Cu-K-alpha radiation without monochromator, 100 W, steps of 0.019° in a range of 4° to 60° 2theta. Following Thorez (1976), first the non-oriented sample powder <50 micrometers were analysed, then the finer fraction was suspended in deionized water and placed on a slide for subsequent desiccation and orientation of the clay minerals. For the analysis of expansive clays, ethylene glycol was included in their crystalline structure to increase the interlaminar distance (Thorez, 1976). Finally, the samples were heated at 515°C to extract the water molecules from the hydrated mineral structure. The diffraction patterns were analysed using the Rietveld method integrated in the Profex v5.1 software.

In addition, for radiation measurement on the UPW-E2 sample, a Probe VB6 VGO 2 gamma-ray spectrometer was used (Fig 5).

3 Comparison of results from XRD- and XRF analyses

The average P_2O_5 concentration in active phosphorite mines in Colombia was assumed to be 30% (Cantera et al. 2008). Our XRD phosphorite analyses reveal an average fluorapatite concentration of 49% in rocks ranging in thickness from 2 to 30 cm (Figs 2 and 3). Figure 4 compares XRF values in phosphorite samples UPW-E1 and UPW-C3TF, showing enrichment of Si, Al, Fe, S, Ce, Pb, and U at similar values of ~25% P_2O_5 and 300 ppm Cl in the Si-richer and Ca-poorer level UPW-C3TF. The 300 ppm Cl indicates a certain Cl-apatite content in the F-apatite determined by XRD. Total cerium of 600 ppm, lanthanum of 300 ppm and yttrium of 195 ppm are comparable to those obtained in seamount phosphorites described by Hein et al. (2016). Figure 6 shows a 124-fold enrichment process for Y, 1265-fold for La and 978-fold for Ce in the studied phosphorites compared to chondrites.

Figure 3 exhibits an inverse relationship between the amount of quartz and the amount of fluorapatite + calcite. This reflects a sedimentological process where the richest phosphate levels also show enriched Ce-La-Y concentrations and low silicification, which determines the ease of extraction of the material because silicification increases the costs of the beneficiation processes.

Data on REEs concentrations presented by Grosz et al. (1995) report on average 460 ppm REEs in phosphorite commonly contained in the francolite (a CO_2- and F-rich apatite) crystal structure. The phosphorites studied in this work (from the Lidita Superior Formation) contain up to 800 ppm Ce-La-Y contained in the fluorapatite structure, a 73% enrichment with respect to those compiled by Grosz et al. (1995). Assuming a typical phosphorite used in fertilizer manufacturing has the same REEs content, the amount of phosphate rocks mined worldwide annually contains more than 70,000 t of REEs.

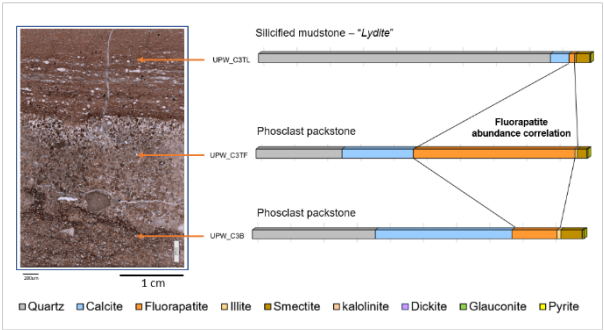

Figure 3. XRD results at three levels with distinguishable sedimentological features in the digitalized thin section C3A which shows the predominant lithologies (silicified mudstone "lydite" and phosphorites) in the lower and upper segment of the studied lithostratigraphic unit (Fig 2). Nomenclature after Trappe (2001).

4 Approach to new paradigms for phosphate rock exploration and exploitation in Colombia

From sixty-three phosphatic rocks mining titles in Colombia, 70% were being exploited and 30% were under construction and assembly (UPME 2018). The production of phosphate rock in Colombia in 2016 was 66,324 tonnes per year. Assuming a 50% benefaction rate when extracting RE-Y as a co-product of phosphoric acid, considering the average production of phosphate rock in Colombia and the total values of ∑Ce-La-Y exposed in this work, Colombia has the potential to extract up to 1300 tonnes of RE-Y and become one of the main REE-producers in Latin America.

Wu et al. (2018) and Emsbo et al. (2015) demonstrated the feasibility of solvent extraction of REEs as a co-product of phosphate mining, thus phosphorites are now considered an important potential source for industrial REEs supply. This work may awake the interest of private exploration companies and public entities such as the SGC or the ANM in a new exploration target which includes REEs beneficiation processes during the phosphate extraction emulating the circular mining models of developed countries such as China, USA and Russia, thus providing an opportunity for Colombia to diversify its mineral basket, provide competitive conditions that promote the exploration and exploitation of REEs, generate new sources of employment and tax revenues for the regions, making the country more attractive to investors and, at the same time, allowing the areas to be exploited in an orderly and efficient manner, contributing to social development, in harmony with the environment and with other economic activities.

Different methods exist to extract REEs from phosphorites, including acid leaching, solvent extraction and precipitation; these methods are expensive and require specialized technologies, but the growing demand for REEs has prompted research and development of more efficient and economic processes that will have to be implemented to optimize the beneficiation process. Recovery of these marine-sediment-hosted REEs would require the addition of costly infrastructure and changes in extractive processing to the existing mining operations. Production of RE-Y as a co-product of phosphorite mining would be advantageous if considered in the early stages of planning a new mining operation.

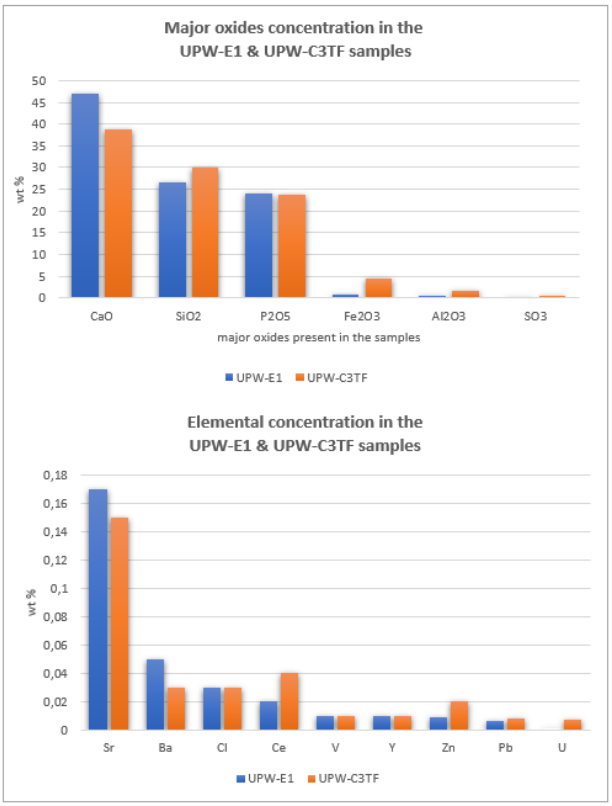

Figure 4. Bar charts of XRF-element concentrations in phosphorite samples UPW-E1 and UPW-C3TF.

Isotope	Concentration	Contribution of total radioactivity
Uranium	8.0 ppm	59.7%
Thorium	5.4 ppm	40.3%

Figure 5. Gamma-ray spectroscopy results for sample UPW-E2.

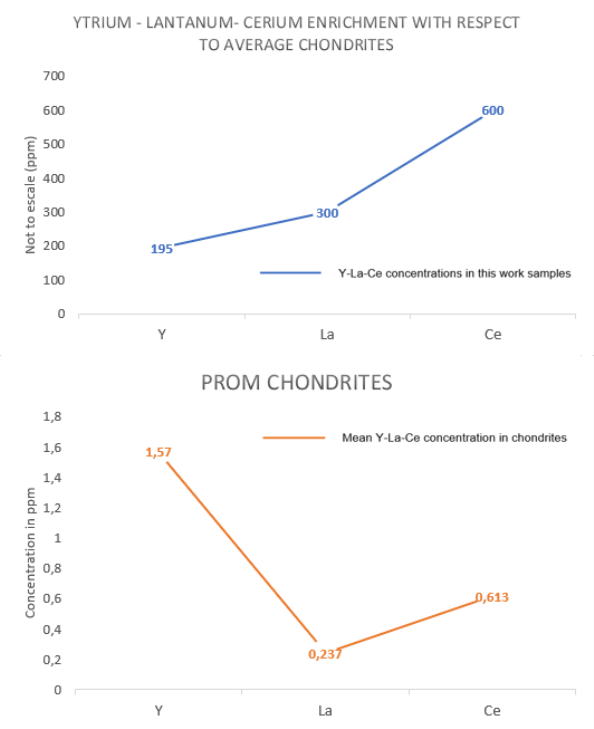

Figure 6. Ce-La-Y abundance of the UPW-E1 & UPW-C3TF samples and the average abundance of Ce-La-Y in chondrites after McDonough and Sun (1995).

5 Conclusions

Deposits with high RE-Y contents, such as the marine phosphorites analysed in this research, could help supply the RE-Y needed for high-tech and green technology applications without creating an oversupply. The Ce-La-Y concentrations (up to 800 ppm in total) are high enough to be considered as a co-product of phosphorite extraction. Combined XRF and XRD analysis indicates that fluorapatite is the main host of P and REE; elements such as Ce, La, Y, Sr and U replace Ca- cations in the crystal structure of fluorapatite (Trappe 1998). This inquiry provides evidence that Colombia's phosphate exploration and extraction endeavours must be invigorated by novel exploratory paradigms that allow for the assessment of beneficial phosphate recovery processes. Phosphorite, a potentially economic REEs resource, represents a prospect that warrants extensive and systematic investigation to ensure that its extraction not only persists but is optimized to capitalize on elements that will be instrumental in the nation's development and energy transition.

Acknowledgments

We are grateful to the SGA for the financial support to present this work at the 17th SGA Biennial Meeting, also to Professor Carlos Alberto Sánchez for his advice and support, as well as to Denis Oi Ulu for giving us his time and experience to carry out this research, to the Lattice laboratory with Professor Gustavo Sarmiento for supporting us in carrying out the XRD-analysis and to the MicrofluidSpectral Laboratory for the digitization of the thin sections.

References

Acosta J, Guatame R, Torres O, Solano F (1999) Geología de la Plancha 245 Girardot [Map]. INGEOMINAS.

Bürgl H, Botero D (1967) Las capas fosfáticas de la Cordillera oriental. Boletín Geol 15:7-44.

Cantera V (2008) Selección de la mejor alternativa para la industrialización de la roca fosfórica del Dpto. del Huila. Gobernación Huila 1:1-33

Catchcart J, Zambrano F, Mojica P (1967) Roca fosfática en Colombia. Boletín Geol 15:65-162.

Emsbo P, McLaughlin P, Breit G, du Bray E, Koenig A (2015) Rare earth elements in sedimentary phosphate deposits: Solution to the global REE crisis? Gondwana Research Int Geol J 27(2):776–785. https://doi.org/10.1016/j.gr.2014.10.008

Grosz A, Meier A, Clardy B (1995) Rare earth elements in the Cason Shale of Northern Arkansas: a geochemical reconnaissance. Arkansas Geological Commission Circular IC-33:22-55

Guerrero J, Sarmiento G, Navarrete R (2000) The Stratigraphy the W Side the Cretaceous Colombian Basin in the Upper Magdalena Valley. Reevaluation of Selected Areas and Type Localities Including Aipe, Guaduas, Ortega, and Piedras. Geol Colombina 25:45-110.

Hein J, Koschinsky A, Mikesell M, Mizell K, Glenn C, Wood R (2016) Marine Phosphorites as Potential Resources for Heavy Rare Earth Elements and Yttrium. Min: 6:88-92. doi:10.3390/min6030088

Irving E (1967) Conceptos preliminares sobre el Desarrollo y uso de fertilizantes en Colombia. Boletín Geol 15:163-174.

McDonough W, Sun S (1995) The composition of the Earth. Chemical Geol 120(3-4):223–253. doi:10.1016/0009-2541(94)00140-4.

McKlevey V (1967) Nuevas técnicas en la prospección para yacimientos de fosfatos. Boletín Geológico 15:45-64.

Thorez J (1976). Practical identification of clay minerals. Min 13(2): 238–239. doi.org/10.1180/claymin.1978.013.2.11.

Trappe J (1998) Phanerozoic Phosphorite Depositional Systems. A Dynamic Model for a Sedimentary Resource System. Springer, Germany

Trappe J (2001) A nomenclature system for granular phosphate rocks according to depositional texture. Sedimentary Geol 145(1–2): 135–150. doi.org/10.1016/s0037-0738(01)00103-8

Unidad de Planeación Minero-Energética (2018) Informe de gestión. https://www1.upme.gov.co/InformesGestion. Accessed 05 January 2023.

World Energy Trade (2021) Canada's first rare earth producer begins shipping concentrate. https://www.mining.com/canadas-first-rare-earth-producer-begins-shipping-concentrate/. Accessed 26 December 2022.

Wu S, Wang L, Zhao L, Zhang P, El-Shall H, Moudgil B, Huang X, Zhang L (2018) Recovery of rare earth elements from phosphate rock by hydrometallurgical processes – A critical review. Chem Eng J 335:774–800 doi.org/10.1016/j.cej.2017.10.143

Fluid inclusions host germanium in acicular sphalerite from the carbonate-hosted Zhulingou Pb-Zn deposit, South China

Alexandre Cugerone[1], Kai Luo[2], Denis Fougerouse[3,4], Jia-Xi Zhou[2], Vincent Motto-Ros[5]
[1] *Department of Earth Sciences, University of Geneva, Switzerland*
[2] *Key Laboratory of Critical Minerals Metallogeny in Universities of Yunnan Province, Yunnan University, China*
[3] *School of Earth and Planetary Sciences, Curtin University, Australia*
[4] John de Laeter Centre, Curtin University, Australia
[5] *Institut Lumière Matière UMR 5306, Université Lyon 1 - CNRS, France*

Abstract. Sphalerite is frequently considered to host critical metal concentrations such as Ge, Ga and In. These elements are thought to be mainly incorporated via substitution mechanisms into the sphalerite lattice. However, the nanoscale distribution of Ge, Ga and In is still poorly understood, especially if these elements are incorporated in the sphalerite crystal lattice or in other discrete mineral and/or fluid phases. Using a combination of microstructural, geochemical and nanoscale observations, a new type of Ge occurrence is recognized in stratabound sphalerite from the Zhulingou carbonate-hosted Zn(-Ge) deposit. Early stage sphalerite is represented by acicular crystals with high Ge concentrations (up to ~2000 ppm), which are positively correlated with Pb, Fe, and Mn concentrations. High Ge concentrations usually occur in dark brown oscillatory coloured bands, which are interpreted to have formed through rapid precipitation of sphalerite. Preliminary nanoscale data, performed with atom probe tomography (APT), indicate that Ge and related elements are mainly found in nanoscale fluid inclusions, and subordinately in nanoscale Ge-Pb rich phases. This study promotes the use of nanoscale studies to better understand the sequestration of critical metals in sulfides.

1 Introduction

Sphalerite frequently contains significant quantities of critical metals such as Ge, Ga and In. Solely based on chemical data conducted at the micron scale, these concentrations are frequently considered to be hosted in the sphalerite lattice (Cook et al. 2009; Belissont et al. 2016; Hu et al. 2021). The distribution of Ge, Ga and In in sphalerite may be complex and trace elements might be hosted in various microscale chemical zones such as sector zones, micrometric rhythmic bands or millimetric oscillatory color bands.

Acicular sphalerite frequently exhibits millimeter scale oscillatory color bands and can host significant amount of Ge (Cook et al. 2015; Luo et al. 2022). In this case, Ge is frequently correlated with Pb, Mn, Fe. However, in euhedral sphalerite, Ge is commonly correlated with Cu (Belissont et al. 2016).

Very few studies exist at the nanoscale, and presently, they don't consider all the sphalerite types, especially acicular sphalerite. A recent study describes the nanoscale distribution of Ge in Cu-rich sphalerite, showing Ge mostly occurring in sphalerite lattice in euhedral sphalerite, or Ge hosted in Ge-Cu rich minerals (briartite) in deformed sphalerite (Cugerone et al. 2021; Fougerouse et al. 2023).

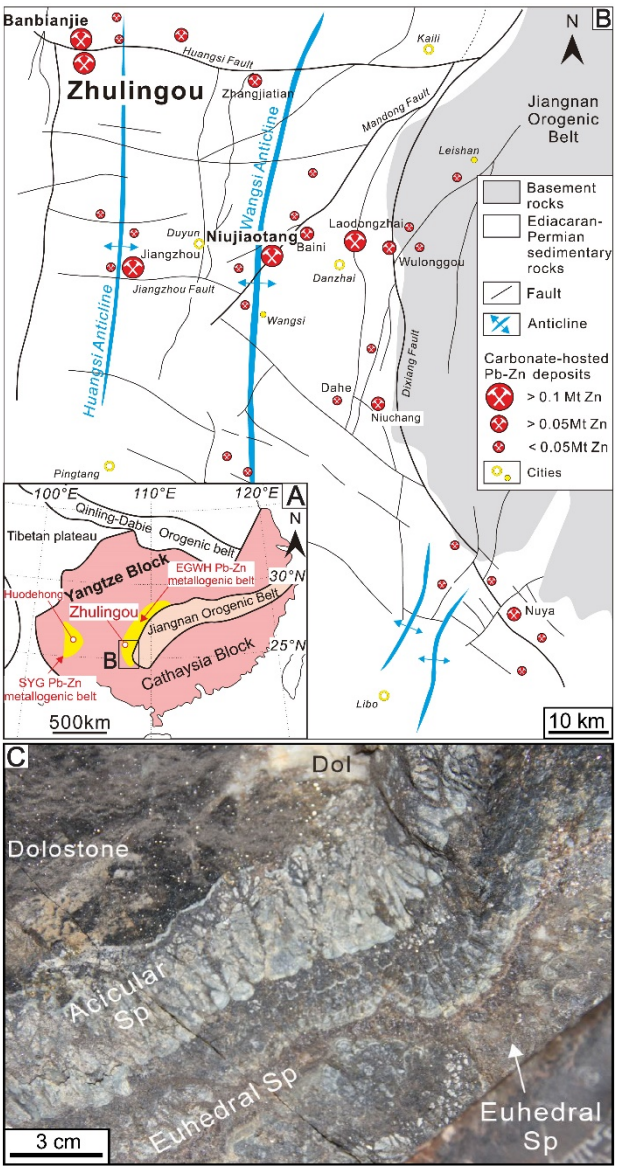

Figure 1. A. Location of the Zhulingou deposit in the eastern Guizhou-western Hunan (EGWH) metallogenic belt, South China. B. Simplified structural map showing the location of Zhulingou and the E-W Huangsi fault. C. Outcrop photo of a typical stratabound Pb-Zn ore body from Zhulingou. Note the presence of euhedral sphalerite generally more developed at the center of the stratabound bodies.

At Zhulingou, a mix of acicular and euhedral sphalerite represent a perfect material to study the incorporation of Ge depending on the sphalerite texture and their related formation conditions. In this study, we performed textural and chemical measurements with multiple techniques, from the microscale with electron back-scattered diffraction (EBSD), laser ablation coupled plasma mass spectrometry (LA-ICPMS), and laser-induced breakdown spectroscopy (LIBS), to the nanoscale with high-angle annular dark-field scanning transmission electron microscopy (HAADF-STEM) and atom probe tomography (APT) measurements.

2 The Zhulingou deposit

South China is known to host about one thousand Pb-Zn(-Ge) carbonate-hosted deposits. The Zhulingou Zn-Ge deposit (0.28 Mt Zn and >400 t Ge @ 97.9 g/t) is part of the eastern Guizhou-western Hunan (EGWH) metallogenic belt, South China (Figure 1A). This deposit is hosted in Devonian carbonate rocks and is lithologically and structurally controlled. The deposit is composed of stratabound orebodies hosted in carbonate-mudstone facies transition zones and late Paleozoic faults (Huangsi fault; Figure 1B).

At Zhulingou, two hydrothermal (< 200 °C) stages are recognized (Figure 1C; Luo et al. 2022): i) an early stage is composed of acicular sphalerite with oscillatory color bands and ii) a late stage is constituted of euhedral sphalerite with sector zones. From acicular to euhedral sphalerite, Ge concentrations decrease progressively with mean contents from 1009 to 490 ppm Ge, respectively (Luo et al. 2022).

3 Methods

In this study, we have analysed two representative samples where acicular and acicular-euhedral sphalerite are well preserved. These two samples were selected among sixty samples collected at Zhulingou.

EBSD analyses were carried out by the NordlysNano + AZtecHKL electron backscattered diffraction (EBSD) system from Oxford Instruments, on a FEI Quanta 450 FEG environmental scanning electron microscope at China University of Geosciences, Wuhan, China. Working conditions were as follows: 20 kV accelerating voltage, 25 mm working distance, 70°sample tilt angle. The sample was uncoated and well-polished for better pattern quality in a low-vacuum mode of 30 Pa. A step size of 1 µm was chosen. The Channel 5+ software was used for processing the data and generating the maps.

Laser-Induced Breakdown Spectroscopy (LIBS) multi-elemental imaging was performed at the Institute Lumière Matière, University of Lyon 1 (France). The two samples were analysed using a nanosecond Nd:YAG laser with a pulse energy of 600 lJ operating at 100 Hz at the fundamental wavelength (1064 nm). A 15x magnification lens (LMM-15X-P01, Thorlabs, Germany) was used to focus the laser pulses on the sample surface. In this configuration, the size of the ablation craters for a single laser shot was in the range of 8 µm. In the shown images, the lateral resolution (step size) was 19 µm. All experiments were conducted at room temperature under ambient pressure conditions. In addition, the laser pulse energy and its focus onto the sample were strictly controlled. Two spectrometers were configured to detect intense lines of Ge, Pb and Fe. The general protocol used for the construction of the elemental images is described in Motto-Ros et al. (2019).

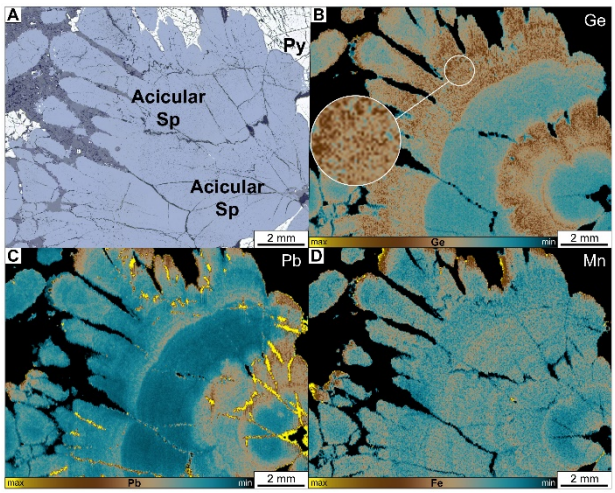

Figure 2. A. Reflected light microphotograph of acicular sphalerite from Zhulingou. B-D. LIBS Ge, Pb and Mn maps of the area in (A). Note the positive correlation in Ge and Pb in acicular sphalerite. In oscillatory bands, Ge does not show a homogeneous distribution in the Ge-rich oscillatory bands. Very high Pb concentrations are observed in fractures associated with organic matter.

LA-ICP-MS mapping was performed on a sphalerite sample with a mix of acicular and euhedral textures to determine minor and trace element concentrations, using a NWR ablation system (λ = 193 nm) coupled to an iCAP RQ ICP-MS instrument at Guangzhou Tuoyan Analytical Technology Co., Ltd., Guangzhou, China. LA-ICP-MS elemental mapping was performed using the same laser ablation system with similar carrier gas settings as for spot analysis. The selected area (~1 mm * 5 mm) was mapped using laser energy of 3.5 J/cm^2, a repetition rate of 20 Hz, 10 µm spot size, and stage translation speed of 40 µm/s. The following isotopes were selected: ^{23}Na, ^{29}Mg, ^{32}S, ^{55}Mn, ^{57}Fe, ^{65}Cu, ^{70}Zn, ^{71}Ga, ^{74}Ge, ^{75}As, ^{107}Ag, ^{111}Cd, and ^{208}Pb. Data were processed using an Excel-based software Iolite 3.6 to perform off-line selection and integration of background and analysed signals, time-drift correction, and quantitative calibration.

Transmission electron microscopy (TEM) on the acicular sphalerite was prepared by Ga-ion milling using a Focused Ion Beam device (FEI-FIB200) at the Institute of Geochemistry, Chinese Academy of Sciences, Guiyang, with an acceleration voltage of

30 kV. High-angle annular dark-field scanning transmission electron microscopy (HAADF-STEM) and high-resolution TEM (HRTEM) analyses were performed at the Electron Microscopy Center of the Guangzhou Institute of Geochemistry, Chinese Academy of Sciences, Guangzhou.

Five APT specimens adjacent to TEM targets were prepared from the investigated sphalerite to investigate the detailed chemical composition. A TESCAN Lyra3 Ga^+ focused ion beam scanning electron microscopy (FIB-SEM) was used to prepare atom probe needle-shaped specimens. The specimens were then analysed by the CAMECA LEAP 4000X HR Geoscience Atom Probe in the John de Laeter Centre at Curtin University (Perth, Australia). During the ~ 5 h acquisitions, 15 million ions were collected from each of two specimens (specimen 1 and 2) at an evaporation rate of 0.01 ions/pulse, a UV laser (l = 355 nm) energy of 45-50 pJ per pulse, and a pulse rate of 125 kHz. The data was reconstructed in 3D using parameters suggested by Fougerouse et al. (2022).

4 Trace element distribution in acicular sphalerite

Acicular sphalerite is composed of pluri-centimeter-size crystals (Figure 2A) with radial shapes which can be observed with light grey to brown colors in hand specimens (Figures 1C and 2A). Oscillatory zoning coloured from dark to light brown under plane polarized light are perpendicular to the maximum length of acicular crystals (Figures 2 and 3). Importantly, Ge and Pb concentrations (up to few thousands of ppm) are noticed, with a generally positive correlation, except in fractures where Pb-rich organic matter is noticed (Figures 2B-C). Manganese concentrations are also broadly correlated but occur in lower concentrations than Pb and Ge in sphalerite (up to ~ 100ppm Mn; Figure 2D).

In Figures 3A-B, EBSD maps show higher amounts of low-angle misorientation (1-5°) as well as twin boundaries (Figures 3C-E) in acicular sphalerite compared to euhedral sphalerite. LA-ICP-MS maps (Figures 3F-L) show important zoning patterns. Dark brown bands are rich in Mn, Ge, Fe, and Pb. Zones with high Ge concentrations generally correspond to zones with high Na concentrations. Gallium and Cd are negatively correlated to Ge.

5 Nanoscale study in acicular sphalerite

At nanoscale, APT measurements were performed on acicular sphalerite to detect the distribution of Ge and related elements. Numerous up to ~ 60 nm-sized clusters are identified and contain Na, Fe, Ca, Ga, Ge, Cd, H_3O^+, and Pb (Figure 4). They are generally distributed homogeneously but locally depleted close to twin boundaries (low cluster density area in Figure 4A). Germanium and Ga reach up to 2516 ppm and 416 ppm in the clusters, and 285 ppm and 173 ppm in the lattice, respectively. Hydrogen concentrations in Na-Pb clusters are up to 4230 ppm, considerably higher than in the lattice (10 ppm) and suggest the presence of aqueous fluids in the clusters based on the geometrical outlines and relatively light contrast TEM/HAADF bright-field image. HAADF and TEM images show the occurrence of germanium particles associated with galena and porosity in acicular sphalerite (Figure 4).

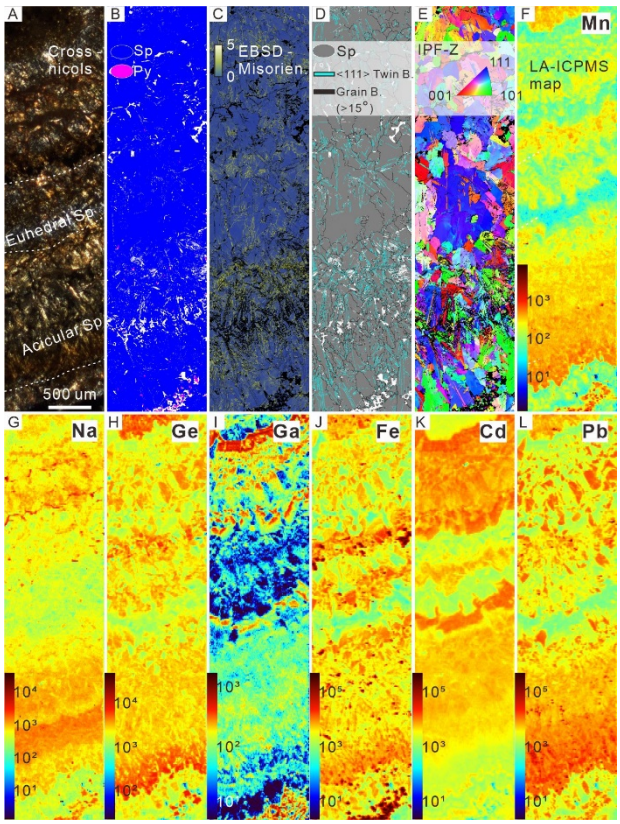

Figure 3. Micro-textures and LA-ICP-MS maps of acicular-euhedral sphalerite. A. Plane polarized transmitted light scan. B. Phase map acquired with EBSD. C. EBSD map showing low angle misorientation (1-5°). C. EBSD map showing high angle misorientation boundaries such as twins (60°) and grain boundaries (15°). D. EBSD inverse pole figure according to the Z-axis map. F-L. LA-ICP-MS maps of Mn, Na, Ge, Ga, Fe, Cd and Pb.

6 Discussion and implications

One of the most common sulphides with observed oscillatory banded textures is sphalerite (Ramdohr 1969; Barrie et al. 2009). These textures can be associated with acicular crystals (Ramdohr 1969; Beaudoin 2000) typically formed by supercooling (< 150 °C) and/or supersaturation conditions, inducing rapid crystal growth. Based on our observation at Zhulingou, we suggest that these conditions of quick precipitation of zinc sulphide are optimal for the preservation of significant concentrations of critical metals (Ge, Ga). Paradoxically, these conditions may not be ideal for the incorporation of trace metals in the sphalerite lattice. Most of the Ge and other elements like Na, K, Pb, Mn are observed in nanoscale clusters. These

clusters are interpreted as nanoscale fluid inclusions because of their concentrations in light elements (Na, Ca, K, H) and their characteristic rounded to elongated shapes. These nanoscale fluid inclusions are primary and not associated to late structures such as fractures or low angle misorientation (1-5°). Local nanoscale mineral phases are also inferred but directly associated with nanoscale fluid inclusions.

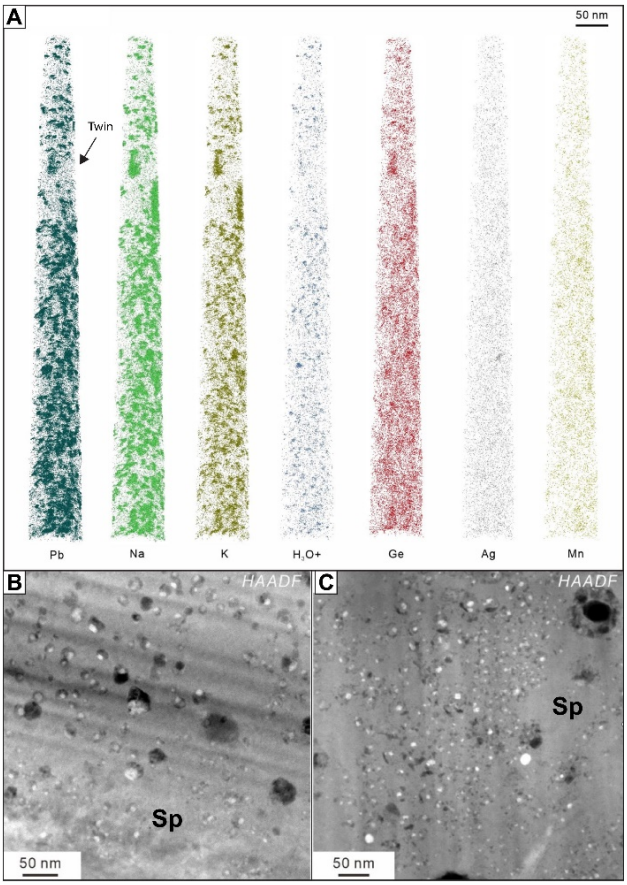

Figure 4. Nanoscale distribution of Ge and related elements in clusters/fluid inclusions hosted in acicular sphalerite. A. Atom probe map showing the distribution of Pb, Na, K, H3O+, Ge, Ag and Mn. B-C. HAADF images showing random distribution of the clusters at nanoscale. In these clusters, two phases (presumably liquid+vapor) are frequently observed, indicating occurrence of fluid inclusions. Brighter spots represent Pb(-Ge) solids.

Nanoscale studies are key to understanding the precise incorporation mechanism of critical metals in sphalerite. Although previous studies interpreted (based on geochemical analyses) that Ge was mostly incorporated in the sphalerite crystal lattice (Cook et al. 2009; Belissont et al. 2016), our results could indicate that Ge and associated elements such as Pb, Ca, K are generally associated with nanoscale fluid inclusions in acicular sphalerite. This study shows that Ge enrichment is higher in acicular sphalerite, and we interpret this relationship to be caused by the quick precipitation of acicular sphalerite. These conditions are not favorable to the incorporation of Ge in the sphalerite lattice but then preserves considerable amounts of Ge (up to 2000 ppm Ge) in nanoscale particles associated with the primary fluid phase.

Acknowledgements

This research was financially supported by the National Natural Science Foundation of China (42172082 and 92162218), Major collaborative innovation projects for prospecting breakthrough strategic action of Guizhou Province, China ([2022] ZD004), Guangdong Basic and Applied Basic Research Foundation (2022B1515020007), and Youth Innovation Promotion Association CAS (2021353).

References

Barrie CD, Boyce AJ, Boyle APP, Williams PJJ, Blake K, Wilkinson JJJ, Lowther M, McDermott P, Prior DJ, MacDermott P, Prior DJ (2009) On the growth of colloform textures: a case study of sphalerite from the Galmoy ore body, Ireland. J Geol Soc London 166:563–582. doi: 10.1144/0016-76492008-080

Beaudoin G (2000) Acicular sphalerite enriched in Ag, Sb, and Cu embedded within color-banded sphalerite from the Kokanee Range, British Columbia, Canada. Can Mineral 38:1387–1398. doi: 10.2113/gscanmin.38.6.1387

Belissont R, Munoz M, Boiron M-C, Luais B, Mathon O (2016) Distribution and oxidation state of Ge, Cu and Fe in sphalerite by µ-XRF and K-edge µ-XANES: Insights into Ge incorporation, partitioning and isotopic fractionation. Geochim Cosmochim Acta 177:298–314. doi: 10.1016/j.gca.2016.01.001

Cook N, Etschmann B, Ciobanu C, Geraki K, Howard D, Williams T, Rae N, Pring A, Chen G, Johannessen B, Brugger J (2015) Distribution and Substitution Mechanism of Ge in a Ge-(Fe)-Bearing Sphalerite. Minerals 5:117–132. doi: 10.3390/min5020117

Cook NJ, Ciobanu CL, Pring A, Skinner W, Shimizu M, Danyushevsky L, Saini-Eidukat B, Melcher F (2009) Trace and minor elements in sphalerite: A LA-ICPMS study. Geochim Cosmochim Acta 73:4761–4791. doi: 10.1016/j.gca.2009.05.045

Cugerone A, Cenki-tok B, Muñoz M, Kouzmanov K, Oliot E, Motto-ros V, Goff E Le, Motto-ros V (2021) Behavior of critical metals in metamorphosed Pb-Zn ore deposits : example from the Pyrenean Axial Zone. Miner Depos 56:685–705. doi: doi: 10.1007/s00126-020-01000-9

Fougerouse D, Cugerone A, Reddy SM, Luo K, Motto-ros V (2023) Nanoscale distribution of Ge in Cu-rich sphalerite. Geochim Cosmochim Acta 346:223–230. doi: 10.1016/j.gca.2023.02.011

Fougerouse D, Saxey DW, Rickard WDA, Reddy SM, Verberne R (2022) Standardizing Spatial Reconstruction Parameters for the Atom Probe Analysis of Common Minerals. Microsc Microanal 28:1221–1230. doi: 10.1017/S1431927621013714

Hu X, Chen Y, Liu G, Yang H, Luo J, Ren K, Yang Y (2021) Numerical modeling of formation of the Maoping Pb-Zn deposit within the Sichuan-Yunnan-Guizhou Metallogenic Province, Southwestern China: Implications for the spatial distribution of concealed Pb mineralization and its controlling factors. Ore Geol Rev 140:104573. doi: 10.1016/j.oregeorev.2021.104573

Luo K, Cugerone A, Zhou M-F, Zhou J-X, Sun G-T, Xu J, He K-J, Lu M-D (2022) Germanium enrichment in sphalerite with acicular and euhedral textures: an example from the Zhulingou carbonate-hosted Zn(-Ge) deposit, South China. Miner Depos. doi: 10.1007/s00126-022-01112-4

Motto-Ros V, Moncayo S, Trichard F, Pelascini F (2019) Investigation of signal extraction in the frame of LIBS imaging. Spectrochim Acta - Part B At Spectrosc 155:127–133. doi: 10.1016/j.sab.2019.04.004

Ramdohr P (1969) The ore minerals and their intergrowths. Pergamon Press Ltd, Head Hill Hall, Oxford 4 5 Fitzroy Square, London W 1 1179

Critical raw material potential of the North Pennine Orefield, England

David Currie[1] Eimear Deady[2], Alicja Lacinska[1], Kathryn M Goodenough[2]
[1] British Geological Survey, Keyworth, Nottingham NG12 5GG, UK
[2] British Geological Survey, The Lyell Centre, Research Avenue South, Edinburgh, EH14 4AP, UK

Abstract. In 2019, the UK became the first major economy to legislate a net zero emissions target by 2050. The process of achieving this goal is multifaceted and, to do so, a robust understanding of the critical raw material (CRM) potential of the UK is essential. CRMs are commonly associated with base metal sulfides and other common metals as minor and trace elements and can play a key role in increasing the economic feasibility and circularity of an ore deposit throughout its lifecycle. The North Pennine Orefield (NPO) was selected as an area of interest by using GIS-based mineral systems analysis for exploration targeting. Historically, the NPO has produced approximately 4 Mt Pb, 0.3 Mt Zn, 2.1 Mt fluorite, 1.5 Mt barite, 1 Mt witherite ($BaCO_3$) plus a substantial amount of Fe and Cu ore from vein-hosted, stratabound, and skarn mineralisation in Carboniferous limestones. In this study, petrographic and geochemical data on CRM deportment in ore minerals across the NPO will be incorporated into a larger scale future project, aimed at creating a series of data-driven studies on areas of CRM potential across the UK.

1 Introduction

Over the coming decades, the mining of minerals and metals, with an emphasis on CRMs, is likely to increase as economies progress toward net zero emission targets (Lusty et al. 2021). Technologies needed to combat the effects of climate change, and decarbonise energy generation, transport, and digital systems, will consume increasing amounts of minerals and metals for decades (Bloodworth et al. 2019). This increase in demand coupled with potential issues with future supply chains has led governments to conduct criticality assessments to understand which materials are at risk of supply disruption, to assess the severity of impacts resulting from disruption and to recognise appropriate mitigation of these risks (Lusty et al. 2021; Australian Government 2022). Therefore, it is necessary for governments to understand domestic CRM supply chains and resources.

Tracing back ~6000 years, the United Kingdom has an extensive history of resource extraction (Edinborough et al. 2020). Metals like Fe, Pb, Cu, Zn, Au, Ag, and Sn dominated production during this time. Cornwall, for example, supplied up to 45% of world copper between 1800 and 1860 (Culver and Reinhart 1989). Renewed interest in Li, Sn and W has attracted investors to the area and sparked further exploration across the UK including the North Pennine Orefield (NPO) (Cornish Lithium 2023).

The NPO has produced approximately 4 Mt Pb, 0.3 Mt Zn, 2.1 Mt fluorite, 1.5 Mt barite, 1 Mt witherite plus a substantial amount of Fe and Cu ore from vein-hosted, stratabound, and skarn mineralisation in Carboniferous limestones (Dunham 1990). However, no systematic assessment of CRM potential has been conducted despite known occurrences of uneconomic Co, Ni, Bi, and Sb mineralisation across the orefield (Ixer et al. 1996; Fairbairn et al. 2020). Here, we provide a framework for the analysis of Pb, Zn, Cu, and Fe sulfides to assess the association of CRMs, chiefly In, Ga, and Ge, with these minerals. Ultimately, this petrographic and geochemical workflow can then be replicated for any geographical area for any CRM to create a user-friendly resource for future exploration and resource security analysis.

2 The North Pennine Orefield

2.1 Setting, geology, and ore mineralisation

Covering approximately 1500 km^2 across northern England, the NPO was the most significant UK producer of Pb and Zn through the 18th and 19th centuries (Stone et al. 2010). Commercial mining ceased in 1999, but collector specimens of fluorspar are still mined at the Diana Maria mine.

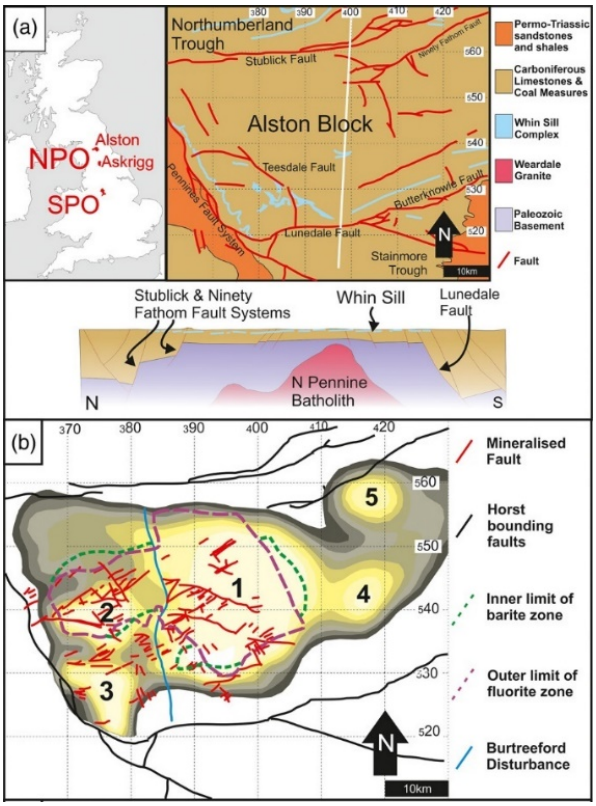

Fig. 1 (a) Simplified geological map and cross-section of the Alston Block. (b) Main mineralised faults in red with bounding structures in black. Green and purple

dashed lines represent the inner limit of the barite zone and outer limit of the fluorite zone, respectively. Image from Dempsey et al. (2021).

The Alston Block of the NPO comprises Lower Palaeozoic sedimentary and volcanic rocks intruded by Caledonian-aged granite (Selby et al. 2008; Kimbell et al. 2010) and overlain by up to 600 m of cyclothemic limestones, sandstones, mudstones, and minor coals (Dunham 1990). It is a horst structure bound by crustal-scale faults and suggested to have come in to existence due to north-south Carboniferous extension above the Iapetus Convergence Zone (Chadwick et al. 1995). The thin cyclothem sequences are attributed to the Alston Block being underlain by a concealed relatively buoyant batholith (Dunham et al. 1965). An Early Permian phase of transtensional deformation and magmatism resulted in the emplacement of a doleritic complex across the NPO known as the Whin Sill. It is recorded across northern Britain (Dempsey et al. 2021).

Veins and stratabound 'flats' are hosted in Carboniferous limestone sequences. Minor skarn mineralisation was also mined (Young et al. 1985). The main ore phases are galena, sphalerite, siderite, ankerite, limonite, fluorspar, witherite, barite, and chalcopyrite (Dunham 1990). NPO deposits are structurally controlled along faults and steeply dipping conjugate fracture systems (Dunham 1990). Stratabound deposits are often overlain by impervious mudstone, whereas vein ore-shoots are overlain by sandstones thus suggesting a hydrological and lithological control on ore mineralisation styles (Dunham 1990). Stratabound mineralisation is typically 5 to 20 m wide and up to 3 m thick and can extend for hundreds of metres laterally (Dunham 1990), whereas veins can extend for 10s of km and be hundreds of metres thick; the Great Sulphur vein for example.

2.2 Existing geochemistry and geochronology

Ore fluid temperatures range from >200°C in the central fluorite zone to around 100 °C at the margins (Cann and Banks 2001; Sawkins 1966). Homogenisation temperature of sphalerite in stratabound mineralisation ranged between 80-150°C (Bouch et al. 2008). Barite zone temperatures ranged from 120°C to 50°C (Cann and Banks 2001).

Salinities of fluid inclusions in ore, gangue, and host rock range from around 2 to about 25 wt.% NaCl equivalent (Cann and Banks 2001; Bouch et al. 2008). Fluids are reported to be enriched in K and Li relative to oil field brines (Rankin and Graham 1988; Cann and Banks 2001) and interpreted as a mixed $CaCl_2$–NaCl-bearing brine containing significant dissolved Fe, Cu, Zn and Pb.

The timing of ore mineralisation across the NPO is thought to be restricted to the time of Whin Sill emplacement and cooling (~295 Ma; Fitch and Miller 1967; Young et al. 1985; Dunham 1990; Dempsey et al. 2021). However, other data suggest that the main phase of mineralisation was restricted to between the latest Permian (~250–260 Ma) (Dunham et al. 1968; Davison et al. 1992; Lenehan 1997) and end Triassic (~210-200 Ma; Cann and Banks 2001; Shepherd et al. 1982; Halliday et al. 1990).

2.3 Ore-forming processes

It has been suggested the NPO is a fluoritic sub-type of Mississippi-Valley type deposits (Dunham 1983; Halliday et al. 1990). Cann and Banks (2001) proposed deep fluid circulation and interaction with underlying granite and country rock allowed fluid temperature and salinity to rise and scavenge metals during Late Permian extension. They suggest chimney-like systems drove convection above hotter granitic centres leading to zoning of ore mineralisation in host rock (Cann and Banks 2001). An 'emanative centres' hypothesis was also proposed by Johnson and Dunham (1963) and supported by Ixer et al. (1996). Bouch et al. (2006) suggest that the zonation may be due to two distinct phases of ore mineralisation.

Bott and Smith (2018) used geophysical modelling to suggest that the underlying batholith was not hot enough to facilitate a chimney effect of heat channelling, rather the batholith was underplated by alkali magma associated with the intrusion of the Whin Sill. Dempsey et al. (2021) rule out any link between granite-related hydrothermal fluid circulation and/or MVT models previously proposed and link ore mineralisation with Whin Sill emplacement.

3 CRMs in MVT and skarn sulfides

3.1 Sphalerite

Mississippi-Valley type (MVT) and related carbonate-hosted vein, breccias and skarn deposits are distributed globally and, in a few cases, have been assessed for CRM potential. Textural characterisation of sphalerite from MVT deposits in Peru revealed some of the most Ge- and Ga-rich samples ever reported (Torró et al. 2023). Ga in reddish-brown sphalerite from the Chilpes prospect reached 4000 ppm, whilst Ge in Fe-poor orange sphalerite from San Vicente deposit reached >1800 ppm (Torró et al. 2023). Fe-poor sphalerite is preferred for Ge enrichment (Frenzel et al. 2014; Cook et al. 2009), though sphalerite from the Tres Marias Zn deposit in Mexico showed Ge is preferentially incorporated within Fe-rich bands (Cook et al. 2009).

MVT deposits across South China have elevated amounts of Ge in sphalerite, whilst skarn deposits across the same area have shown incorporation of Co and Mn (Ye et al. 2011). Fe-poor sphalerite with up to 2300 ppm Co is noted at Ocna de Fier skarn, Romania (Cook et al. 2009).

Frenzel et al. (2016) show that Ga and Ge concentration will tend to increase with decreasing formation temperature whilst In will do the opposite.

Higher temperature sphalerite-bearing ore deposits, like skarns, are the primary source of global In supply (Xu et al. 2021). Fractionation of a given element into sphalerite is also influenced by metal source and the amount of sphalerite in the deposit relative to other metallic minerals (Cook et al. 2009).

3.2 Galena

Galena is the preferred host for Ag, Bi, Sb, Se, Te, and Tl in co-existing sphalerite-galena-chalcopyrite bearing ore systems (George et al. 2015). Bi and Sb are more likely to favour higher temperature zones of ore deposits like in skarns where concentrations in galena can reach >6400 ppm and 4600 ppm respectively like at Herja epithermal deposit, Romania (George et al. 2015). Tellurium in galena has been recorded at >1000 ppm at the Baita Bihor skarn, Romania (George et al. 2015)

3.3 Fe and Cu sulfides

Pyrite is the most common sulfide mineral on Earth and is known to incorporate several CRMs during the crystallization process or during reprecipitation (Dmitrijeva et al. 2020). Across the Beishan Pb-Zn MVT ore zone, south China, pyrite is enriched in Co, Ni, and Sb (Zhou et al. 2022). The Illinois-Kentucky fluorite district, Co and Ni are recorded at up to 10,000 ppm in early pyrite (Hall and Heyl 1968). Partitioning of CRMs in marcasite is not known across MVT-type deposits, though it can act like pyrite in massive sulfide deposits (Grant et al. 2018). Chalcopyrite is a known host of several CRMs (George et al. 2018), although it will not be studied here as it forms a minor component of the NPO.

4 Future work

Collection of sample material from spoil heaps related to historic underground mine sites began in late 2022. We propose the following petrographic and geochemical analysis framework to quantify CRM potential of the NPO: reflected light petrography to initially identify sulfides (Fig. 2); cathodoluminescence imaging to identify areas of zonation, particularly in sphalerite; quantitative microanalysis using scanning electron microscopy energy-dispersive X-ray microanalysis (SEM-EDXA); and trace element analysis of ore sulfides by laser ablation - inductively coupled plasma - mass spectrometry (LA-ICP-MS). Data collected form part of a larger UK scale reassessment of UK CRM potential.

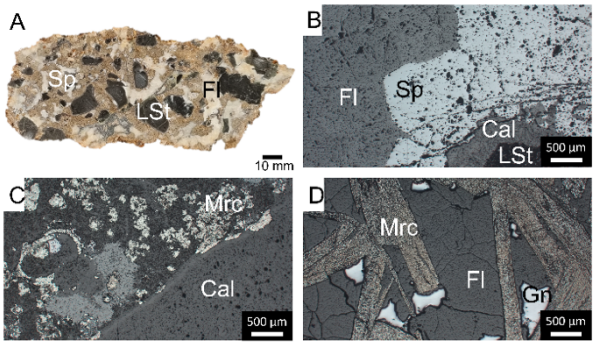

Fig. 2 Representative images from Lady's Rake Mine. A) Hand sample showing breccia with sphalerite, fluorspar, and calcite-rimmed limestone country rock. B) Reflected light image of image A. C) Reflected light image of marcasite mineralisation adjacent to calcite veining in nodule. D) Marcasite, galena, and fluorspar.

Acknowledgements

This work was carried out as part of the British Geological Survey Critical Minerals Intelligence Centre programme. Thanks to Nenthead Mining Museum, Brian Young, and Dr Charlotte Vye-Brown for field assistance and their invaluable knowledge of the North Pennine Orefield. Thanks to Richard Shaw for providing internal peer review.

References

Australian Government (AG) (2022) Critical Minerals Strategy, Department of Industry, Science, Energy and Resources, Australian Government.

Bott MH and Smith FW (2018) The role of the Devonian Weardale Granite in the emplacement of the North Pennine mineralization. Proceedings of the Yorkshire Geological Society 62(1):1-15.

Bloodworth A, Petavratzi E, Gunn G (2019) METALS AND DECARBONISATION: A GEOLOGICAL PERSPECTIVE.

Bouch JE, Naden J, Shepherd TJ, McKervey JA, Young B, Benham AJ, Sloane HJ (2006) Direct evidence of fluid mixing in the formation of stratabound Pb–Zn–Ba–F mineralisation in the Alston Block, North Pennine Orefield (England). Mineralium Deposita 41:821-835.

Bouch J, Naden J, Shepherd T, Young B, Benham A, McKervey J, Sloane H (2008) Stratabound Pb-Zn-Ba-F mineralisation in the Alston Block of the North Pennine Orefield (England): origins and emplacement.

Cann JR, Banks DA (2001) Constraints on the genesis of the mineralization of the Alston Block, Northern Pennine Orefield, northern England. Proceedings of the Yorkshire Geological Society 53(3):187-196.

Chadwick RA (1995) The structure and evolution of the Northumberland-Solway Basin and adjacent areas: Subsurface Memoir. HM Stationery Office.

Cook NJ, Ciobanu CL, Pring A, Skinner W, Shimizu M, Danyushevsky L, Saini-Eidukat B, Melcher F (2009) Trace and minor elements in sphalerite: A LA-ICPMS study. Geochimica et Cosmochimica Acta 73(16):4761-4791.

Cook NJ, Ciobanu CL, George LL, Crowe B, Wade BP (2014) December. Trace element distributions in sulphides: Progress, problems and perspectives. In Acta Geologica Sinica-English Edition; 88:1444-1446.

Cornish Lithium (2023) Cornish lithium and northern lithium announce collaboration to deliver domestic supply of lithium for the UK, Cornish Lithium Plc. Available at: https://cornishlithium.com/company-announcements/cornish-lithium-and-northern-lithium-

announce-collaboration-to-deliver-domestic-supply-of-lithium-for-the-uk/ (Accessed: March 6, 2023).
Culver W, Reinhart CJ (1989) Capitalist Dreams: Chile's Response to Nineteenth-Century World Copper Competition. Comparative Studies in Society and History 31(4):722-744.
Davison JM, Ineson PR, Mitchell JG (1992) Potassium-argon isotopic age determinations from the metasomatic alteration of the Great Limestone, Northern Pennine Orefield. Proceedings of the Yorkshire Geological Society 49:71-74.
Dempsey ED, Holdsworth RE, Selby D, Bird A, Young B, Le Cornu C (2021) A revised age, structural model and origin for the North Pennine Orefield in the Alston Block, northern England: intrusion (Whin Sill)-related base metal (Cu–Pb–Zn–F) mineralization. Journal of the Geological Society 178(4).
Dmitrijeva M, Cook NJ, Ehrig K, Ciobanu CL, Metcalfe AV, Kamenetsky M, Kamenetsky VS, Gilbert S, (2020) Multivariate statistical analysis of trace elements in pyrite: Prediction, bias and artefacts in defining mineral signatures. Minerals 10(1):61.
Dunham KC (1990) Geology of the Northern Pennine Orefield Volume I—Tyne to Stainmore Economic memoir covering the areas of 1: 50 000 and one-inch geological sheets 19 and 25, and parts of 13, 24, 26, 31, 32 (England and Wales).
Dunham KC, Dunham AC, Hodge BL, Johnson GAL (1965) Granite beneath Viséan sediments with mineralization at Rookhope, northern Pennines. Quarterly Journal of the Geological Society 121(1-4):383-414.
Dunham KC, Fitch FJ, Ineson PR, Miller JA, Mitchell JG (1968) The geochronological significance of argon-40/argon-39 age determinations on White Whin from the northern Pennine orefield. Proceedings of the Royal Society of London. Series A. Mathematical and Physical Sciences 307(1490):251-266.
Edinborough K, Shennan S, Teather A, Baczkowski J, Bevan A, Bradley R, Cook G, Kerig T, Pearson MP, Pope A Schauer P (2020) New radiocarbon dates show Early Neolithic date of flint-mining and stone quarrying in Britain. Radiocarbon 62(1):75-105.
Fairbairn RA, Ixer RA,Young B, (2020) Ore mineralogy of the Clargillhead Vein, Tynehead, Cumbria: the first report of native silver from the Northern Pennine Orefield. Journal of the Russell Society 23:48-52.
Fitch FJ, Miller JA (1967) The age of the Whin Sill. Geological Journal 5(2):233-250.
Frenzel M, Ketris MP Gutzmer J (2014) On the geological availability of germanium. Mineralium Deposita 49:471-486.
Frenzel M, Hirsch T, Gutzmer J (2016) Gallium, germanium, indium, and other trace and minor elements in sphalerite as a function of deposit type—A meta-analysis. Ore Geology Reviews 76:52-78.
George L, Cook NJ, Ciobanu CL, Wade BP (2015) Trace and minor elements in galena: A reconnaissance LA-ICP-MS study. American Mineralogist 100(2-3):548-569.
George L, Cook NJ, Ciobanu CL (2015) August. Trace element partitioning between co-existing sphalerite, galena and chalcopyrite. In Mineral Resources in a Sustainable World, 13th Biennial SGA Meeting, Nancy, France, Proceedings:737-740
George LL, Cook NJ, Crowe BB, Ciobanu CL (2018) Trace elements in hydrothermal chalcopyrite. Mineralogical Magazine 82(1):59-88.
Grant HL, Hannington MD, Petersen S, Frische M Fuchs SH (2018) Constraints on the behavior of trace elements in the actively-forming TAG deposit, Mid-Atlantic Ridge, based on LA-ICP-MS analyses of pyrite. Chemical Geology 498:45-71.
Hall WE, Heyl AV (1968) Distribution of minor elements in ore and host rock, Illinois-Kentucky fluorite district and Upper Mississippi Valley zinc-lead district. Economic Geology 63(6):655-670.
Halliday AN, Shepherd TJ, Dickin AP, Chesley JT (1990) Sm–Nd evidence for the age and origin of a Mississippi Valley Type ore deposit. Nature 344(6261):54-56.
Ixer RA, Young B, Stanley CJ (1996) Bismuth-bearing assemblages from the Northern Pennine Orefield. Mineralogical Magazine 60(399):317-324.
Johnson GAL, Dunham KC (1963) The geology of Moor house. HM Stationery Office.
Kimbell GS, Young B, Millward D, Crowley QG (2010) November. The North Pennine batholith (Weardale Granite) of northern England: new data on its age and form. Geological Society of London.
Lenehan T (1997) An investigation into thermo-tectonic and maturation histories in north-west Britain. Ph.D. Thesis, University of Leeds
Lusty PAJ, Shaw RA, Gunn AG, Idoine NE (2021) UK criticality assessment of technology critical minerals and metals. British Geological Survey Commissioned Report, CR/21/120:76pp
Rankin AH, Graham MJ (1988) Na, K and Li contents of mineralizing fluids in the Northern Pennine Orefield, England, and their genetic significance. Transactions of the Institution of Mining and Metallurgy. Section B. Applied earth science 97:99-107.
Sawkins FJ (1966) Ore genesis in the North Pennine orefield, in the light of fluid inclusion studies. Economic Geology 61(2):385-401.
Selby D, Conliffe J, Crowley QG Feely M (2008) Geochronology (Re–Os and U–Pb) and fluid inclusion studies of molybdenite mineralisation associated with the Shap, Skiddaw and Weardale granites, UK. Applied Earth Science 117(1):11-28.
Shepherd TJ, DPF D, GR M, DA G (1982) Rare earth element and isotopic geochemistry of the North Pennine ore deposits.
Stone P, Millward D, Young B, Merritt J, Clarke S, McCormac M,Lawrence D (2010) Northern England. British Geological Survey.
Torró L, Millán-Nuñez AJ, Benites D, González-Jiménez JM, Laurent O, Tavazzani L, Vallance J, Chelle-Michou C, Proenza JA, Flores C. Melgarejo JC (2023) Germanium- and gallium-rich sphalerite in Mississippi Valley–type deposits: the San Vicente district and the Shalipayco deposit, Peru. Mineralium Deposita, 1-28.
Xu J, Cook NJ, Ciobanu CL, Li X, Kontonikas-Charos, A, Gilbert S,Lv Y (2021) Indium distribution in sphalerite from sulfide–oxide–silicate skarn assemblages: a case study of the Dulong Zn–Sn–In deposit, Southwest China. Mineralium Deposita 56:307-324.
Ye L, Cook NJ, Ciobanu CL, Yuping L, Qian Z, Tiegeng L, Wei G, Yulong Y, Danyushevskiy L (2011) Trace and minor elements in sphalerite from base metal deposits in South China: A LA-ICPMS study. Ore Geology Reviews 39(4):188-217.
Young B, Styles MT, Berridge NG (1985) Niccolite-magnetite mineralization from Upper Teesdale, North Pennines. Mineralogical Magazine 49(353):555-559.
Zhou C, Yang Z, Sun H, Koua KAD, Lyu C, (2022) LA-ICP-MS trace element analysis of sphalerite and pyrite from the Beishan Pb-Zn ore district, south China: Implications for ore genesis. Ore Geology Reviews, p.105128.

Towards a better understanding of a Co-rich hydrothermal system: Punta Corna (Western Alps, Italy)

Giulia Domenighini[1], Licia Santoro[1], Marilena Moroni[2]
[1]Department of Earth Sciences University of Torino, Italy.
[2]Department of Earth Sciences "Ardito Desio" University of Milan, Italy.

Abstract. This study presents new geochemical, mineralogical, and petrographic data on the Co-Fe-Ni vein system of Punta Corna (PC) in the Western Alps, Italy. The mineralogical phases identified include arsenides belonging to the skutterudite and safflorite (Fe-Co-Ni tri- and di-arsenides) solid solutions, tetrahedrite, and sulfides (chalcopyrite, minor pyrite and rare sphalerite and galena). Gangue minerals comprise carbonates (mainly siderite, ankerite and calcite) and quartz. Field and mineralogical observations show a distinct geochemical zonation within the deposit system. No Co or Ni occur to the west, with only Fe-bearing minerals observed. Co-Ni arsenides are present in the central region, with a higher proportion of Ni di-arsenides than Co-bearing phases. To the east, Co arsenides prevail. Additional sampling, micro-textural characterization and geochemical investigations are ongoing, yet these preliminary observations agree with the genetic model recently proposed for similar types of deposits and suggest that the hydrothermal system may have formed through a complex geological history, with multiple mineralizing events and variations in fluid composition and possibly temperature.

1 Introduction

The Co-Ni-bearing Punta Corna (PC) hydrothermal vein system is located in the western sector of the Alpine belt near the Lanzo Massif, Northern Italy. Despite being a historically known mining complex, exploited until the 20th century, formerly for Fe and later for Co (used as a pigment), this vein system has received little scientific attention until recently. In 2020, the Australian Junior Mining Company (Altamin l.t.d.) acquired the exploration license of ca. 22 Km^2 area around ancient mining galleries. The PC mining complex holds great potential from an economic standpoint, both for the main ores consisting of Co-rich arsenides, and for the poor exposure of the vein system, likely preserved at depth.

The literature lacks detailed information on the geochemistry of the deposit and high-resolution geological maps. Preliminary paragenetic studies based on museum samples (Moroni et al., 2019 andref. therein) suggest a multi-stage mineralizing process with early siderite, ankerite, quartz and baryte followed by deposition of Fe-Co-Ni di- triarsenides with native elements (As, Bi), and thenbase metal sulphides and tetrahedrite with siderite, ankerite, quartz and late baryte gangue.

There are analogies between the PC mineralization and the five-element vein-type deposits according to Kissin' (1992), to more recent studies (e.g., Markl etal 2016) as well as the mineralized veins in theworld-class Bou Azzer ore district (Tourneur et al 2021).

Nevertheless, definitive constraints on the genetic conditions of the PC hydrothermal vein system are still missing.

In this work, we summarize geological, mineralogical, and geochemical data of a new set of surface samples of the poorly known Fe-Co-Ni- bearing Punta Corna ore deposit. Drilling is plannedin order to verify the features of the vein system at depth. Moreover, we illustrate some investigations inprogress about the possible sources of Co in the mineralization, the age of the mineralizing process and the properties of the fluid and its origin.

2 Geological setting

The ore bodies of the PC hydrothermal vein systemare located in the Arnàs, Servin, Veil, and Autour valleys, some small offshoots of the Viù valley, close to the village of Usseglio (TO, Fig1 A, B).

The Fe-Co-Ni-bearing veins extend for 2 Km along an east-west axis, from the "Lago dietro la Torre" lake to the "Torre d'Ovarda" peak, with elevations ranging from 2200 to 2900m. The average thickness of the outcropping veins is in the cm/dm range. Mineralized bodies are hosted in metabasites and, subordinately, in heavily foliated calcschists of the Internal Piedmont Zone tectonic unit (IPZ), a portionof oceanic lithosphere and its sedimentary cover related to the Middle-Jurassic Piedmont-Ligurian Ocean (Dal Piaz 1999, Fig1). The IPZ is structurallylocated above the Gran Paradiso (to the North) and the Dora Maira (to the South) Units, which representthe external continental margin of the EuropeanPlate. With the subduction of the oceanic crust below the Adria plate leading to the Alpine orogenesis (90-35 Ma), the oceanic rocks of the IPZregistered an eclogitic peak metamorphism followed by green-schist facies re-equilibration during exhumation (35-23 Ma, Sandrone 1986). The rocks record several ductile deformations phases, while the mineralized veins are related to a post-metamorphic brittle event and are associated with faults and fractures. Two late steep E-W trending fault systems occur throughout the whole deposit. The first system is represented by a subvertical normal fault system, interacting with a diverging high-angle transtensional fault system.

Field evidence of a geochemical zonation affecting the vein system occurs across the mining district. The presently accessible portions of the veins in thewestern sector are characterized by siderite- ankerite, once exploited for Fe. In contrast, the eastern sector displays high Co/Ni ore minerals

(di-and tri-arsenides). It is worth mentioning the presence of Ag, mined since historical times, in the southernmost part of the district.

The ophiolite terranes in the surroundings of the studied area host several metamorphosed volcanogenic massive sulfides deposits (VMS) exploited in historical mines like Fragnè-Chialamberto, Uja di Calcante and Beth-Ghinivert, where recent studies signalled anomalous Co contents in the pre-metamorphic pyrite (Giacometti et al 2014). For this reason, we have started sampling variably deformed portions of some of these volcanogenic sulfides layers for evaluating them as possible sources for Co in the PC vein system.

3 Methods

Several samples collected in the field, both on surface and in the ancient mining tunnels, were cut to obtain thin and polished sections for optical microscopy (OM). The powder x-ray diffraction (PXRD) analyses of carbonates, alteration and supergene phases were carried out using a Rigaku SmartLab XE diffractometer in Bragg-Brentano geometry (Cu-Kα radiation, Ni filter, generator operating at 40 kV and 30 mA, soller slit 2.5 deg) equipped with a 2D HyPix-3000 detector. The detector was employed in 1D XRF-reduction mode to increase peak resolution and limit the background signal due to the fluorescence from Fe. In addition, each measurement was collected by mounting a frontal knife edge and a direct beam stop to reduce the background. The patterns were collected from 5to 75º 2θ angles, with a step size of 0.02º and a scan speed of 1 º/min. The qualitative analysis was carried out with EVAluation software (Bruker) and employing the PDF-2 database.

Scanning electron microscope (SEM) equipped with an energy dispersive spectrometer (EDS) was employed for preliminary petrography and chemical semi-quantitative analyses. Carbon-coated polished thin sections were analysed with a JEOL JSM-IT300LV SEM equipped with an EDS Energy 200 and an SDD X-Act3 detector (Oxford Inca Energy). The operating conditions were 20 kV accelerating voltage, 5 nA probe current, 30 s counting time. Thedata were acquired and processed using the Suite AzTec ID, version 6.0 (Oxford Instruments). Samplepreparation, PXRD, and SEM-EDS were carried out at the Department of Earth Sciences, University of Turin, Italy.

Quantitative electron probe microanalysis (EPMA) was performed at the University of Milan "Ardito Desio" on carbon-coated polished thin sections using a JEOL JXA — 8200 EPMA equipped with five wavelength-dispersive spectrometers (WDS). The analytical conditions for the electron beam were an accelerating voltage of 15 kV, a beam current of 5 nA, and a beam diameter of 1-2 μm. Counting timesfor each element (Sb, Co, Bi) were 30 s on peaks and 10 s on the background. Elemental concentrations were determined after applying the

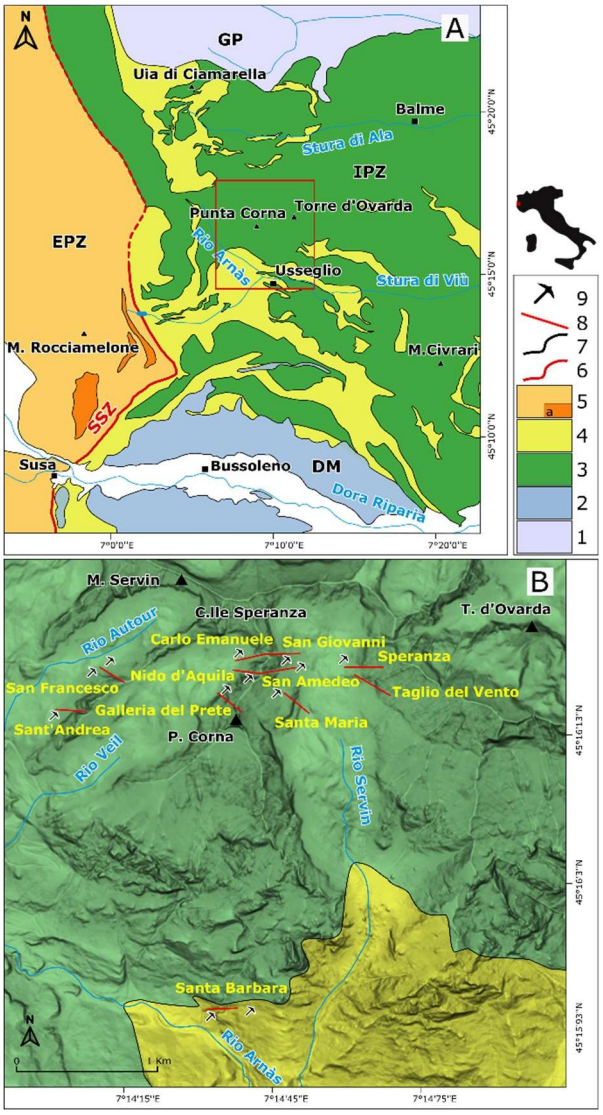

Fig 1. A) simplified tectonic sketch-map of the central sector of the Western Alps, modified after De Togni et al. 2021. In red is marked the location of the studied area. B) geological map of the studied area. 1 Gran Paradiso (GP); 2 Dora Maira (DP); 3 meta-ophiolites of the Internal Piedmont Zone (IPZ); 4 metasedimentary coverof IPZ; 5 oceanic metasediments with a) meta-ophiolite bodies of the External Piedmont Zone (EPZ); 6 Susa Shear Zone (SSZ); 7 tectonic contacts; 8 main mineralized veins; 9 ancient mining adits.

φ(ρz) algorithm and corrections for X-ray fluorescence, absorption, atomic number (Z), and matrices and by evaluating spectral interferences.

4. Petrography, Mineralogy and Geochemistry

The new surface samples display abundant gangue minerals encompassing calcite, dolomite, siderite, ankerite, quartz, and baryte. Hydrothermal alterations of wall rock commonly result in the presence of very fine-grained chlorite and white mica. Supergene oxidation of primary arsenides sulphides and siderite results in erythrite, annabergite, and abundant goethite. The veins exhibit a brecciated texture with clasts from the host

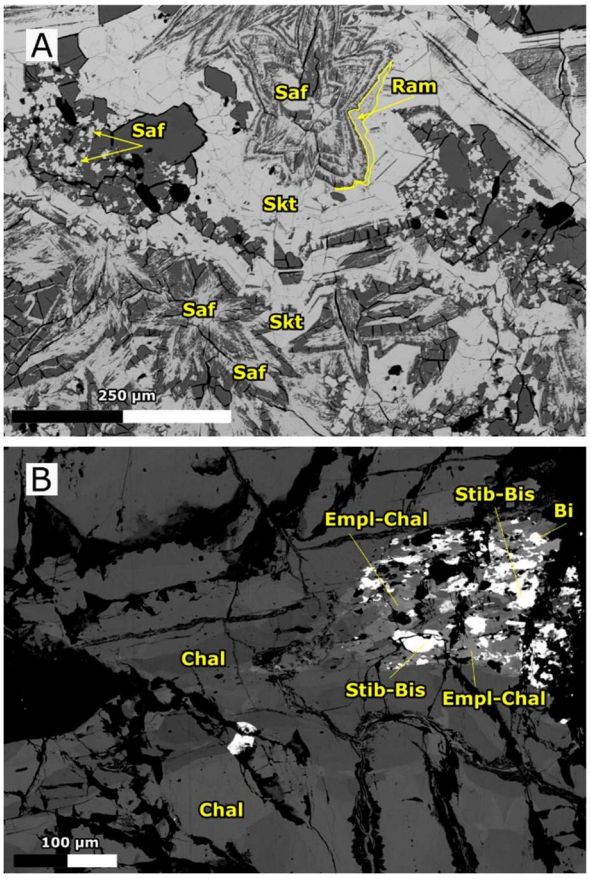

Fig 2. BSE images of Nido d'aquila vein, A and Santa Barbara vein, B. A) coarse-grained safflorite (Saf) crystals exhibiting star-shaped twinning alternating with thin grained disseminated aggregates of safflorite. Rammelsbergite (Ram) rim and well-formed euhedral crystals of skutterudite (Skt) can be observed. B) Sulfosalt belonging to emplectite-chalcostibite (Empl-Chal) solid solution and stibnite-bismiuthinite (Stib-Bis) solid solution. Chal = chalcopyrite, Bi = native bismuth.

rock, sometimes reaching centimetric sizes, cemented by a fine-grained gangue minerals matrix. Bladed siderite and euhedral quartz growing radially around brecciated clasts is also a typical texture of the mineralized veins. Veins can also present a banded structure with different compositional and textural layers. The ore minerals observed so far are represented by dominant Co-Ni di-triarsenides and base metal sulfides as those previously mentioned, although SEM and EPMA analyses helped in detecting additional sulfosalt minerals. Ore minerals show variable textures from well-preserved coarse-grained to brecciated or fine-grained disseminated crystals. The precipitation sequence starts with carbonates and quartz, followed by arsenides. They are characterized by di-arsenides either overgrowing coarse-grained tri-arsenides Fig2A,B) or disseminated along preferential directions or bands throughout the veins. Tri-arsenides (skutterudite series: (Fe,Co,Ni)As_3) are often zoned, with banding marked by alteration products (erythrite,annabergite). Di-arsenides belong to the safflorite series: loellingite ($FeAs_2$), clinosafflorite ($CoAs_2$), and rammelsbergite ($NiAs_2$)**.** The latter commonly occur as a rim on di- and tri-arsenides. The last precipitation stage is represented by base metal sulfides (chalcopyrite, minor pyrite and rare sphalerite and galena), tetrahedrite and several Bi- rich sulfosalts intergrown with native Bi (Fig **2**B). Rare droplets of secondary Ag sulfides were observed along rims of altered tetrahedrite crystals. Skutterudite composition is characterized by an average Co content of 9,25 wt%, Ni content of 7,65 wt% and Fe content of 4,93 wt%, but the compositions are quite homogeneous (Fig **2**A). Di- arsenides, on the other side, present wide variation in composition, with a range in Co content varying from 3,16 wt% to 16,52, Ni content from 0 to 30,23 wt% and Fe content from 0,12 to 19,94 wt% (**Error! Reference source not found.**A,B**)**. Tetrahedrite belong to the tetrahedrite end memberof the tennantite-tetrahedrite series: $Cu_6(Cu_4\mathbf{C}_2{}^{2+})As_4S_{12}S$ - $Cu_6(Cu_4\mathbf{C}_2{}^{2+})Sb_4S_{12}S$, where **C** can be Zn, Fe, Hg, Cd, etc.

The analysed samples show low values of both Zn (ranging from 0,88 wt% to 6,46 wt%) and Ag (ranging from 0 to 0,87 wt%).

Beside Bi-Sb alloys, Bi-rich sulfosalts display highly variable compositions including horobetsuite (related to stibnite - bismuthinite solid solution) and Cu-rich varieties like wittichenite and emplectite-chalcostibite solid solution. It is worth noting that

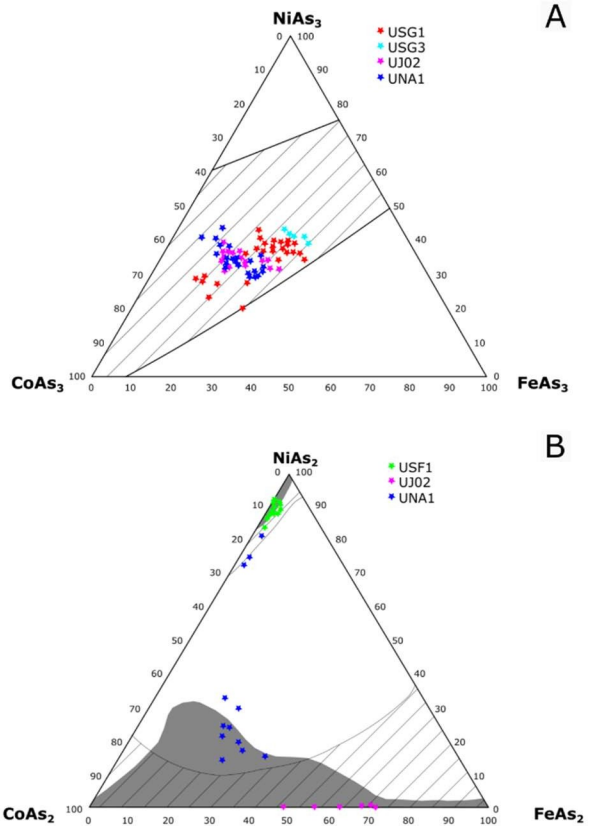

Fig 3. A) plot of skutterudite mineral series for the investigated veins. The solid-solution field for the system FeAs3–CoAs3–NiAs3 is defined by shaded area, according to Roseboom (1962). B) plot of safflorite mineral series (system FeAs2–CoAs2–NiAs2), compositional limits of natural Fe, Co, Ni diarsenides, according to Roseboom (1963) in dashed areas and Radcliffe & Berry (1968), full areas.

these Bi sulfosalts are especially characteristic of the post-metamorphic Au-bearing veins of the nearby Gran Paradiso nappe.

5. Work in progress

We are preparing a set of double polished sections from the new samples for fluid inclusion analyses in gangue minerals. From the same samples we are selecting portions with ore-related and post ore carbonates for performing U-Pb geochronology, together with carbonates from other post-metamorphic mineralized veins in the Gran Paradiso and Monte Rosa nappes. Carbon isotope analyses will be performed for obtaining indications about the origin of C-bearing gases in the fluids. Also, the origin of the great amount of Co in the PC vein system is a topic of interest. Therefore, a series of pyrite-rich samples from the VMS deposits in the Western Alpine ophiolites are in preparation for testing their possible role as sources for hydrothermal Co enrichment. Preliminary EMPA analyses on cm-sized metamorphosed py-cpy layerslocated at the contact between metabasites and calcschists, in the Arnàs valley, have been promising so far by revealing anomalous Co contents (up to 2%) in irregularly zoned pyrites.

6. Conclusion

The data from the characterization of the new surface samples from the Co-rich post-metamorphicveins in the Western Alpine ophiolites at Punta Corna — Usseglio are revealing that the mineralized system is more complex than previously indicated from historical samples. Beside indications about the distribution of Co and Ni, the new data suggest a role to previously unknown Bi enrichment which also contributes to establishing a possible link with the nearby domain of the Pennidic Gran Paradiso nappe. Therefore, the upcoming drilling campaign isbringing great expectations.

Because of the poor exposure of the PC veins, plenty of work is still needed to fully understand the features and the genetic process that led to the deposition of the hydrothermal system associated with the Fe-Co-Ni arsenides. To gain further insight into these issues, fluid inclusion, geochronological and isotopical analyses will likely provide significant data for better defining the hydrothermal fluids and their components, the origin of the vein system and potentially explain the zonation. The fluid inclusion analyses will be focused in particular on potential reduction mechanisms/agents (e.g. hydrocarbons) proposed in various models in literature for hydrothermal Co-Ni mineralization. Last but not least, the study of the metamorphosed exhalative pyrite ores in the western alpine ophiolites will be interesting for tracing possible Co sources for the PC mineral system and beyond. Further research and investigations could have significant implications for the evaluation of mineral resources and mining exploration in the region.

Acknowledgements

The project is part of the “Progetto Nazionale Operativo” (PON) “Ricerca e Innovazione” 2014-2020, of the Ministry of Education, University and Research dedicated to PhD Research Projects on green topics reducing the impacts of climate change and promoting sustainable development.
(DM 1061/2021). The authors would like to acknowledge AltaMin L.d.t. for co-founding the project. Furthermore, the authors would like to extend their thanks to the lab technicians at UniTo and UniMi as well as the staff at AltaMin for their assistance in preparing the samples and accompanying the research team in the field. Their expertise and support have been invaluable to the success of this project.

References

Dal Piaz GV (1999) The Austroalpine-Piedmont nappe stack and the puzzle of Alpine Tethys. Mem. Sci. Geol. 51:155-176.

De Togni M, Gattiglio M, Ghignone S, Festa A (2021) Pre-Alpine Tectono-Stratigraphic Reconstruction of the Jurassic Tethys in the High-Pressure Internal Piedmont Zone (Stura di Viù Valley, Western Alps). Minerals 11:361.

Giacometti F, Evans KA, Rebay G, Cliff J, Tomkins AG, Rossetti P, Adams DT (2014) Sulfur isotope evolution in sulfide ores from Western Alps: Assessing the influence of subduction-related metamorphism. Geochemistry, Geophys. Geosystems 15:3808-3829.

Kreissl S, Gerdes A, Walter BF, Neumann U, Wenzel T, MarkIG (2018) Reconstruction of a> 200 Ma multi-stage “five element” Bi-Co-Ni-Fe-As-S system in the Penninic Alps, Switzerland. Ore Geol. Rev. 95:746-788.

Moroni M, Rossetti P, Naitza S, Magnani L, Ruggieri G, AquinoA, Secchi F (2019) Factors controlling hydrothermal nickeland cobalt mineralization—Some suggestions from historical ore deposits in Italy. Minerals 9:429.

Markl G, Burisch M, Neumann U (2016) Natural fracking and the genesis of five-element veins. Miner Deposita 51:703-712.

Peucker-Ehrenbrink B, Hofmann AW, Hart SR (1994) Hydrothermal lead transfer from mantle to continentalcrust: the role of metalliferous sediments. Earth Planet. Sci. Lett. 125:129-142.

Radcliffe D, Berry LG (1968) The safflorite-loellingite solid solution series. Am Min 53:1856-1881.

Roseboom EH (1962) Skutterudites (Co, Ni, Fe) As3− x: composition and cell dimensions. Am Min 47:310-327.

Roseboom EH (1963) Co-Ni-Fe diarsenides: compositions and cell dimensions. Am Min 48:271-299.

Sandrone R, Leardi L, Rossetti P, Compagnoni R (1986) P-T conditions for the eclogitic re-equilibration of the metaophiolites from Val d’Ala di Lanzo (Internal Piedmontese Zone, Western Alps). J. Metamorph. Geol. 4:161-178.

A lithological context for stratabound REE mineralisation at the birthplace of REE – Bastnäs, Riddarhyttan, Sweden

Robert Dunst[1], Iain Pitcairn[1], Hein Raat[2], Nils F Jansson[3], Andreas Karlsson[4]
[1]Department of Geological Sciences, Stockholm University, Stockholm, Sweden
[2]EMX Royality Corp., Vancouver, Canada
[3]Division of Geosciences and Environmental Engineering, Luleå University of Technology, Luleå, Sweden
[4]Department of Geosciences, Swedish Museum of Natural History, Stockholm, Sweden

Abstract. The Bastnäs ore field, in central Sweden, is the cradle of the rare earth elements (REE). It is the place of the discovery of several REE and important REE-minerals (e.g., Bastnäsite one of the primary REE-ore minerals). In recent years there has been an increased interest due to rising demand of REE for technological applications. Several recent studies have focused on the mineralogy and geochemistry but a lack of fresh in situ samples has meant that textural and stratigraphic relationships are not as well described. Recent exploration in the area has produced drill core traverses across the host stratigraphy of the Bastnäs deposit, allowing the collection of relatively fresh in situ samples which can be placed in lithological context. Here we present new mineralogical and textural information linked to the lithology indicating that the REE-mineralisation in Bastnäs is commonly associated with magnetite skarn and that it occurs over a wide range of stratigraphic levels.

1 Introduction

The Bastnäs deposit in central Sweden played an important role in the discovery of the rare earth elements (REE) in the mid 19th century. Chemists tried to identify the constituents of samples from Bastnäs called “Bastnäs-Tungsten” (heavy rock from Bastnäs) and found several new elements with very similar properties. Cerium, Lanthanum and Didymium (a mixture of Praseodymium and Neodymium) were isolated from the material (Öhman et al. 2004). The mining field which originally produced Fe-oxide and Cu-sulphide became the first hard-rock REE-mine. The REE ore sat in two small bodies of mainly cerite-(Ce) and ferriallanite-(Ce) (the larger one: 6–7 m long and 0.6 m wide) up to a depth of 30 m (Geijer 1921). Circa 160 t of REE ore was produced in the Ceritgruvan and Sankt Göransgruvan (both primarily Cu-mines) in the late 19th to early 20th century before the mine was closed (Andersson et al. 2004).

The Riddarhyttan ore field (of which Bastnäs is part) has been recently explored for polymetallicsulphide deposits. Drill core from this exploration campaign have also intersected REE-enrichedzones, allowing this mineralisation type to be investigated in lithological context. For this study twodrill cores were studied, RID-19-008 which was drilled under Gamla Bastnäsfältet (the old Bastnäs mines) and RID-19-013 drilled in the Morbergfältet roughly a km northwest of Gamla Bastnäs.

Previous studies of the Bastnäs mineralisation have mainly been mineralogical and geochemical in nature. They include detailed isotopic analyses on a small number of samples. The mineralised samples were collected from mine waste pile and old samples in archives from the time of active mining (Geijer 1921; Ulf B. Andersson et al. 2004; Holtstam and Andersson 2007; Jonsson and Högdahl 2013; Holtstam et al. 2014; Sahlström et al. 2019).

2 Geological setting

The Bastnäs deposit lies within a inlier of Paleoproterozoic metavolcanic andmetasedimentary rocks with ages of ~1.91–1.88 Ga (Holtstam et al. 2014). These dominantly felsic metavolcanics show commonly volcanoclastic textures if they are not overprinted by intense synvolcanic hydrothermal alteration. This alterationoccurs in zones of different intensity and is very widespread in the Riddarhyttan area. It led to rocksstrongly enriched in either K, Na and Mg and depleted in most other elements. Mg-enriched varieties are especially common in the Riddarhyttan area, where least-altered metavolcanic rocks are almost completely lacking (Trägårdh 1988). Metasediments and marble occur as interlayers in the metavolcanic rocks. The iron oxide deposits are historically the most economically important ores in the region. They occur as banded magnetite or hematite ores as well as associated with the marbles in magnetite skarns. Sulphide mineralisation is subordinate even though some of the mines in the area were producing Cu sulphide ore.

The metavolcanic succession was intruded by plutonic rocks of two generations. The first generation has dominantly a granitic composition butranges from granodiorite to tonalite and subordinate mafic compositions. It intruded between 1.90–1.85 Ga (Holtstam et al. 2014) and is spatially dominant.A later generation intruded between 1.81–1.75 Ga (Holtstam et al. 2014) and has more strictly granitic compositions.

Several stages of Svecokarelian metamorphism and deformation complicate the geology in the region. Svecofennian metamorphism peaked at

1.85–1.80 Ga reaching greenschist to amphibolite facies (Stephens and Jansson 2020).

2.1 REE-mineralisation in western Bergslagen

After the discovery of the Bastnäs REE-deposits several additional iron oxide deposits strongly enriched in REE were recognized. These deposits are all of similar geology and mineralogy and are classified as Bastnäs type deposits. They occur along a narrow strip of over 100 km length in western Bergslagen called the REE-line (**Figure 1**).Holtstam and Andersson 2007 introduced a classification of the Bastnäs type deposits in twogroups. Type 1 with the type deposits Bastnäs, and Rödbergsgruvan at the southern end of the REE line which shows enrichment in LREE and Fecharacterised by cerite-(Ce) and ferriallanite-(Ce) as primary ore minerals. Type 2 is relatively enriched in,HREE, Y and Mg, Ca, F and occurs mainly in theNorberg district at the northern end of the REE line.

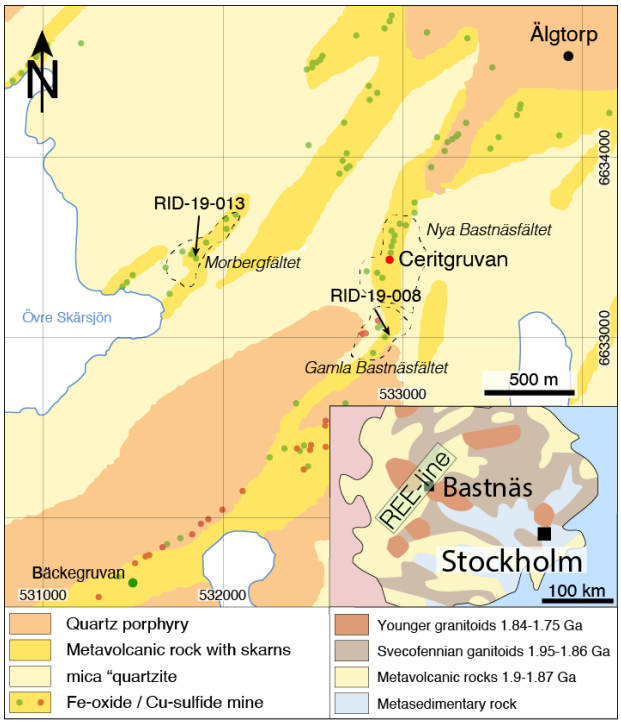

Figure 1. Geological map of the Bastnäs ore field (after Holtstam et al. 2014). The two studied drill cores are shown by arrows, both plunge with -50° while the generalbedding is sub-vertical, striking NO-SW. The location of the Nya Bastnäs iron oxide deposit and the Ceritgruvan isshown by the alchemical iron symbol. The coordinate frame is in SWEREF99. The location of Bastnäs in Bergslagen is given in the inset geological map.

3 Existing data, sampling, and methods

As part of this study, two drill cores from a drilling campaign in 2019 were re-logged and selectively sampled. The sampled sections were scanned by X-ray tomography to identify the 3-dimensional textures of the REE-bearing minerals. Samples representing the different structural and textural REE-ore types were then selected for thin sections. Twelve thin sections were examined at the SEM (Scanning Electron Microscope) at the Swedish Museum of Natural History. Mineral compositions were semi-quantitively analysed by EDS (energy-dispersive X-ray spectroscopy).

4 Lithological controls

The bulk rock assay data shows that all magnetite skarn units in the two studied drill cores contain very high REE concentrations, whereas the magnetite and hematite banded iron formations (BIF) are not significantly enriched in REE (Figure 2). Within the magnetite skarns there is no correlation between magnetic susceptibility (as a proxy for magnetite) and REE concentration. The magnetite and REE mineralisation in drill core RID-19-008 occur mainlyat the margins of the marble unit. In drill core RID- 19-013, the whole upper marble/skarn unit is strongly mineralised with magnetite whereas the REE mineralisation is more pronounced in the lowerpart of the skarn.

5 Mineralogy and Textures

The REE-rich sections in the drill cores are typically characterised by mm- to cm-sized grains or massive veins and bands of dark brown to black epidote supergroup REE-minerals (ESM) (~80-90%; e.g. ferriallanite-(Ce), dollaseite-(Ce) and dissakissite-(Ce)), which strongly dominate the REE paragenesis. REE-carbonates and halides are rare,an exception is bastnäsite-(Ce), which is a more common accessory phase. There are two main groups of REE-mineralisation textures and paragenesis described below.

The first and most common REE mineral paragenesis is a granoblastic intergrowth of magnetite and ESM (dominantly ferriallanite-(Ce), dissakisite-(Ce) and dollaseite-(Ce)) in a matrix of tremolite and in some samples (mostly magnetite free samples) actinolite; diopside and serpentineoccur in the lower part of drillhole RID-19-013. The matrix generally shows a granoblastic to fibrousunoriented texture which appears recrystallised. However, the skarn shows decimeter scale variations in magnetite content and type of tremolitetextures (massive fine grained to asbestiform). ESM contain inclusions of britholite-(Ce) and gadolinite- (Y, Ce, Nd). Bastnäsite-(Ce) occurs at the contact tocalcite and calcsilicates (Figure 3a) as well as fibrous loose clusters in the vicinity of other REE phases (Figure 3c). This style of mineralisation is the dominant REE mineralisation type in drillhole RID- 19-013.

The second group is associated with structures such as veins, faults, and shear bands. The REEs are almost exclusively hosted by ESM whilexenotime-(Y) occurs as accessory phase. The REE paragenesis is commonly associated withserpentine, calcite (as vein, fracture-filling) and talc. Ferriallanite-(Ce) is the dominant REE. It commonly

occurs as overgrowth and rims on, and as veins in allanite-(Ce) (Figure 3d). As in the first group bastnäsite-(Ce) occurs as secondary mineral in contact to calcite and calc-silicates but also as fracture filling in allanite-(Ce). In some samples ESM bearing veins crosscut older REE mineralisation in skarn.

A notable exception to the above-described groupings is a sample at 230 m in core RID-19-008 which shows cerite-(Ce) as an intergrowth with magnetite and chalcopyrite (Figure 3b).

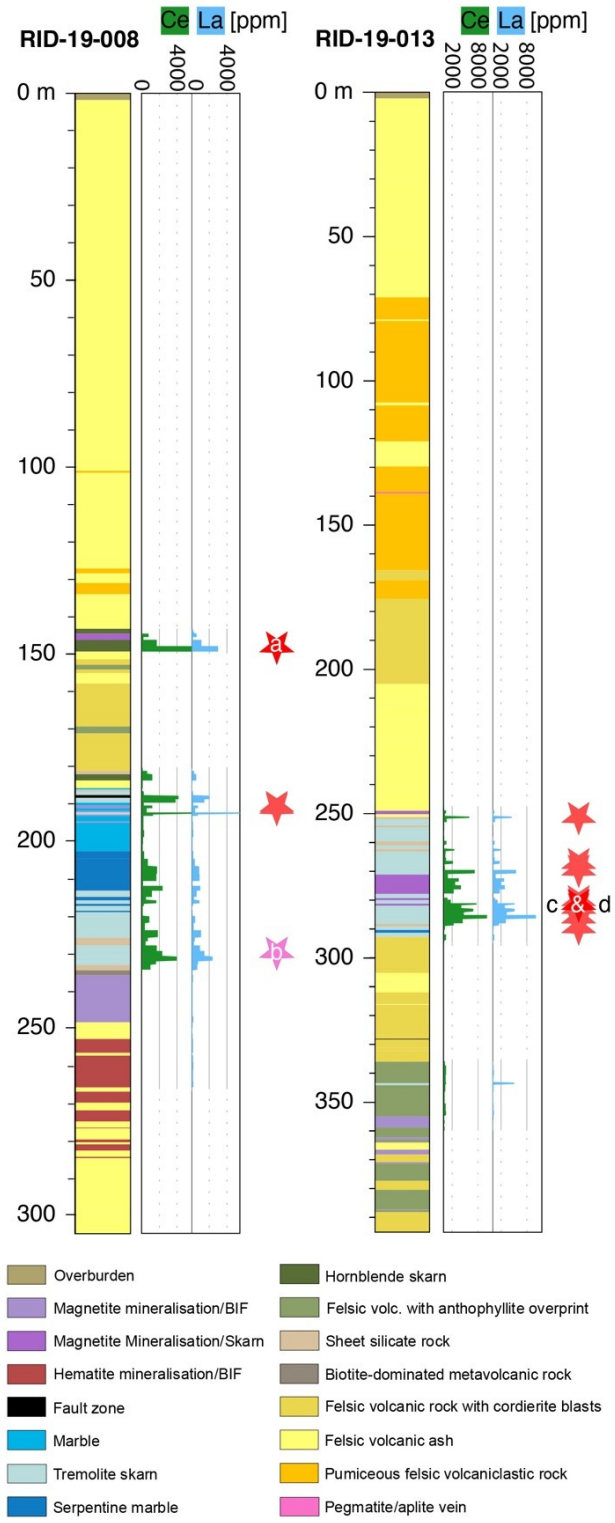

Figure 2. Simplified core logs (EMX) of the twoinvestigated drillcores showing the stratigraphy with the position of the iron ores and in separate columns the sections of high REE concentration according to assay data from EMX. The two drill cores are from different stratigraphic intervals (position shown in Figure 1). The stars indicate the position of the analysed samples, (the letters refer to the images in Figure 3). The sample containing cerite is shown by the pink star.

6 Discussion and conclusions

The results show that the REE mineralisation at Bastnäs is associated with skarn horizons as previously reported (e.g. Jonsson and Högdahl 2013, Holtstam et al 2014). However, the drill cores investigated in this study allow this relationship to be seen in more detail. We report two main textural groups of REE mineralisation. The first and most common group comprises a recrystallised intergrowth of REE-minerals and magnetite hosted in tremolite skarn and in some sections also by actinolite or diopside skarn. Group 2 mineralisation shows evidence of extensive remobilisation and recrystallisation, such as strongly foliated chlorite and talc layers (5-20 cm thick) containing coeval intergrown ferriallanite-(Ce). The intensity of REE mineralisation appears to peak at lithological boundaries such as with BIF in RID-19-008 which is not mineralised with REE (Fig. 2).

The mineralogy we observe is generally similar to the type 1 mineralisation (Riddarhyttan area / Rödbergsgruvan) reported by Holtstam et al. (2014) as the mineralisation is dominated by REE-silicates, but there are some key differences and variations. Cerite-(Ce) which is described as a major constituent by Holtstam and Andersson (2007) only occurs as a minor constituent in one layer at the bottom of the thick marble/skarn unit in RID-19-008.Old mine maps (Mannerstråle 1886) indicate the cerite ore at Nya Bastnäs at a similar stratigraphic position. The differences in REE mineralogy between Nya Bastnäs and Gamla Bastnäs which appear to lie in the same stratigraphic position possibly indicate lateral variability in REE mineralisation style. We observe bastnäsite-(Ce) but contrary to the observations of Holtstam and Andersson (2007), only as minor, secondary mineralat the contact of REE-silicates and Ca-bearing phases (Figure 3c). Furthermore, in our textural group 1, gadolinite-(Ce, Y, Nd) occurs as a common mineral, and britholite-(Y, Ce) and fluorbritholite-(Ce)as rarer mineral forming inclusions in ESM (Figure 3a) whereas Holtstam et al. (2014) describes fluorbritholite-(Ce) only in type 2 mineralisation (Norberg district) and gadolinite-(Y) only as accessory phase in type 1. Britholite-(Y) and britholite-(Ce) have previously not been reportedfrom Bastnäs type deposits.

Our observations combined with those previously reported indicate a large variety of REE mineralisation with different styles possibly occurring at different stratigraphic levels, laterally within the same horizon and due to recrystallisation driven by

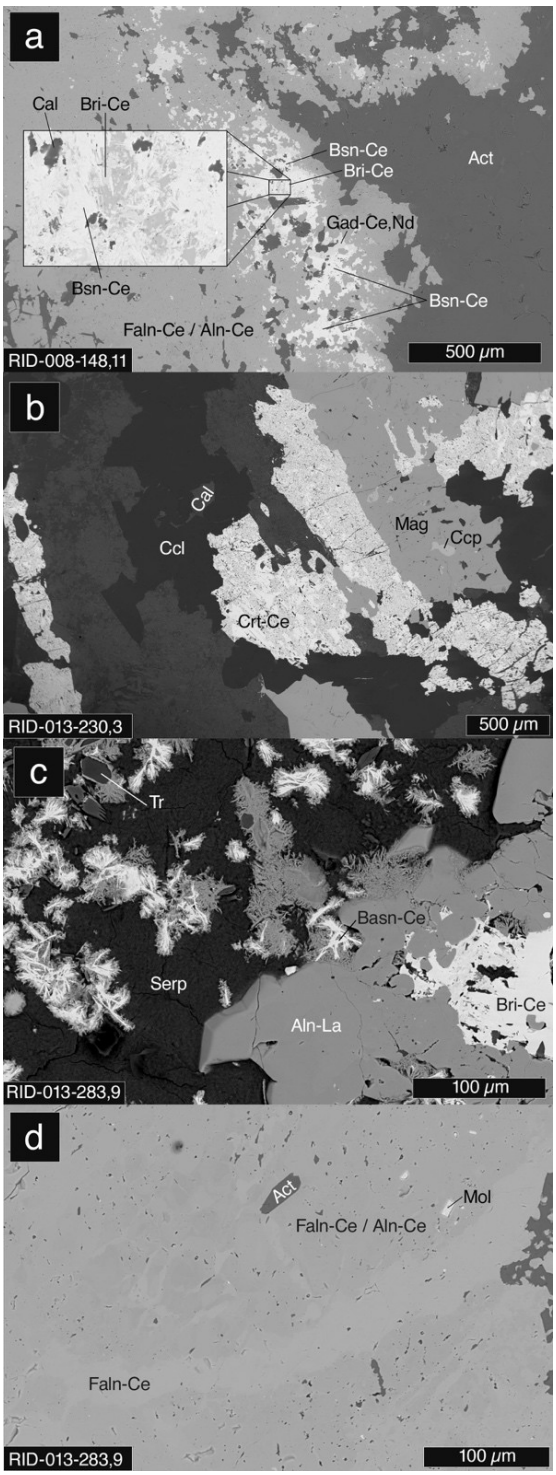

Figure 3. Backscattered electron images showing the textural relationships between different REE phases. The position of the samples is referenced with the letters in the top left corner corresponding to Figure 2. The sample ID is given in the lower left corner. **a**) shows the typical paragenesis in magnetite skarns (group 1), **b**) shows the cerite ore, **c**) shows secondary Basn-Ce and **d**) shows Faln-Ce veins in Aln-Ce (group 2).
Abbreviations: Act=actinolite; Aln=allanite; Bsn=bastnäsite;Bri=britholite; Cal=calcite; Ccl=clinochlore; Ccp=chalcopyrite; Crt=cerite; Faln=ferriallanite; Gad=gadolinite; Mag=magnetite; Mol=molybdenite; Serp=serpentine; Tr=tremolite.

deformation. The stratigraphic sections from Gamla Bastnäs (RID-19-008) and Morbergfältet (RID-19-013) contain different styles of REE mineralisation and most likely represent different stratigraphic levels. The higher abundance of minerals rich in HREE and Y in RID-19-013 indicates some similarities with the REE mineralisation described atNorberg (Holtstam et al. 2014). The abundance of heavily remobilised group 2 mineralisation and the occurrence of wide, talk and chlorite filled fractures in RID-19-008 may indicate proximity to a fault zone (also indicated by Öhman et al. 2004). The combined observations indicate a complex mineralisation history with several temporal stages and later remobilisation. The REE-ore is best described as stratabound. Most REE mineral textures are paragenetically late, but it remains unclear whether primary REE mineralisation occurred during initial skarn formation or at a later stage.

Acknowledgements

EMX Royalties Corp. are thanked for the access to the drill cores logs and assay data.

References

Andersson UB, Holtstam D, Lundström I, Langhof J, Nysten P (2004) The Bastnäs-type REE-mineralisations in north-western Bergslagen, Sweden: a summary with geological background and excursion guide. Geological Survey of Sweden, Uppsala

Geijer P (1921) The cerium minerals of Bastnäs at Riddarhyttan. Geological Survey of Sweden, Uppsala, C304:1–24

Holtstam D, Andersson UB (2007) The REE minerals of the Bastnäs-type deposits, south-central Sweden. CanMineral 45: 1073-1114. https://doi.org/10.2113/gscanmin.45.5.1073

Holtstam D, Andersson UB, Broman C, Mansfeld J (2014) Origin of REE mineralization in the Bastnäs-type Fe-REE-(Cu-Mo-Bi-Au) deposits, Bergslagen, Sweden. Miner Deposita 49:933-966. https://doi.org/10.1007/s00126-014-0553-0

Jonsson E, Högdahl K (2013) New evidence for the timing of formation of Bastnäs-type REE mineralization in Bergslagen, Sweden. Mineral deposit research for a high-tech world: Proceedings of the 12th SGA Biennial Meeting 2013 pp 1724–1727.

Mannerståle CM (1910) Karta över Bastnäs Gruvfält i Skinnskattebergs Bergslag av Westerås län, Gruvkarta 491.

Öhman L, Nysten P, Langhof J (2004) The Bastnäs Mines, Riddarhyttan ore field, Bergslagen district, Västmanland, Sweden. The minerlogical Record 35:187-200

Sahlström F, Jonsson E, Högdahl K, Troll VR, Harris C, Jolis EM, Weis F (2019) Interaction between high-temperature magmatic fluids and limestone explains 'Bastnäs-type'REE deposits in central Sweden. Sci Rep 9:15203. https://doi.org/10.1038/s41598-019-49321-8

Stephens MB, Jansson NF (2020) Chapter 6 Paleoproterozoic (1.9-1.8 Ga) syn-orogenic magmatism, sedimentation and mineralization in the Bergslagen lithotectonic unit, Svecokarelian orogen. Geological Society, London, Memoirs 50:155–206. https://doi.org/10.1144/M50-2017-40

Trägårdh J (1988) Cordierite-mica-quartz schists in a Proterozoic volcanic iron ore-bearing terrain, Riddarhyttan area, Bergslagen, Sweden. Geol Mijnb 67:397–409

Genesis, Sedimentology, and Geochemical Features of Stratiform Phosphorites of the Upper Lydite Formationand Rare Earth Element Content

Juan F. Galán[1], Juan F. Correa[1]
[1]Departamento de Geociencias, Universidad Nacional de Colombia, Sede Bogotá

Abstract. This study presents a petrological and geochemical analysis of phosphorites deposited during the Upper Cretaceous near the municipality of Piedras, inthe department of Tolima, Colombia and found within the Upper Lydite Formation of the Oliní Group characterized by a sedimentary sequence composed of fine-grained terrigenous and calcareous marine. rocks. The objective is to provide a better understanding of the mineralogy, genesis, and formation environments of these phosphorus-rich rocks, as well as their economic viability for exploitation. Petrographic analysis reveal that the rocksare mainly composed of fluorapatite, calcite, and quartz, with accessory minerals such as glauconite, pyrite, smectite, and other clay minerals, which were confirmed by crystallographic results obtained using XRD. Sedimentological analysis from petrography indicate that the rocks belong to a calcareous sequence of benthic foraminiferal biomicrites, which are highly silicified, suggesting that the entire sequence was formed in an offshore marine environment with an influence of upwelling currents and processes of increasing and decreasing system energy. Geochemical analysis using X-ray fluorescence showed the presence of REE such as cerium, lanthanum, and yttrium in appreciable concentrations in the phosphorite using a semi- quantitative method, which opens the possibility of future exploitation of this type of deposit focused on obtaining these elements in Colombia. This would be of great scientific and economic interest as these elements are key in various technological applications, have high demand inthe global market, and especially in the energy transition that is beginning in the country. The importance and detailed information of this type of reservoir in global REE demand is discussed in depth in McLaughlin et al. (2016). The relatively high concentrations of REE in the rocks were associated with the replacement of calcium in the structure of fluorapatite by these elements during their formation.

1 Introduction

Phosphorites are sedimentary rocks that contain high concentrations of phosphate (P_2O_5), an essential element for life and agriculture. Colombia has important phosphorite deposits, mainly in the Eastern Cordillera, where phosphorites of marine origin of Cretaceous age are found (Cathcart et al. (1967)). These rocks have been exploited for decades to produce fertilizers. Colombia is the 5th largest producer of phosphates in the continent, after the United States, Brazil, Peru, and Mexico. Currently, Colombia has been extracting the mineral, with an average annual production of 60,377 tons in the last 5 years (ANM 2021). However, domestic demand exceeds the national supply, so it is necessary to import this mineral from other countries, which makes it necessary to increase the production of this resource in a sustainable manner and with world standards of environmental care.

In addition to their importance for agriculture and life in general, in recent years it has become evident that these rocks present concentrations of rare earth elements, which are a group of elements considered critical due to their unique properties and strategic applications in various industrial sectors. The high REE concentrations in phosphorites have been explained that their relatively high concentrations are due to the substitution of Ca2+ cations, which is the most common cation in phosphates. These are similar in size to rare earths (REE), which facilitates substitution. In addition, rare earths have a charge of 3+, which is the same as that of the anionic group of (PO4)3-phosphates, which promotes electrical neutrality and stability of the crystal structure.

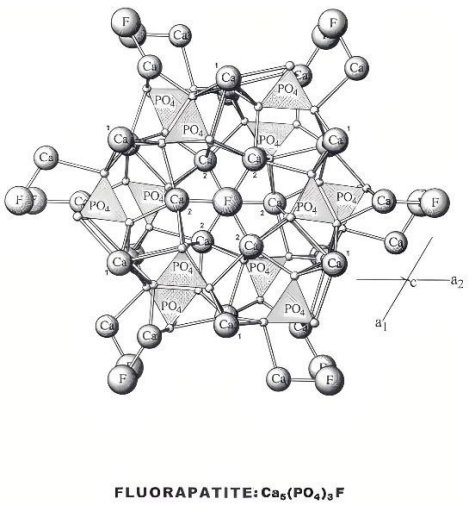

Figure 1. Molecular structure of fluorapatite ($Ca_5(PO_4)_3F$) taken from Skinner (2004).

Constituent ion	Substituting ion
Ca^{2+}	Na^+, K^+, Ag^+
	Mg^{2+}, Sr^{2+}, Ba^{2+}, Cd^{2+}, Mn^{2+}, Zn^{2+}
	Bi^{3+}, Sc^{3+}, Y^{3+}, REE^{3+}
	U^{4+}
PO_4^{3-}	CO_3^{2-}, SO_4^{2-}, CrO_4^{2-}
	CO_3, F^{3-}, CO_3, OH^{3-}, AsO_4^{3-}, VO_4^{3-}
	SiO_4^{4-}
F^-	OH^-, Cl^-, Br^-
	O^{2-}

Figure 2. Possible substitutions in the fluorapatitestructure. taken from Jarvis et al. (1994).

Phosphorites are formed through a complex series of geological processes that involve the concentration of phosphorus and other elements in sedimentary deposits. Understanding these processes and the factors that control the formation and distribution of phosphorites is essential for identifying potential deposits and developing sustainable strategies for their extraction.

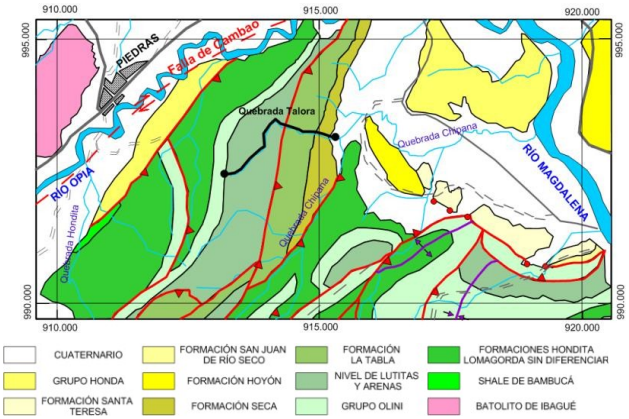

Figure 3. Regional geology and location of the study area taken from Hernández Duran (2021).

2 Methodology

Two field trips were made to Piedras town to collect representative samples of the bedrock (silicified calcareous rocks) and especially of the phosphorites. We also tried to know the general formation environment of the outcropping units in the area, through sedimentological and stratigraphic observations, and with the support of a bibliographic review of previous studies of the area, such as Guerrero et al. (2000) and De Porta (1965). A mostly marine environment was interpreted, with evidence of transgressive and regressive events, but with a trend towards marine regression towards the end of the Cretaceous. The samples were then observed and analysed macroscopically and microscopically, from hand samples and thin sections prepared for petrographic analysis.

XRD and XRF methods were used to compare and quantify the mineralogical and chemical composition of the samples. XRD was carried out with a D2 Phaser equipment, following the methodology of Thorez (1976), which consists of crushing the sample to a size <50 um and then making the 4 analyses which are disoriented powder, natural orientation, ethylene glycol and calcined at 515 °C. This allows a correct and unbiased interpretation of the semi-quantitative composition of the samples, which was performed in the profex program. XRF was performed on phosphorite samples UPW-E2 and UPW-C3 (Fig. 4), which were reduced to powder, dried at 105 °C for 12 hours, mixed with Merck spectrometric wax in a 10:1 ratio, homogenized by shaking and pressed at 120 kN for one minute, forming two granules of 37 mm diameter and measured in the SEMIQ-2020 application. Semiquantitative analysis was performed with Semio 5 software, with 11 scans, to detect all elements present in the sample, except H, C, Li, Be, B, N, O, and transuranic elements. An X-ray fluorescence spectrometer, MagixPro PW 2440 Philips (WDXRF) with a rhodium tube and a maximum power of 4 KW was used. This equipment has a sensitivity of 100ppm (0.01%) for heavy metallic elements.

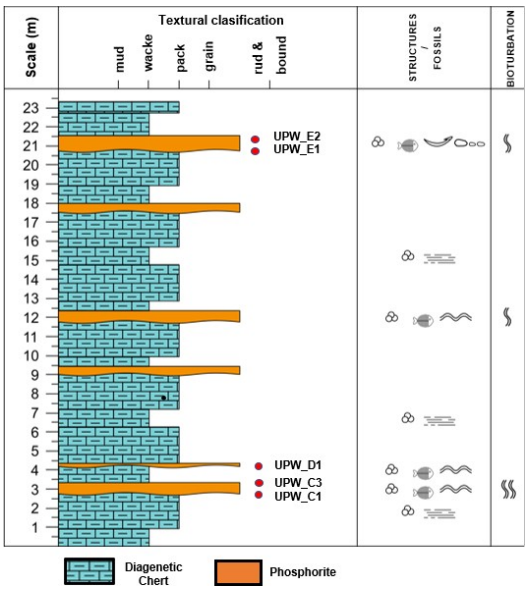

Figure 4. Generalized stratigraphic column of the last 24 meters of the top of the Upper Lidita Formation modified from Guerrero et al. (2001).

3 Petrography analysis

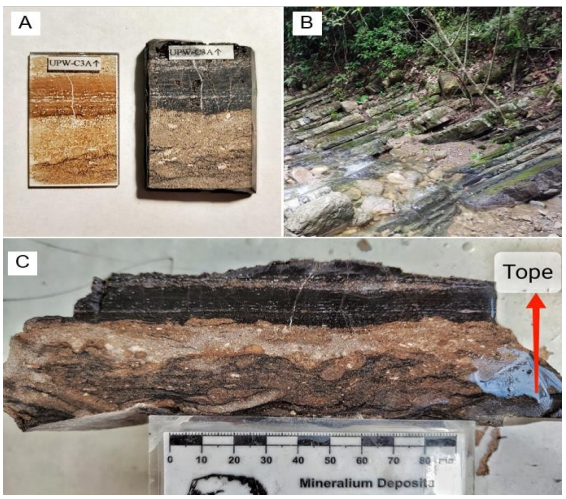

Figure 5. Thin section and rock slice of phosphorite sample. B: outcrop view of Upper Lydite Formation. C: Cut and polished hand phosphorite sample.

The petrographic analysis was performed on 10 thin sections of the Upper Lidita formation, this analysis showed two types of sedimentary rocks: cherts and phosphorites. The cherts are siliceous rocks that originated from the silicification of carbonate rocks of marine origin, which formed in a low-energy

environment, possibly in the lower off-shore. These rocks were classified as wackstone biomicrites and benthic foraminiferal packstones, according to Dunham's (1962) classification. The cherts contain mainly benthic foraminifers as allochems and micrite as matrix. The samples show plane-parallel lamination, indicating settling sedimentation, and an absence of bioturbation, indicating little biological activity. Silicification was aided by ions in solution brought by upwelling currents, which precipitated in the pores of the carbonate rocks, replacing micrite and foraminifera. The presence of framboidal pyrites within some foraminifera suggests that conditions were reducing and that sulfate-reducing bacteria were involved in diagenesis.

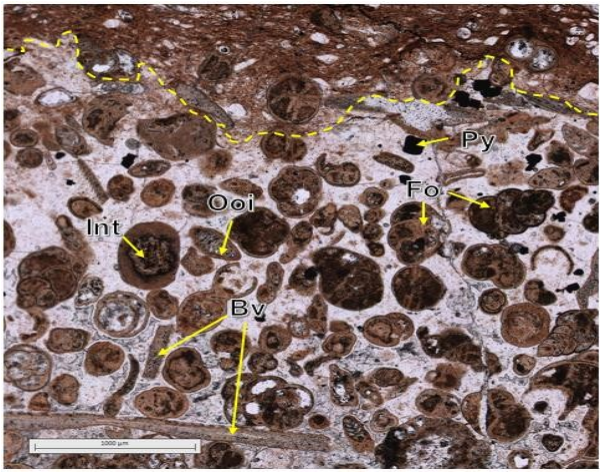

Figure 6. Phosclast-grainstone of Benthic foraminifera (C3TF sample): Benthic foraminifera (Fo), phosphate intraclasts (Int), bivalve fragments (Bv), immature phosphate ooids (Ooi) with benthic foraminifera cores, pyrite (Py).

Phosphorites originated from the accumulation of remains of phosphorus-rich marine organisms such as fish bones and from the replacement of calcium carbonate by dissolved phosphate in the water largely contributed by upwelling currents (e.g.: Föllmi 1995). These rocks were classified as phosclast packstone and grainstone of benthic foraminifera, fish remains, intraclasts and bivalve fragments, as classified by Trappe (1998). The phosphorites also contain quartz, clay minerals indicating a greater terrigenous input than in the cherts. The phosphorites show an absence of sedimentary structures such as lamination but some bioturbation structures, indicating higher energy and greater biological activity. The net increase in grain size and the presence of erosional surfaces towards the base of the phosphorite indicate sudden changes in the energy of the environment that reworked and concentrated the phosphate particles. A noticeable increase in pyrite and glauconite concentrations was also observed with respect to the chert layers.

4 X-ray diffraction quantification

X-ray diffraction (XRD) analysis was carried out to corroborate the information obtained by petrography and to complete the mineralogical part of the investigation. This analysis revealed the presence of fluorapatite, quartz and calcite as rock-forming minerals (Fig. 7). Smectite and kaolinite were identified as main clay minerals, and pyrite and glauconite as accessory minerals. In addition to knowing the specific composition of each sample some additional interpretations were reached, such as that the clay minerals and quartz content increase towards the top of the studied section. Also, from sample C3 which was divided into 3 parts, the whole history of the rocks was better understood.

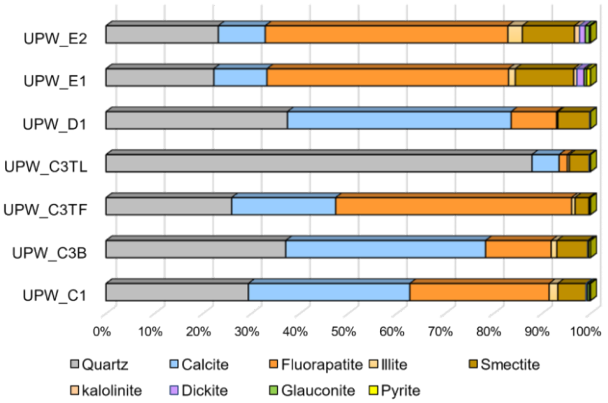

Figure 7. Semi-quantitative mineral composition of phosphorite and lydite samples analysed by X-ray diffraction.

Higher concentrations of fluorapatite are observed in lydite samples (Samples C3B and D1) stratigraphically located just before a phosphorite genesis event compared to lydite samples located just after the event (C3TL). Phosphorite samples (E1, E2, C3TF, and C1) yielded a maximum of 50% by weight of the total rock, and it was discovered that the thickness of the phosphorite layer is directly related to the percentage of phosphate. Furthermore, the phosphate content is inversely proportional to the silica content of the phosphorite samples.

5 XRF Analysis

According to the results obtained by X-ray fluorescence, these rocks were identified as containing a high percentage of P2O5 (~25 wt%), which is the main indicator of the quality of phosphate rocks. In addition, the rocks present considerable concentrations of REE, such as cerium (~400 ppm), lanthanum (~300 ppm) and yttrium (~100 ppm), the relationship of P2O5 with other major oxides such as CaO and SiO2 is not clear, and more information is needed to correctly interpret these associations. Other components found in the samples are shown in detail in Figure 8.

Further geochemical analysis is needed on the phosphorites and especially on associated rocks such as lydites to identify if there are compositional variations and what they might be associated with.

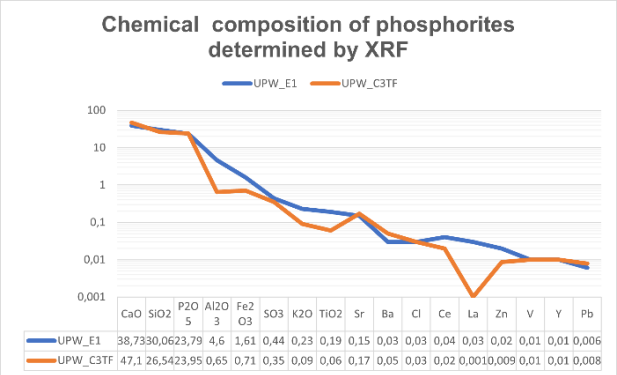

	CaO	SiO2	P2O5	Al2O3	Fe2O3	SO3	K2O	TiO2	Sr	Ba	Cl	Ce	La	Zn	V	Y	Pb
UPW_E1	38,73	30,06	23,79	4,6	1,61	0,44	0,23	0,19	0,15	0,03	0,03	0,04	0,03	0,02	0,01	0,01	0,006
UPW_C3TF	47,1	26,54	23,95	0,65	0,71	0,35	0,09	0,06	0,17	0,05	0,03	0,02	0,001	0,009	0,01	0,01	0,008

Figure 8. Chemical composition in weight percent of total rock from two samples of phosphorites C3TF and E1 determined by XRF.

6 Conclusions

The Upper Lidita Formation consists of two types of sedimentary rocks: cherts and phosphorites. Petrographic analysis reveals their different origins and environments. The cherts have planoparallel lamination, with calcareous allochemicals and orthochemicals replaced by silica. They lack erosional structures, suggesting that they formed from the silicification of carbonate rocks in a low energy setting. The phosphorites have microerosive structures at the base, randomly arranged allochemicals, no matrix, calcite cementation and phosphatization of the fossils. These features indicate that they resulted from the accumulation of phosphorus-rich marine organisms, with substitution of calcium carbonate by dissolved phosphate, in a higher-energy setting. Possible upwelling currents may have contributed phosphate to the system. The petrographic results agree with previous studies that interpret the Upper Lidita Formation as a transgressive-regressive sequence, reflecting changes in sea level and tectonics during the Upper Cretaceous (Guerrero et al. 2001).

The phosphorites contain fluorapatite, quartz, calcite, smectite, kaolinite, pyrite and glauconite, as confirmed by X-ray diffraction analyses. They also show evidence of a phosphorite genesis event, which started with a rapid enrichment of fluorapatite in the rock. After a high-energy event, fluorapatite reached up to 50% by weight of the rock. When the system returned to normal (low energy environment producing biomicrites), fluorapatite decreased to only 3%.

The phosphorites have a high percentage of P2O5 and significant concentrations of REE such as cerium, lanthanum, and yttrium. These make them potentially valuable as a source of these elements, which are highly demanded and scarce. Most of the production of REE is concentrated in a few countries, such as China. Phosphate rocks are an abundant and accessible resource that can also provide phosphorus, which is a critical element for food security and economic development.

Acknowledgements

I would like to express my sincere thanks to Professor Carlos Sánchez for his guidance and support throughout the project. I also thank the Lattice and MicroFluidSpectral laboratories for facilitating the use of their analytical equipment. I would also like to acknowledge the help and advice of Denis Oi ulu and Carlos Esquivel in the final part of the project. Finally, thanks to SGA UNAL Bogota and Professor Thomas Heinrich Cramer for doing everything.

References

ANM (2021). “Los fosfatos son un mineral de interés estratégico para Colombia”: presidente ANM. Agencia Nacional de Minería ANM. https://www.anm.gov.co/?q=los-fosfatos-son-un-mineral- de-interes-estrategico-para-colombia

Cathcart JB, Zambrano F, Mojica PE (1967). Roca fosfática en Colombia, con una sección sobre fosfatos de Turmequé, Boyacá. Boletín Geológico, 15(1-3): 65-162.

De Porta J (1965). La estratigrafía del Cretácico Superior y Terciario en el Extremo S del valle Medio del Magdalena. Boletín De Geología 19: 5-50

Dunham RJ (1962). Classification of carbonate rocks according to depositional texture. American Association of Petroleum Geologists Memoir 1(108): 108–121.

Föllmi KB (1995). The phosphorus cycle, phosphogenesis and marine phosphate-rich deposits. Earth-Science Reviews, 40(1-2): 55-124.

Guerrero J (2000). The Stratigraphy of the W Side of the Cretaceous Colombian Basin in the Upper Magdalena Valley. Reevaluation of Selected Areas and Type Localities Including Aipe, Guaduas, Ortega, and Piedras. Geología Colombiana 25:45-110

Hernández Duran S (2021). Litogeoquímica de las unidades del Cretácico Superior, su relación con las áreas de aporte y evolución de los medios sedimentarios, Cuenca del Valle Superior del Magdalena, Colombia; M.Sc. thesis, Universidad Nacional de Colombia, 225 p. https://repositorio.unal.edu.co/handle/unal/80337

Jarvis I, Murphy AM, Gale AS, Thirlwall MF, Busfield ME (1994). Phosphorus cycling in the sedimentary record. Philosophical Transactions of the Royal Society B: Biological Sciences 346(1318): 27–35.

McLaughlin PI, Emsbo P, Breit GN, du Bray EA, Koenig AE (2016). Rare earth elements in sedimentary phosphate deposits: Solution to the global REE crisis? Gondwana Research 36(1): 145-157.

Skinner C (2004). Molecular structure of fluorapatite. https://serc.carleton.edu/download/images/1809/CatherineS_ice.jpg

Thorez J (1976). Practical Identification of Clay Minerals: A Handbook for Teachers and Students in Clay Mineralogy. 90 p.

Trappe J (1998). Phanerozoic phosphorite depositional systems: A dynamic model for a sedimentary resource system. Lecture Notes in Earth Sciences, v. 76, 323 p. https://doi.org/10.1007/BFb0009670

The Circular Economy Challenge: Re-use of processing granite wastes for REEs-recovery: preliminary results

Silvia Gioiello[1], Licia Santoro[1], Alberto Cazzaniga[2]
[1] Department of Earth Sciences, University of Torino, Italy
[2] Minerali Industriali S.r.l., Italy

Abstract. Chemical and minero-petrographic analyses by ICP-MS, XRPD, and SEM-EDS have been performed on scraps from the industrial processing of granite. The work aims to study the optimization of industrial processes by re-using the feldspar-treated waste material to recover Critical Raw Materials in the view of economic circularity and sustainable mining. The material used for this work derives from Montorfano quarry wastes (Piemonte, Italy). The ICP-MS analyses on the 1.2 to 0.1 mm fraction discarded after magnetic separation of granitic material for pure feldspar production show enrichment in Rare Earth Elements (REEs), mainly Ce, La, Nd, and Y. The XRPD and SEM-EDS analyses indicate that monazite, allanite, and xenotime are the main REE-bearing minerals, commonly locked within phyllosilicates. The results suggest that a further grinding on the unprocessed material is probably required to enhance particle liberation. Comminution to a particle size smaller than 0.1 mm, will lead to a more effective concentration of REEs minerals during magnetic separation.

1 Introduction

The growing economic importance and high supply risk make the availability of Critical Raw Materials (CRMs) a crucial issue for the European Union, which translates into the need to promote their exploration and recovery optimization to meet the foreseeable increase in demand. Most of these materials are essential for transitioning from the traditional energy system to a more sustainable one. However, domestic production is severely limited, resulting in a strong dependence on imports and uncertain access to resources. The present study focuses particularly on Rare Earth Elements (REEs), mainly used to manufacture components for high-tech and green technologies applications (European Comission 2017, 2021; Bobba et al. 2020). Currently, China holds the monopoly on REEs production. Moreover, mineral processing to recover such materials still represents a considerable challenge. Re-processing and re-use from quarry and mining wastes represent a good option to face the supply risk, leading to diversification of the supply chain and likely enhancement of domestic supply. In light of the above, this work aims to assess the viability of REEs recovery from mineral-processing industrial wastes, hence favoring a possible valorization and sustainable management of the processing scraps through their re-use in the frame of the Circular Economy.

The object of this research is a quarry disposal site located in the Lake District of the Verbano-Cusio-Ossola area (Piedmont, Italy), on the southern slope of the Montorfano massif (Figure 1a), where granite bodies were quarried as dimension stones for ornamental purposes, producing a huge volume of waste material. Such material is presently exploited to recover feldspar for ceramic and glass industries. The Montorfano pluton is intruded into gneissic rocks of the *Scisti dei Laghi* subunit, belonging to the *Serie dei Laghi* unit (Figure 1b). It is part of a NE-SW elongated batholith composed of many plutons occurring from the Biella area to the western shore of Lago Maggiore (Boriani et al. 1988).

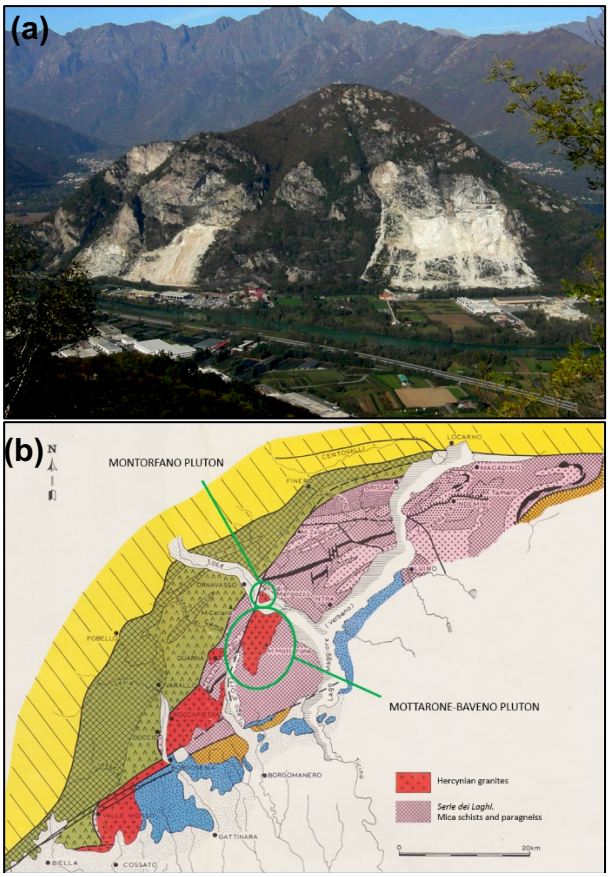

Figure 1. a Granite quarries on the southern side of Montorfano massif (Dino et al. 2012). **b** Tectonic sketch map of a portion of the central-southern Alps (Piedmont, Italy) and location of Montorfano and Mottarone-Baveno granitic plutons into *Serie dei Laghi* unit. Adapted from 1:50.000 geological map of the Verbania area (Boriani A et al. 1977).

The pluton is a medium-grain white granite, whose mineralogical assemblage consists primarily of plagioclase, quartz, K-feldspar, and biotite, including typical accessory minerals such as apatite, zircon, and allanite (Boriani et al. 1988). The occurrence of allanite-(Ce), together with other REEs-bearing minerals (e.g., Y-Sc-REEs-silicates, Y-REEs phosphates and Nb-Ta-Y-REEs oxides) has already been described in previous studies on the niobium-yttrium-fluorine (NYF) granitic pegmatite at Baveno (Guastoni et al. 2017).

A key purpose of the study was to evaluate the concentration process of ore minerals during the granite waste treatment aimed at feldspar production, performing detailed mineralogical and geochemical analyses on milled samples coming from different processing stages, as described in the following paragraph.

2 Methodology

Granite waste rock samples were collected in the Montorfano quarry and subsequently prepared and analyzed to define the behavior of REEs minerals in different types of concentrates resulting from industrial processing. All samples were crushed and ground in appropriate mills to achieve a grain size between 0.1 and 1.2 mm and then subjected to two different steps of magnetic separation, thus replicating the method used to obtain a pure feldspar concentrate. This process produces a "waste" magnetic fraction. The first separation step was applied on unprocessed material with grain size between 0.1 and 1.2 mm using a current of 2.5 Amp. Subsequently, the magnetic concentrate was sieved, and a second step was carried out on grain size of 0.1-0.6 mm using 2.5 Amp.

Wet chemical analyses by Inductively Coupled Plasma Mass Spectrometry (ICP-MS) were performed by ALS Laboratories on both the unprocessed material and the magnetic fraction for a large number of elements, including REEs (Sc, Ce, La, Nd, Sm, Pr, Eu, Dy, Er, Y, Gd, Ho, Lu, Tb, Tm and Yb) and other critical metals (e.g., Nb, Ta). Furthermore, the magnetic concentrates were investigated in terms of mineralogical and chemical composition through qualitative and quantitative analyses. Particularly, X-Ray Powder Diffraction (XRPD) analyses were carried out at the Minerali Industriali Engineering's central laboratory to characterise the material. The acquisitions were carried out by using a Siemens D5000 Diffraktometer, operating at 40 kV, 40 mA, divergence slit 1, antiscatter slit 1, rotation 30, start 4 and stop 70. SEM-EDS analyses were carried out with a JEOL IT300LV Scanning Electron Microscope at the Department of Earth Sciences, University of Torino. The instrument was equipped with an energy dispersive spectrometry (EDS) Energy 200 system and an SDD X-Act3 detector (Oxford Inca Energy). Operating conditions were: 20 kV accelerating voltage, 5 nA probe current, 30 s counting time. SEM data were acquired and processed using the AzTec software (Oxford Instrument), version 6.0. In detail, microanalyses were acquired by using AzTec point ID suite. The use of SEM-EDS was combined with Automated Mineralogy (AM) analytical systems using a specific software package for data processing and automation (i.e., AztecFeature), which provides detailed particle analyses to be classified on the morphology and on the chemistry and combination of the two.

3 Results

Preliminary results described below refer to a representative sample indicated as *SNG*, which consists of a magnetic concentrate resulting from the first separation step, sieved to a grain size greater than 0.6 mm.

3.1 Wet chemical analyses (ICP-MS)

As shown in Table 1, chemical analysis on samples from different processing stages highlights a REEs enrichment in the magnetic concentrate compared to unprocessed material, particularly on the course fraction obtained from the first separation step. Light REEs (from Sc to Eu) are generally more abundant than heavy REEs (from Dy to Yb), and the highest values, are found for Ce, La and Nd. In addition, there is an increase in P from the unprocessed material to the magnetic fraction coinciding with the trend in REEs concentrations.

Table 1. ICP-MS results for REEs and P. (TQ = unprocessed material; SNG = magnetic fraction >0.6 mm, 1st separation step) SNS = magnetic fraction <0.6 mm, 2nd separation step).

		TQ	SNG	SNS			TQ	SNG	SNS
Sc	ppm	8.6	55.3	32.9	**Dy**	ppm	4.86	22.2	12.45
Ce	ppm	89.9	434	256	**Er**	ppm	2.25	9.78	5.53
La	ppm	42	197	118	**Y**	ppm	22.8	99	64.3
Nd	ppm	40.5	198.5	125	**Gd**	ppm	6.76	32	17.9
Sm	ppm	8.34	39.2	23.3	**Ho**	ppm	0.86	3.82	2.19
Pr	ppm	10.8	51.9	32.5	**Lu**	ppm	0.28	1.13	0.69
Eu	ppm	0.77	1	0.82	**Tb**	ppm	0.92	4.24	2.28
					Tm	ppm	0.3	1.28	0.79
P	ppm	280	1460	700	**Yb**	ppm	1.91	8	4.95

3.2 Mineralogy and petrography (XRPD/SEM-EDS)

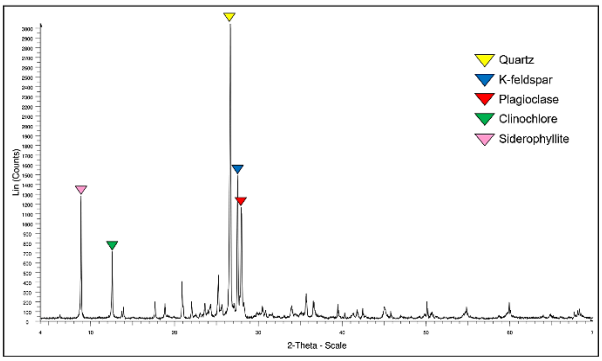

Figure 2. XRPD pattern showing prevailing gangue minerals in the coarse magnetic fraction (SNG sample).

Mineralogical characterization by XRPD helped identify the dominant gangue minerals in the SNG sample, represented by quartz, K-feldspar, plagioclase, clinochlore, and mica group minerals (e.g., siderophyllite), as shown in Figure 2. Peaks representative of REEs-minerals in the diffractogram are absent due to their concentrations falling below the instrument's detection limit.

Backscatter Electron (BSE) images and EDS on target minerals are presented respectively in Figure 3 and Table 2. The most common REEs mineral is monazite-(Ce), in agreement with the high P concentration of ICP-MS analyses (Table 1). Monazite locally shows tiny inclusions of thorite. Additionally, xenotime-(Y) and allanite (light grey) grains were

spotted. REEs-bearing minerals seem generally associated with phyllosilicates (e.g., biotite, annite, siderophyllite, clinochlore) also observed on the XRPD pattern but are characterized by far smaller grain size. However, allanite has a larger grain size than monazite and xenotime. Zircon and ilmenite, often Nb-bearing, were also detected.

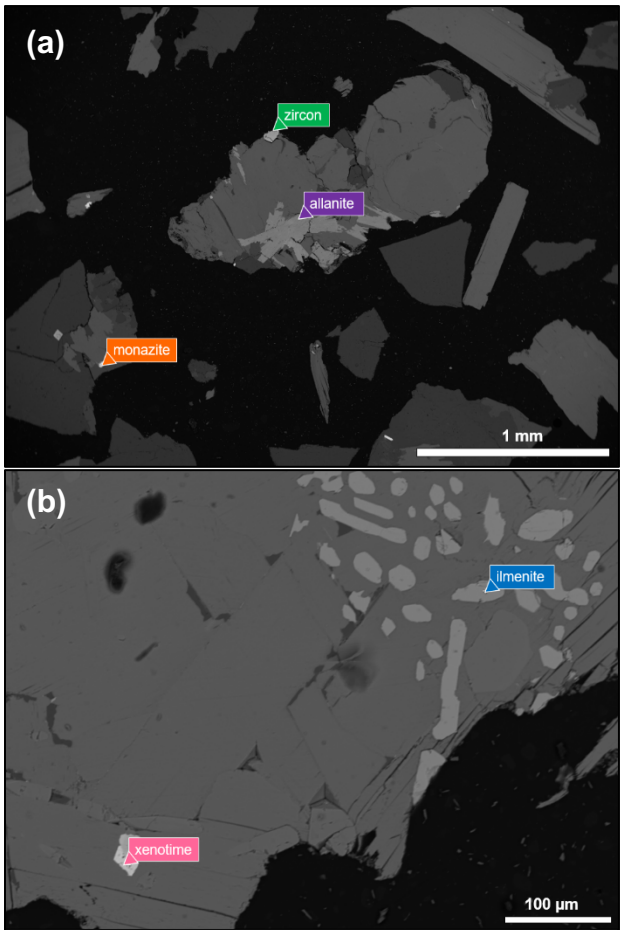

Figure 3. BSE images of selected areas on SNG sample, showing target minerals: **a** zircon (green, Spectrum 24), allanite (purple, Spectrum 25), monazite (orange, Spectrum 32) and **b** xenotime (pink, Spectrum 23), ilmenite (blue, Spectrum 22).

Table 2. EDS analyses of target minerals.

Monazite

	Spectrum 26 (normalised)				Spectrum 32 (normalised)				
	Oxide	Oxide %	Oxide % Sigma	Number of Ions		Oxide	Oxide %	Oxide % Sigma	Number of Ions
O				4	O				4
Si	SiO2	3.3	0.05	0.13	Al	Al2O3	2.45	0.22	0.11
P	P2O5	24.47	0.15	0.83	Si	SiO2	5.45	0.21	0.22
Ca	CaO	6.28	0.05	0.27	P	P2O5	22.21	0.52	0.74
La	La2O3	9.85	0.1	0.14	Ca	CaO	1.26	0.08	0.05
Ce	Ce2O3	27.41	0.18	0.4	Fe	Fe2O3	1.75	0.19	0.05
Pr	Pr2O3	2.74	0.11	0.04	Y	Y2O3	0.08	0.37	0
Nd	Nd2O3	10.2	0.12	0.15	La	La2O3	9.87	0.35	0.14
Sm	Sm2O3	9.62	0.49	0.13	Ce	Ce2O3	25.57	0.64	0.37
Gd	Gd2O3	1.43	0.09	0.02	Pr	Pr2O3	2.53	0.38	0.04
Th	ThO2	4.69	0.09	0.04	Nd	Nd2O3	8.82	0.4	0.12
Total		100		2.15*	Sm	Sm2O3	11.18	1.77	0.15
					Gd	Gd2O3	1.13	0.34	0.01
					Tb	Tb2O3	0.07	0.35	0
					Dy	Dy2O3	0.41	0.33	0.01
					Ho	Ho2O3	0.07	0.3	0
					Th	ThO2	7.16	0.35	0.06
					Total		100		2.10*

* Cation Sum

Allanite

	Spectrum 1				Spectrum 25				
	Oxide	Oxide %	Oxide % Sigma	Number of Ions		Oxide	Oxide %	Oxide % Sigma	Number of Ions
O				12	O				12
Mg	MgO	0.13	0.33	0.02	Al	Al2O3	20.2	0.07	2.04
Al	Al2O3	13.65	0.09	1.47	Si	SiO2	32.43	0.09	2.77
Si	SiO2	30.09	0.09	2.76	Ca	CaO	11.72	0.04	1.07
Ca	CaO	10.65	0.04	1.05	Mn	MnO	1.02	0.05	0.07
Ti	TiO2	2.17	0.05	0.15	Fe	Fe2O3	11.18	0.07	0.72
Mn	MnO	0.29	0.05	0.02	Y	Y2O3	1.14	0.07	0.05
Fe	Fe2O3	14.81	0.08	1.02	La	La2O3	3.59	0.07	0.11
Y	Y2O3	0.49	0.07	0.02	Ce	Ce2O3	8.7	0.11	0.27
La	La2O3	3.58	0.1	0.12	Pr	Pr2O3	1.03	0.08	0.03
Ce	Ce2O3	10.11	0.12	0.34	Nd	Nd2O3	3.58	0.09	0.11
Pr	Pr2O3	1.11	0.09	0.04	Sm	Sm2O3	5.96	0.46	0.18
Nd	Nd2O3	4.21	0.1	0.14	Gd	Gd2O3	0.77	0.1	0.02
Sm	Sm2O3	6.03	0.52	0.19	Dy	Dy2O3	0.26	0.1	0.01
Eu	Eu2O3	0.08	0.1	0	Total		101.58		7.46*
Gd	Gd2O3	0.93	0.12	0.03					
Tb	Tb2O3	0.15	0.13	0					
Dy	Dy2O3	0.41	0.12	0.01					
Er	Er2O3	0.09	0.1	0					
Lu	Lu2O3	0.07	0.09	0					
Total		99.05		7.39*					

* Cation Sum

Xenotime

	Spectrum 23			
	Oxide	Oxide %	Oxide % Sigma	Number of Ions
O				4
Si	SiO2	1.42	0.07	0.05
P	P2O5	34.14	0.13	0.98
Fe	FeO	0.92	0.05	0.03
Y	Y2O3	38.66	0.16	0.7
Ce	Ce2O3	0.03	0.06	0
Nd	Nd2O3	0.44	0.06	0.01
Pm	Pm2O3	-0.13	0.07	0
Sm	Sm2O3	4.17	0.42	0.05
Gd	Gd2O3	2.43	0.08	0.03
Dy	Dy2O3	5.13	0.11	0.06
Ho	Ho2O3	1.34	0.11	0.01
Er	Er2O3	4.38	0.11	0.05
Tm	Tm2O3	0.44	0.11	0
Yb	Yb2O3	3.11	0.12	0.03
Lu	Lu2O3	0.44	0.11	0
Th	ThO2	0.97	0.09	0.01
U	UO2	1.31	0.08	0.01
Total		99.2		2.00*

Ilmenite

	Spectrum 22			
	Oxide	Oxide %	Oxide % Sigma	Number of Ions
O				3
Si	SiO2	0.16	0.03	0
K	K2O	0.07	0.01	0
Ti	TiO2	50.79	0.09	0.99
Mn	MnO	7.03	0.05	0.15
Fe	FeO	39.11	0.1	0.85
Nb	Nb2O5	0.47	0.05	0.01
Total		97.63		2.00*

* Cation Sum

Zircon

	Spectrum 24				Spectrum 18 (normalised)				
	Oxide	Oxide %	Oxide % Sigma	Number of Ions		Oxide	Oxide %	Oxide % Sigma	Number of Ions
O				4	O				4
Si	SiO2	30.85	0.09	0.98	Si	SiO2	32.06	0.13	0.99
K	K2O	0.12	0.02	0	Ca	CaO	0.42	0.02	0.01
Ca	CaO	0.24	0.02	0.01	Fe	FeO	0.63	0.04	0.02
Fe	FeO	0.38	0.04	0.01	Zr	ZrO2	65.9	0.21	0.99
Zr	ZrO2	64.35	0.18	1	Pr	Pr2O3	0.06	0.06	0
Sm	Sm2O3	0.47	0.38	0.01	Nd	Nd2O3	0.08	0.06	0
Eu	Eu2O3	0.08	0.07	0	Eu	Eu2O3	0.04	0.07	0
Gd	Gd2O3	0.11	0.09	0	Gd	Gd2O3	0.02	0.09	0
Tb	Tb2O3	0.12	0.09	0	Tb	Tb2O3	0.1	0.09	0
Dy	Dy2O3	0.09	0.09	0	Ho	Ho2O3	0.16	0.09	0
Ho	Ho2O3	0.1	0.09	0	Er	Er2O3	0.15	0.09	0
Er	Er2O3	0.11	0.09	0	Yb	Yb2O3	0.11	0.09	0
Tm	Tm2O3	0.08	0.09	0	Hf	HfO2	0.27	0.2	0
Yb	Yb2O3	0.14	0.09	0	Total		100		2.02*
Hf	HfO2	0.51	0.21	0					
U	UO2	0.19	0.07	0					
Total		97.93		2.02*					

* Cation Sum

4 Discussion and conclusions

Chemical and minero-petrographic analyses pointed out an enrichment in REEs (mostly Ce, La, Nd in monazite and allanite and Y in xenotime) in the magnetic fraction resulting from the industrial processing of the Montorfano granite. The results show that magnetic separation enhances the concentration of REEs minerals in the source rock. However, SEM-EDS-based automated analysis (AZtecFeature Suite) used for automatic identification of REEs-bearing minerals (Figure 4a) and particles/grain size revealed likely liberation issues preventing the effectiveness of the magnetic separation process; the average grain size of target minerals is extremely small compared to the associated gangue phases, although slight

differences in size are noticeable between allanite, monazite, zircon, and ilmenite (Figure 4b).
Preliminary results of the work indicate that the major problem encountered lies in the limited particle liberation of REEs-bearing minerals, which are always locked within micas. It denotes that the particle size obtained by crushing and grinding the material before the magnetic separation process is too big to allow the liberation of monazite and other REEs minerals and their subsequent concentration in the following processing stages.

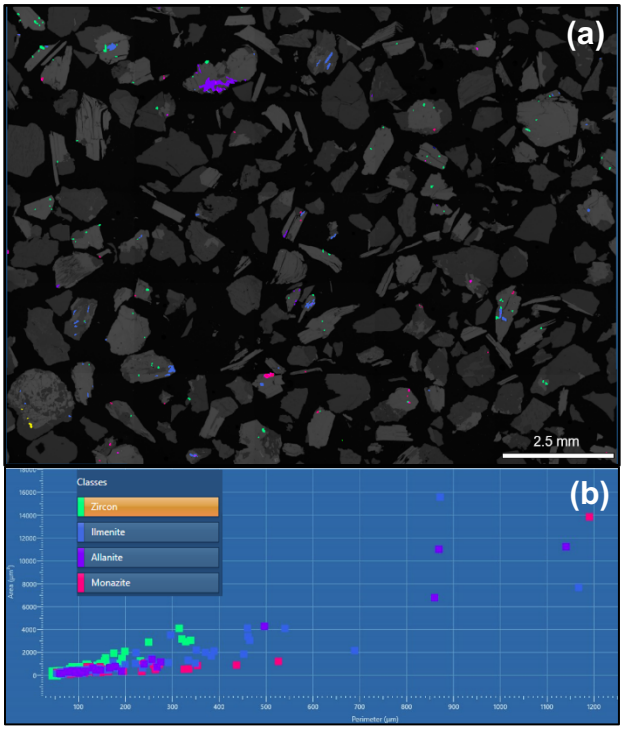

Figure 4. a Particle classification of ore minerals referring to the selected area of the SNG sample **b** Binary diagram showing the correlation between grain size area (μm^2) and perimeter (μm) of target minerals.

Hence, an additional grinding step on the unprocessed material is probably required to achieve a roughly homogeneous grain size below 0.1 mm. This could make the particle liberation more effective, leading to a better concentration of ore minerals during magnetic separation and the possible consequent extraction of REEs metals through specific techniques.

In conclusion, the work assesses that the concentration of the REEs-bearing minerals in magnetic scraps from feldspar production, aiming at reusing such processing waste with economic benefits and reducing landfill volumes, is potentially feasible upon further concentration. Additional lab tests (i.e., hydrometallurgy tests on improved concentrated material) will confirm the viability of the recovery.

Acknowledgements

The work is part of the Ph.D. project “Exploration and recovery optimization of Critical Raw Materials for the green transition, toward zero-waste Circular Economy model” in the framework of “National Recovery and Resilience Plan (PNRR)”- PHD-Innovation 352. The project is partially co-funded by Minerali Industriali S.r.l., which provides part of the facilities and equipment. The authors thank Minerali Industriali Engineering’s laboratory staff for their support during the sample preparation and analysis procedures.

References

Bobba S, Carrara S, Huisman J, Mathieux F, Pavel C (2020) Critical Raw Materials for Strategic Technologies and Sectors in the EU - a Foresight Study. Publications Office of the EU, 98pp

Boriani A, Bigioggero B, Giobbi Origoni E (1977) Geological map of the Verbania area. Mem Sci Geol 32

Boriani A, Buruni L, Caironi V, Giobbi Origoni E, Sessa ANGEUCA, Sesana ELENA (1988) Geological and petrological studies on the hercynian plutonism of Serie dei Laghi-geological map of its occurrence between Valsesia and Lago Maggiore (N-Italy). Rend Soc It Mineral Petrol 43:367-384

Dino GA, Fornaro M, Trentin A (2012) Quarry Waste: Chances of a Possible Economic and Environmental Valorisation of the Montorfano and Baveno Granite Disposal Sites. J Geol Res 2012:1–11. https://doi.org/10.1155/2012/452950

European Comission (2017) Study on the review of the list of critical raw materials. Publications Office of the EU, 153pp

European Comission (2021) Critical Raw Materials Resilience: Charting a Path towards greater Security and Sustainability

Guastoni A, Nestola F, Schiazza M (2017) Post-magmatic solid solutions of CaCeAl2(Fe3+2/3□1/3)[Si2O7][SiO4]O(OH),allanite-(Ce) and REE-bearing epidote in miarolitic pegmatites of Permian Baveno granite (Verbania, central-southern alps, Italy). Mineral Petrol 111:315-323. https://doi.org/10.1007/s00710-016-0475-x

The world-class Schlema-Alberoda U-(Ag-Co-Ni) deposit (Germany): mineralogy and fluid characteristics

Marie Guilcher[1,2], Jens Gutzmer[1,2], Axel Hiller[3], Joachim Krause[1], Nigel Blamey[4], Birk Härtel[5], Mathias Burisch[1,2,6]
[1]Helmholtz-Zentrum Dresden-Rossendorf, Helmholtz Institute Freiberg for Resource Technology, Chemnitzer Straße 40, 09599 Freiberg, Germany
[2]Institute of Mineralogy, Technische Universität Bergakademie Freiberg, Brennhausgasse 14, 09599 Freiberg, Germany
[3]Wismut GmbH, Talstraße 7, 08118 Hartenstein, Germany
[4]Department of Earth Sciences, Western University, London (Ontario), N6A 5B7, Canada
[5]Department of Geoscience, University of Calgary, Calgary (Alberta), T2N 1N4, Canada
[6]Mineral Systems Analysis Group, Department of Geology and Geological Engineering, Colorado School of Mines, 1516 Illinois Street, Golden, CO, 80401, USA

Abstract. The Schlema-Alberoda deposit is one of the largest uranium deposits in Europe with uranium ores closely associated with native metal-arsenide ore shoots. All ore styles occur in veins and stockwork zones that crosscut carbon-rich Devonian to Silurian metasediments and metabasites. This study investigates the native metal-arsenide veins in the district and provides an update on mineral paragenesis and novel fluid inclusion data. Native metal-arsenide ore occurs as vein-hosted ore shoots with native metals (Ag, Bi, As) and Co-Ni-Fe arsenides. Within the native metal-arsenide stage, five mineral associations are identified: (i) bismuth-skutterudite-safflorite, (ii) silver-rammelsbergite-skutterudite, (iii) arsenic-silver-loellingite, (iv) loellingite and (v) arsenic-sulfosalt-sulphide. Fluid inclusions measured in dolomite-ankerite that occur as gangue minerals have homogenization temperatures of ~115-150°C with fluid salinities of ~24.4-27.3 wt. % ($NaCl+CaCl_2$) eq. The spatial relationship between native metal-arsenide across the deposit and carbon-rich lithologies suggest reduction of the ore fluid as a decisive precipitation process. Microthermometric data indicate mixing of a sedimentary and a basement brine, which is also documented for other occurrences of native metal-arsenide ore across Europe that are all related to Mesozoic continental rifting.

1 Introduction

The world-class uranium deposit of Schlema-Alberoda is part of the Erzgebirge metallogenic province located in the European Variscan belt. Whilst ages for uranium mineralisation range between Permian and Mesozoic (Hiller and Schuppan 2008 and references therein), closely associated native metal-arsenide veins have recently been found to have a Cretaceous age (Guilcher et al. 2021a).

The native metal-arsenide veins consist of native metal (Ag, Bi, As) followed by arsenides within a quartz/carbonate gangue (Markl et al. 2016). The exploitation focused on uranium resources in Schlema-Alberoda between 1945 and 1991 (~80,000 t of U produced; Hiller and Schuppan 2008). The other metals (e.g., Ag, Co, Ni) were of minor relevance. Only 199 t of Co metal were extracted from ore with grades from 0.51% to 3.78 % between 1958 and 1978. Except for mineralogical studies published by Lipp and Flach (2003), no modern investigation has been carried out to understand the genesis of the native metal-arsenide veins in the Schlema-Alberoda district.

Here, we provide new petrographic observations and microthermometric measurements, complemented by mineral chemistry and fluid inclusion bulk-gas analysis aiming to better understand the origin of the native metal-arsenide veins in the Schlema-Alberoda district.

2 Geological setting of the Schlema-Alberoda district

The Erzgebirge is located within the Saxo-Thuringian zone of the Variscan Orogen. Following peak regional metamorphism at ca. 340 Ma the metamorphic units of the Variscan basement were rapidly exhumed and intruded by post-collisional granitoids followed by voluminous rhyolitic volcanic rocks between ~335 and 290 Ma (Förster and Romer 2010; Tichomirowa and Leonhardt 2010; Tichomirowa et al. 2022). Extensional tectonics dominated from the Permian to the Jurassic and were associated with rapid erosion. Extensive subsidence formed a ~2-3 km thick sedimentary cover on top of the crystalline basement (Ziegler and Dèzes 2006; Wolff et al. 2015).

In the western part of the Erzgebirge, the Schlema-Alberoda district mainly comprises phyllites and carbonaceous schist of Ordovician to Devonian age, marble and metabasic rocks; this succession experienced greenschist facies regional metamorphism. Exhumation is associated with the intrusion of the Aue granite at 328.6±2 Ma and the development of a ~1,000 m wide contact metamorphic halo (Fig. 1; Tichomirowa and Leonhardt 2010; Hiller and Schuppan 2008). The lithological units are crosscut by a NW-SE fault system hosting three main ore stages: (1) quartz-calcite-uraninite association (~280-267 Ma; Förster and Haak 1995; Golubev et al. 2000); (2) dolomite-uraninite-fluorite association (~190-140 Ma; Förster and Haak 1995; Golubev et al. 2000) and (3) native metal-arsenide ± uranium association (~129-86 Ma, Guilcher et al. 2021a). Textural observations suggest extensive remobilization and reprecipitation of uranium from the quartz-calcite-uraninite association during the dolomite-uraninite-fluorite stage (Hiller and Schuppan 2008). The native metal-arsenide ore shoots represent a second and minor remobilization of uranium. All three associations occur within a

distance of 200-800 m from the contact of the metamorphic rocks to the Aue granite. Importantly, veins pinch out or become barren beyond the limit of the contact metamorphic aureole (800-1,100 m; Lipp and Flach 2003; Hiller and Schuppan 2008). Only a few uranium and native metal-arsenide mineralised veins were observed at the contact or within the granite (less than 10 m inside the granite; Lipp and Flach 2003; Hiller and Schuppan 2008).

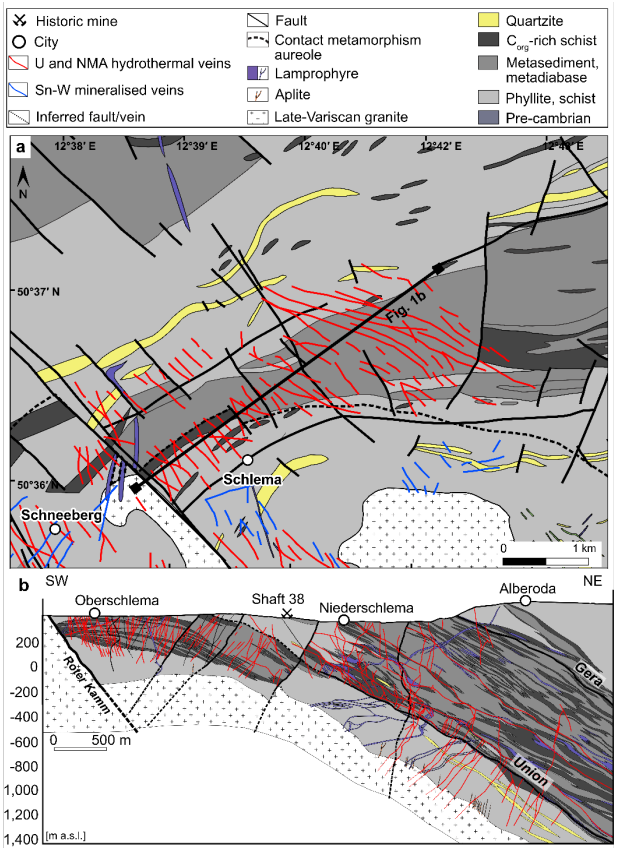

Figure 1. a Simplified geological map of the Schlema-Alberoda deposit (modified after Hoth et al. 1980; Hiller and Schuppan 2008). Red lines represent major hydrothermal veins hosting U and NMA ores. **b** SW-NE cross-section of the Schlema-Alberoda deposit.

3 Methods

Forty-nine mineralised hand specimens were selected from a large suite of well-documented samples in the geoscientific collections (including the Flach collection of U. Lipp) of the TU Bergakademie Freiberg (TU BAF) and the archives of the Wismut GmbH. Samples were selected to represent a wide range of sample depth from different veins. Petrographic descriptions are based on optical microscopy and mineral identification were supported by scanning electron microscopy (SEM) and high-resolution backscattered electron (BSE) images carried out on a FEI Quanta 650F SEM equipped with two Bruker Quantax X-Flash 5030 energy-dispersive X-ray spectrometers (EDS) at the Helmholtz Institute Freiberg for Resource Technology (HIF). The instrument was operated with a 25 kV acceleration voltage and a beam current of 13 nA to produce the BSE images. A total of 20 samples were selected for investigation of fluid inclusions in carbonates related to the native metal-arsenide mineral associations identified. Fluid inclusions suitable for microthermometric analysis were measured in 6 samples using a Linkam THMSG600 heating-cooling stage at TU BAF. Total salinities (wt. % [$NaCl+CaCl_2$] eq.) and the Na/(Na+Ca) ratio were calculated according to Steele-MacInnis et al. (2011) in the ternary $NaCl+CaCl_2-H_2O$ system. Fluid inclusions showing post-entrapment modifications (e.g., necking) were excluded. The bulk composition of gases in fluid inclusions was analysed using the crush-fast scan (CFS) method at University of Western Ontario, London, Canada (Blamey 2012). Mineral separates of carbonates were cleaned with H_2O_2 and were incrementally crushed (typically 10 crushes per sample) at room temperature under vacuum of about 10^{-7} to 10^{-8} Torr.

4 The native metal-arsenide veins

4.1 Mineral associations

Based on petrographic observations and in good agreement with mineral descriptions from Lipp and Flach (2003), we identified five distinct native metal-arsenide subtypes, namely (i) bismuth-skutterudite-safflorite, (ii) silver-rammelsbergite-skutterudite, (iii) arsenic-silver-loellingite, (iv) loellingite and (v) arsenic-sulfosalt-sulphide.

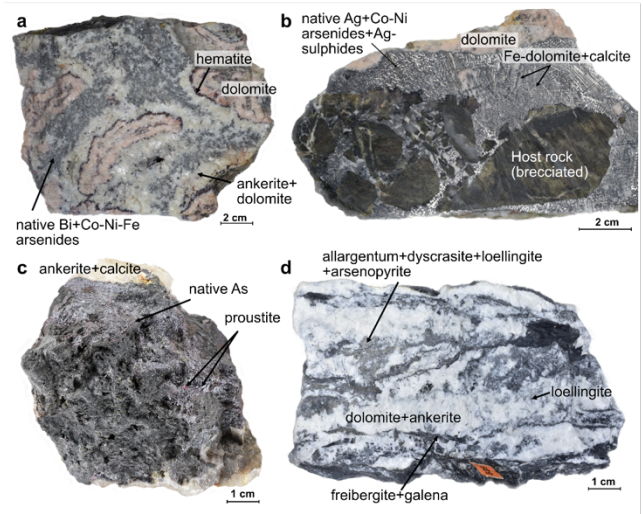

Figure 2. Main native metal-arsenide subtypes observed in the Schlema-Alberoda district. **a** Bismuth-skutterudite-safflorite with pink dolomite from the dolomite-uraninite-fluorite association. **b** Silver-rammelsbergite-skutterudite. **c** Arsenic-silver-loellingite. **d** Loellingite with Ag-sulfosalts, arsenopyrite and galena.

The bismuth-skutterudite-safflorite subtype comprises skeletal crystals or irregularly shaped grains of native bismuth overgrown by euhedral, often zoned, (nickel-)skutterudite followed by safflorite and rare loellingite (Fig. 2a). Rammelsbergite and nickeline are scarce. Occasionally, multiple layers of gersdorffite and cobaltite occur in between layers of rammelsbergite and safflorite. Dolomite, ankerite, and siderite occur

as gangue minerals either coeval with safflorite and loellingite or they overgrow arsenides. Calcite and quartz usually form the youngest minerals in this mineral paragenesis.

The silver-rammelsbergite-skutterudite subtype consists of fern-like dendritic native silver overgrown by rammelsbergite, nickeline, safflorite, and euhedral (nickel-)skutterudite (Fig. 2b). Loellingite, if at all present, invariably occupies the youngest paragenetic position within the arsenide sequence. Iron-dolomite, dolomite-ankerite, calcite, and paragenetically younger quartz compose the gangue minerals that accompany the arsenides.

The arsenic-silver-loellingite subtype shows native silver and rammelsbergite encapsulated by aggregates of fine-grained native arsenic (Fig. 2c). The latter minerals are either rimmed by a thin layer of loellingite or overgrown by euhedral loellingite crystals. Loellingite is accompanied by ankerite and dolomite, followed by younger calcite.

Native elements are rarely present in the loellingite subtype (Fig. 2d). Loellingite is the main arsenide and often replaces or encapsulates relics of uraninite, freibergite, sphalerite, galena, nickeline or (nickel-)skutterudite. Scarce native As occasionally overgrows loellingite. The main gangue minerals are dolomite, ankerite and calcite. This subtype is often associated with the paragenetically younger arsenic-sulfosalt-sulphide subtype.

This arsenic-sulfosalt-sulphide subtype overgrows or replaces paragenetically older native metal-arsenide subtypes described above. Arsenides are usually not replaced but overgrown, whereas native metals tend to be replaced by minerals related to the arsenic-sulfosalt-sulphide subtype. This mineral association encompasses secondary native silver, acanthite, proustite, cobaltite, gersdorffite, bismuthinite, arsenopyrite, argentopyrite, chalcopyrite, pyrite, galena, realgar, Bi-tennantite, allargentum, dyscrasite, Fe-oxides, REE minerals, dolomite-ankerite, calcite and quartz.

4.2 Vertical mineral zoning

All investigated native metal-arsenide subtypes, except for the silver-rammelsbergite-skutterudite and loellingite subtypes, occur across the entire vertical profile from ~200 to –1,155 m a.s.l. (meter above sea level) exposed by uranium exploitation. The silver-rammelsbergite-skutterudite subtype, however, appears absent from deeper portions of the Schlema-Alberoda deposit (-350 to -1,155 m a.s.l.), whereas the loellingite subtype mainly occurs in the deepest parts (between -650 and -1,155 m a.s.l.). Rammelsbergite, safflorite and nickeline are rarely recognized below ~ -500 m a.s.l. and loellingite abundance increases towards depth.

4.3 Mineralizing fluid

Primary and pseudosecondary fluid inclusion assemblages (*n*=23, *n*FIs=122) hosted in dolomite and ankerite coeval with safflorite and loellingite in bismuth-skutterudite-safflorite, silver-rammelsbergite-skutterudite, and loellingite subtypes have homogenization temperature (Th) between 115° and 150°C. There is no systematic variation in Th of various native metal-arsenide subtypes. Hydrohalite nucleation was observed in 6 fluid inclusion assemblages with average salinities of ~26.4 wt. % ($NaCl+CaCl_2$) eq. and Na/(Na+Ca) ratios between 0.61 and 0.78. Fluid inclusion gas compositions span a large range with respect to their CO_2/CH_4 and N_2/Ar ratios (Fig. 3).

5 Discussion and conclusions

At Schlema-Alberoda, the native metal arsenide tenor locally varies, including Ag-, Bi-, or As-dominated veins. Nickel-richer arsenides tend to be associated with native Ag, whereas Co-richer arsenides tend to be associated with native Bi. Similar observations were reported from other native metal-arsenide localities in Central Europe (e.g., Mackenheim and Urberg; Burisch et al. 2017; Scharrer et al. 2022).

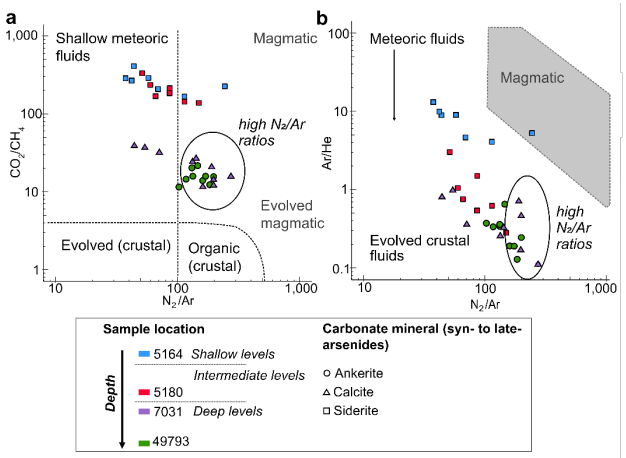

Figure 3. Crush-fast scan data for fluid inclusions. All data are in mol. %. **a** CO_2/CH_4 versus N_2/Ar. **b** Ar/He versus N_2/Ar. Field boundaries are from Blamey and Norman (2002) and Blamey (2012). Samples are classified according to the levels of the deposit they originate.

The spatial relationship between the native metal-arsenide veins and carbon-rich metasediments is striking. It supports the notion of recent studies (Markl et al. 2016; Burisch et al. 2017) that ore formation is likely related to reduction caused by interaction of the metal-bearing fluids with carbonaceous host rocks.

Microthermometric data of native metal-arsenide veins show that the ore fluids are of low temperature and high salinity. A wide range of Na/(Na+Ca) ratios (0.61-0.78) supports fluid mixing of two saline fluids, again consistent with evidence from other native metal-arsenide occurrences (Burisch et al. 2017; Scharrer et al. 2022). Although, not as obvious as for other localities, fluid mixing is furthermore supported by the large scatter in CO_2/CH_4 and N_2/Ar ratios of the fluid inclusions. The presented data is thus in agreement with previous studies, which proposed that the formation of native metal-arsenide veins in

Europe, is related to mixing between a metal-rich basement brine and a sedimentary-derived fluid under anomalously low fO_2 conditions (Markl et al. 2016; Burisch et al. 2017; Guilcher et al. 2021b).

Laser-ICP-MS U-Pb carbonates ages (113.1±1.8 Ma; Guilcher et al. 2021a) of the native metal-arsenide stage at Schlema-Alberoda constrain the timing of arsenide mineralisation to Mesozoic continental rifting in conjunction with the disintegration of the supercontinent Pangea (Guilcher et al 2021a; Burisch et al. 2022). Progressive mantle exhumation and crustal thinning in continental rift zones (Staude et al. 2009; Burisch et al. 2022) are assumed to be the driving mechanism for episodic injection of deep-seated basement brines into shallower aquifers across Europe (Bons et al. 2014; Burisch et al. 2016, 2022). Hence, we also assume this process is to have caused local formation of native metal-arsenide ore shoots, where metal-bearing basement fluids encountered carbon-rich lithologies at the Schlema-Alberoda deposit.

Acknowledgements

We thank our colleagues from the Helmholtz Institute Freiberg for Resource Technology (HIF) and the Technische Universität Bergakademie Freiberg (TU BAF) for their support with sampling, sample preparation and SEM work. This project was partly funded by the European Social Fund and the Federal State of Saxony (Project no. 100339454 received by M. Burisch).

References

Blamey N, Norman D (eds) (2002) New interpretations of geothermal fluid inclusion volatiles: Ar/He and N2/Ar ratios-a better indicator of magmatic volatiles, and equilibrium gas geothermometry, 27th edn.

Blamey NJF (2012) Composition and evolution of crustal, geothermal and hydrothermal fluids interpreted using quantitative fluid inclusion gas analysis. Journal of Geochemical Exploration 116-117:17–27. https://doi.org/10.1016/j.gexplo.2012.03.001

Bons PD, Fusswinkel T, Gomez-Rivas E, Markl G, Wagner T, Walter B (2014) Fluid mixing from below in unconformity-related hydrothermal ore deposits. Geology 42:1035–1038. https://doi.org/10.1130/G35708.1

Burisch M, Walter BF, Wälle M, Markl G (2016) Tracing fluid migration pathways in the root zone below unconformity-related hydrothermal veins: insights from trace element systematics of individual fluid inclusions. Chemical Geology 429:44–50. https://doi.org/10.1016/j.chemgeo.2016.03.004

Burisch M, Gerdes A, Walter BF, Neumann U, Fettel M, Markl G (2017) Methane and the origin of five-element veins: mineralogy, age, fluid inclusion chemistry and ore forming processes in the Odenwald, SW Germany. Ore Geology Reviews 81:42–61. https://doi.org/10.1016/j.oregeorev.2016.10.033

Burisch M, Markl G, Gutzmer J (2022) Breakup with benefits - hydrothermal mineral systems related to the disintegration of a supercontinent. Earth and Planetary Science Letters 580:117373. https://doi.org/10.1016/j.epsl.2022.117373

Förster B, Haack U (1995) U/Pb-Datierungen von Pechblenden und die hydrothermale Entwicklung der U-Lagerstätte Aue-Niederschlema (Erzgebirge). Zeitschrift für Geologische Wissenschaften 23:581–588

Förster H-J, Romer RL (2010) Carboniferous magmatism. In: Linnemann U, Romer RL (eds) Pre-Mesozoic geology of Saxo-Thuringia: from the Cadomian active margin to the Variscan Orogen. Schweizerbart, Stuttgart, pp 287–308

Golubev VN, Cuney M, Poty B (2000) Phase composition and U-Pb pitchblende systems of quartz-calcite-pitchblende veins at the Schlema-Alberoda deposit (Erzgebirge). Geology of Ore Deposits 42:513–525

Guilcher M, Albert R, Gerdes A, Gutzmer J, Burisch M (2021a) Timing of native metal-arsenide (Ag-Bi-Co-Ni-As±U) veins in continental rift zones – in situ U-Pb geochronology of carbonates from the Erzgebirge/Krušné Hory province. Chemical Geology 584:120476. https://doi.org/10.1016/j.chemgeo.2021.120476

Guilcher M, Schmaucks A, Krause J, Markl G, Gutzmer J, Burisch M (2021b) Vertical zoning in hydrothermal U-Ag-Bi-Co-Ni-As systems: a case study from the Annaberg-Buchholz district, Erzgebirge (Germany). Economic Geology 116:1893–1915. https://doi.org/10.5382/econgeo.4867

Hiller A, Schuppan W (2008) Geologie und Uranbergbau im Revier Schlema-Alberoda. Bergbau in Sachsen Bergbaumonographie, vol 14. Sächsisches Landesamt für Umwelt und Geologie (LfUG), Germany

Hoth K, Tischendorf G, Berger HJ, et al. (1980) Geologische Karte Erzgebirge/Vogtland. Sächsisches Landesamt für Umwelt, Landwirtschaft und Geologie, Dresden

Lipp U, Flach S (2003) Wismut-, Kobalt-, Nickel- und Silbererze im Nordteil des Schneeberger Lagerstättenbezirkes. Bergbau in Sachsen Bergbaumonographie, vol 10. Sächsisches Landesamt für Umwelt und Geologie, Dresden

Markl G, Burisch M, Neumann U (2016) Natural fracking and the genesis of five-element veins. Mineralium Deposita 51:703–712. https://doi.org/10.1007/s00126-016-0662-z

Scharrer M, Epp T, Walter B, Pfaff K, Vennemann T, Markl G (2022) The formation of (Ni-Co-Sb)-Ag-As ore shoots in hydrothermal galena-sphalerite-fluorite veins. Mineralium Deposita 57:853–885. https://doi.org/10.1007/s00126-021-01059-y

Staude S, Bons PD, Markl G (2009) Hydrothermal vein formation by extension-driven dewatering of the middle crust: an example from SW Germany. Earth and Planetary Science Letters 286:387–395. https://doi.org/10.1016/j.epsl.2009.07.012

Steele-MacInnis M, Bodnar RJ, Naden J (2011) Numerical model to determine the composition of H2O–NaCl–CaCl2 fluid inclusions based on microthermometric and microanalytical data. Geochimica et Cosmochimica Acta 75:21–40. https://doi.org/10.1016/j.gca.2010.10.002

Tichomirowa M, Leonhardt D (2010) New age determinations (Pb/Pb zircon evaporation, Rb/Sr) on the granites from Aue-Schwarzenberg and Eibenstock, Western Erzgebirge, Germany. Zeitschrift für Geologische Wissenschaften 38:99–123

Tichomirowa M, Käßner A, Repstock A, Weber S, Gerdes A, Whitehouse M (2022) New CA-ID-TIMS U–Pb zircon ages for the Altenberg–Teplice Volcanic Complex (ATVC) document discrete and coeval pulses of Variscan magmatic activity in the Eastern Erzgebirge (Eastern Variscan Belt). International Journal of Earth Sciences (Geologische Rundschau) 111:1885–1908. https://doi.org/10.1007/s00531-022-02204-2

Wolff R, Dunkl I, Lange J-M, Tonk C, Voigt T, Eynatten H von (2015) Superposition of burial and hydrothermal events: post-Variscan thermal evolution of the Erzgebirge, Germany. Terra Nova 27:292–299. https://doi.org/10.1111/ter.12159

Ziegler PA, Dèzes P (2006) Crustal evolution of western and central Europe. In: Gee DG, Stephenson RA (eds) European Lithosphere Dynamics, vol 32. Geological society, London, pp 43–56

The MINES thermodynamic database for simulating the hydrothermal mobilization of REE in critical mineral deposits

Alexander P. Gysi[1,2]
[1]*New Mexico Bureau of Geology & Mineral Resources, New Mexico Institute of Mining and Technology, Socorro, NM 87801, USA*
[2]*Department of Earth and Environment Science, New Mexico Institute of Mining and Technology, Socorro, NM 87801, USA*

Abstract. The rare earth elements (REE) are essential for the high-tech and green technology industries, and used, for example, in computers, smartphones, and wind turbines. The REE are considered critical minerals and can be highly enriched in certain magmatic-hydrothermal systems including alkaline complexes and carbonatites. Almost all of the critical mineral deposits show a complex overprint by hydrothermal processes during their genesis. However, our understanding of the mobility in these ore-forming systems and our knowledge about the stability of REE minerals is still very limited. The MINES thermodynamic database is an open-access database and continuously updated with the most up to date thermodynamic data for REE aqueous species and minerals. This database also includes rock-forming minerals and permits simulating the mineralogy and alteration geochemistry that relates to the formation of these critical mineral deposits. This study gives a short overview of the MINES thermodynamic database and the GEMS code package for simulating the formation of hydrothermal calcite, fluorite and bastnäsite-(Ce) veins relevant to interpreting critical mineral deposits.

1 Introduction

Critical mineral deposits evolve through a complex sequence of magmatic-hydrothermal processes, and most of them, are overprinted by late auto-metasomatic processes (e.g. Gysi et al. 2016; Elliott et al. 2018). The mobilization, fractionation and/or enrichment of critical elements, such as the rare earth elements (REE), can be predicted using thermodynamic modeling (Migdisov et al. 2016; Perry and Gysi 2018). These geochemical models yield insights about the controls and distribution of REE in these deposits and can potentially be used together with field geochemical data to predict alteration vectors for mineral exploration. However, our current ability to predict the behavior of REE in high temperature aqueous fluids and interpret these natural systems depends on the availability of thermodynamic data for the REE minerals and aqueous species.

The hydrothermal solubility of the REE phosphates, monazite and xenotime, has only recently been determined experimentally (Gysi et al. 2015, 2018; Van Hoozen et al. 2020; Gysi and Harlov 2021). The same applies to the thermodynamic properties of bastnäsite-(Ce) (e.g. Gysi and Williams-Jones 2015; Shivaramaiah et al. 2016; Goncharov et al. 2022). Furthermore, new models are developed based on experimental work, which aid in simulating the mechanisms of REE incorporation into gangue vein minerals such as apatite, calcite, and fluorite (Perry and Gysi 2020; Payne et al. 2023).

Thermodynamic data are available to predict the mobility of REE in acidic aqueous fluids to ~350-400ºC, whereas more experimental work is needed to simulate the mobility of REE in alkaline and supercritical fluids >350-400ºC. The properties of many aqueous REE species have been determined experimentally, including fluoride, sulfate, and chlorite complexes that control REE transport in acidic fluids (Migdisov et al. 2016). Previous modeling studies further indicate the potential importance of REE hydroxyl and carbonate complexes in alkaline fluids (Perry and Gysi 2018). The thermodynamic properties of these aqueous species are, however, still poorly known at elevated temperature, and the properties of a few of the REE carbonate complexes were determined only recently in hydrothermal solutions (Louvel et al. 2022; Nisbet et al. 2022).

Here, I present the MINES thermodynamic database and a modeling study using the GEMS code package (Kulik et al. 2013) to show an application of geochemical modeling in economic geology. This study gives an example of the replacement of a calcite vein by hydrothermal fluorite and bastnäsite-(Ce), and related compositional changes in fluorite to highlight advances and capabilities for modeling critical mineral deposits.

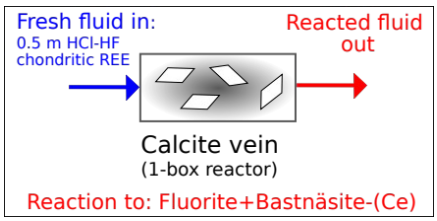

Figure 1. Conceptual model of a multipass leaching model (or 1-box flow-through reactor model), showing the input/output of fresh/reacted aliquots of acidic REE-F-bearing fluids passing through a calcite vein.

2 Methods

The MINES thermodynamic database (https://geoinfo.nmt.edu/mines-tdb) is an open-access database updated on a rolling release model (i.e., as new data become available, andhave been implemented and tested). The current database comprises >700 aqueous species and minerals relevant to modeling hydrothermal ore-

forming processes and fluid-rock interaction. The database includes aqueous REE species (Migdisov et al. 2009, 2016), REE phosphate minerals, and REE fluorocarbonates (Gysi and Williams-Jones 2015; Gysi et al. 2015, 2018; Van Hoozen et al. 2020; Gysi and Harlov 2021). The database also includes rock-forming minerals (Robie and Hemingway 1995; Holland and Powell 1998), zeolites, and clay minerals (Gysi and Stefánsson 2011).

The program GEM-Selektor (https://gems.web.psi.ch) was used with the MINES thermodynamic database to simulate the replacement reaction of calcite vein by secondary fluorite and REE fluorocarbonates (Fig. 1); a typical reaction texture observed in many critical mineral deposits. The simulations were carried out in the Ca-REE-F-Cl-C-H-O system at 400ºC and 500 bar with an acidic REE-F-Cl-bearing starting fluid (0.5 m HCl/HF) interacted with a calcite vein. The REE concentrations used are the chondrite values listed in McDonough and Sun (1995).

The first model is a multipass leaching model (Figs. 1-3) where at each step a fresh aliquot of acidic REE-F-Cl-bearing fluid interacts with the calcite vein while the alteration mineralogy, fluid chemistry, and the compositions of both calcite and fluorite can be monitored. The second model is a 1-D reactive transport model (Fig. 4), which permits simulating fluid-flow using the GEM2MT module implemented in the GEMS code package. In this model, 50 sequential rock nodes containing calcite were interacted simultaneously with the acidic fluid, which is flushed as sequential "waves" through each of the rock nodes. The resulting mineral distribution is then recorded after 200 and 2000 steps or waves.

3 Modeling examples

3.1 Multipass leaching model

Figure 2 shows the progressive replacement of the calcite vein by fluorite and bastnäsite-(Ce) upon increased fluid-rock interaction (i.e., aliquots of fluid added). The pH is initially buffered by calcite to a value slightly below ~6.5. Interaction of the acidic REE-F-bearing fluid with calcite leads to the formation of bastnäsite-(Ce) and fluorite according to:

$CaCO_3$ (calcite) + $3F^-$ + REE^{3+} = CaF_2 (fluorite) + $REEFCO_3$ (bastnäsite) **(Eq. 1)**

Once all calcite is consumed (~140 aliquots of fluidin Fig. 2), bastnäsite-(Ce) becomes unstable and all the remaining REE (i.e., not flushed out through the reactor box) are retained in fluorite. Figure 3 shows the compositional evolution of the simulatedREE-bearing fluorite. These preliminary simulations indicate that fluid-rock reaction can lead to significant REE variations in fluorite including the light (L) and heavy (H) REE. Furthermore, the simulations show a REE enrichment in fluorite of up to ~100 times chondrite.

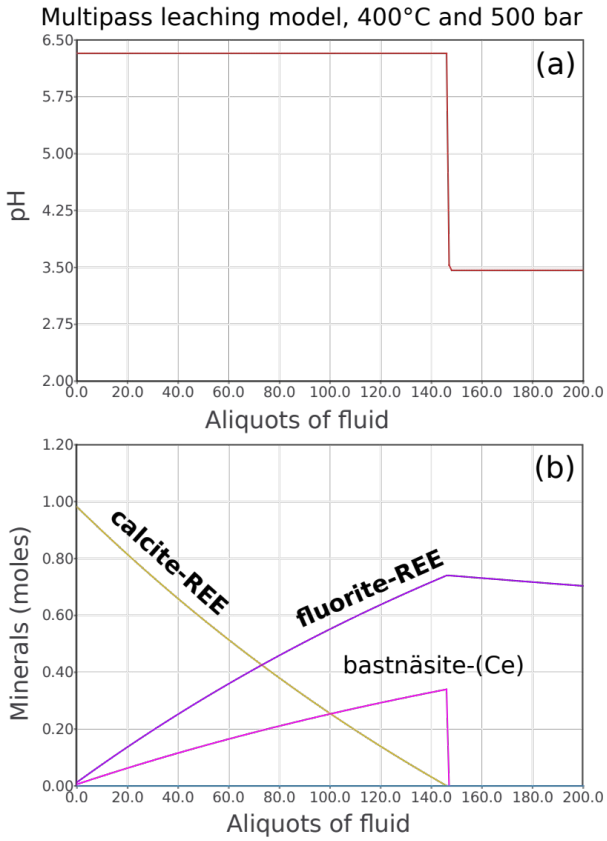

Figure 2. Multipass leaching model (or 1-box reactorflow-through) showing (a) the simulated pH and (b) the simulated mineralogy as a function of aliquots of fluids flushed through the calcite vein. Calcite-REE and fluorite-REE both indicate that the REE concentrations were simulated for these minerals.

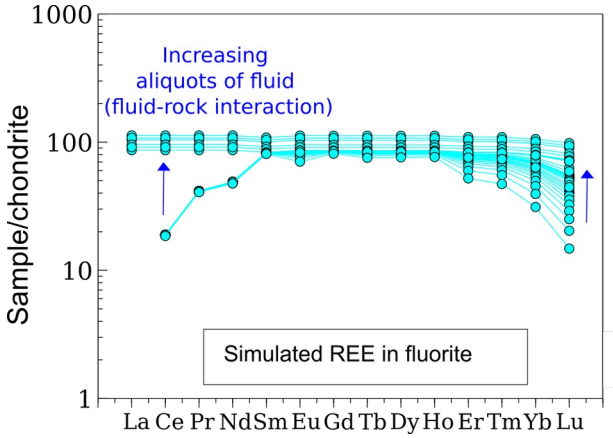

Figure 3. Simulated REE variations in fluorite normalized to chondrite. The stability of fluorite is shown in Figure 2 and variations correspond to various degrees of fluid- rock interaction or aliquots of fluid flushed through the rock.

3.21-D reactive transport model

Figure 4a shows the evolution of a calcite vein after 200 steps, with the development of a large zone of REE mineralization (i.e., fluorocarbonate veins) and a smaller zone of fluorite plus bastnäsite-(Ce). Upon increased fluid-rock interaction (Fig. 4B; after 2000 simulations steps), a large zone of fluorite develops at the input side of the acidic REE-F-

bearing fluid, and a large zone of calcite plus bastnäsite-(Ce) forms on the output side of the reactive fluid flow path. A smaller zone comprising fluorite plus bastnäsite-(Ce) forms at the interface between the calcite and fluorite rich zones.

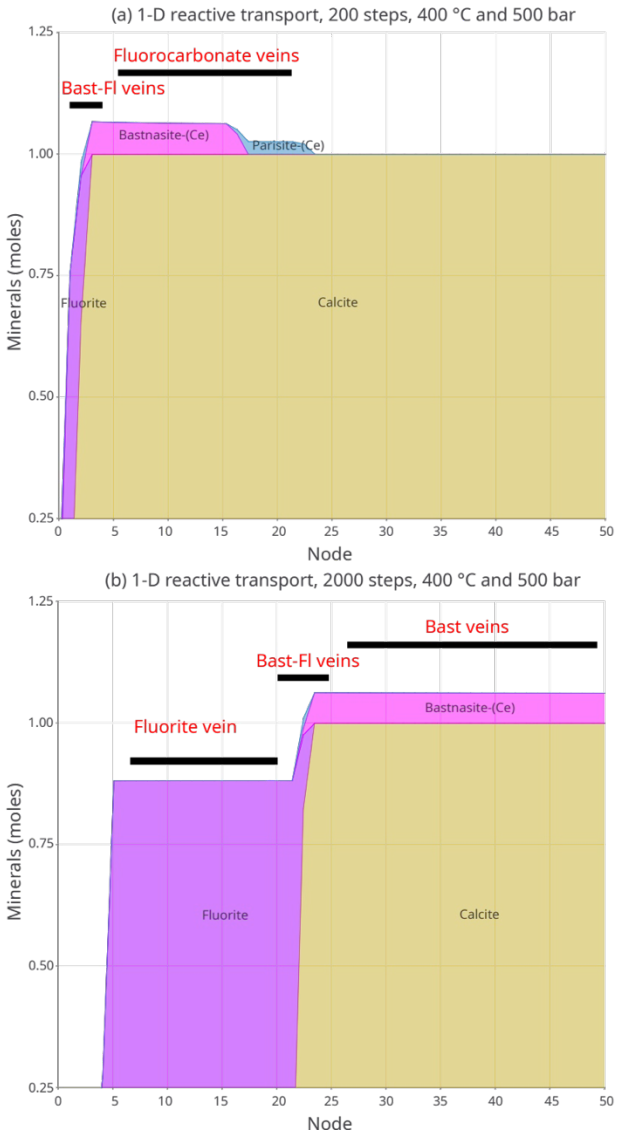

Figure 4. 1-D reactive transport simulations showing the mineralogy in 50 nodes or boxes of rock after (a) 200 steps and (b) 2000 steps, representing the number of fluid "waves" flushed through all the calcite boxes.

4 Conclusions

Numerical modeling provides a powerful tool to interpret the mineralogy, geochemistry, and alteration zones developed in natural critical mineral deposits. The MINES thermodynamic database was used here to show an example application to fluid-rock interaction processes that control REE mobilization. This can be extended to different mineral systems (Gysi and Williams-Jones 2013; Perry and Gysi 2018; Payne et al. 2023). Many of the REE mineral deposits associated with carbonatites and alkaline deposits contain hydrothermal barite, calcite, fluorite, and/or bastnäsite-(Ce) bearing veins. Hence the simulations presented in Figures 2-4 provide a first step in quantifying the processes that affect the stability of these minerals and concurrent change in fluorite REE chemistry. Prominent examples where this type of reactions could be of importance include the hydrothermal fluorite-REE-bearing breccia/vein deposit in Gallinas Mountains in New Mexico (McLemore et al. 2021), Bear Lodge in Wyoming (Andersen et al. 2019), the giant Bayan Obo carbonatite deposit in China (Gao et al. 2021), and the Mianning-Dechang REE belt in China (Guo and Liu 2019).

Acknowledgments

I like to thank my colleagues who contributed to the project including Nicole Hurtig and Ruiguang Pan (New Mexico Tech), Dan G. Miron and Dmitrii Kulik (Paul Scherrer Institute). The work on the MINES thermodynamic database and REE experimental data acquired were supported through the following National Science Foundation (NSF) and U.S. Department of Energy (DOE) grants: NSFCAREER EAR-2039674 and EAR-2032761; DOE DE-SC0021106 and DE-SC0022269.

References

Andersen AK, Larson PB, Cosca MA (2019) C–O stable isotope geochemistry and $^{40}Ar/^{39}Ar$ geochronology of the Bear Lodge carbonatite stockwork, Wyoming, USA. Lithos 324:640-660.

Chappell JC, Gysi AP, Monecke T, Chang Z (in press) Experimental apatite-fluid interaction and partitioning of rare earth elements at 150 and 250°C. Am Mineral. https://doi.org/10.2138/am-2022-8589

Elliott HAL, Wall F, Chakhmouradian AR, Siegfried PR, Dahlgren S, Weatherley S, Finch AA, Marks MAW, Dowman E, Deady E (2018) Fenites associated with carbonatite complexes: A review. Ore Geol Rev 93:38-59.

Gao Z, Liu Y, Jing Y, Hou Z, Liu H, Zheng X, Shen N (2021) Mineralogical characteristics and Sr–Nd–Pb isotopic compositions of banded REE ores in the Bayan Obo deposit, Inner Mongolia, China: Implications for their formation and origin. Ore Geol Rev 139:104492.

Goncharov VG, Nisbet H, Strzelecki A, Benmore CJ, Migdisov AA, Xu H, Guo X (2022) Energetics of hydroxyl bastnäsite solid solutions, $La_{1-x}Nd_xCO_3OH$. Geochim Cosmochim Acta 330:47-66.

Guo D, Liu Y (2019) Occurrence and geochemistry of bastnäsite in carbonatite-related REE deposits, Mianning–Dechang REE belt, Sichuan Province, SW China. Ore Geol Rev 107:266-282.

Gysi AP, Harlov D (2021) Hydrothermal solubility of $TbPO_4$, $HoPO_4$, $TmPO_4$, and $LuPO_4$ xenotime endmembers at pH of 2 and temperatures between 100 and 250°C. Chem Geol 567:120072.

Gysi AP, Stefánsson A (2011) CO_2–water–basalt interaction. Numerical simulation of low temperature CO_2 sequestration into basalts. Geochim Cosmochim Acta, 75:4728-4751.

Gysi AP, Williams-Jones AE (2013) Hydrothermal mobilization of pegmatite-hosted REE and Zr at Strange Lake, Canada: A reaction path model. Geochim Cosmochim Acta 122:324-352.

Gysi AP, Williams-Jones AE (2015) The thermodynamic properties of bastnäsite-(Ce) and parisite-(Ce). Chem Geol 392:87-101.
Gysi AP, Williams-Jones AE, Collins P (2016) Lithogeochemical vectors for hydrothermal processes in the Strange Lake peralkaline granitic REE-Zr-Nb deposit. Econ Geol 111:1241-1276.
Gysi AP, Harlov D, Miron GD (2018) The solubility of monazite ($CePO_4$), $SmPO_4$, and $GdPO_4$ in aqueous solutions from 100 to 250°C. Geochim Cosmochim Acta 242:143-164.
Holland TJB, Powell R (1998) An internally consistent thermodynamic data set for phases of petrological interest. J Metamorph Geol 16:309-343.
Kulik DA, Wagner T, Dmytrieva SV, Kosakowski G, Hingerl F F, Chudnenko KV, Berner UR (2013) GEM-Selektor geochemical modeling package: revised algorithm and GEMS3K numerical kernel for coupled simulation codes. Comput Geosci 17:1-24.
Louvel M, Etschmann B, Guan Q, Testemale D, Brugger J (2022) Carbonate complexation enhances hydrothermal transport of rare earth elements in alkaline fluids. Nature Commun 13:1456.
McDonough WF, Sun SS (1995) The composition of the Earth. Chem Geol 120:223-253.
McLemore VT, Kelley S, Zimmerer MJ, Owen E, Haft EB, Cantrell T, Gysi AP, Dietz H, Cherotich S, Trivitt A (2021) Geology and mineral deposits of the Gallinas Mountains, Lincoln and Torrance counties, New Mexico. New Mexico Bureau of Geology and Mineral Resources, Open-File Report 617.
Migdisov AA, Williams-Jones AE, Wagner T (2009) An experimental study of the solubility and speciation of the Rare Earth Elements (III) in fluoride-and chloride-bearing aqueous solutions at temperatures up to 300°C. Geochim Cosmochim Acta 73:7087-7109.
Migdisov A., Williams-Jones AE, Brugger J, Caporuscio FA (2016) Hydrothermal transport, deposition, and fractionation of the REE: Experimental data and thermodynamic calculations. Chem Geol 439:13-42.
Nisbet H, Migdisov AA, Goncharov V, van Hinsberg V, Williams-Jones AE, Xu H, Guo X (2022) The solubility and speciation of Nd in carbonate-bearing hydrothermal fluids up to 250°C. Chem Geol 611:121122.
Payne MR, Gysi AP, Hurtig NC (2023) Hydrothermal fluorite solubility experiments and mobility of REE in acidic to alkaline solutions from 100 to 250°C. Chem Geol 617:121256.
Perry EP, Gysi AP (2018) Rare earth elements in mineral deposits: speciation in hydrothermal fluids and partitioning in calcite. Geofluids 2018:1-19.
Perry EP, Gysi, AP (2020) Hydrothermal calcite-fluid REE partitioning experiments at 200°C and saturated water vapor pressure. Geochim Cosmochim Acta 286:177-197.
Robie RA, Hemingway BS (1995) Thermodynamic properties of minerals and related substances at 298.15 K and 1 bar (10^5 Pascals) pressure and at higher temperatures. U.S. Geological Survey Bulletin Vol. 2131.
Shivaramaiah R, Anderko A, Riman RE, Navrotsky A (2016) Thermodynamics of bastnaesite: A major rare earth ore mineral. Am Mineral 101:1129-1134.
Van Hoozen CJ, Gysi AP, Harlov DE (2020) The solubility of monazite ($LaPO_4$, $PrPO_4$, $NdPO_4$, and $EuPO_4$) endmembers in aqueous solutions from 100 to 250°C. Geochim Cosmochim Acta 280: 302-316.

A green future from a contentious past: Gold and critical metals in a historic arsenic mining district Strassegg (Styria)

Hiller, J.M.[1], Bertrandsson Erlandsson, V.[1], Mottram, C.[2], Gopon, P.[1]
[1] *Chair of Geology and Economic Geology, Montanuniversität Leoben, Peter-Tunner Straße, 8770, Leoben, Austria*
[2] *School of the Environment, Geography and Geosciences, University of Portsmouth, Burnaby Building, Portsmouth, PO 1 3QL, United Kingdom*

Abstract. Metals such as Bi, Co, Sb, Te, and W are needed in large amounts for renewable technologies central to reaching net-zero carbon and have therefore been termed as critical metals by the European Union. A stable supply chain for these raw materials into the EU is urgently needed, especially considering the current geo-political instabilities. In light of this, domestic production of raw materials is a priority, and we therefore investigate the historic Au-Ag-As mining district Strassegg in the north of Graz (Styria) for precious and critical metals. Our study combines whole rock geochemistry from tailings piles as well as scanning electron microscope (SEM) and laser ablation inductively coupled plasma mass spectrometry (LA-ICP-MS) analyses of sulfide minerals to show the amount precious and critical metals still present, as well as characterizing in what form these metals are found (i.e., inclusions or lattice bound). Additionally, in-situ calcite U-Pb dating was done for Strassegg and other Au-Cu deposits in the eastern Alps to constrain the age of ore mineralization in the region.

1 Introduction

The European Union and the USGS regularly update their lists of critical metals, i.e., those of importance to national security and industry whose sourcing has been deemed at risk. Most of the producers of these important commodities lie outside of the EU / North America, putting this nations at a supply risk. Therefore, the EU has decided to promote raw material production in their own territory.

The mining in EU already has a long history, with many documented historic deposits, which potentially still contain abundant resources. One such mining area is the historic mining district of Strassegg (Styria, Austria), which was mined for Au, Ag, and As (Figure 1) (Bojar 1989). The rudimentary mining and ore processing methods used at the time, however, means that there is a potential for a significant portion of the ore underground as well as significant quantities of raw materials in the tailings.

The fact that many of the elements that remain in the tailings piles are important for modern technologies, and pose a potential environmental risk, is a strong argument to re-process these materials. For example, As is an important dopant in Si based semi-conductors but is also poisonous when ingested. These As containing minerals are therefore hugely important, even more so because they are known for being hosts for several trace elements that are needed for the green energy transition (i.e., Sb, Te, Bi, W, etc.).

1.1 Ore mineralization and mining history

The mineralization at Strassegg, occurs in the Graz Paleozoic nappe system both in the form of vein-type as well as stratabound bodies hosted in greenschists (Figure 1). The mineralization generally strikes NNW and lies subparallel, cross-cutting the

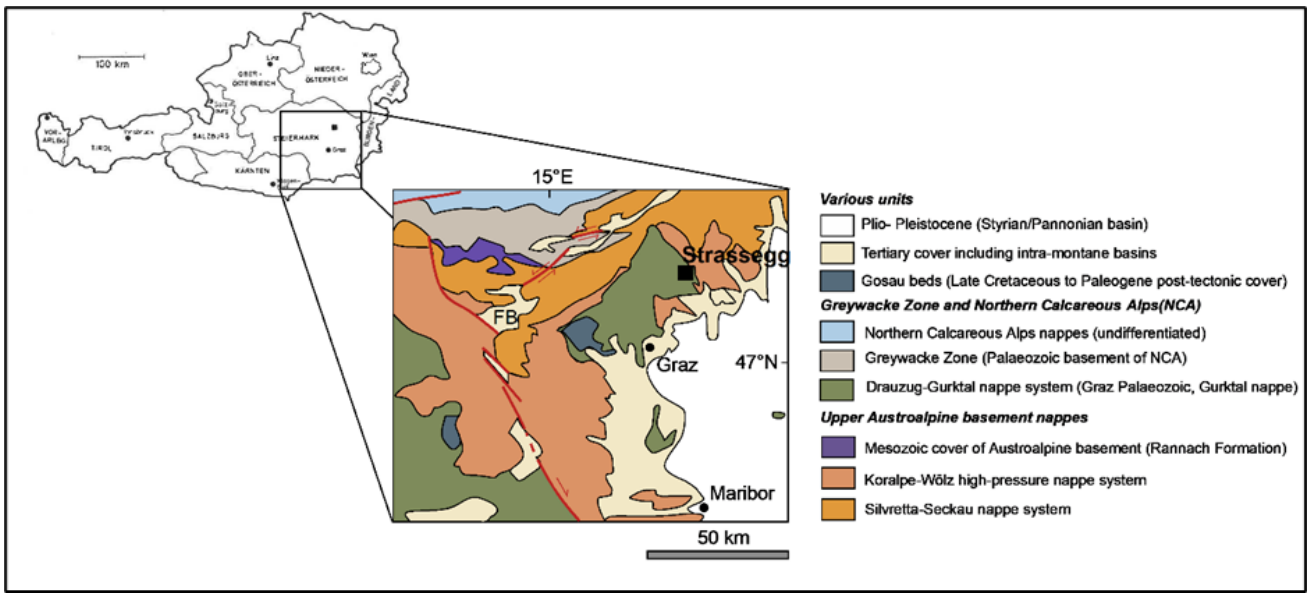

Figure 1. Geologic map of the Eastern-Alps with Strassegg noted (modified after MINEREX report 1987; Raith et al.2015)

low angle NW-SE foliation of the host rock (MINEREX report 1987; Bojar et al. 2002).

The mineralization formed through two main stages. The first mineralization stage is dominated by arsenopyrite-pyrite-gold, and the second by e.g. galena, Pb-sulfosalts, and minor Cd-, Ni-, and Te-phases.

The main mining activity stopped in the 18th century due to the high number of miner/ore processers deaths, combined with a poor economic situation. Most of the deaths were associated with long term arsenic exposure from the ore roasting. However, artisanal workings continued into the 20th century (Bojar 1989), and much of the old ore processing facilities and tailing piles still contain appreciable amounts of arsenic. In fact, the central ore processing waste dump (from which sample 21TB01 is taken from; Figure 2) is so contaminated that the local farmers have been barred from grazing their livestock in a 500m radius from the site.

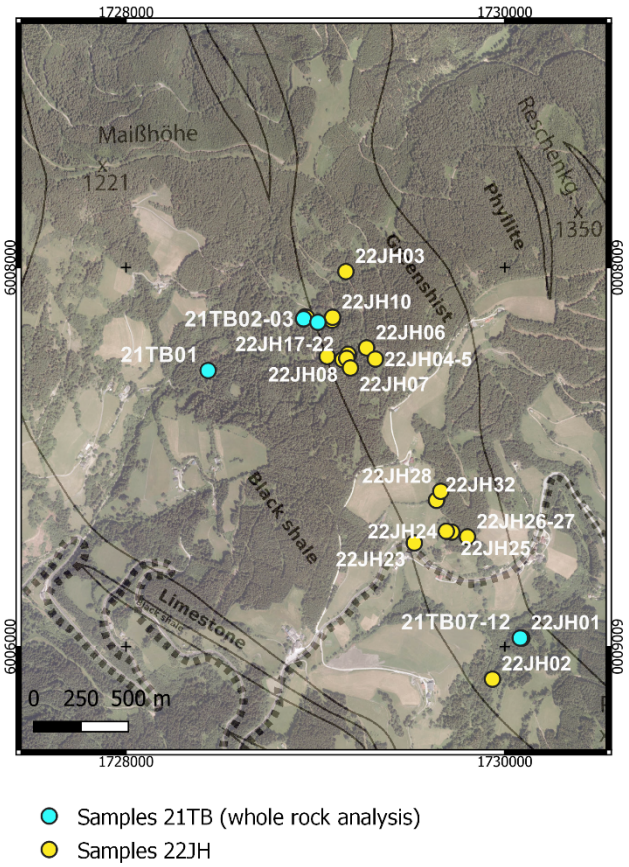

Figure 2. Sample map of Strassegg. On the sample map are the geologic unit boundaries, taken from Antes (1998). Whole rock analysis has been done on sample 21TB, whilst the petrogical work presented herein is from sample 22JH.

Much of the mining was conducted at or near the surface, and it is suspected that the main ore vein was mostly untouched at depth.

Additionally, at the time little was known of the ability of sulfide minerals to host significant quantities of Au. Most of these sulfides were disposed of in tailings which are still present in the area. The aim of our work is to examine the potential of these tailing piles for the primary elements (As, Au, and Ag) as well as critical metals that might be won as a byproduct (esp. Bi, Co, Sb, Te, and W).

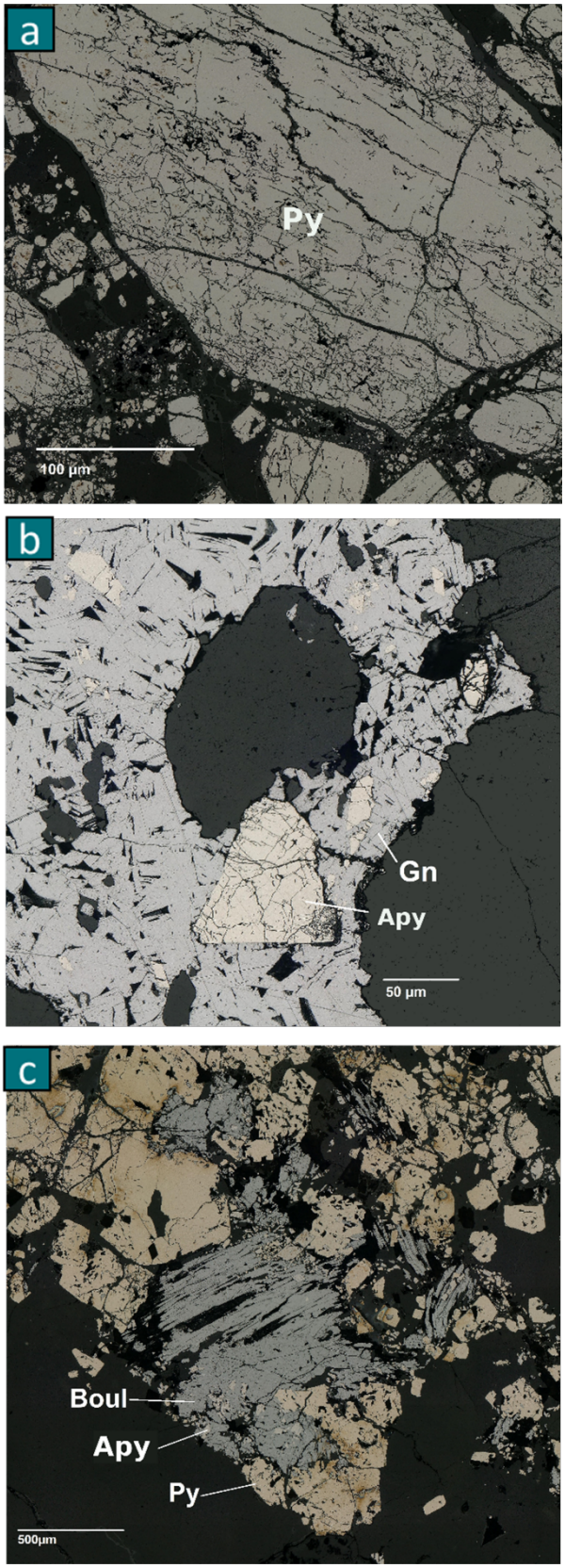

Figure 3. a) Cracked pyrite (Py) in a quartz; **b)** two stages of ore mineralisation – stage 2 galena (Gn) surrounding cracked stage 1 arsenopyrite (Apy); c) Boulangerite (Boul), arsenoypyrite (Apy) and pyrite (Py). Boulangerite filling cracked zones in the other ore minerals.

2 Analytical Methods

We collected 34 ore samples from tailing piles in the historic mining district of Strassegg, Styria, Austria (Figure 2). These 34 samples were supplemented with polished sections from the ore geology collection of the Montanuniversität Leoben (Austria). Samples were investigated using a combination of whole rock geochemistry, optical microscopy, SEM, and laser ablation inductively coupled mass spectrometry. A first impression of optical microscopy is given in Figure 3. Different ore phases are indicated.

Additional LA-ICP-MS U-Pb analyses (methods after Roberts et al. 2020) where conducted on calcite veins from Strassegg and three additional closely associated deposits (Pusterwald, Flatschach, and Kothgraben) to constrain the age of mineralization.

3 Futher work

Further work is planned to investigate exactly how these sulfide minerals are able to host concentrations of Au, Ag, and to see if critical metals are associated with Au/Ag at the atomic scale. Therefore, we plan to use atom probe tomography (APT) to investigate is the gold is hosted as nanoparticles (Fougerouse et al. 2016), lattice bound (Gopon et al. 2019), or in deformation-related dislocation sites (Fougerouse et al. 2021).

Acknowledgements

The work is financed by in part by the State of Styria (Green Transformations grant, ABT08-247901/2021), as well AUREX Biomining AG.

References

Antes G (1998) Geochemische und geophysikalische Anomalien im Bereich des Arsenkies-Goldvorkommens Strassegg, Steiermark (die „Straßegger Anomalie“). – Unveröff. Dissertation Geol. Inst. Univ. Wien, III + 92

Bojar H-P (1989) Zur Geschichte der Bergbaue am Straßegg. -In: CHRISTIAN, G. (Hrsg.): Die Breitenau. Marktgemeinde am Fusse des Hochlantsch.- Eigenverlag d. Marktgemeinde Breitenau am Hochlantsch:19-22.

Bojar H-P, Mogessie A, Bojar AV (2002) The genesis of the gold-arsenopyrite mineralisation Strassegg, Styria: evidence for local fluid flow during late Cretaceous extension. PANGEO Austria, 2002:23

Fougerouse D, Reddy SM, Saxey DW, Rickard WDA, Riessen A Van, Micklethwaite S (2016) Nanoscale gold clusters in arsenopyrite controlled by growth rate not concentration: Evidence from atom probe microscopy k: American Mineralogist, v. 101:1916–1919.

Fougerouse D, Reddy SM, Aylmore, M, Yang L, Guagliardo P, Saxey DW, Rickard WDA, Timms N, (2021) A new kind of invisible gold in pyrite hosted in deformation-related dislocations: v.XX:1–5

Gopon P, Douglas JO, Auger MA, Hansen L, Wade J, Cline JS, Robb LJ, Moody MP (2019) A Nanoscale Investigation of Carlin-Type Gold Deposits: An Atom-Scale Elemental and Isotopic Perspective: Economic Geology, v. 114: 1123–1133, doi:10.5382/econgeo.4676.

MINEREX (1987) Statusbericht Projekt: Gold - Strassegg. Berichtszeitraum VII - XII / 1986.- Unveröff. Ber. (Lagerst. Arch. Geol. B.-A.), 13 S.

Raith JG, Leitner T, Paar WH (2015) Orogenic-type copper-gold-arsenic-(bismuth) mineralization at Flatschach (Eastern Alps), Austria. Mineralogy and Petrology 109:531–553

Roberts NM, Drost K, Horstwood MS, Condon DJ, Chew D, Drake H, Milodowski AE, McLean NM, Smye AJ, Walker RJ, Haslam R (2020) Laser ablation inductively coupled plasma mass spectrometry (LA-ICP-MS) U–Pb carbonate geochronology: strategies, progress, and limitations. Geochronology, *2*(1):33-61

Critical Minerals Potential of Armenia: An Overview for Future Exploration

Samvel Hovakimyan[1], Robert Moritz[2], Marianna Harutunyan[3], Karen Hambaryan[3], Kima Charatanyan[3]
[1]*Institute of Geological Sciences of the National Academy of Sciences of the Republic of Armenia*
[2]*Department of Earth Sciences, University of Geneva, Switzerland*
[3]*Institute of Geological Sciences of the National Academy of Sciences of the Republic of Armenia*

Abstract. Armenia is well endowed with significant mineral resources, including copper, molybdenum and gold, that can be found in different metallogenic belts recording diverse geological and geodynamic environments, ranging from island-arc to collisional and post-collisional settings. Critical metals potential in Armenia is related to alkaline complexes, granitic pegmatite and tourmaline-bearing intrusions, but also various ore deposit types, such as porphyry Cu-Mo, Au and base metal epithermal, Cu-rich and polymetallic deposits, magnetite-apatite deposits, mine tailings andwaste rocks, as well as metamorphic basement rocks. They contain variable amounts of critical minerals, including REE, chromium, cobalt, nickel, PGE, rhenium, selenium, tellurium, titanium, tungsten, vanadium, and zirconium, which are considered as by-products, and are typically not recovered during mining. The potential of these metals remains largely unknown and requires future investigations.

1 Introduction

The Armenian mountain belts belong to the Caucasian segment of the Tethyan metallogenic belt, located between the Black Sea and the Caspian Sea (Fig.1, inset). The Lesser Caucasus contains two metallogenic belts, including the Late Jurassic - Early Cretaceous Somkheto-Karabagh island arc and the Kapan block, and the Cenozoic Gondwana-derived South Armenian block (Fig. 1).

Critical minerals occur in diverse geological environments and mineralized systems in Armenia, including alkaline complexes, epithermal Au and base metal, Cu-rich and polymetallic type deposits, porphyry Cu-Mo deposits, as well as granitic pegmatite and carbonatite (Fig. 1).

The existing mines (e.g. Kadjaran, Agarak, Teghout etc.) generate huge volumes of waste rock and tailings. They can be source of significant amounts of critical minerals, including REE, Cr, Ni, Co, Li, PGE, Re, Se, Te, Bi, Ti, W, V, Zr etc., whichare considered as by-products, and are typically not recovered (Avagyan 2004). Consequently,characterization and reprocessing of existing surface waste materials at active and inactive mines have the potential to transform waste into a resource by providing new sources of critical minerals. Recovery of these metals from mine wastes and tailings can be an environmentally friendly alternative to opening new mines.

This contribution provides an overview on critical minerals potential of Armenia based on literature review, with the aim to highlight the critical minerals distribution in different ore deposit types, and in various magmatic settings. Future investigations are required to evaluate the potential of critical metals for exploration to meet their growing demands for technological development in fields such as renewable energy and clean technologies.

2 REE in nepheline syenite complexes

Two major alkaline complexes are known in Armenia, which are the Cenozoic Tejsar and Meghri alkaline syenite complexes (Meliksetian 1971). They are situated at the northern and southern edges of the South Armenian Block, respectively (Fig. 1). They formed during the Cenozoic Arabia-Eurasia collision and post- collision evolution of the Lesser Caucasus (Grosjean et al. 2022).

2.1 The Tejsar alkaline syenite complex

The Tejsar alkaline complex consists of mid- Eocene to Pliocene magmatic rocks (Bagdasaryan et al. 1969), and includes a mid-Eocene nepheline syenite (Meliksetian 1971; Sokoł et al. 2018; Grosjean et al. 2022), which has been identified as a major source of lanthanides, Sc, and Y in Armenia. Nepheline syenite of this complex contains 457Mt grading at 21.49 % Al_2O_3 (Uzumova 1983). The magmatic rocks of the Tejsar complex are also characterized by high concentrations of Zr, Hf, Ga, Th, Ce and Nb. Other elements that have been reported (Maghakyan et al. 1972; Grosjean et al. 2022) include: 0.3 wt% Li; 0.0008 wt % Be; 0.008 wt % Rb; 0.03 wt % La; 0.01 wt % Sr; 0.03 wt % Ce; 0.001 wt % Sc; 0.003 wt % Cs; 0.003 wt % Ga, 0.003 wt % Tl, and 0.001 wt % Y.

The Tejsar alkaline syenite complex may also be interesting for Sc resources. Scandium is dominantly sourced by magmatic deposits (about 90% of the total), where it is primarily hosted in clinopyroxene ± amphibole in mafic–ultramafic intrusions (Wang et al. 2021). The recent discoveryof a Sc deposit in the Crater Lake syenite complex,

Canada (Beland and Williams-Jones 2023) documents that carbonatite-related metasomatic deposits provide an alternative resource for Sc in magmatic rocks. At the Tejsar alkaline complex, Sc concentrations range from 3.8 to 39.8 ppm (Grosjean et al. 2022).

2.2 The Meghri-Ordubad pluton

The highly mineralized Cenozoic Meghri-Ordubad pluton was formed by repeated intrusive activity from mid-Eocene subduction to Miocene post- collisional evolution of the southernmost Lesser Caucasus (Moritz et al. 2016b; Rezeau et al. 2016, 2019). It hosts major porphyry Cu-Mo and epithermal Au and base metal deposits, many of which are currently under production (Moritz et al. 2016a). Dextral strike-slip tectonics controlled mid- Eocene ore deposit and magma emplacement during the convergence between the Arabian and Eurasian plates. This tectonic system has been repeatedly reactivated during Neogene collision and post-collision ore formation and magmatism (Hovakimyan et al. 2019). The Meghri alkaline syenite complex within the Meghri-Ordubad pluton is characterized by high Zr,Hf, Be, Nb, and Th concentrations (Maghakyan et al. 1972; Rezeau et al. 2019). Concentrations of 0.025 wt% Zr, 0.0003 wt% Hf, and 0.01 wt% Nb have been reported (Maghakyan et al. 1972). The Li potential of granitic pegmatite and tourmaline-bearing intrusions of the Meghri-Ordubad pluton is still unknown and requires future investigations. An additional potential source of Li might be clay minerals, such as hectorite, which might be related to hydrothermally altered rhyolite.

3 Critical minerals in epithermal gold and base metal deposits

Gold deposits of Armenia are located in both the Mesozoic Somkheto-Karabagh belt and the Kapan block, and the Cenozoic South Armenian Block. They are highly prospective for Cu, Se, Te, Bi, Cd, Ga, In, Ge, Zr, Ti, REE, Co, Sb, W, Sc and other associated critical minerals, which are considered as by-product commodities with further unexplored potential (Maghakyan et al. 1972; Amiryan 1984; Avagyan 2004). Tellurium is present in most of the epithermal Au deposits (e.g., Meghradzor, Tey- Lichkvaz, Sotk, Terterasar etc.), generally together within common sulfides (pyrite, arsenopyrite) and as discrete Te minerals (Amiryan 1984).

The Armanis high-sulfidation and the Sotk low-sulfidation epithermal Au deposits are hosted by the Jurassic-Cretaceous Amasia-Sevan-Akera ophiolite suture zone (Fig. 1), and contain significant concentrations of Se, Te, Bi, and Cd (Maghakyan et al. 1972; Amiryan 1984).

The Azatek deposit (Fig. 1) is characterized by a Au-Pb-Sb type mineralization, with significant concentrations of Te, Bi, Ga, In, Ge, and Cd in polymetallic ores (Amiryan 1984).

The Shahumyan gold – polymetallic deposit in the Kapan block is hosted by Middle Jurassic subvolcanic rocks (Fig. 1). Gold-polymetallic veins are characterized by significant Te concentrations with Au–Ag-tellurides (Mederer et al. 2014). Indium (0.008%), gallium (0.01%), cadmium (1%), and germanium (0.003%) have also been reported in sphalerite (Maghakyan et al. 1972).

4 Critical minerals in porphyry Cu-Mo deposits

Porphyry Cu-Mo deposits in Armenia are characterized by high concentrations of Re, Se, Te, Ge, Bi, Ag and other critical metals as by-products. They include the Late Jurassic Teghout deposit (Fig. 1), where molybdenite-rich ore contains up to 0.073 wt% Re (Avagyan 2004).

Cenozoic porphyry Cu-Mo deposits in southernmost Armenia are the major sources of Cu and Mo, and critical minerals like Re, Se, and Te. They include the mid-Eocene subduction-related Agarak (0.038 wt% Re, 0.0275 wt% Se, 0.003 wt% Te), Aygedzor (0.13 wt% Re; 0.05 wt% Se; 0.0055 wt% Te, 0.0016 wt% Bi), and Dastakert (0.0212 wt% Re, 0.0055 wt% Se, 0.0035 wt% Te) deposits,and the Oligocene to early Miocene collisional to post-collisional giant Kadjaran deposit (0.04 wt% Re, 0.018 wt% Se, 0.0066 wt% Te) in the Meghri- Ordubad pluton (Fig. 1; Faramazyan et al. 1970; Avagyan 2004).

Another Cenozoic porphyry Cu-Mo deposit at Hanqavan is located in the northern part of the Gondwana-derived South Armenian Block (Fig. 1), where the molybdenite ores contain significant amounts of Re (0.015-0.034 wt%), Se (0.112 wt%), Te (0.072 wt%), and Bi (0.03-0.3 wt%) (Maghakyanet al. 1972).

5 Critical minerals in Cu-rich and polymetallic deposits

The major Cu pyrite and polymetallic deposits are located along the Jurassic- Cretaceous Somkheto –Karabagh belt of the Eurasian margin and its southern extension the Jurassic Kapan block. They include the Alaverdi Cu–Au, the Shamlugh Cu-rich pyrite, and the Akhtala Ba-rich polymetallic deposits in the Alaverdi mining district (Fig. 1; Moritz et al. 2016a; Calder et al. 2019), and the Kapan Cu mines in the Kapan block (Mederer et al. 2014). These deposits and their tailings are characterized by significant concentrations of Se, Te, as well as Bi and Ga. Selenium and Tellurium concentrations at the Alaverdi deposit are, respectively 52.1 ppm and 83.9 ppm, and 10.5 ppm Se and 25.4 ppm Te at the Shamlugh deposit. At the Kapan Cu deposit, 19.25 ppm Se, and 12.38 ppm Te have been reported (Maghakyan et al.1972).

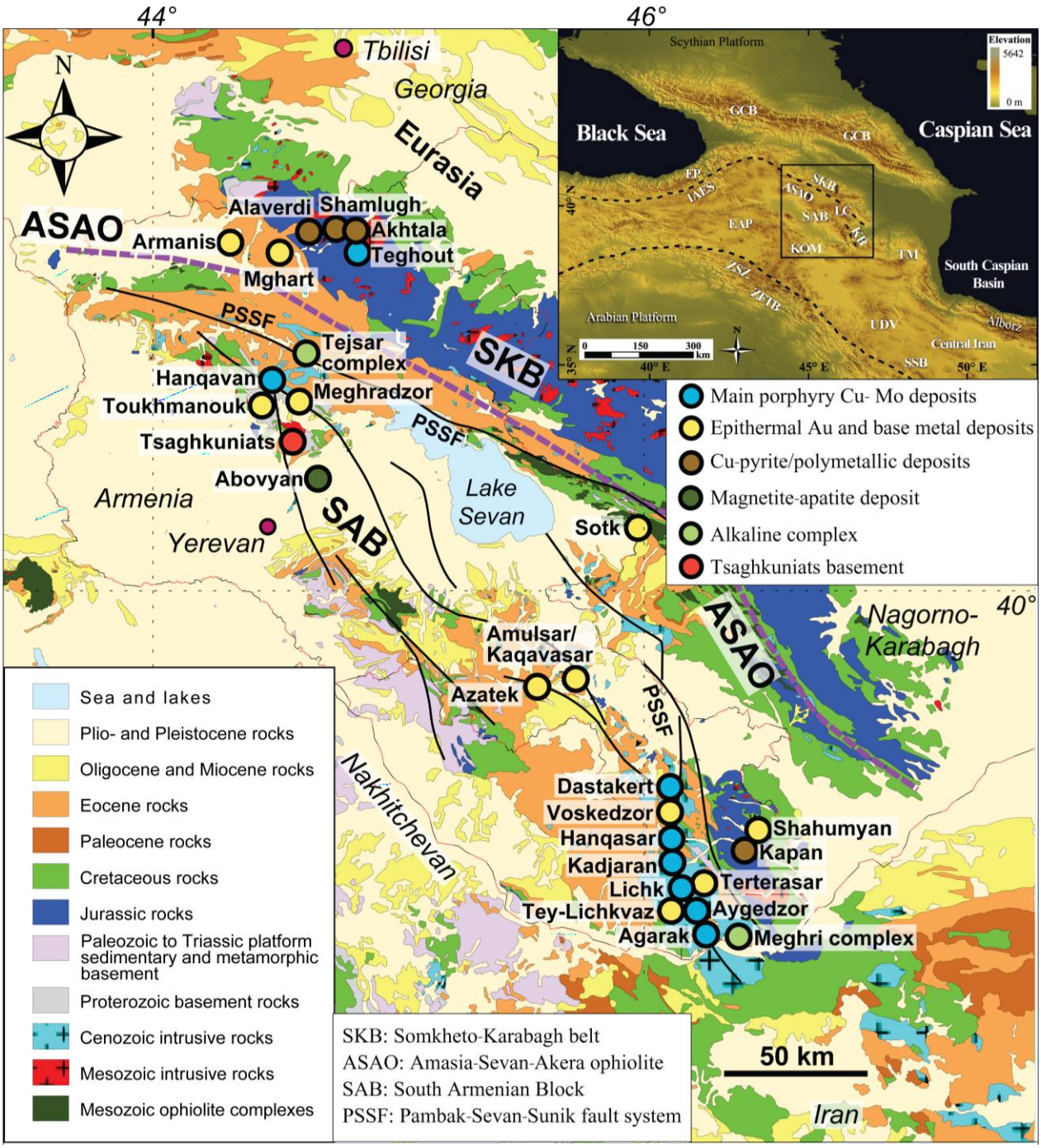

Figure 1. Geology of the Lesser Caucasus (modified after Mederer et al. 2014), with locations of the intrusive complexes and mineral deposits described in this abstract.

6 REEs in the Abovyan Kiruna-type magnetite-apatite deposit

The Abovyan magnetite-apatite deposit is a Kiruna-type iron oxide - apatite deposit (Fig. 1; Frietsch and Perdahl 1995). It is hosted by post-Middle Miocene andesite porphyritic rock, tuff and tuffite (Sarukhanyan and Mkrtchyan 1968). Apatite and magnetite in various ore types at Abovyan make upto 85-90% of the total volume. The ore consists of massive and breccia type ores with a subvolcanic character connected to fault zones (Sarukhanyan and Mkrtchyan 1968; Frietsch and Perdahl 1995).

The interest for this deposit has increased recently,because apatite can have significant REEs concentrations (Chakhmouradian and Wall 2012). Apatite from the Abovyan deposit belongs to an alkaline trend, and has a high concentration of REEs (Frietsch and Perdahl 1995). The apatite ores contain 0.64-1.10 wt% La, 1.36-2.30 wt% Ce, 0.22-0.44 wt% Nd, and 0.10-0.14 wt% Y (Sarukhanyan and Mkrtchyan 1968), which can be considered as a potential source of REEs. Further investigations are required to understand the originof this deposit.

7 Critical minerals potential of the Neoproterozoic basement

The Tsaghkuniats massif consists of Neoproterozoic metamorphic basement rocks (Fig. 1). These rocks are potential targets for criticalminerals, because of the presence of granitic rockswith high silica content (Critical Minerals Mapping Initiative). Fertility of these rocks for critical minerals have been recognized in several districts of the Tsaghkuniats massif, such as the Arzakan titanium prospect, where the mineralization is related to schist, and silicified zones of the Arzakanmetamorphic complex. This prospect contains 2.35wt% of TiO_2, with an estimated 14,075 tons of probable reserves of Ti (Harutchyan 1995).

8 Conclusions

The Armenian segment of the Tethyan metallogenic belt represents a potential target for some critical metals, including Re, Te, Se, REE, PGE, and potentially Li, associated with various geological environments and mineralized systems. Significant potential resources of critical metals in existing mines, in mine wastes and tailings remain underexplored. Reprocessing and recoveries of existing deposits and their tailings are required, aimed at an environmentally sustainable production of critical metals. For instance,significant quantities of Re and Te can be recovered from most of the porphyry Cu-Mo and epithermal Au deposits, respectively. Further investigations are required for the assessment of critical metals enrichment of alkaline complexes, granitic pegmatite, and Neoproterozoic metamorphic basement rocks.

Acknowledgements

This study was financially supported by the Science Committee of Republic of Armenia (Research project № 22IRF-08), and by the Swiss National Science Foundation grant200021_188714.

References

Amiryan ShH (1984) Gold ore formation of Armenian SSR. Pub House Acad Sci Arm SSR p 304 (in Russian)

Avagyan H (2004) Armenian mineral resources: “Gitutyun” publishing house of the National Academy of Sciences of the Republic of Armenia, Yerevan, p 432 (in Armenian)

Bagdasaryan GP, Ghukasian RKh, Karamyan KA (1969) Absolute dating of Armenian ore formations. Int Geol Rev 11:1166-1172

Beard ChD, Goodenough KM, Borst AM, Wall F, Siegfried PR et al (2023) Alkaline-Silicate REE-HFSE Systems. Econ Geol 118:177–208

Beland CMJ, Williams-Jones AE (2023) The genesis of a potential scandium ore deposit at Crater Lake, Canada. Chemical Geology 615:121223

Calder MF, Moritz R, Ulyanov A, Chiaradia M, Spangenberg J E, Melkonyan RL (2019) Jurassic ore-forming systems during the Tethyan orogeny: Constraints from the Shamlugh deposit, Alaverdi district, Armenia, Lesser Caucasus. Miner Deposita 54:1011–1032

Chakhmouradian AR, Wall F (2012) Rare earth elements: minerals, mines, magnets (and more). Elements 8 (5): 333–340

Critical Minerals Mapping Initiative (CMMI) https://portal.ga.gov.au/persona/cmmi

Faramazyan AS, Kalinin SK, Terekhovich SL (1970) Geochemistry of PGE in ores of Cu-Mo deposits of Armenia: Proceedings of the Academy of Sciences of the Armenian SSR. Earth Sciences 23(4):25–32 (in Russian) Frietsch R, Perdahl JA (1995) Rare earth elements in apatiteand magnetite in Kiruna-type iron ores and some other iron ore types. Ore Geol Rev 9:489-510

Grosjean M, Moritz R, Rezeau H, Hovakimyan S, Ulianov A, Chiaradia M, Melkonyan R (2022) Arabia-Eurasia convergence and collision control on Cenozoic juvenile K-rich magmatism in the South Armenian block, Lesser Caucasus. Earth-Science Reviews, Vol. 226:103949

Harutchyan AG (1995) The Arzakan titanium prospect. Ministry of Energy and Natural Resources of the Republic of Armenia, Unpublished report 105:6 (in Russian)

Hovakimyan S, Moritz R, Tayan R et al (2019) Cenozoic strike-slip tectonics and structural controls of porphyry Cu-Mo and epithermal deposits during geodynamic evolution of the southernmost Lesser Caucasus, TethyanMetallogenic Belt. Econ Geol 114:1301–1337

Maghakyan HG, Pidjyan GO et al (1972) Rare and precious elements in ore formations of the Armenian SSR. Publishing House of the Academy of Sciences of the Armenian SSR, Yerevan, p 393 (in Russian)

Mederer J, Moritz R, Zohrabyan S, Vardanyan A (2014) Base and precious metal mineralization in Middle Jurassic rocks of the Lesser Caucasus: a review of geology and metallogeny and new data from the Kapan, Alaverdi and Mehmana districts. Ore Geol Rev 58:185–207

Meliksetian BM (1971) Mineralogy, geochemistry and petrology of Tezhsar Alkaline Complex. In: Intrusive Complexes of Principal Ore Provinces of Armenia. Academy of Sciences, Armenian SSR, Yerevan: pp 117–298 (in Russian)

Moritz R, Melkonyan R, Selby D et al (2016a) Metallogeny of the Lesser Caucasus: From Arc Construction to Postcollision Evolution. Special Publication of the Societyof Economic Geology 19:157–192

Moritz R, Rezeau H, Ovtcharova M, Tayan R et al (2016b) Long-lived, stationary magmatism and pulsed porphyry systems during Tethyan subduction to postcollision evolution in the southernmost Lesser Caucasus, Armenia and Nakhitchevan. Gondwana Res 37:465-503

Rezeau H, Moritz R, Wotzlaw JF, Tayan R, Melkonyan R et al (2016) Temporal and genetic link between incremental pluton assembly and pulsed porphyry Cu-Mo formationin accretionary orogens. Geology 44:627–630

Rezeau H, Moritz R, Wotzlaw J-F, Hovakimyan S, Tayan RN (2019) Zircon petrochronology of the Meghri-Ordubad pluton, Lesser Caucasus: fingerprinting igneous processes and implications for the exploration of porphyry Cu-Mo deposits. Econ Geol 114:1365–1388

Sarukhanyan LB, Mkrtchyan GM (1968) Distribution of accessory rare earth elements in apatite. Proceedings of the Academy of Sciences of Armenian SSR, Earth Sciences 21(4):16–27 (in Russian)

Sokół K, Halama R, Meliksetian K, Savov IP, Navasardyan G, Sudo M (2018) Alkaline magmas in zones of continental convergence: The Tezhsar volcano- intrusive ring complex, Armenia. Lithos 320–321:172–191

Uzumova AI (1983) The Tejsar aluminum deposit. Ministry of Energy and Natural Resources of the Republic of Armenia, Unpublished report 13 (in Russian)

Wang Zh, Li MYH, Liu ZRR, Zhou MF (2019) Scandium: Ore deposits, the pivotal role of magmatic enrichment and future exploration. Ore Geol Rev 128:103906

Environmentally sustainable production of critical metals: a Tasmanian approach

Julie Hunt[1], Michael Roach[2], Lejun Zhang[1], Sharon Fraser[3], Yamila Cajal[1], Mohammad Fathi[1], Wei Hong[1], Owen Missen[1], David R Cooke[1]
[1]Centre for Ore Deposit and Earth Sciences (CODES), University of Tasmania, TAS, Australia
[2]Earth Sciences, College of Science and Engineering, University of Tasmania, TAS, Australia
[3]School of Education, College of Arts, Law and Education, University of Tasmania, TAS, Australia

Abstract. Tasmania, Australia is host to significant critical metal resources and currently produces tungsten (W) and tin (Sn). Exploration is underway for rare earth elements (REE) and magnesium (Mg). Additional critical metals, e.g. cobalt (Co), occur as minor components in operating base and ferrous metals mines and in legacy waste materials. A partnership between industry, academic and government organisations focused on the characterisation of critical metal deportment, pathways to production, plus education and engagement, has been commenced to aid growth of the critical metals industry in Tasmania. This includes outreach and training to engage with regional communities. Innovative tools are being developed including immersive 3D visualisations of mining operations. Example visualisations have been completed for the Dolphin tungsten deposit and the Savage River mining operations. Development of visualisations for the Kara iron-tungsten mine and processing plant are underway.

1 Introduction

Critical metals (including cobalt, magnesium, nickel REE, tin, and tungsten) are essential to industry in developed economies but are vulnerable to market uncertainties and supply chain disruptions. Domestic production of critical metals is therefore of strategic importance to individual countries or regions from a resource security perspective. Within Australia, Tasmania has a significant critical metals resource and currently produces tungsten (used in steel manufacturing and superalloys) and more than 95% of Australia's tin (important for renewables such as electric vehicles, photovoltaics, batteries etc; Geoscience Australia 2023). Tasmania's existing base and ferrous metal mines also have potential to produce critical metals such as cobalt either as a by-product of existing processing operations and/or from historical waste repositories. Recent discoveries of unconventional REE occurrences and significant discoveries of magnesium are currently being evaluated for potential development (ABx 2023; Australian Resources 2023).

The growth of a sustainable critical metals industry in Tasmania is being supported by an innovative collaboration between industry, academic, and government partners centred on three themes: novel tools for characterisation of critical metals deportment; optimisation and development of methods and workflows for critical metals processing and waste management strategies; and innovative community education and outreach strategies. Besides the University of Tasmania, there are nine industry partners, plus the University of Liege, the University of Queensland, Mineral Resources Tasmania (MRT), and the Tasmanian Minerals, Manufacturing and Energy Council (TMEC) involved in the collaboration.

The collaborative project includes fundamental research into deposit characterisation and genesis as well as detailed studies of mineral and element deportment that will inform mineral processing options. Sources of critical metals being examined include primary ore deposits plus mine waste materials. Processing options are also being addressed. In addition, there is a significant focus on outreach and training targeted at regional communities to help with workforce capacity building.

2 Critical metals in Tasmania

Most of the known critical metal resources are in north-western Tasmania as shown by the distribution of properties owned by collaborating organisations (Fig. 1). This area is largely underlain by Proterozoic sedimentary and volcanic rocks; Middle Cambrian sedimentary and felsic rocks, including the Mt Read Volcanics; Cambrian medium to high grade metamorphic complexes, including the Arthur Lineament; and Devonian granites (e.g., Rawlinson et al. 2010). Recent discoveries of REE-bearing clays have been made further east (9 on Fig. 1).

At the Dolphin mine (1 on Fig. 1) scheelite is hosted within carbonate-rich rocks proximal to granite. The site is currently undergoing re-development due to increased tungsten prices and contained high grade reserves (4.43 Mt of 0.92% WO_3) and resources (Group6 Metals, 2023). Prospect Ridge (2 on Fig. 1) hosts magnesium in a number of magnesite deposits (e.g., Perry 2011). At the Kara mine (3 on Fig. 1) iron and tungsten are hosted by limestone and calcareous sandstones proximal to Devonian granite (e.g., Singoyi 2001). Savage River (4 on Fig. 1) is an operating mine producing Fe from magnetite but has potential for production of Co and Ni from legacy waste materials (Grange Resources, 2023). Rosebery (5 on Fig.1) is a world class polymetallic volcanic-hosted massive sulphide deposit producing Cu, Pb, Ag, Zn and Au (Denwer et al. 2017). It also has potential to produce W, Sn and In as by-products (Geoscience Australia

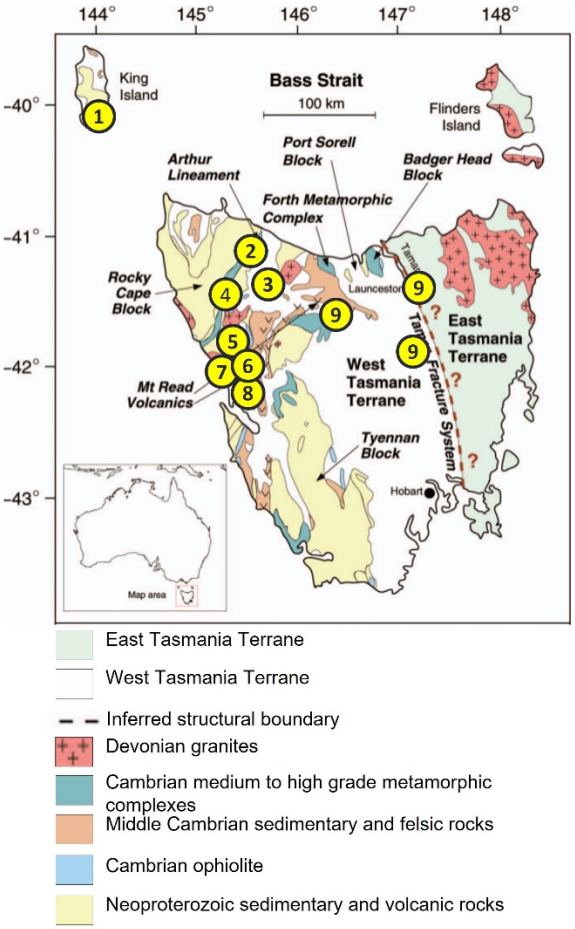

Figure 1. Simplified geology map of Tasmania (after Rawlinson et al. 2010) showing the location of industry partner properties. 1: Dolphin (W). 2: Prospect Ridge (Mg). 3: Kara (Fe, W). 4: Savage River (Fe, Mg, Co). 5: Rosebery (Zn-Pb-Ag-Au-Cu, Cu, In). 6: Renison (Sn). 7: Avebury (Ni, Co). 8: Mount Lyell (Cu, Co). 9: Deep Leads (REE).

2023). Renison (6 on Fig. 1) is a carbonate replacement tin deposit and is Australia's largest tin producer (Patterson et al. 1981; Metals X 2023). The potential for recovery of critical metals (e.g., In, Co, Ni) from ores, gangue and waste is being explored. Avebury (7 on Fig. 1) is a Ni sulphide deposit associated with an ophiolite sequence that has been intruded by granite (Kamenetsky et al. 2016). Portions of the ultramafic rocks are variably enriched in critical metals (W, Sn, Co). Mount Lyell (8 in Fig. 1) is a copper deposit hosted in volcanic rocks and has significant Co potential contained in legacy mine wastes (van Balen 2019). Deep Leads (9 on Fig. 1) are unconventional REE prospects associated with bauxite (Abx Group 2023).

3 Outreach and community engagement

A significant part of the project is targeted at outreach and training to engage with and educate regional communities. Innovative tools are being developed including immersive 3D visualisations of mining operations. Example visualisations have been completed for the Dolphin tungsten deposit and the Savage River mining operations. Development of visualisations for the Kara mine and processing plant are underway. The visualisations are created from various types of photography, including aerial images from drones, images from multi-lens 360º cameras, still and video photography, and detailed 3D renderings of rock samples. Also included are videos and sound for individual pieces of equipment along with oral descriptions and interviews with equipment operators. Snapshots are shown in Figures 2 and 3. In the visualisations information is available at a variety of scales from regional to local to outcrop to hand specimen to microscopic, as shown by the examples in Figures 4 and 5.

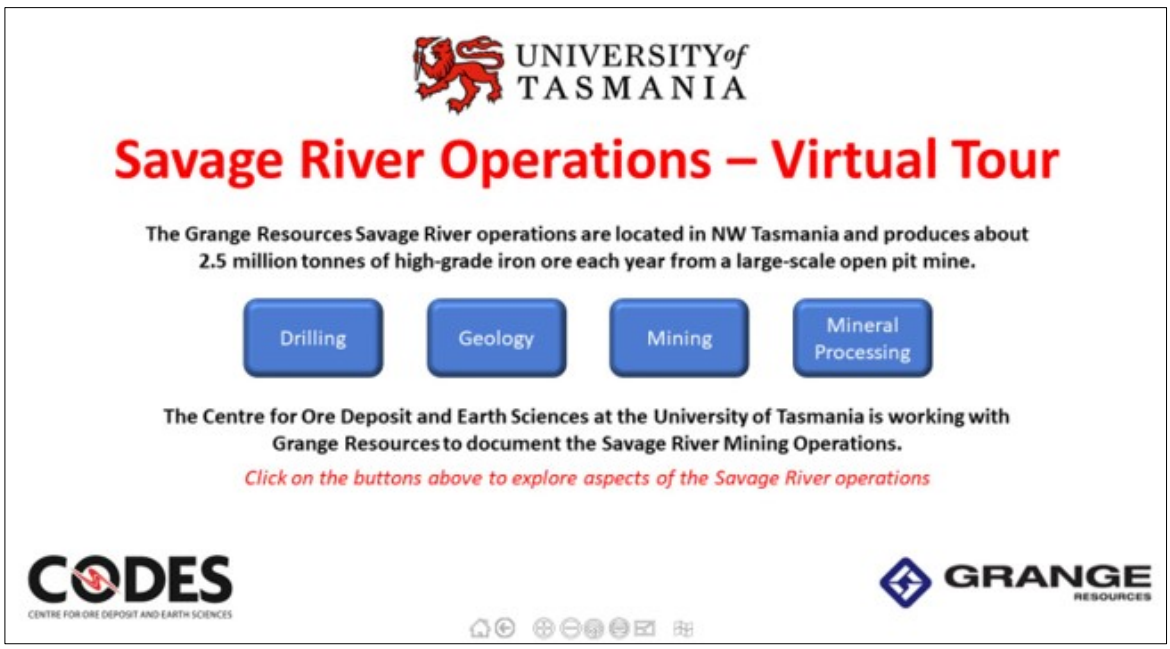

Figure 2. Snapshot of 3D visualisation for the Savage River mining operations. Buttons provide links to additional information, videos etc. All visualisations by M. Roach.

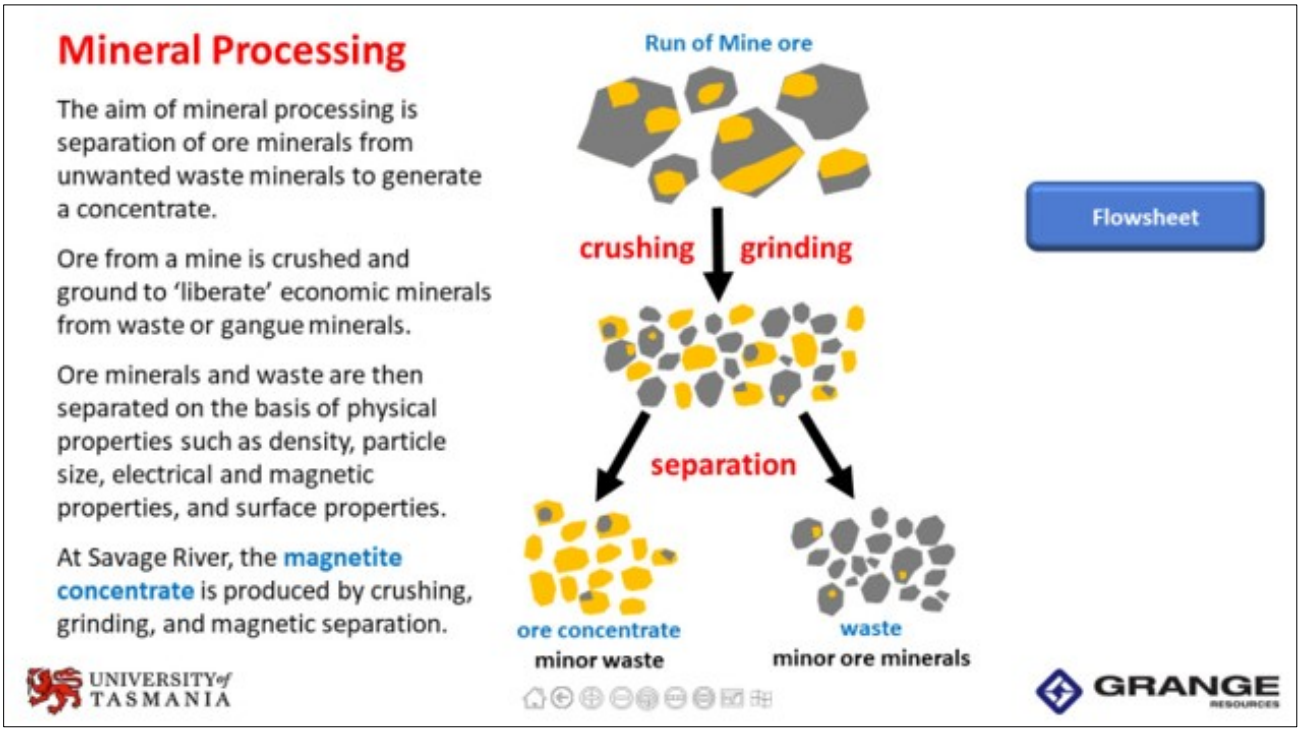

Figure 3. Information for the Savage River mining operations that can be seen by clicking on the mineral processing button shown in Figure 2. Clicking on the flowsheet button takes the user to details and videos of the processing plant.

Figure 4. Snapshot of 3D visualisation for the Dolphin mine showing the variety of scales of information available to the viewer. This includes regional geology, a virtual tour of the mine area, details of hand samples, as well as zoomable 3D renderings of samples.

Figure 5. Illustration of Information types available for sample K12LZ003 from the Dolphin tungsten deposit, including: visible light, ultra violet (UV) light, high resolution imagery, back-scattered electron (BSE), SEM-based automated mineral classification (AMICS), cathode luminescence (CL), and hyperspectral (TIR = thermal infra-red). Buttons at the bottom show links to geochemical data available for specific minerals.

Acknowledgements

The authors would like to thank all industry, academic and government collaborators for their participation and enthusiasm for the project. They have all been very generous with access to field sites, data and their time.

References

ABx Group (2023) Rare earth elements (REE) discovery. ABx Group website. https://www.abxgroup.com.au/site/about/about-us. Accessed 21 February 2023.

Australian Resources (2023) GWR to acquire Prospect Ridge magnesite project in Tasmania. Australian Resources website. https://www.australianresources.com.au/gwr-to-acquire-prospect-ridge-magnesite-project-in-tasmania/. Accessed 21 February 2023.

Denwer K, Garrick L and Robertson M (2017) Rosebery Cu-Pb-Zn-Ag-Au volcanogenic massive sulphide deposit. In Phillips GN (Ed) 2017 Australian Ore Deposits. Australasian Institute of Mining and Metallurgy, Monograph 32, p. 817-822.

Geoscience Australia (2023) Australia's potential for critical commodities. Geoscience Australia website. https://www.ga.gov.au/data-pubs/data-and-publications-search/publications/critical-commodities-for-a-high-tech-world/australias-potential. Accessed 21 February 2023.

Grange Resources (2023) Annual Report 2022. Grange Resources website. https://grange.blob.core.windows.net/public/2327e5a5-7a9e-453a-9fcd-89a142dc7e76.pdf. Accessed 8 May, 2023.

Group6 Metals (2023) Dolphin project. Group6 Metals website. https://g6m.com.au/dolphin-project/overview/. Accessed 15 February 2023.

Kamenetsky VS, Lygin AV, Foster JG, Meffre S, et al. (2016) A story of olivine from the McIvor Hill complex (Tasmania, Australia): Clues to the origin of the Avebury metasomatic Ni sulfide deposit. American Mineralogist 101:1321-1331

Metals X (2023) Renison tin operation. Metals X website. https://www.metalsx.com.au/renison-tin-operation/. Accessed 21 February 2023.

Patterson DJ, Ohmoto HH, Solomon M (1981) Geological setting and genesis of cassiterite-sulfide mineralisation at Renison Bell, western Tasmania. Economic Geology 76:393-438.

Perry OC (2011) A geophysical and geological study of the Arthur River magnesite deposit, northwest Tasmania. Dissertation, University of Tasmania.

Rawlinson N, Tkalcic H, Reading AM (2010) Structure of the Tasmanian lithosphere from 3D seismic tomography. Australian Journal of Earth Sciences 57:381-394.

Singoyi B, Zaw K (2001) A petrological and fluid inclusion study of magnetite-scheelite skarn mineralization at Kara north-western Tasmania: implications for ore genesis. Chemical Geology 173:239-253.

van Balen JFM (2019) Determining the mineralogical and geochemical properties of tailings at Copper Mines of Tasmania. Honours thesis, University of Tasmania, 126 p.

Potential for sulfide-hosted by-products from the iron oxide-apatite deposits at Kiruna? A mineralogical perspective

Patrick Krolop', Ulf B. Andersson[1], Katie McFall[2], Jana Kalmbach[3], Sabine Gilbricht[4], Thomas Seifert[4]
[1]Luossavaara Kiirunavaara AB (publ), Kiruna, Sweden
[2]University College London, Department of Earth Sciences, London, UK
[3]Avannaa Exploration Services AB, Kiruna, Sweden
[4]TU Bergakademie Freiberg, Institute of Mineralogy, Freiberg, Germany

Abstract. Sulfide mineralisation types in the Kiirunavaara and Per Geijer iron oxide-apatite deposits in the Kiruna district have been studied by mineralogical means to infer a preliminary potential for future by-products of Co, Cu, and sulfuric acid. Based on the dominance of pyrite over other sulfides, e.g., chalcopyrite and bornite-digenite solid solution series minerals, the main potential can be attributed to pyrite as the source of sulfuric acid. Significant concentrations of cobalt in pyrite types from both deposits may indicate an economic potential if proven processable in the future. Copper minerals have low concentrations of deleterious elements but occur less frequently compared to pyrite, so their potential is not yet tangible. Further studies are planned to evaluate the full potential of sulfides.

1 Introduction

Circular business models are key aspects in all mining operations as they increase materials efficiency, create diversity in assets and thus greater potential financial stability. The need for critical raw materials to the European economy to achieve the green energy transition enhances the investigation for potential by-products from existing mines. Reduction of the environmental impact of mining by recovery of by-products from waste streams is an additional important factor.

Nowadays, upgrading waste material in search for potential by-products is also being evaluated for iron ore mining operations in the Kiruna district. However, the focus is on phosphorus and rare earth elements, based on the high modal abundance of phosphates in tailings and large quantities in current exploration targets, e.g., the Per Geijer (PG) deposits. So far, the potential of Cu, Co, and sulfuric acid from sulfide minerals present in association with the iron ore has not been investigated in detail.

As a first approach, preliminary characterisation studies of the different sulfide species and varying types in the Kiirunavaara (KV) and PG iron oxide-apatite deposits near Kiruna were conducted (Kalmbach 2022, Andersson et al. 2022). Most of the information obtained in these investigations were mainly utilized to decipher the origin of mineralisation. In this contribution, the mineralogical information from previous studies is used to deliver preliminary implications for the potential of Co, Cu, and sulfuric acid as by-products from iron ore mining.

2 General characteristics of Kiruna IOA deposits

Iron oxide-apatite (IOA) deposits are the most important ore deposits in the Kiruna region of northern Sweden. The expression “Kiruna-type” has been introduced to signify the special character of the ores with over 40 orebodies in the Kiruna district (Geijer 1931, Martinsson et al. 2016). Early studies of IOA deposits in Kiruna district (e.g., Geijer 1910, 1931, Parák 1975) revealed high iron grades above 60 % Fe and the large tonnages for the Kiirunavaara deposit. The PG exploration targets potentially display significant mineral resources for future production for Luossavaara-Kiirunavaara Aktiebolag (publ.), known as LKAB, who exploits the iron ores in the district. Most of the IOA deposits in the Kiruna area display almost pure magnetite ores with minor impurities in the form of gangue minerals such as apatite, calcite, actinolite, mica, chlorite, titanite, sulfates, allanite, and quartz (Nordstrand & Andersson 2013, Martinsson et al. 2016). However, large differences in texture, mineralogy and relation to wall rocks occur in the PG deposits (Frietsch 1979, Martinsson 2015, Krolop 2022) compared to KV. Common features are the presence of sulfides hosted both disseminated in the iron ore and wall rocks as well as vein-hosted occurrences.

3 Methodology

Sampling was conducted according to styles of sulfide mineralisation in the deposits with regards to textural variability and mineral associations. Kiirunavaara samples were selected from recently blasted mining areas underground and partly from drill cores while exploration drill cores were sampled from the PG deposits. Samples were prepared by the Helmholtz Institute Freiberg for Resource Technology (PG samples) and the University of Gothenburg (KV samples). All 64 samples were studied with transmitted and reflected light and further investigated by scanning electron microscopy at TU Bergakademie Freiberg. Mineral chemical analysis was obtained on 18 samples by electron probe microanalysis (EPMA) and electron probe mapping with a JEOL JXA-8320 equipped with five wavelength dispersive spectrometers (WDS) at TU Bergakademie Freiberg. Additional trace element analysis was carried out on 14 samples using the

Analyte Excite 193 nm ArF* excimer-based laser ablation (LA) system, coupled to the quadrupole-ICPMS iCAP at the German Research Centre for Geosciences (GFZ).

4 Sulfides in the deposits

Preliminary investigation on sulfides based on textural and mineral chemical observation revealed 5 respective types of sulfides in both the KV and PG IOA deposits (Table 1). Sulphide minerals encountered in the deposits include pyrite, chalcopyrite, bornite, molybdenite, copper-rich minerals (in the bornite-digenite solid solution series), and pyrrhotite in some of the samples.

Table 1. Sulfide types in the Kiirunavaara and Per Geijer deposits and their characteristics.

Type	Sulfides	Setting	Assemblage
K1	Py	diss. in iron ore	Mgt
K2	Py > Cpy	vein-hosted	Mgt-Qtz-Cc
K3	Py > Cpy	vein-hosted	Qtz-Cc-Anh-Spec
K4	Py > Cpy	vein-hosted	Mgt-Clay
K5	Py > Cpy	diss. in wall rocks	Ttn-Act-Qtz-Cc-Alb
PG1	Cpy > Bo	diss. in iron ore	Mgt-Hem
PG2	Py > Cpy > Bo-Dig	vein-hosted	Cc-Qtz-Spec
PG3	Py > Cpy	vein-hosted	Chl-Alb-Cc-Alla
PG4	Py > Cpy	alteration nests	Mus-Chl-Alb-Cc-Qtz
PG5	Py > Cpy > Bo-Dig	vein-hosted	Mgt-Hem-Ap-Cc

Mineral chemical differences are most pronounced in pyrite compared to the other sulfide minerals. Significant variations from the ideal composition of pyrite occur particularly in sulfide types PG2 and PG4 expressed in the stoichiometric variability of $Fe_{0.87\text{-}1.02}Co_{0.00\text{-}0.14}As_{0.00\text{-}0.01}S_{1.93\text{-}2.00}$ and $Fe_{0.61\text{-}1.01}$ $Co_{0.05\text{-}0.38}As_{0.00\text{-}0.27}S_{1.42\text{-}2.01}$, respectively. The fluctuations relate mainly to the incorporation of Co and As. The other pyrite types are rather homogenous showing minor trace element concentrations of < 0.6 wt.% Ni and < 300 ppm As (PG3). Pyrite from the KV deposit reveals less elemental variation compared to PG but can be enriched in cobalt in sulfide type K1 up to 2.3 wt.% Co. Here, cobalt occurs unrelated to As with low concentrations of all trace elements (< 260 ppm). Chalcopyrite composition is relatively homogenous with low amounts of impurities (< 0.2 wt.%) independent of the sulfide type and deposit. However, mineral chemical complexity is introduced by the presence of minerals of the bornite-digenite solid solution series varying in Cu content between 57.7 wt.% and 77.4 wt.% and elevated Bi content up to 880 ppm for $bornite_{ss}$. Generally, the Cu-rich phases are poor in trace elements (< 0.2 wt.%).

5 Implications for potential by-products

5.1 Cobalt (Co)

Cobalt is an important element for the energy transition commonly used in batteries for electric vehicles and regarded a critical element by the European Union (e.g., Blengini et al. 2020).

Cobalt in the studied IOA deposits occurs either in iron oxides or in sulfide minerals, mainly pyrite. The content in Fe oxides, however, is negligible in PG and KV, with mineral chemistry of different Fe oxide types showing < 200 ppm Co (Krolop 2022).

Cobalt is enriched in pyrite from PG (types PG2 and PG4) with concentrations up to 10.2 wt.%. This is higher than Co concentrations in pyrite from KV (up to 2.3 wt.% Co) and other IOA deposits containing up to 3.9 wt.% Co (Reich et al. 2016, Liu et al. 2020). Cobalt in PG and KV does, however, show positive correlation with As in some types (Figure 1). Arsenic is regarded a deleterious element in pyrite (e.g., Anawar et al. 2006, Mileusnić et al. 2014).

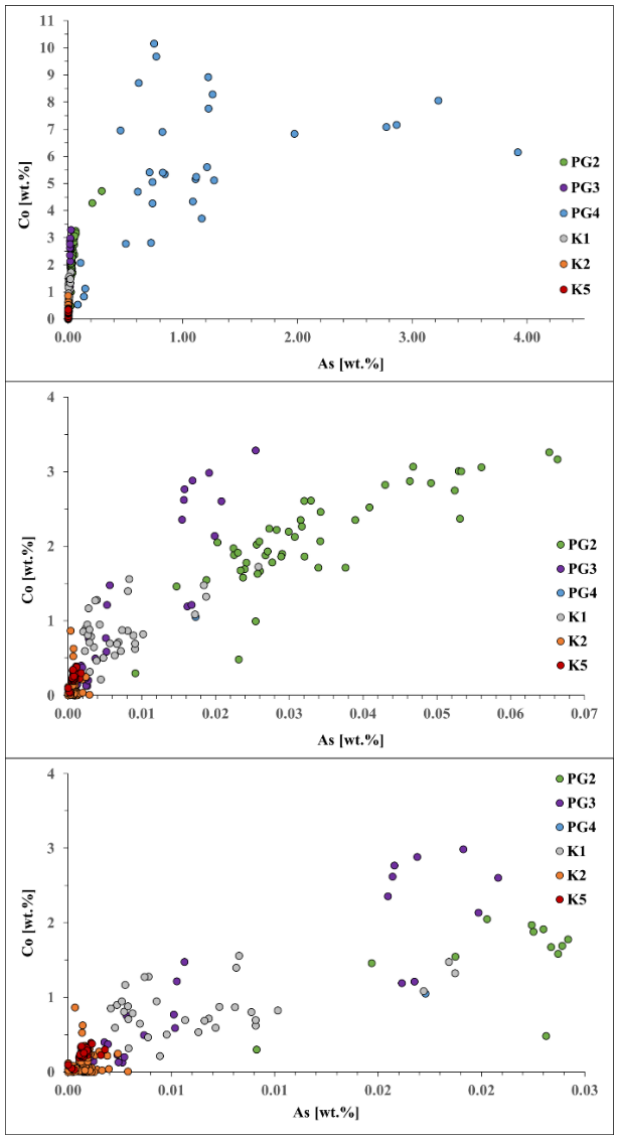

Figure 1. Cobalt vs As plot of sulfide types in the Kiirunavaara and Per Geijer deposits. Note that the x-axis has been adjusted in the lower two plots to illustrate variation at lower As concentration. Data derived by LA-ICP-MS.

Production of Co from sulfide ores is dependent on the parent sulfide mineral. Commonly, cobalt is extracted as a by-product in magmatic Ni-Cu-PGE deposits, therein mainly hosted in pentlandite. According to Moa and Davenport (2014), the process includes: 1) concentration by flotation, 2) concentrate is then smelted in a flash smelter or roasted and then smelted in an electric furnace, 3) the resulting matte treated either hydrometallurgically or pyrometallurgically to produce high-purity nickel and cobalt.

So far, pyrite-hosted Co is only being extracted from the Broken Hill deposit in Australia by Cobalt Blue. The method includes: 1) concentration of pyrite by gravity and flotation operations, 2) thermal treatment producing artificial pyrrhotite (calcine) and elemental sulfur, 3) leaching and further processing for sulfur recovery by remelting, 4) minor metals (Fe, Cu, Zn, Mn) removed by precipitation, ion exchange, and solvent extraction, resulting in final cobalt-hydroxide, which is further refined for production of high purity cobalt sulfate heptahydrate (Washbourne 2018).

However, to date this method has not been utilised by a mine in Europe. The deposit types at LKAB are different to those being processed using this method in Australia. Therefore, detailed characterisation of the Co-bearing sulfides in LKAB's deposits is needed, including the influence of As, before this process can be applied and commercialized if evaluated as positive by further investigation.

5.2 Copper (Cu)

The copper content in drill core assay data from KV seems to be lower than those reported for PG. The higher concentration of Cu in the in-situ ore is also reflected in magnetite concentrates achieved by process mineralogical test work, being elevated in PG compared to KV (Krolop et al. 2022). The relevant source for copper is in Cu-bearing sulfides, e.g., chalcopyrite and minerals of the bornite-digenite solid solution series (Figure 2).

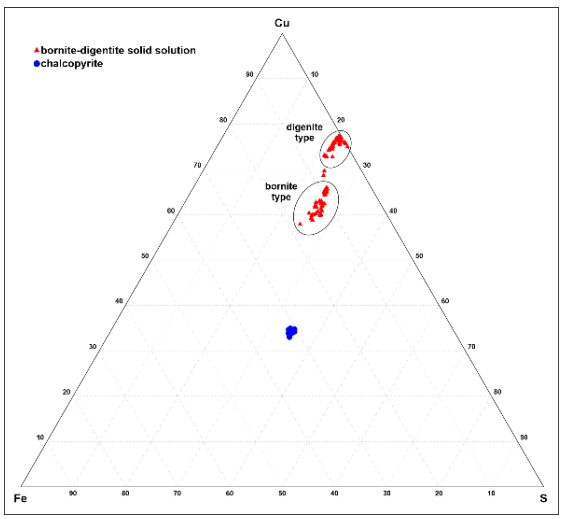

Figure 2. Cu-Fe-S plot showing the Cu-bearing sulfides based on EPMA-derived composition.

Other minerals that incorporate Cu as a trace element, e.g., magnetite, hematite, pyrite etc. can be neglected based on insignificant concentrations (< 100 ppm; Krolop 2022)

Chalcopyrite can function as a scavenger for other elements that may be regarded as economically relevant, such as Ag (Ayres et al. 2013). Furthermore, Cu-mineral concentrates can become enriched during processing in elements including As, Sb, Hg, Bi and Se. The concentration of those elements is regarded crucial in terms of financial penalties applicable when sold as a by-product on the world market (Fountain 2013). However, on the positive side the deleterious elements in the investigated chalcopyrite grains are entirely below the reported concentrate limits, being As < 0.2 wt.%, Sb = 0.05 wt.%, Bi = 0.02 wt.%, Cd = 0.03 wt.%, Hg = 0.0005 wt.%, Ni+Co = 0.5 wt.%, and Zn = 3 wt.% following Salomon-de-Friedberg and Robinson (2014).

5.3 Sulfuric acids

Sulfuric acid is predominantly used in the production of phosphate fertilizers, chemical (e.g., detergents, resins, coatings, water treatment) or other industrial applications, such as manufacture of explosives or automobile batteries. Since sulfuric acid is planned for use in recovering phosphorus (and REE) as side products from apatite during iron ore mining, this is also of importance for LKAB. Sulfuric acid is commonly produced from pyrite. Pyrite is the most common sulfide in both studied deposits, KV and PG, based on its relative abundance (Andersson et al. 2022). Nevertheless, pyrite can also host a range of elements that are deleterious from a processing and/or environmental perspective. The latter is predominantly influenced by Hg, Tl, and As (Deditius and Reich 2016, George et al. 2019) having ramifications for environmental management at mine sites, especially waste piles and tailings treatment.

Pyrite has been characterised in different textural and mineral chemical composition in the IOA deposits (see chapter 4). Notably, the contents of Hg and Tl are generally below detection limit and can be regarded as negligible for processing and environmental aspects. Arsenic, however, occurs in significant concentration in the weight percentage range in pyrite of some sulfide types, as shown in Figure 1. However, As has been shown to be treatable from copper concentrates by recovering the metal value (Salomon-de-Friedberg et al. 2014).

Recently, the two Swedish mining companies LKAB and Boliden agreed to investigate the possibility of extracting pyrite concentrate from mining waste at Boliden's Aitik mine. Subsequently, LKAB will process the concentrate into fossil-free sulfuric acid, to be further used in processes for extracting rare earth elements and phosphorus from LKAB's mining waste. However, it can be expected that the volumes of pyrite concentrate from Aitik are unlikely to cover the full amount of what LKAB requires in the future. To produce the predicted

volume of sulfuric acid needed to process the high modal abundance of phosphates in the Per Geijer deposits (8 times as much as the currently operated mines), additional pyrite concentrate is needed that could originate from LKAB's mine waste. However, the full potential is under investigation.

In addition, if pyrite could be added from LKAB's own deposits to the supplied waste stream from the Aitik mine, this will reduce the cost and environmental impact of this processing method as it would remove the need to import sulfuric acid to cover the shortfall for this process left by the current arrangement. This will continue the move towards a circular business model and will allow the production of these critical and strategic metals in Europe from mine waste, while also reducing the amount of waste from the mines.

6 Conclusions

The economic potential of pyrite is investigated, as the most abundant sulfide mineral in both the KV and PG deposits, both for producing sulfuric acid and cobalt based on preliminary mineralogical investigation. However, further information, e.g., distribution and quantity in the deposits, contents in current waste and tailing material, possibilities for processing and other economic criteria need to be addressed to evaluate the full potential of sulfides in IOA deposits.

Acknowledgements

The authors acknowledge colleagues at LKAB for support during sample acquisition. Personnel at the sample preparation laboratories are thanked for high quality thin sections and embeddings. We further acknowledge Marcus Oelze for LA-ICP-MS data acquisition and LKAB for approval of publication.

References

Anawar HM, Garcia-Sanchez A, Murciego A, Buyolo T (2006) Exposure and bioavailability of arsenic in contaminated soils from the La Parrilla mine, Spain. Environ Geol 50:170-179. https://doi.org/10.1007/s00254-006-0196-2

Andersson UB, Kalmbach J, Gilbricht S, Seifert T, Karlsson A, Krolop P (2022) Preliminary data on sulphides at Kiruna, Sweden. In 16th SGA Biennial Meeting, Proceedings, Rotorua, New Zealand, Proceedings volume 1, 1 (Vol. 4).

Ayres RU, Ayres LW, Råde I (2013) The life cycle of copper, its co-products and by-products. Eco-efficiency in industry and science, Vol. 13. Kluwer Academic Publishers, Amsterdam

Blengini GA, El Latunussa C, Eynard U, De Matos CT, Wittmer DMAG, Georgitzikis K, Pavel CC, Carrara S, Mancini L, Unguru M, Blagoeva D (2020) Study on the EU's list of critical raw materials. Publications Office of the European Union, Luxembourg

Deditius AP, Reich M (2016) Constraints on the solid solubility of Hg, Tl, and Cd in arsenian pyrite. Am Min, 101(6):1451-1459. https://doi.org/10.2138/am-2016-5603

Fountain C (2013) The whys and wherefores of penalty elements in copper concentrates. MetPlant 2013: Metallurgical Plant Design and Operating Strategies, Australasian Institute of Mining and Metallurgy, Melbourne, Australia

Frietsch R (1979) Petrology of the Kurravaara Area Northeast of Kiruna northern Sweden; Serie C; Sveriges Geol Undersoekg, Uppsala

Geijer P (1910) Igneous rocks and iron ores of Kiirunavaara, Luossavaara and Tuollavaara. Econ Geol 5 (8):699–718

Geijer (1931) The iron ores of the Kiruna type. Sveriges Geol Undersoekg, Uppsala

George LL, Biagioni C, Lepore GO, Lacalamita M, Agrosì, G, Capitani GC, Bonaccorsi E and d'Acapito F (2019) The speciation of thallium in (Tl, Sb, As)-rich pyrite. Ore Geol Rev 107:364-380. https://doi.org/10.1016/j.oregeorev.2019.02.031

Kalmbach J (2022) Sulfides in iron oxide-apatite and greenstone-hosted copper deposits in the Kiruna area, northern Sweden – characterization by mineralogy, mineral chemistry and sulfur isotopy. M. Sc. Thesis, TU Bergakademie Freiberg

Krolop P (2022) The Per Geijer iron ore deposits: Characterization based on mineralogical, geochemical and process mineralogical methods. Dissertation, TU Bergakademie Freiberg

Krolop P, Larsson A, Körtge M (2022) Per Geijer Deep geometallurgical tests. LKAB internal report

Liu Y, Fan Y, Zhou T, Wang J, Fu B, Ireland TR, White NC, Zhang L (2020) Geochemical characteristics of pyrite in the Dabaozhuang deposit in the Middle-Lower Yangtze River Metallogenic Belt, Eastern China, Ore Geol Rev 124:103-662. https://doi.org/10.1016/j.oregeorev.2020.103662

Martinsson O (2015) Genesis of the Per Geijer apatite iron ores, Kiruna area, northern Sweden. Proceedings of the SGA Biennal Meeting, 23–27.

Martinsson O, Billström K, Broman C, Weihed P, Wanhainen C (2016) Metallogeny of the northern Norrbotten ore province, northern Fennoscandian Shield with emphasis on IOCG and apatite-iron ore deposits. Ore Geol Rev 78:447-492. https://doi.org/10.1016/j.oregeorev.2016.02.011

Mileusnić M, Mapani BS, Kamona AF, Ružičić S, Mapaure I, Chimwamurombe PM (2014) Assessment of agricultural soil contamination by potentially toxic metals dispersed from improperly disposed tailings, Kombat mine, Namibia. J Geochem Explor 144: 409-420. https://doi.org/10.1016/j.gexplo.2014.01.009

Moats MS, Davenport WG 2014. Nickel and cobalt production. In Seetharaman S (ed) Treatise on process metallurgy, 3rd edn. Elsevier, Amsterdam, pp 625-669

Nordstrand J, Andersson UB (2013) Mineral chemistry of gangue minerals of the Kiirunavaara iron ore, evidence for a transition from magmatic to hydrothermal conditions. 12th SGA Biennial Meeting, Proceedings, Geological Survey of Sweden, 1663, 1666.

Reich M, Simon AC, Deditus A, Barra F, Chryssoulis S, Lagas G, Tardani D, Knipping J, Bilenker L, Sanchez-Alfaro P, Roberts MP, Munizaga R (2016) Trace element signature of pyrite from the Los Colorados iron oxide-apatite (IOA) deposit, Chile: a missing link between Andean IOA and iron oxide copper-gold systems? Econ Geol 111 (3):743-761. https://doi.org/10.2113/econgeo.111.3.743

Salomon-De-Friedberg H, Robinson T, Lossin A, Omaynikova V (2014) Developing copper arsenic resources with CESL technology. In Proceedings of the COM 2014, 53rd Annual Conference of Metallurgists, Vancouver

Parak T (1975) Kiruna iron ores are not" intrusive-magmatic ores of the Kiruna type". Econ Geol 70(7):1242-1258. https://doi.org/10.2113/gsecongeo.70.7.1242

Washbourne M (2018) Cracking the cobalt code. Australia's Paydirt, 1(258):86

Geochemical trends of lithium-bearing minerals in LCT-pegmatites in Central Namibia

Nico Kropp[1, 2], **Gregor Borg**[1,2]
[1]*Martin Luther University Halle-Wittenberg, Institute for Geoscience and Geography, Economic Geology and Petrology Research Unit, Von-Seckendorff-Platz 3, 06120 Halle (Saale)*
[2]*ITEL- Institute for Technologies and Economics of Lithium - Deutsches Lithiuminstitut GmbH, Leipziger Str. 70, 06108 Halle (Saale)*

Abstract. In the central area of Namibia, between the Erongo, Swakopmund, and the Brandberg, five separate pegmatite belts run in a southwest-northeast direction, which have been previously explored primarily for tin ("tin belts") and uranium ("Rössing belt") and have also been commercially mined from various deposits. Since the demand for lithium has increased drastically worldwide, lithium minerals, which are especially associated with tin-bearing pegmatites, have also become the new focus of exploration and mining. Besides spodumene-bearing pegmatites, petalite and lepidolite-bearing pegmatites are also attracting the interest of industry and researchers.
For a feasibility study on lithium fingerprinting, as proof of origin of mineral sources of lithium, three pegmatite provinces in Namibia were sampled and are now being investigated for their distinguishability using geochemical analyses. The investigations cover the mineralogy, the isotopic signature, and the trace element composition of different lithium minerals (spodumene, petalite and lepidolite) from several deposits.

1 Introduction

In the past, intensive exploration and mining for tin in cassiterite-bearing pegmatites was the most common exploration target in Central Namibia because of several pegmatite swarms in this region. Nowadays, these pegmatites are of interest since they contain lithium-bearing minerals such as spodumene, petalite, and lepidolite.

Lithium-Caesium-Tantalum pegmatites (LCT) are the most important hard rock source of lithium, which is a key element for the green energy transition and is needed as an accumulator material in the electronic vehicles industry and for energy storage in general.

Transparency and regulations for the traceability of products and raw materials need a database, which verifies the origin of raw materials by the natural properties or with artificially added tracers. To decide, which methods will be used in the future, case studies are necessary, which generate data of the different lithium deposits and compare data sets to use them as a database for a possible lithium fingerprint as proof of origin. The idea of fingerprinting mineral raw materials is not new and has already been applied for columbite-tantalite minerals (Melcher et al. 2008), gold (Schlosser et al. 2009), and ancient building material such as marble (Antonelli and Lazzarini 2015). In the field of lithium minerals, there have only been a few studies dealing with primary raw materials so far (Desaulty et al. 2022).

In this study, preliminary data from samples of different deposits in Central Namibia is presented.

2 Geological Setting

The Neoproterozoic Damara Belt in Namibia was formed during the different phases of rifting, spreading, subduction, and continental collision, which resulted in the amalgamation of Gondwana between the Kalahari, Congo, and Rio de la Plata Cratons between 900 and 460 Ma with the formation of two coastal and one inland branching orogenic belts (Borg and Gauert 2018, Ashworth 2020).

The Pre-Damaran Abbabis Complex, as basement of the Damara Belt, is overlain by metasedimentary complexes. Granitic intrusions of Pan-African age divide the belt into tectono-stratigraphic units of different metamorphic overprint and igneous activity (Ashworth 2020).

Different pegmatite swarms occur in the central portion, i.e., close to the triple point of the three orogenic branches (Ashworth 2020). According to the mining history of Central Namibia, these swarms are called Northern Tin Belt, Central Tin Belt (CTB), Southern Tin Belt, Karibib Pegmatite Belt (KPB), and Rössing Pegmatite Belt (Fig. 1).

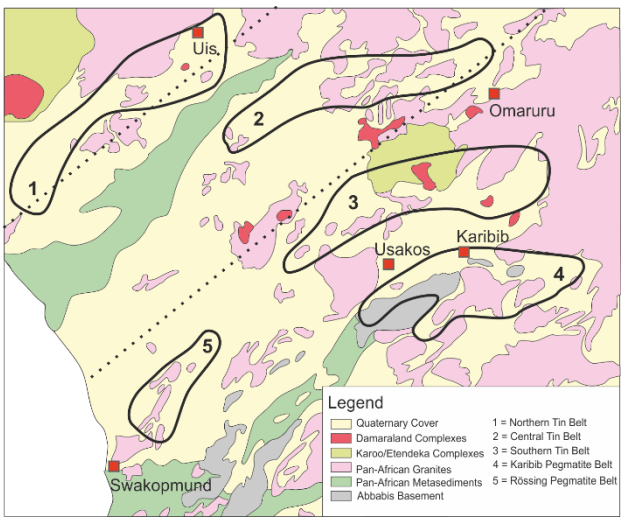

Figure 1. The regional geology of Central Namibia with five pegmatite belts, showing a similar orientation (modified after Ashworth 2014).

The Northern Tin Belt is a northeast-trending zone between the Brandberg and Cape Cross with different pegmatite swarms (Uis, Karlowa, and Strathmore swarms) intruded in Damara meta-

sediments (Diehl 1986). The pegmatites are commonly unzoned and intrude as sigmoidal structures into biotite-schists.

Pegmatites of the Central Tin Belt intruded into mica schists of the Kuiseb Formation and show minor textural internal zonation.

The Karibib Pegmatite Belt, as the southernmost pegmatite belt in this area, is host to the Rubicon and Helikon pegmatites. The Rubicon pegmatites show an internal zonation with separate zones of petalite and lepidolite-rich units and are enclosed in granodioritic host rocks. In contrast, the Helikon pegmatites are similar in orientation but intruded into marbles (Ashworth 2020).

3 Material and Methods

3.1 Samples and Sample Preparation

Sample material from three different pegmatite belts was analysed: Four Lepidolite samples and one petalite sample from two deposits in the Karibib Pegmatite Belt, two spodumene samples and four petalite samples from the Northern Tin Belt, as well as one lepidolite sample from the Central Tin Belt.

Thin sections were used to determine the mineral paragenesis by polarisation microscopy.

3.2 SEM-EDX and Electron Microprobe

For the mineralogical investigation of the sample material, thin sections were characterised using scanning electron microscopy-assisted energy dispersive spectroscopy (EDX) at the Martin Luther University Halle-Wittenberg. A SEM JSM 6300 149 (JEOL, Akishima - Tokyo, Japan) was used for this purpose. The excitation voltage was 20 kV and an XFlash 5010 EDX detector with a resolution of 123 eV and a working distance of 25 mm was used.

For further mineral chemistry, trace elements were measured using wavelength dispersive spectroscopy (WDX) on a JEOL JXA-8230 equipped with WDX-spectrometers at Friedrich Schiller University Jena. For the measurements at 15 kV and 15 nA with a measurement time of 20s for point measurements, standards were used for the following elements (as oxides): bismuth (Mα, Bi-100, DL 0.09 mass%), caesium (Lα, Cs glass, DL 0.09 mass%), iron (Kα, Fe_2O_3, DL 0.05 mass%), manganese (Kα, Rhodonite, DL 0.05 mass%), sodium (Kα, Albite, DL 0.04 mass%), niobium (Lα, Nb-100, DL 0.13 mass%), rubidium (Lα, Rb glass, DL 0.12 mass%), zinc (Kα, ZnS, DL 0.09 mass%).

4 Results

The petalite samples from the Northern Tin Belt are fresh and show only minor occurrences of clay minerals along some fissures. Different colour variations are visible, from slightly orange to salmon-coloured and greenish to white. Only small inclusions of cassiterite and minerals from the columbite-tantalite series occur. The petalites contain only minor concentrations of trace elements like rubidium (0.14 mass%), niobium (0.08 mass%), bismuth (0.11 mass%), and zinc (0.089 mass%), which seems to occur randomly. The spodumene from the Karlowa pegmatite swarm can reach large crystal sizes of about 1 metre. The analysed hard rocks contain only spodumene with minor inclusions of cassiterite, sphalerite, and apatite. The WDX data indicate minor concentrations of sodium (0.12 mass%), niobium (0.08 mass%), and bismuth (0.11 mass%). Spodumene from the DeRust pegmatite swarm shows similar niobium concentrations (0.09 mass%), but higher rubidium concentrations (0.16 mass%). In general, the concentrations of trace elements detectable with the electron microprobe are low for both, spodumene and petalite.

Lepidolite from the Central Tin Belt is only found in minor amounts closely associated with feldspar and quartz in small artisanal pits. The lepidolites are intergrown with feldspar, quartz, topaz, apatite, and minor cassiterite. The mineral chemistry of the pinkish mica shows low contents of rubidium (0.45 mass%), manganese (0.19 mass%), and caesium (0.31 mass%, Fig. 2) and concentrations for iron are below the detection limit.

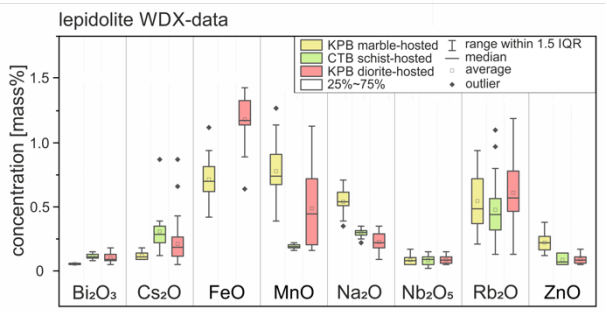

Figure 2. Comparison of selected trace elements in lepidolite from Karibib Pegmatite Belt (KPB) and Central Tin Belt (CTB), showing minor variations for bismuth, niobium, and zinc, whereas the variation is bigger for iron, manganese, and sodium.

The pegmatites in the Karibib area contain mainly petalite and lepidolite as Li-minerals. The lepidolites from diorite-hosted pegmatites show different colour variations, typically pinkish and greyish mica. The trace element composition shows a difference in rubidium between those two types of samples (pinkish lepidolite with 0.64 mass%, greyish lepidolite with 0.72 mass%), caesium (pinkish lepidolite with 0.15 mass%, greyish lepidolite with 0.32 mass%) and manganese (pinkish lepidolite with 0.46 mass%, greyish lepidolite with 0.82 mass%) concentrations (Fig. 3).

This indicates a wider range for trace element variance in this deposit, compared to lepidolite-bearing pegmatites without colour variations. Additionally, lepidolite from the marble-hosted pegmatites shows also colour variations from pinkish to light greyish. The microprobe data revealed minor zinc concentrations (0.22 mass%), which are higher, than in the other analysed lepidolite samples.

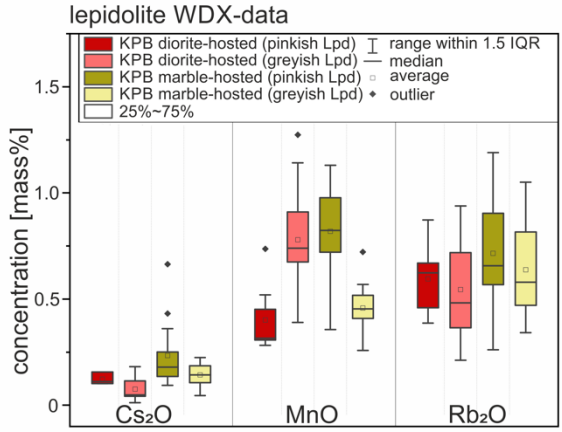

Figure 3. WDX-data of different coloured lepidolite from diorite-hosted pegmatite (n=40) and marble-hosted (n=29) from the Karibib Pegmatite Belt (KPB) shows different concentrations of caesium, manganese, and rubidium where only caesium behaves the same in both deposits.

5 Discussion and Conclusions

Although the petalite samples are of different colours, they are not distinguishable by microprobe analyses alone. If the colour changes are due to the incorporation of trace elements, their concentrations seem to be below the detection limit of microprobe analyses, which can only be investigated by other methods.

The different concentrations of sodium and manganese in the lepidolite from the Central Tin Belt and the Karibib Pegmatite Belt suggest three clusters (Fig. 4). Both elements are common in lepidolite but are present in different positions inside the crystal lattice. In complement with other methods, the trace element composition can be used as a parameter for the differentiation of pegmatite provinces. As already shown by Roda et al. 2007, mica minerals in the Karibib Pegmatite Belt can be chemically differentiated by their location within the pegmatite zonation but are similar on a regional scale.

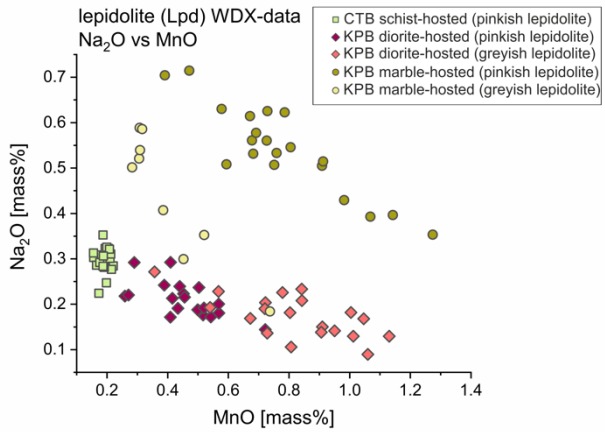

Figure 4. WDX-data of lepidolite from the Central Tin Belt (n=20) and Karibib Pegmatite Belt (n=69) shows different concentrations of manganese and sodium, resulting in three distinguishable clusters probably reflecting the three different host rocks.

Due to the different trace element contents of lithium-rich minerals (spodumene, petalite and lepidolite) in the various pegmatite belts in central Namibia, it is possible to distinguish these based on their geochemical signature.

The different geochemical signatures are probably due to the different genesis of the pegmatites and their zonation, their different metamorphic and deformational history, and the different host rocks.

In order to be able to make reliable statements about the distinguishability also across different sections of pegmatitic lithium deposits, narrower sampling patterns are necessary. However, based on our preliminary data, it is indicated that the pegmatite provinces can be distinguished from each other with the help of the mineral chemistry of the lithium minerals. For the differentiation between individual pegmatite bodies, further analyses are also necessary, including additional methods and parameters, such as the investigation of trace elements by LA-ICP-MS and the behaviour of the lithium isotopes, which are currently carried out.

Acknowledgements

The authors are grateful to Stefan Kiefer for the supply of microprobe analyses at the Friedrich Schiller University Jena. Andreas Kamradt (MLU Halle) and Michael Schmidt (DERA) are gratefully acknowledged for their support during fieldwork and many fruitful discussions.

References

Antonelli F, Lazzarini L (2015) An updated petrographic and isotopic reference database for white marbles used in antiquity. Rend Fis Acc Lincei 26:399–413

Ashworth L (2014) Mineralised Pegmatites of the Damara Belt, Namibia: Fluid inclusion a geochemical characteristic with implications for post collisional mineralisation. Dissertation, University of Witwatersrand. Faculty of Science

Ashworth L, Kinnaird JA, Nex PAM, Harris C, Müller AB (2020) Origin of rare-element-mineralized Damara Belt pegmatites: A geochemical and light stable isotope study. Lithos 372-373(2020):105655

Borg G, Gauert C (2018) The African Metallotects of Southwest Gondwana. In: Siegesmund S, Basei MAS, Oyhantçabal P, Oriolo S (eds) Geology of Southwest Gondwana. Springer International Publishing (Regional Geology Reviews) 615–676

Desaulty AM, Climent MC, Lefebvre G, Cristiano-Tassi A, Peralta D, Perret S (2022) Tracing the origin of lithium in Li-ion batteries using lithium isotopes. Nature communications 13:4172

Diehl M (1986) Preliminary report on the Cape Cross-Uis pegmatite field. Communs geol Surv S W Africa/Namibia 2:37–42

Melcher F, Graupner T, Henjes-Kuns, F, Oberthür T, Sitnikova, M, Gäbler E (2008) Analyitical Fingerprint of Columbite-Tantalite (Coltan) Mineralisation in Pegmatites - Focus on Africa. Ninth International Congress for Applied Mineralogy 2008:615–624

Roda E, Keller P, Pesquera A, Fontan F (2007) Micas of the muscovite–lepidolite series from Karibib pegmatites, Namibia. Mineralogical Magazine 71(1):41-62

Schlosser S, Kovacs R, Pernicka E, Günther D, Tellenbach M (2009) Fingerprints in Gold. In: Reindel M, Wagner GA (eds) New Technologies for Archaeology. Berlin, Heidelberg: Springer Berlin Heidelberg (Natural Science in Archaeology) 409–436

Can the mining industry meet global demand for critical minerals?

Jeffrey L. Mauk[1], Jonathan A. Funk[1], Nicholas A. Karl[1]
[1]U.S. Geological Survey, Denver, Colorado, USA

Abstract. We define U.S. Fortiers as the 5-year average of annual U.S. consumption of a commodity, and global Fortiers as the 5-year average of annual global production of a commodity. Comparison of global Fortiers to previously published mineral deposit size classifications reveals that humankind is consuming approximately one supergiant deposit of Ag, Au, Cu, Pb, and Zn every year. Because increasing environmental, social, and governmental factors make it more difficult to open new mines and expand existing mines, and because new discoveries are increasingly coming from deeper deposits, the mining industry may struggle to meet future needs. We infer that some critical minerals—Bi, Mo, PGE, Sb, Re, REE, Sn, and Te—might have current production rates that are equivalent to the endowment of one of the largest 1-10% of all deposits for each commodity. We conclude that detailed, fit-for-purpose data are required to rigorously evaluate evolving supply risk.

1 Introduction

There is no single unified definition of "critical mineral", but most definitions share common attributes that can be summarized as: a critical mineral is an element or commodity that is essential for modern technologies, economies, or national security, and has a supply chain that is vulnerable to disruption. Many of these critical minerals are essential for 21st century applications such as green energy and technology, so their supply has become an increasing cause for concern for governments and industry.

Mineral deposits can be ranked by size, and classified as large, giant, or supergiant (e.g., Singer 1995; Laznicka 2014). However, despite the increasing visibility of critical minerals, there does not appear to be a definition of whether a critical mineral deposit can play a leading role in addressing humankind's needs for critical minerals. We refer to these as *significant deposits*.

We provide a brief overview of some attempts to quantify giant deposits for base and precious metals to help inform establishing thresholds for significant deposits of critical minerals. We then propose a method that can be applied to determine significant deposits of critical minerals, we provide threshold values for the majority of commodities that are considered critical minerals in the United States, and then we discuss how applying this method sheds some light on the question of whether the global mining industry can meet growing demand for critical minerals.

2 Deposit size and societal significance

2.1 Deposit size

Ranking of mineral deposits by size has mostly used two approaches. One approach is to use the average crustal concentration of each element (Clarke values) to calculate the tonnage of each element in large, giant, and supergiant deposits (Laznicka 2014). For example, Ni has a Clarke value of 5.5×10^1 ppm, and the threshold values for contained metric tons of Ni in different deposit sizes are (I) large: 5.5×10^5; (II) giant: 5.5×10^6; and (III) supergiant 5.5×10^7 (Table 1). The principal benefits of this system are its near-universal applicability and simplicity. Complexities such as political, economic, technical, and geological factors that determine "ore" are not embedded in this classification scheme. Because Clarke values are relatively well-known, mineral deposit size classifications can be calculated for any element, though calculations for actual minerals that are considered critical—such as barite, fluorspar, graphite, and potash—cannot be directly determined.

Another common approach to evaluating deposit size is statistical treatment based on cumulative frequency graphs, with the largest 10% of deposits classified as giant, and the largest 1% of deposits classified as supergiant (Table 1; Singer 1995). By plotting data from actual deposits, this technique assimilates considerations of what determines ore, such as those factors mentioned above. However, the technique requires enough deposits for each commodity to be statistically rigorous, so commodities that are produced from only a few deposits might not yield meaningful results. Conversely, the technique is based on compiling historical records, so some datasets may contain deposits that would not meet current criteria to be classified as orebodies. Furthermore, to our knowledge, byproduct commodities have not been classified by this methodology, perhaps because the economic viability of the deposit depends on factors for the primary commodity, and perhaps because in many cases byproduct production is not reported.

2.2 Societal significance

The transition of the global energy system to clean energy is bringing about unprecedented increases in demand for battery and energy commodities such as Cu, Li, Ni, Co, and REEs (International Energy Agency 2021). There are two main ways to evaluate demand, and both provide valuable insights. On the one hand, forecasting based on assumptions of

future targets and needs can identify possible future demands. For example, the International Energy Agency (2021) projects that to meet the Paris Agreement's climate stabilisation at "well below 2°C global temperature rise", would mean quadrupling mineral requirements for clean energy technologies by 2040.

On the other hand, the winds of change can be fickle, and it is possible to extrapolate demand from current consumption and production. Both approaches are complimentary, but we use the latter to define significant deposits of critical minerals. Herein, we refer to the 5-year average of annual U.S. consumption of a commodity as one U.S. Fortier (Table 1). Loosely translated from the French, a fortier is a fortress, and deposits with endowments of one Fortier or more may help to fortify humankind by helping to meet the need for critical minerals and other commodities.

Metal	Clarke ppm	U.S. Fortier	Global Fortier	Large Deposits			Giant deposits			Supergiant deposits		
		consumption	*production*	Low	Mid	High	Low	Mid	High	Low	Mid	High
Al	8.0×10^{4}	4.7×10^{5}	6.4×10^{7}	8.0×10^{8}	3.2×10^{9}	5.6×10^{9}	8.0×10^{9}	3.2×10^{10}	5.6×10^{10}	8.0×10^{10}	3.2×10^{11}	5.6×10^{11}
Mg	2.2×10^{4}	5.6×10^{4}	1.0×10^{6}	2.2×10^{8}	8.8×10^{8}	1.5×10^{9}	2.2×10^{9}	8.8×10^{9}	1.5×10^{10}	2.2×10^{10}	8.8×10^{10}	1.5×10^{11}
Ti	4.0×10^{3}	1.2×10^{6}	8.1×10^{6}	4.0×10^{7}	1.6×10^{8}	2.8×10^{8}	4.0×10^{8}	1.6×10^{9}	2.8×10^{9}	4.0×10^{9}	1.6×10^{10}	2.8×10^{10}
Mn	7.2×10^{2}	7.1×10^{5}	1.9×10^{7}	7.2×10^{6}	2.9×10^{7}	5.0×10^{7}	7.2×10^{7}	2.9×10^{8}	5.0×10^{8}	7.2×10^{8}	2.9×10^{9}	5.0×10^{9}
Sr	3.3×10^{2}	7.5×10^{3}	2.8×10^{5}	3.3×10^{6}	1.3×10^{7}	2.3×10^{7}	3.3×10^{7}	1.3×10^{8}	2.3×10^{8}	3.3×10^{8}	1.3×10^{9}	3.3×10^{9}
Zr	2.0×10^{2}	4.0×10^{4}	1.4×10^{6}	2.0×10^{6}	8.0×10^{6}	1.4×10^{7}	2.0×10^{7}	8.0×10^{7}	1.4×10^{8}	2.0×10^{8}	8.0×10^{8}	1.4×10^{9}
REE	1.5×10^{2}	8.3×10^{3}	2.1×10^{5}	1.5×10^{6}	6.0×10^{6}	1.1×10^{7}	1.5×10^{7}	6.0×10^{7}	1.1×10^{8}	1.5×10^{8}	6.0×10^{8}	1.1×10^{9}
V	1.0×10^{2}	9.7×10^{3}	8.8×10^{4}	1.0×10^{6}	4.0×10^{6}	7.0×10^{6}	1.0×10^{7}	4.0×10^{7}	7.0×10^{7}	1.0×10^{8}	4.0×10^{8}	7.0×10^{8}
Zn	6.5×10^{1}	8.8×10^{5}	1.2×10^{7}	6.5×10^{5}	2.6×10^{6}	4.6×10^{6}	6.5×10^{6}	2.6×10^{7}	4.6×10^{7}	6.5×10^{7}	2.6×10^{8}	4.6×10^{8}
Ni	5.5×10^{1}	2.3×10^{5}	2.5×10^{6}	5.5×10^{5}	2.2×10^{6}	3.9×10^{6}	5.5×10^{6}	2.2×10^{7}	3.9×10^{7}	5.5×10^{7}	2.2×10^{8}	3.9×10^{8}
Cu	2.5×10^{1}	1.8×10^{6}	2.0×10^{7}	2.5×10^{5}	1.0×10^{6}	1.8×10^{6}	2.5×10^{6}	1.0×10^{7}	1.8×10^{7}	2.5×10^{7}	1.0×10^{8}	1.8×10^{8}
Co	2.4×10^{1}	8.8×10^{3}	1.4×10^{5}	2.4×10^{5}	9.6×10^{5}	1.7×10^{6}	2.4×10^{6}	9.6×10^{6}	1.7×10^{7}	2.4×10^{7}	9.6×10^{7}	1.7×10^{8}
Nb	1.9×10^{1}	8.2×10^{3}	7.8×10^{4}	1.9×10^{5}	7.6×10^{5}	1.3×10^{6}	1.9×10^{6}	7.6×10^{6}	1.3×10^{7}	1.9×10^{7}	7.6×10^{7}	1.3×10^{8}
Li	1.8×10^{1}	2.0×10^{3}	8.8×10^{4}	1.8×10^{5}	7.2×10^{5}	1.3×10^{6}	1.8×10^{6}	7.2×10^{6}	1.3×10^{7}	1.8×10^{7}	7.2×10^{7}	1.3×10^{8}
Ga	1.5×10^{1}	1.6×10^{1}	3.7×10^{2}	1.5×10^{5}	6.0×10^{5}	1.1×10^{6}	1.5×10^{6}	6.0×10^{6}	1.1×10^{7}	1.5×10^{7}	6.0×10^{7}	1.1×10^{8}
Pb	1.5×10^{1}	1.6×10^{6}	4.6×10^{6}	1.5×10^{5}	6.0×10^{5}	1.1×10^{6}	1.5×10^{6}	6.0×10^{6}	1.1×10^{7}	1.5×10^{7}	6.0×10^{7}	1.1×10^{8}
Be	2.4×10^{0}	1.9×10^{2}	2.4×10^{2}	2.4×10^{4}	9.6×10^{4}	1.7×10^{5}	2.4×10^{5}	9.6×10^{5}	1.7×10^{6}	2.4×10^{6}	9.6×10^{6}	1.7×10^{7}
Sn	2.3×10^{0}	4.3×10^{4}	3.0×10^{5}	4.3×10^{4}	9.2×10^{4}	1.6×10^{5}	2.3×10^{5}	9.2×10^{5}	1.6×10^{6}	2.3×10^{6}	9.2×10^{6}	1.6×10^{7}
As	1.7×10^{0}	6.9×10^{3}	4.0×10^{4}	1.7×10^{4}	6.8×10^{4}	1.2×10^{5}	1.7×10^{5}	6.8×10^{5}	1.2×10^{6}	1.7×10^{6}	6.8×10^{6}	1.2×10^{7}
Ge	1.4×10^{0}	3.0×10^{1}	1.3×10^{2}	1.4×10^{4}	5.6×10^{4}	9.8×10^{4}	1.4×10^{5}	5.6×10^{5}	9.8×10^{5}	1.4×10^{6}	5.6×10^{6}	9.8×10^{6}
Ta	1.1×10^{0}	8.8×10^{2}	1.9×10^{3}	1.1×10^{4}	4.4×10^{4}	7.7×10^{4}	1.1×10^{5}	4.4×10^{5}	7.7×10^{5}	1.1×10^{6}	4.4×10^{6}	7.7×10^{6}
Mo	1.1×10^{0}	2.0×10^{4}	2.9×10^{5}	1.1×10^{4}	4.4×10^{4}	7.7×10^{4}	1.1×10^{5}	4.4×10^{5}	7.7×10^{5}	1.1×10^{6}	4.4×10^{6}	7.7×10^{6}
W	1.0×10^{0}	N/A	8.2×10^{4}	1.0×10^{4}	4.0×10^{4}	7.0×10^{4}	1.0×10^{5}	4.0×10^{5}	7.0×10^{5}	1.0×10^{6}	4.0×10^{6}	7.0×10^{6}
Sb	3.0×10^{-1}	2.6×10^{4}	1.3×10^{5}	3.0×10^{3}	1.2×10^{4}	2.1×10^{4}	3.0×10^{4}	1.2×10^{5}	2.1×10^{5}	3.0×10^{5}	1.2×10^{6}	2.1×10^{6}
Bi	8.5×10^{-2}	1.7×10^{3}	2.0×10^{4}	8.5×10^{2}	3.4×10^{3}	6.0×10^{3}	8.5×10^{3}	3.4×10^{4}	6.0×10^{4}	8.5×10^{4}	3.4×10^{5}	6.0×10^{5}
Ag	7.0×10^{-2}	6.9×10^{3}	2.6×10^{4}	7.0×10^{2}	2.8×10^{3}	4.9×10^{3}	7.0×10^{3}	2.8×10^{4}	4.9×10^{4}	7.0×10^{4}	2.8×10^{5}	4.9×10^{5}
In	5.0×10^{-2}	1.2×10^{2}	8.6×10^{2}	5.0×10^{2}	2.0×10^{3}	3.5×10^{3}	5.0×10^{3}	2.0×10^{4}	3.5×10^{4}	5.0×10^{4}	2.0×10^{5}	3.5×10^{5}
PGE	1.3×10^{-3}	1.4×10^{2}	4.1×10^{2}	1.3×10^{1}	5.2×10^{1}	9.1×10^{1}	1.3×10^{2}	5.2×10^{2}	9.1×10^{2}	1.3×10^{3}	5.2×10^{3}	9.1×10^{3}
Te	5.0×10^{-3}	N/A	5.2×10^{2}	5.0×10^{1}	2.0×10^{2}	3.5×10^{2}	5.0×10^{2}	2.0×10^{3}	3.5×10^{3}	5.0×10^{3}	2.0×10^{4}	3.5×10^{4}
Au	2.5×10^{-3}	1.8×10^{2}	3.2×10^{3}	2.5×10^{1}	1.0×10^{2}	1.8×10^{2}	2.5×10^{2}	1.0×10^{3}	1.8×10^{3}	2.5×10^{3}	1.0×10^{4}	1.8×10^{4}
Re	4.0×10^{-4}	4.2×10^{1}	5.4×10^{1}	4.0×10^{0}	1.6×10^{1}	2.8×10^{1}	4.0×10^{1}	1.6×10^{2}	2.8×10^{2}	4.0×10^{2}	1.6×10^{3}	2.8×10^{3}

Table 1. Crustal abundances (Clarkes in ppm), thresholds and ranges of "large", "giant" and "supergiant" accumulations of elements (in metric tons). Modified from Laznicka (2014), with values for Mg, Sr, Rb, and Hf calculated from crustal abundance values in Wedepohl (1995). We have removed Cr, Cs, Hf, Rb, Sc, U, and Y because available data do not allow calculation of global Fortier values. Heavy black outlines show giant deposits, and heavy red outlines show supergiant deposits of Singer (1995). Blue cells show one U.S. Fortier, yellow cells show one global Fortier, and for Re, U.S. and global Fortier values are similar, so the cell is green.

We do not know of any global commodity consumption data that are updated annually, but U.S. Geological Survey (USGS) Mineral Commodity Summary reports provide global production values (e.g., U.S. Geological Survey 2022), so we define a global Fortier as the 5-year average of annual global production of a commodity (Table 1). In this case, we assume that global production is approximately equal to global consumption. We recognize that there are flaws in this assumption, and weaknesses in the underlying data, but this currently appears to be the best metric to capture global need through time.

3 Discussion

3.1 Comparison of size-based classifications

As described above, the crustal concentration method of determining large, giant, and supergiant deposits, and the statistical method of determining giant and supergiant deposits both have merits (Singer 1995; Laznicka 2014). Table 1 presents the Laznicka (2014) endowments of large, giant, and supergiant deposits for commodities that are on the 2022 final list of critical minerals for the United States. (Applegate 2022), or recently were on that list (Petty 2018), plus Ag, Au, Cu, and Pb. Each size category is subdivided into three bins of equal size that are designated "Low", "Mid", and "High".

Superimposed on Table 1, we show the threshold values for giant deposits (the largest 10% of known deposits) of Ag, Au, Cu, Pb, and Zn as defined by Singer (1995), and we also show threshold values for his supergiant deposits (the largest 1% of known deposits). This comparison shows that all "giant"

deposits from Singer (1995) fall within the "large" deposits of Laznicka (2014). Furthermore, most of the "supergiant" deposits of Singer (1995) have threshold values that fall within the range of "giant" deposits of Laznicka (2014); only for Cu is there consensus about what constitutes a supergiant deposit.

On the one hand, this comparison demonstrates that confusion about what constitutes large, giant, and supergiant deposits is fully justified. On the other hand, this graphically demonstrates that the two approaches produce different results. For Ag, Au, and Zn, the giant and supergiant deposits of Singer (1995) vary in size by one order of magnitude, but for Pb the variation is less than one order of magnitude, and for Cu it is more than one order of magnitude. Geological, technical, economical, environmental, social, and governmental factors are significant controls on which mineral deposits will be mined, which then controls the statistical classification of deposits.

3.2 Comparison of U.S. and global Fortier values

Global Fortier values range from 1.3 (Re) to 44 (Li) times greater than U.S. Fortier values, with a median value of 11 times for commodities where both values can be determined. The relative change in values reflects the fact that U.S. Fortier values predominantly reflect the needs of the United States for manufacturing and other sectors, and global Fortier values come closer to approximating the total needs of humankind.

3.3 The needs of humankind versus endowment

The highlighted values in Table 1 provide insights into consumption and production of commodities versus deposit size. Overall, 39% and 16% of the commodities with available data have U.S. Fortier values that exceed the threshold values of Laznicka's (2014) large and giant deposits, respectively, and 56%, 38%, and 3% of the commodities have global Fortier values that exceed the threshold values of Laznicka's (2014) large, giant, and supergiant deposits, respectively. Put another way, for more than half of the commodities in Table 1, humankind is consuming the equivalent endowment of at least one large deposit every year. This consumption must be replaced by increased reserves at existing mines, and by adding new mines to the global supply chain.

Much of the conversation about humankind's ability to mine resources in sufficient quantity can be summarized in two ways: (1) increasing demand compared to known resources or reserves indicates future inability to meet demand, or (2) history shows that production rises to meet demand, and there are much larger resources in Earth than are quantified in formal resource and reserve calculations (e.g., Arndt et al. 2017; Schipper et al. 2018; Jowitt et al. 2020, and references therein). We recognize the strength of these approaches and their importance in assessing whether production of Earth resources will continue to meet the needs of humankind.

In addition to these approaches, evaluation of Table 1 suggests another possible approach. Some commodities—Al, Be, Co, Ga, Ge, Li, Mg, Nb, REE, Sr, Ta, Ti, and V—have U.S. and global Fortier values that are less than Laznicka's (2014) threshold values for large deposits. For these commodities, demand from humankind may still be small enough that Earth resources can meet these demands without significant risk. However, the inclusion of REE in this group underscores a limitation of this approach, because REE are not geochemically rare, but economically viable deposits of REE are rare (Van Gosen et al. 2018). Furthermore, some commodities are byproducts, so their availability is controlled by technological and economic factors that differ markedly from the factors that control production of product commodities.

Some commodities have global Fortier values that fall in Laznicka's (2014) range of large deposits. For these commodities—As, In, Mn, Ni, W, and Zr—consideration of the rate of opening of new mines, and the rate of expansion of reserves at existing mines may provide insight into the likelihood of supply shortages. For example, Mudd and Jowitt (2022) concluded that current Ni resources and reserves can meet the current need for several decades, providing that those materials can be mined. In some cases, such as As, the limitations may not be mining, but rather processing or recovery from waste streams, because As is recovered from smelting operations, and many of those operations in the United States and Europe have closed due to environmental concerns. Arsenic-alkali residue is a hazardous waste produced by antimony smelting operations that is increasing in China at the rate of approximately 5,000 metric tons per year (Long et al. 2020), so recovery of As from waste streams in China and elsewhere might supply any future growth in need.

The base and precious metals considered by Singer (1995)—Ag, Au, Cu, Pb, and Zn—have global Fortier values that exceed the endowments of his giant deposits. For Cu and Zn, global Fortier values are slightly less than the metal content of his supergiant deposits; for Pb and Ag, global Fortier values are approximately equal to the metal content of his supergiant deposits; and for Au, the global Fortier value is greater than the metal content of his supergiant deposits (Table 1). In other words, to a first approximation, humankind is currently consuming approximately one supergiant deposit of these commodities every year. By analogy, we infer that other commodities whose global Fortier values lie within Laznicka's (2014) giant deposit range—Bi, Mo, PGE, Sb, Re, REE, Sn, and Te—are also being produced at a rate that is equivalent to the endowment of one of the largest 1-10% of all deposits for each commodity.

Production can come from primary production from existing and new mines, and secondary

production from recycling. In a world where increasing environmental, social, and governmental factors make it more difficult to open new mines and expand existing mines (e.g., Jowitt et al. 2020), and where new discoveries are increasingly coming from deeper deposits (e.g., Arndt et al. 2017), is it reasonable to expect that the mining industry can keep pace with increasing needs for critical minerals? This question is essentially a practical one, but we know of no publicly available 21st century databases that would allow us to quantitatively address this question. Specifically, there is a need for (1) statistical classifications of critical minerals from global producing orebodies into giant and supergiant deposits, (2) commodity-specific grade-tonnage plots from producing deposits worldwide, (3) quantitative data on the time that it takes to go from discovery to production in the 21st century, and (4) the change in failure rate through time (perhaps averaged over 10 or 20 year increments) to achieve production due to environmental, social, and governmental factors.

4 Conclusions

Records of national and global consumption of commodities can be averaged over five years to derive U.S. and global Fortier values. Comparison of Fortier values to size classifications based on the endowment of mineral deposits (Laznicka 2014) might suggest that some critical minerals—Al, Be, Co, Ga, Ge, Li, Mg, Nb, REE, Sr, Ta, Ti, and V—are sufficiently abundant that their deposits can provide reliable supplies for the future. However, this does not take into consideration the distinction between economic mineral deposits and crustal abundance, nor does it consider the complications of byproduct critical minerals. For other commodities whose global Fortier values fall within the range of Laznicka's (2014) large deposits—As, In, Mn, Ni, W, and Zr—consideration of the rate of opening of new mines, and the rate of expansion of reserves at existing mines may provide insight into the likelihood of supply shortages. Global Fortier values for Ag, Au, Cu, Pb, and Zn indicate that humankind is consuming these commodities in quantities that are approximately equivalent to the endowment in supergiant deposits: the largest 1% of deposits for these commodities on Earth (Singer 1995). It is not known whether the global mining industry can keep pace with this demand. By analogy, other critical minerals—Bi, Mo, PGE, Sb, Re, REE, Sn, and Te—might also be difficult for the mining industry to produce at rates that are commensurate with increasing demand. We conclude that this is a cautionary tale, but more fit-for-purpose granular data are needed to critically compare supply and demand.

Acknowledgements

We thank the current and former members of the U.S. Geological Survey's mineral deposit database project (USMIN) for many helpful discussions that have helped develop the ideas presented herein. We thank Eric Anderson and Katharina Pfaff for thoughtful reviews that helped improve this manuscript. Any use of trade, firm, or product names is for descriptive purposes only and does not imply endorsement by the U.S. Government.

References

Applegate JD (2022) 2022 Final list of critical minerals. Federal Register 87:10381-10382.

Arndt NT, Fontboté L, Hedenquist JW, Kesler SE, Thompson JFH, Wood DG (2017) Future global mineral resources. Geochemical Perspectives 6:1-171. doi: 10.7185/geochempersp.6.1.

International Energy Agency (2021) The role of critical minerals in clean energy transitions. https://www.iea.org/reports/the-role-of-critical-minerals-in-clean-energy-transitions. Accessed 22 January 2022

Jowitt SM, Mudd GM, Thompson JFH (2020) Future availability of non-renewable metal resources and the influence of environmental, social, and governance conflicts on metal production. Communications Earth & Environment 1:13. doi: 10.1038/s43247-020-0011-0.

Laznicka P (2014) Giant metallic deposits—A century of progress. Ore Geology Reviews 62:259-314. doi: http://dx.doi.org/10.1016/j.oregeorev.2014.03.002.

Long H, Zheng Y-j, Peng Y-l, He H-b (2020) Recovery of alkali, selenium and arsenic from antimony smelting arsenic-alkali residue. Journal of Cleaner Production 251:119673. doi: https://doi.org/10.1016/j.jclepro.2019.119673.

Mudd GM, Jowitt SM (2022) The new century for nickel resources, reserves, and mining: Reassessing the sustainability of the devil's metal. Economic Geology 117:1961-1983. doi: 10.5382/econgeo.4950.

Petty TR (2018) Final list of critical minerals 2018. Federal Register 83:23295-23296.

Schipper BW, Lin H-C, Meloni MA, Wansleeben K, Heijungs R, van der Voet E (2018) Estimating global copper demand until 2100 with regression and stock dynamics. Resources, Conservation and Recycling 132:28-36. doi: https://doi.org/10.1016/j.resconrec.2018.01.004.

Singer DA (1995) World class base and precious metal deposits; a quantitative analysis. Economic Geology 90:88-104. doi: 10.2113/gsecongeo.90.1.88.

U.S. Geological Survey (2022) Mineral commodity summaries 2022. Reston, VA, pp 202.

Van Gosen BS, Verplanck PL, Seal RR, II, Long KR, Gambogi J (2018) Chapter O. Rare-earth elements In: Schulz KJ, DeYoung JH, Jr., Seal RR, II, Bradley DC (eds) Critical mineral resources of the United States—Economic and environmental geology and prospects for future supply. U.S. Geological Survey Professional Paper 1802, Reston, Virginia, pp O1-O31.

Wedepohl HK (1995) The composition of the continental crust. Geochimica et Cosmochimica Acta 59:1217-1232. doi: https://doi.org/10.1016/0016-7037(95)00038-2.

Exploration of indium in sulfidic mine waste and acid mine drainage environments

Olivia Mejías[1], Laura Jackson[1], Anita Parbhakar-Fox[1]
[1]W.H. Bryan Mining & Geology Research Centre, Sustainable Minerals Institute, The University of Queensland, Australia

Abstract. Indium (In) is a critical metal essential for the transition to a low-carbon economy including its use in solar panels. However, there is a significant knowledge gap regarding cycling of indium in mine waste environments. This study aims to understand the mobility of indium in two different geological mine waste environments as an essential first step toward designing a remining process. Core, waste rock, acid mine drainage (AMD)-impacted waters and sediment samples were collected from Mt Morgan (Au-Cu VHMS) and Baal Gammon (Sn granite-related) historic/abandoned mines and subjected to geochemical and mineralogical investigations. Preliminary results suggest that core and waste rock from Baal Gammon contain above 500 ppm In, with sphalerite the main endowed In-bearing mineral (up to 3,776 ppm In). High concentrations, up to 73 µm/L In, were measured in AMD waters along with fluoride (38 to 120 mg/L). In contrast, waste rock and AMD water samples from Mt Morgan reported a maximum of 3.53 ppm and up to 5 µm/L In (with elevated chloride) respectively. This study found that indium is significantly enriched in the sampled Sn-granite mine waste and that pH and fluoride can potentially control indium mobility in AMD waters.

1 Introduction

It is estimated that over 3 billion tonnes of critical metals will be needed to provide green energy to reduce the temperature increase resulting from global warming (Hund et al. 2020). A combination of growing global demand for critical metals paired with decreasing ore grades, is anticipated to results in higher volumes of mine waste over next decades (Jowitt et al. 2018; Watari et al. 2020). For example, a current study has estimated that the global community will generate 10 billion m^3 of new tailings per annum that will require storage in existing or planned facilities (Franks et al. 2021). Increasing volumes of mine waste increases the associated risks such as the formation of AMD and geotechnical failure events. To date, consequences from disasters associated with poor mine waste management have included 3,000 known deaths, over 4,000 km of waterways damaged, and >275 billion litres of waste spilt into natural environments. Mine waste valorisation offers a new solution to safely managing mine waste, enabling the mineral industry to reduce risk and supplement critical metal production to sustain future societies (Nwaila et al. 2021).

Indium is an essential component of solar panels. However, its current supply is dependent on zinc production (i.e., it is a by-product). Thus, indium has been declared a critical metal in Australia, and in at least six other mining countries. At least 230,000 tonnes of indium will be needed worldwide to ensure 14,000 GW of solar PV by 2050. Thus, demand for indium is projected to increase by 231 % by 2050. Despite the anticipated high demand for indium, there remains a knowledge gap regarding the geochemistry, mineralogy and cycling of indium in mine waste environments.

Economic concentrations of indium mineralisation are found in various types of deposits, including volcanogenic massive sulfide (VHMS), sediment-hosted base-metal, epithermal, skarn, porphyry, and granite-related deposits (Schwarz-Schampera 2014).

In Queensland, indium has been reported in ore and mine waste in granite-related deposits in the Herberton mineral province, NE Queensland (Lottermoser and Ashley 2006; Fox et al. 2016; Parbhakar-Fox 2020). Furthermore, slag from the VHMS Mt Morgan mine site, located in Central Queensland, reported a maximum of 26 ppm In (Parbhakar-Fox and Jackson 2022). In addition, there is estimated to be at least 3,000 Mt of waste rock, at least 1,250 million m^3 of stored tailings, and there are about 120 complexes abandoned mine sites in Queensland (The Global Tailings Portal 2019; Mudd, pers. comm. 2021; Geological Survey of Queensland 2021). Consequently, the Queensland state provides an excellent study area in which to explore the potential of indium in the context of tracking its cycling in unconventional environments. This article briefly focuses on the ore results as background and presents in-depth detail on the preliminary results of the content of indium in waste rock and AMD-impacted waters of Mt Morgan (an Au-Cu VHMS historic deposit) and Baal Gammon (a Sn granite-relate abandoned deposit).

2 Geology setting

2.1 Baal Gammon and Mt Morgan mine sites

The Mount Morgan Au-mine is located 38 km southwest of Rockhampton in the Central of Queensland (Figure 1). Over the 108-year mine life, approximately 237 t of Au, 37 t of Ag and 387,000 t of Cu were mined from both underground and open-cut operations (Edraki et al. 2005). Messenger et al. (1997) reported the deposit as an end-member class of volcanogenic massive sulfide deposits. The Devonian rhyolitic Mine Corridor Volcanics are the host rocks for Au–Cu mineralisation and are surrounded and intruded by the Devonian Mount Morgan Tonalite (Edraki et al. 2005). The main ore body (Main Pipe mineralisation) corresponded an irregular form of massive and disseminated sulfide mineralisation that transgressed stratigraphic units

but was cross-cut by a relatively unaltered tonalite stock (Messenger et al. 1997). The minerals in the ore zone included: pyrite, quartz, pyrrhotite, chalcopyrite, magnetite and sphalerite, gold, Au-tellurides, and Ag minerals. Whilst the common gangue minerals were quartz, chlorite, with minor amounts of carbonate and apatite (Edraki et al. 2005).

The Baal Gammon Sn-mine is located 70 km southwest of Cairns, in the NE of Queensland (Figure 1). It is one of the largest Sn deposit in the Herberton region, and it is also reported to be a viable source of indium and tungsten. The Baal Gammon orebody is hosted in the UNA Porphyry, a derivative of the Elizabeth Creek Granite (Fraser 1972). The UNA Porphyry sits within the metasedimentary rocks of the Silurian-Devonian Hodgkinson Formation, occurring as stockwork veins in greisenised regions of the host rock (Schwarz-Schampera and Herzing 2002). Baal Gammon has a JORC-compliant Indicated Resource of 2.77 Mt @ 1% Cu, 40 g/t Ag, 0.2% Sn and 39 g/t In (Gow et al. 2021).

Both mine sites are non-active and pose environmental risks due to large volumes of acid-forming waste rock and AMD contamination into the Dee River and Jamie Creek respectively.

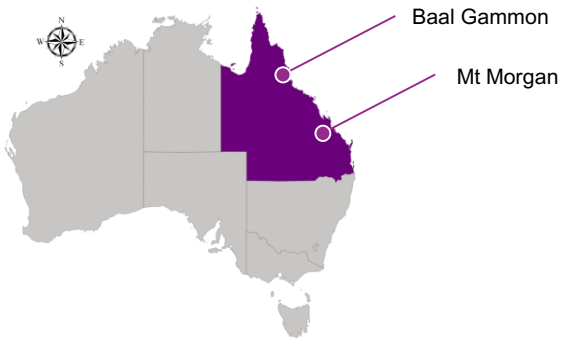

Figure 1. Location map of the mining sites.

3 Methodology

3.1 Sample collection and sample preparation

Fieldwork and sampling (Figure 2) were conducted in November 2022 and February 2023 at Mt Morgan and the Baal Gammon mine sites respectively. Hand-specimen sized waste rock samples (n=66) were selected to provide a range of lithologies from three different locations across the waste rock piles at Mt Morgan, and from one waste rock pile at Baal Gammon; additionally, a few boulders were sampled from along to the Jamie Creek (n=26).

Stream sediment and precipitates samples (n=14 Mt Morgan; n=15 Baal Gammon) were also collected upstream and downstream of the Dee River and Jamie Creek and around districts and represented background and 'mine-impacted' materials. Waste rock samples were cut, as well as a small portion of sediment and precipitates were kept for mineralogical studies. The remaining materials were used for geochemical bulk characterisation.

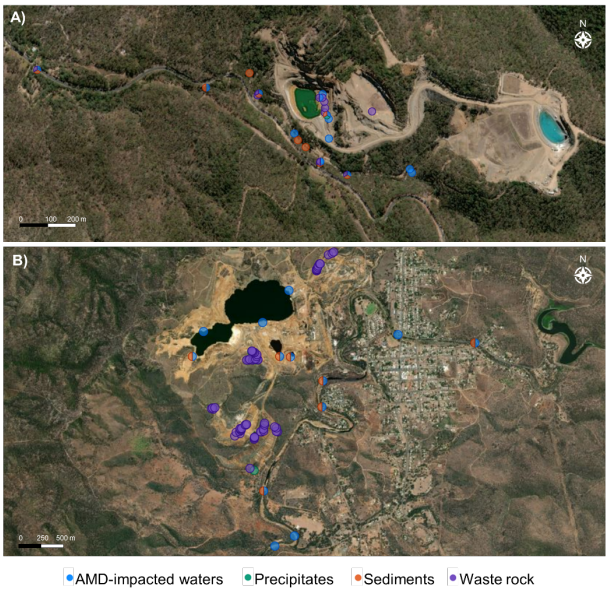

Figure 2. Plan view of AMD-impacted waters, precipitates, sediments and waste rock at Baal Gammon (A) and Mt Morgan (B).

Surface water samples (n=14 Mt Morgan; n=17 Baal Gammon) were collected around the mine sites (open pit and sumps, Figure 3) to allow for comparison of water quality upstream and downstream of the Dee River and Jamie Creek respectively (Figure 3).

Figure 3. Open pit (A and B), sumps (C and D) and AMD-impacted Dee River and Jamie Creek (E and F) sampling locations from Mt Morgan (left) and Baal Gammon (right).

Water samples were collected for analysis of major cations and anions (unfiltered), and trace metals and metalloids (0.45 µm filtered). Duplicate water samples and blanks were considered every five samples. Oxidation-reduction potential (ORP), temperature, conductivity (SPC), and pH were

measured in the field. These values were measured using a YSI ProDSS multiparameter water quality handheld meter, which was calibrated to pH 4 prior fieldwork. For water analyses, sampling equipment were rinsing prior to each sampling by deionised water.

3.2 Chemical and mineralogical analyses

The bulk elemental composition of all waste rock, sediment, and precipitate samples were assessed by four acid ICP-MS with 48 elements measured. Additionally, comparable geochemical data from a previous at Baal Gammon (Parbhakar-Fox 2020) are included here. The water samples included analysis of alkalinity, acidity, sulfate, chloride, fluoride, ionic balance, dissolved major cations (Ca, Mg, Na, K), and dissolved metals by ICP-MS.

In parallel, polished mounts representative of Baal Gammon ore (n=25) and waste rock (n=6) were prepared for mineralogical characterization to learn more about indium's hosting. The samples were characterised by handheld LIBS at the University of Chile, SEM/EDS at the University of Queensland, electron EPMA at the Queensland University of Technology, LA-ICP-MS at the University of Adelaide. These analyses enabled quantification of indium and others trace elements in sulfides and cassiterite. Whilst investigations on ore samples have concluded, ongoing work is being performed on the waste rock using Maps Mineralogy Software, Thermo Fisher Scientific. Similar analyses on polished mounts from Mt Morgan (and additional Baal Gammon) are pending.

4 Results

4.1 Waste rock chemistry and mineralogy

Waste rock from Mt Morgan reported a maximum of 3.53 ppm In (70 times higher than crustal abundance). Additionally, high concentrations of Cu (up to 6.74 %), Au (up to 6.09 ppm), Ag (up to 6.99 ppm), Re (up to 0.14 ppm), Mo (up to 388 ppm), and Te (up to 81 ppm). These samples comprise mainly massive sulfide minerals, gossan, host rocks (tonalite and porphyry), and country rocks (volcanic breccias and tuffaceous volcanics). The main sulfide is pyrite and a lesser amount pyrrhotite, chalcopyrite, and molybdenite.

Waste rock from Baal Gammon reported above 500 ppm In (10,000 times higher than crustal abundance). Additionally, high concentrations of Cu (up to 18.7 %), and Ag (up to 344 ppm). These samples comprise massive sulfide minerals dominated by arsenopyrite, pyrrhotite and chalcopyrite and a lesser amount sphalerite and stannite group (Figure 4). LA-ICP-MS results from ore samples show a maximum of 1,778 ppm In in the cleanest sphalerite, whilst a maximum of 3,776 ppm In in bulk intervals.

Waste rock from both mines show development of Fe oxides in the exterior rind of samples (Figure 5).

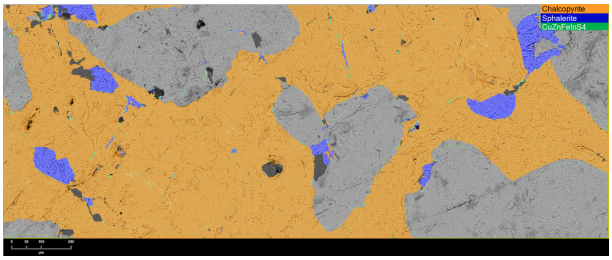

Figure 4. Backscattered electron images of waste rock sample from Baal Gammon using Maps Mineralogy Software.

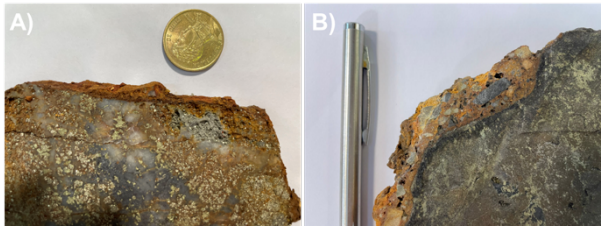

Figure 5. Waste rock samples with a secondary iron oxide rind developed on primary sulfides. A) Mt Morgan; B) Baal Gammon.

4.1 Water chemistry

Background concentrations of metals for surface waters in the Mount Morgan area are represented by a pH of 7.12, 0.02 ppm Al, 0.07 mg/L Fe, 0.53 mg/L Mn and below detection limits for In (<0.001 mg/L), Zn, Co, As, Cd. While fluoride value is 0.2 mg/L and chloride is 42 mg/L. The open pit and seepage sumps at the site contain a range of low pH values (2.79 to 3.06) and high conductivities (6,287 to 12,181 µS/cm). Metal concentrations in the open pit and sumps generally fall in a range from: 1,110 to 2,060 mg/L Al; 94.5 to 578 mg/L Fe; 67.5 to 241 mg/L Mn; 65.5 to 89.3 mg/L Cu; 28.5 to 74.3 mg/L Zn; 2.7 to 6.26 mg/L Co; 0.298 to 0.433 mg/L Cd; and <0.01 mg/L In. Furthermore, 20 to 38 mg/L fluoride; and 2 to 228 mg/L chloride.

Background concentrations of metals for surface waters in the Baal Gammon area are represented by a pH of 6.22, 0.21 ppm Al, 0.07 mg/L Fe, 0.06 mg/L Mn and below detection limits for In (<0.001 mg/L), Zn, Cd. While fluoride value is 0.5 mg/L and chloride is 4 mg/L. The open pit and seepage sumps at the site contain a range of low pH values (2.78 to 4.24) and medium conductivities (135 to 2,437 µS/cm). Metal concentrations in the open pit and sumps generally fall in a range from: 0.79 to 337 mg/L Al; 0.05 to 88.5 mg/L Fe; 0.43 to 36.6 mg/L Mn; 0.67 to 122 mg/L Cu; 0.32 to 62.7 mg/L Zn; 0.005 to 1.19 mg/L Co; 0.007 to 0.4 mg/L Cd; and 0.016 to 0.073 mg/L In. Furthermore, 38 to 120 mg/L fluoride; (Figure 6) and 7 to 9 mg/L chloride.

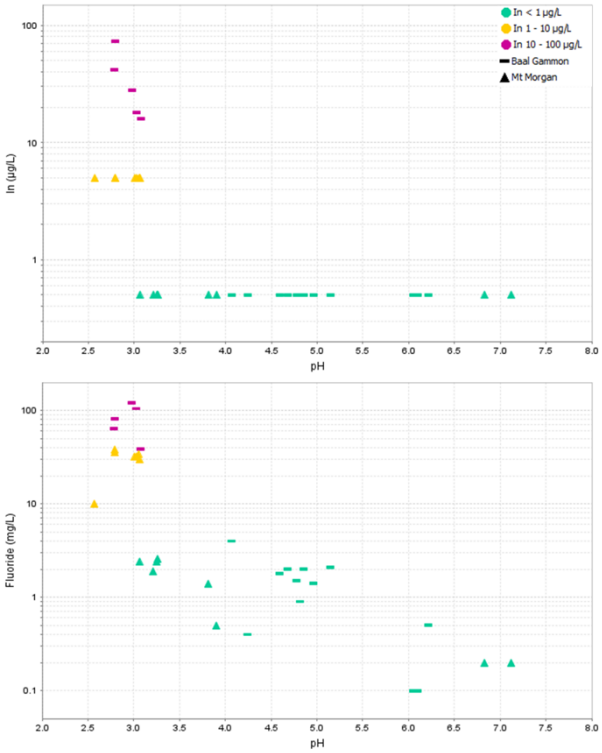

Figure 6. Variations of indium (µg/L) versus contents of pH, and fluoride (mg/L).

5 Conclusions

The highest indium content is reported in waste rock (>500 ppm In) and mine waters (up to 73 µg/L) at the Baal Gammon mine (a granite-related deposit), while low concentrations (3.53 ppm and up to 5 µg/L) were measured at the Mt Morgan mine (Au-Cu VHMS deposit).

Based on this, Mt Morgan is considered an indium-poor system. Therefore, not all VHMS are indium endowed, rather there is a decrease in indium towards Au-rich VHMS. The highest value of indium in mine waters correlate with high content of fluoride and low content of chloride. This observation has been reported in hydrothermal ore-forming systems (i.e., F-rich fluids are commonly related to skarn and greisen-type deposits and Cl-rich fluids with VHMS) showing that the ore geology has an important factor in the indium endowment in the related solid and aqueous mine waste materials. Factors including pH (< 2.8) have a main control of increasing content of dissolved indium, however, the same trend is not observed with the ORP results. Understanding the behaviour of indium (based on an understanding of its mineralogy and geochemistry) in mine waste systems may help identify optimum conditions for its extraction using hydrometallurgical methods, as part of a method to rehabilitate these AMD-forming mine sites.

Acknowledgements

The authors acknowledge the Queensland Department of Resources for supporting this research and allowing access to the Mt Morgan and Baal Gammon sites for sample collection. Thanks are extended to Helen Degeling, Christopher Hansen, Courteney Dhnaram, Sam Pegg, and Mark Eaton. Additional thanks to Kam Bhowany and Thomas Jones for supporting fieldwork and sample preparation respectively. Furthermore, the Thermo Fisher Scientific team for supporting mineral characterization using Maps Mineralogy Software.

References

Edraki M, Golding SD, Baublys KA, Lawrence MG (2005) Hydrochemistry, mineralogy and sulfur isotope geochemistry of acid mine drainage at the Mt. Morgan mine environment, Queensland, Australia. Applied Geochemistry 20:789-805. https://doi.org/10.1016/j.apgeochem.2004.11.004

Fox N, Parbhakar-fox A, Lottermoser B (2016) Critical and Deleterioys Metal Deportment in Sulfidic Waste Rocks, Baal Gammon, North, Queensland. The Third AusIMM International Geometallurgy Conference. Perth, Australia, pp 173-182.

Franks DM, Stringer M, Torres-Cruz LA, Baker E, Valenta R, Thygesen K, Matthews A, Howchin J, Barrie S (2021) Tailings facility disclosures reveal stability risks. Sci Rep 11:5353. https://doi.org/10.1038/s41598-021-84897-0

Gow P, Fox N, Aivazpourporgou S, McGovern J, Valenta R (2021) NE Queensland Mineral Deposit Atlas - Chapter 4 Baal Gammon & Gift. Report, Brisbane, Sustainable Minerals Institute. Sustainable Minerals Institute, pp 25.

Hund K, Porta DL, Fabregas TP, Laing T, Drexhage J (2020) Minerals for Climate Action: The Mineral Intensity of the Clean Energy Transition. The World Bank

Jowitt SM, Mudd GM, Werner TT, Weng Z, Barkoff DW, McCaffrey D (2018) The Critical Metals: An Overview and Opportunities and Concerns for the Future. Metals, Minerals, and Society:25-38. https://doi.org/10.5382/sp.21.02

Lottermoser BG, Ashley PM (2006) Mobility and retention of trace elements in hardpan-cemented cassiterite tailings, north Queensland, Australia. Environmental Geology 50:835-846. https://doi.org/10.1007/s00254-006-0255-8

Messenger PR, Golding SD, Taube A (1997) Volcanic setting of the Mt Morgan Au-Cu deposit, central Queensland: implications for ore genesis. Tectonics and Metallogenesis of the New England Orogen Geological Society of Australia Special Publication 19:109-127.

Nwaila GT, Ghorbani Y, Zhang SE, Frimmel HE, Leon C, Tolmay K, Rose DH, Nwaila PC, Bourdeau JE (2021) Valorisation of mine waste - Part I : Characteristics of , and sampling methodology for , consolidated mineralised tailings by using Witwatersrand gold mines (South Africa) as an example. Journal of Environmental Management 295:113013-113013. https://doi.org/10.1016/j.jenvman.2021.113013

Parbhakar-Fox A (2020) Cobalt and other critical metals in tailings of major mineral deposits in north Queensland: Baal Gammon mine. Report to Government. Sustainable Minerals Institute, University of Queensland, pp 41

Parbhakar-Fox A, Jackson L (2022) Cobalt and other critical metals in tailings of major mineral deposits in north Queensland: Mt Morgan slag study. Report to Government. Sustainable Minerals Institute, University of Queensland, pp 39.

Schwarz-Schampera U (2014) Indium In: Gunn G (ed) Critical Metals Handbook

Watari T, Nansai K, Nakajima K (2020) Review of critical metal dynamics to 2050 for 48 elements. Resources, Conservation and Recycling 155. https://doi.org/10.1016/j.resconrec.2019.104669

Tracking cobalt deportment from primary ore to copper tailings and determining reprocessing potential

Loren Nicholls[1], Elaine Wightman[1], Catherine Evans[1], Lachlan Casey[2], Anita Parbhakar-Fox[1]
[1]Sustainable Minerals Institute, University of Queensland, Australia
[2]Centre of Microscopy and Microanalysis, University of Queensland, Australia

Abstract. The high demand for cobalt in the global energy transition is driving the mining industry to explore alternative and more ethical cobalt sources. Reprocessing of copper flotation tailings is a potential circular economy approach to managing mine waste and supplementing global critical minerals supply. Tracking cobalt deportment from primary ore, through the concentrator and into tailings is a critical first step in assessing the valorisation potential. The mineralogy, particle liberation properties and mineral associations strongly influence the recoverability of cobalt from tailings. This research integrated Micro-X-Ray Fluorescence (μXRF), chemical assay, Mineral Liberation Analysis (MLA) and Advanced Mineral Identification and Characterization System (AMICS) to geometallurgically track cobalt deportment throughout an operating copper flotation circuit and into the fresh tailings. Cobalt was found to be hosted in several mineral phases, including cobaltiferous sulphides and pyrite. Detailed geometallurgical characterisation and deportment studies will assist in identifying mineral processing pathways to recovering value from copper tailings.

1 Introduction

As the global market transitions to more sustainable and green-energy technologies, the demand for critical metals for development is rapidly increasing (Valenta et al. 2023). Cobalt demand is predicted to outpace supply by 2030 with between 235 and 430 kilotonnes required for predominantly the EV lithium-ion battery market, as well as use in superalloys, catalysts, hard metals, permanent magnets and pigments (Hitzman et al. 2017; Fu et al. 2020). Reprocessing of sulfidic tailings for cobalt could supplement the global supply, while also providing an alternative mine waste management approach that incorporates circular economy principles.

The first step in assessing valorisation potential of an ore is to understand cobalt deportment across the mineral processing flow sheet. Given the complexity of cobalt-bearing ores, geometallurgical characterisation is key to recognising cobalt hosts, chemical associations, liberation characteristics and predicting implications for recovery (Dehaine et al. 2021).

In copper sulfide deposits, cobalt tends to occur as a companion metal within cobalt-sulfides and copper-cobalt minerals, or as inclusions in copper-iron sulfides such as chalcopyrite (Mudd et al. 2013). Cobalt can also occur in pyrite as micro-inclusions, as solid-solution in the matrix or as a zonation feature.

Copper flotation circuits are typically optimised to depress pyrite, rejecting it to the tailings stream. An accumulation of cobalt-rich pyrite in the tailings makes for a potential secondary resource for cobalt.

Pyrite is readily recovered by froth flotation under the appropriate conditions and this behaviour may be utilised to generate a pyrite concentrate that can be sold as a cobalt-bearing product for pyrometallurgical or hydrometallurgical extraction and refining.

The case study site for this research is an epigenetic sedimentary copper sulfide deposit that has associated cobalt mineralisation. Trace cobalt minerals have been identified, including carrollite ($CuCo_2S$), linnaeite ($Co^{+2}Co^{+3}{}_2S_4$), cobaltite (CoAsS), siegenite ($(Ni, Co)_3S_4$) and pyrite (FeS_2). Copper and silver are recoverable commodities, but cobalt is yet to be exploited. Understanding cobalt deportment throughout the concentrator is critical to developing a flow sheet to optimise recovery.

A series of plant surveys were conducted over five days to investigate cobalt deportment in the feed, final concentrate and final tail (Fig. 1). Samples of the final tail were then floated in the laboratory to produce a sulfide mineral (mainly pyrite) concentrate and the mineralogy of the concentrate and tail was assessed for mineral liberation and cobalt recovery.

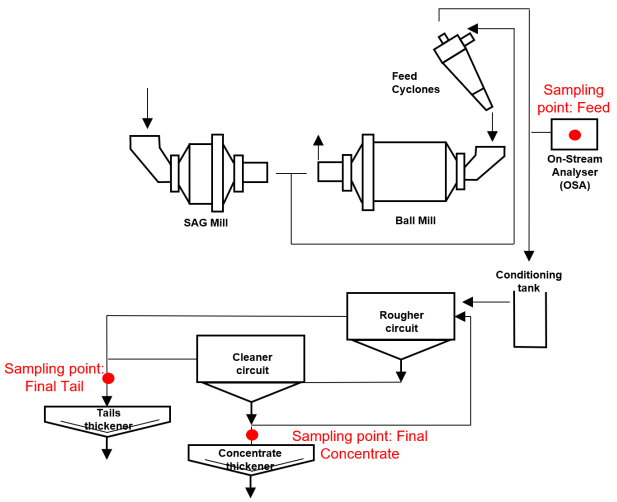

Fig. 1 Simplified schematic of the copper concentrator with plant survey sampling points highlighted.

2 Methodology

2.1 Micro-X-Ray Fluorescence of primary ore

Six (6) slabs of quarter core from the primary ore deposit were scanned using an iXRF ATLAS X XFM (X-ray fluorescence Microscope) at the Centre for Microscopy and Microanalysis, University of Queensland, with a 50W Mo source and 25um polycapillary optic (XOS FlexBeam) and 2x Ketek H150 detectors. Scanning occurred under atmospheric conditions at 40 kV and 200 µA, at 25 ms dwell, 0.5 ms risetime and pixel sizes from 40 to 60 µm. Scans were processed in the GeoPIXE package (CSIRO) via dynamic analysis, assuming a pyrite matrix (Ryan 2001). GeoPIXE generates RGB and spectral intensity images that map elemental distribution and provide qualitative and semi-quantitative data on chemical associations and mineralogy. The overlapping Fe Kβ/Co Kα peaks were excluded from analysis, with abundance calculated only from the Fe Kα and Co Kβ peaks.

2.2 Plant Survey

Representative samples from the flotation feed, final concentrate and final tailings streams of 5 different blend feeds (15 samples in total, ~1.5 kg each) were collected across the plant over 5 days. Samples were weighed (wet), filtered and dried (60 ^{0}C, ~6 hours), weighed (dry), representatively split and bagged. In each plant survey a second tailings sample was split, weighed (wet), stirred to suspend all solids and used for batch flotation tests.

Initially, unsized samples were analysed using the ME MS-61 method (4 acid digest, ICP MS analysis) at ALS Global Brisbane and Mineral Liberation Analysis (MLA) was conducted at the University of Queensland.

Sized fractions included sieved fractions +75, +53, +38 and Cyclosizer C1, C2, C3, C4, C5 and -C5. These fractions were composited into +38 µm (+75, +53, +38), C3 (C1, C2, C3), C5 (C4, C5) and -C5. These composites were also analysed by the same methods at ALS and MLA.

2.3 Batch float tests

Batch flotation laboratory trials were undertaken on four of the tailings samples to produce a pyrite concentrate (Fig. 2) and a desulfurised residual waste product.

The following flotation conditions and reagents were used: Float time: 8 min, Impeller Speed (RPM): 400, pH: 8, adjusted from 11, Frother: Methyl Isobutyl Carbinol (MIBC), Activator: 50g/t CuSO4, Collector: 25g/t Sodium Isobutyl Xanthate (SIBX).

Sized and unsized concentrate and tailings samples were sent for assay using ME MS-61 and to the University of Queensland for MLA.

Fig. 2 Images of the batch float pyrite concentrates floating in float cells from the copper concentrator tailings.

2.4 Advanced Mineral Identification and Characterization System (AMICS)

A Hitachi SU3900 scanning electron microscope (SEM) with a XFlash 6160 Bruker energy dispersive spectroscopy (EDS) detector was used to scan the MLA mounts and generate back scattered electron (BSE) images and X-ray spectra. These data were analysed using the Advanced Mineral Identification and Characterization System (AMICS) software to produce elemental and mineral distribution maps (Bruker 2022).

3 Cobalt distribution in the primary ore

Cobalt occurred in several different phases within the primary deposit. Cobaltiferous pyrite was evident as fine-grained infill around early euhedral pyrites (Fig. 3a). This phase appeared to be deposited post-early pyrite, syn-copper mineralisation and remobilised during supergene enrichment. Cobalt also occurred as carrollite locked in pyrite. A cobaltite-pyrite solid solution was also identified where cobalt was unrelated to copper mineralisation (Fig. 3b).

Variable mineral associations and grain sizes of primary cobalt sulphide hosts inform geometallurgical domaining and cobalt distribution across the flow sheet. Fine-grained cobaltiferous pyrite that is intimately spatially associated with copper minerals will likely deport to the concentrate, whereas more massive cobaltite-pyrite is expected to be rejected to the tailings if the pyrite was sufficiently suppressed during flotation.

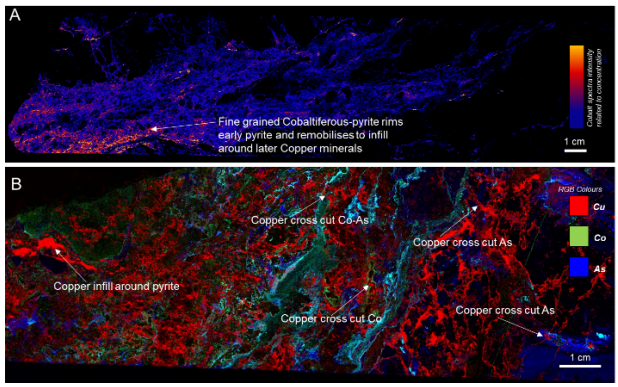

Fig. 3 µXRF images (GeoPIXE) showing examples of cobalt distribution in ¼ core samples of primary ore: A) Spectral intensity image of cobalt rims around early stage pyrite grains and remobilised in copper mineralisation event to infill copper-sulfides, B) Co-As-pyrite solid solution differentiated from Cu-mineralisation event.

4 Cobalt deportment in the concentrator

Four cobalt-bearing sulphide minerals were identified in the plant survey samples: cobaltite, carrollite, alloclasite ((Co,Fe)AsS) and pyrite. MLA modal mineralogy of the final concentrate reported between 33 % and 55 % copper minerals and 33 % to 56 % pyrite (Fig. 4). Copper mineral recoveries were excellent (>80 %), while pyrite recoveries were up to 38 %. Cobalt recovery in the final concentrate was low at approximately 20 % and cobalt sulfides had varying recoveries, indicating poor floatability under the current flotation conditions. The majority of the cobalt was lost to the tailings and may potentially be recovered through reprocessing.

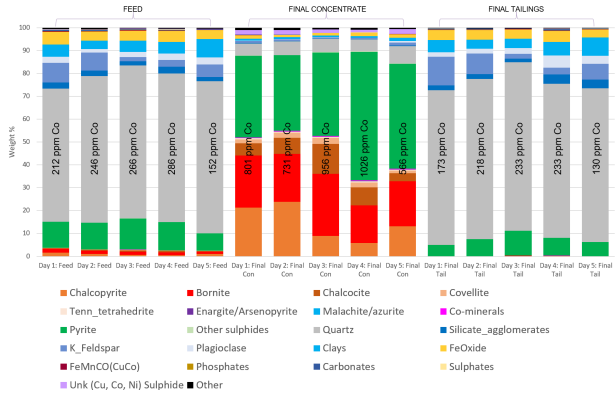

Fig. 4 Unsized modal mineralogy from MLA of the plant survey samples with cobalt assay (mass balanced) data.

In the batch flotation tests, the concentrate was dominated by pyrite up to 65 wt. %. Less than 2 wt. % consisted of other sulfides, including copper and cobalt sulfide minerals (Fig. 5). The non-sulfide gangue (NSG) component ranged between 30 and 50 wt. % of the concentrate and included quartz, K-feldspar, Fe-oxides (<2 wt. %) and clays (<2.5 wt. %). Pyrite recovery to the batch flotation concentrate was excellent, ranging between 87 to 97 % recovery. Recoveries of cobalt minerals carrollite and alloclasite were variable, with some tests recovering as little as 12 %, while others recovered up to 100 %.

The batch flotation tail was almost completely desulfurised, with <1 wt. % sulfide minerals. The tails were predominantly composed of quartz (70 to 85 wt. %), K-feldspar and Fe-oxides (~5 wt. %).

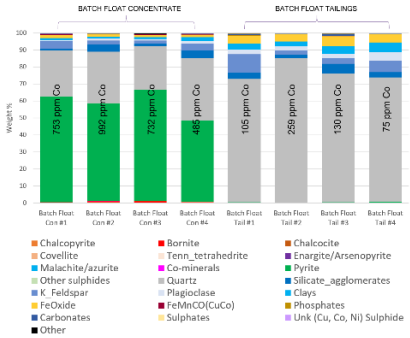

Fig. 5 Unsized modal mineralogy from MLA of the batch float samples with raw cobalt assay data.

Cobalt recovery in the tailings batch float concentrate ranged between 36.5 % and 48.3 %. Several key factors may be controlling cobalt recovery, including fine particle sizes (<10 µm), low primary liberation of cobaltiferous grains (~ 50 to 60 %) (Fig. 6), collector selection for cobalt sulphides or pyrite with trace metal inclusions in the batch float experiment, or unknown cobalt hosts not yet targeted.

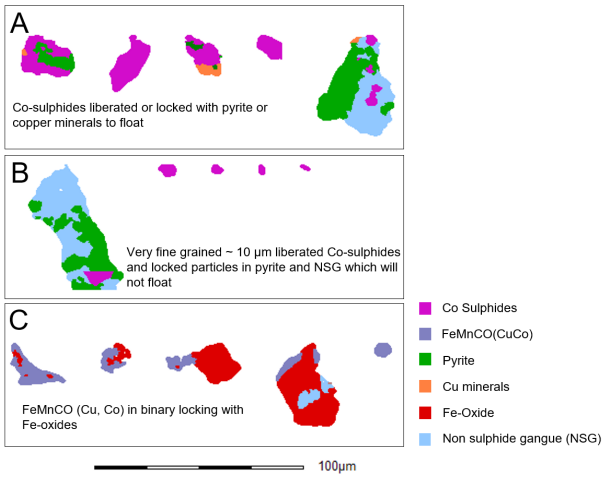

Fig. 6 Individual particles from MLA DataView software from the batch float tests, including: A) Co-sulfide particles in the batch float concentrate, B) Co-sulfide particles in the batch float tailings, C) Co-oxide particles in the batch float tailings.

Elemental distribution mapping using the Bruker EDS detector and processing in AMICS software identified cobaltiferous sulfides (carrollite) locked within NSG minerals in the batch flotation tailings (Fig. 7).

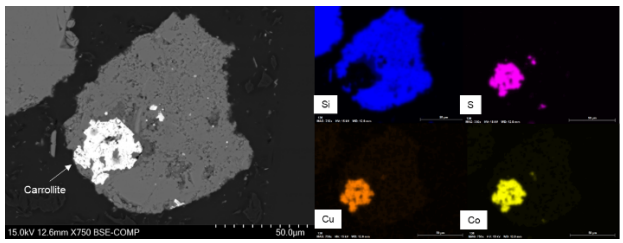

Fig. 7 Cobalt distribution elemental EDS map.

To investigate this further, mass flows were used to identify possible cobalt deportment in the system. The MLA modal mineralogy weight % and MLA estimated assays were generated by grouping key minerals: Cu minerals (chalcopyrite, bornite, chalcocite, covellite, tetrahedrite, enargite, cuprite, malachite, carrollite, FeMnCO, pyrite_group), Co minerals (cobaltite, alloclasite, pyrite_Co-group, FeMnCO and carrollite), pyrite and NSG minerals. The Co mineral mass flows were then calculated using the measured weights of the batch float tests.

Recoveries were calculated from mass flows of cobalt, pyrite, cobalt in pyrite and cobalt not in pyrite. The recoveries of cobalt in pyrite were the same as pyrite recoveries in the system, however the recoveries of cobalt not in pyrite were more

comparable to the measured assay cobalt recoveries (~40 %). This leads to the conclusion that the high-grade cobalt is potentially still sitting in cobaltiferous minerals which are not being optimally recovered in the pyrite concentrate. Carrollite and alloclasite have variable recoveries in the batch float. The elemental distribution of cobalt from the MLA mineralogy shows that a high percentage of cobalt in the batch float tails occurs in carrollite and in the oxide FeMnCO(CuCo), considered to be asbolane.

5 Conclusions

Reprocessing of copper sulfide tailings for secondary cobalt resources is a potential circular economy solution to tailings management and supplement of global critical metal supplies. However, the variability of cobalt mineralogy, locking associations and liberation potential requires detailed geometallurgical characterisation to understand cobalt deportment and opportunities for recovery.

In the case study of a sedimentary copper-sulfide deposit, the dominant cobalt host was expected to be pyrite and therefore floating the pyrite into a pyrite concentrate was expected to also recover the cobalt. Further investigation indicated that fine grained cobalt bearing minerals and pyrite could still be present in the tailings stream, since the pyrite flotation conditions were not optimised to recover these minerals in the batch float experiment.

The integration of chemical, mineralogical and metallurgical data allowed for these key features to be identified and can be used to inform the design of an appropriate mineral reprocessing flow sheet for recovery of cobalt from copper tailings.

Acknowledgements

Many thanks to the case study site and on-site metallurgists (unnamed due to confidentiality reasons) who funded and assisted in this project. The staff at the Julius Kruttschnitt Mineral Research Centre MLA laboratory are thanked for their support and data processing. The Centre for Microscopy and Microanalysis (University of Queensland) is thanked for analytical equipment and technical support.

References

Bruker (2022) ESPRIT 2 – The Powerful 4-in-1 Software for Microanalysis. Bruker https://mbna.bruker.com/acton/fs/blocks/showLandingPage/a/15240/p/p-0036/t/page/fm/2. Accessed 3 March 2023

Dehaine Q, Tijsseling LT, Glass HJ, Törmänen T, Butcher AR (2021) Geometallurgy of cobalt ores: A review. Miner Eng 160:106656. doi: 10.1016/j.mineng.2020.106656

Fu X, Beatty DN, Gaustad GG, Ceder G, Roth R, Kirchain RE, Bustamante M, Babbitt C, Olivetti EA (2020) Perspectives on Cobalt Supply through 2030 in the Face of Changing Demand. Environ Sci Technol 54:2985-2993. doi: 10.1021/acs.est.9b04975

Hitzman M, Bookstrom A, Slack J, Zientek M (2017) Cobalt - Styles of Deposits and the Search for Primary Deposits. USGS https://pubs.usgs.gov/of/2017/1155/ofr20171155.pdf. Accessed 1 March 2023

Mudd GM, Weng Z, Jowitt SM, Turnbull ID, Graedel TE (2013) Quantifying the recoverable resources of by-product metals: The case of cobalt. Ore Geol Rev 55:87-98. doi: 10.1016/j.oregeorev.2013.04.010

Ryan CG (2001) Developments in Dynamic Analysis for quantitative PIXE true elemental imaging. Nucl Instrum Methods in Phys Res Sect B: Beam Interactions with Materials and Atoms 181:170-179. doi: 10.1016/S0168-583X(01)00374-3

Valenta RK, Lèbre É, Antonio C, Franks DM, Jokovic V, Micklethwaite S, Parbhakar-Fox A, Runge K, Savinova E, Segura-Salazar J, Stringer M, Verster I, Yahyaei M (2023) Decarbonisation to drive dramatic increase in mining waste - Options for reduction. Resour, Conserv Recycl 190:106859. doi: 10.1016/j.resconrec.2022.106859

Invisible metals for a green future: Au associated critical elements in historic mining districts Murtal (Styria)

Sandra Niederl[1], Viktor Bertrandsson Erlandsson[1], Peter Felfer[2], Phillip Gopon[1]

[1]Dept. of Applied Geosciences and Geophysics, University of Leoben, Austria

[2]Lehrstuhl für Werkstoffwissenschaften, Friedrich-Alexander-Universität, Erlangen, Germany

Abstract. Gold is often associated with other critical metals bound in the crystal structure of sulfide minerals. Our study is investigating the possibility of re-mining tailings piles from three former gold mining districts in Styria, with a special focus on precious and critical metal containing sulfides. We combine optical microscopy, electronprobe micro analysis, scanning electron microscopy and whole rock geochemistry to characterize these deposits and where the metals are found. Geochemistry confirms the positive correlation between arsenic and gold as well as other elements. To better understand the atomic relations between the metals and to take a look at the way they occur, nanoscale investigations with atom probe tomography are done on selected grains. Gold is occurring in elevated concentrations in arsenic rich pyrite zonation as well as in nano-inclusions in pyrite and arsenopyrite.

1 Introduction

Tailings piles from mining activities from at least 1000 years of active mining are visible in Austria´s landscape. Due to the increasing need of special metals like bismuth, cobalt, lithium, platinum group elements (PGEs) and tungsten for green technologies, those tailings piles are starting to become a major interest. Most of the mentioned elements are considered critical, but are currently not mined in Europe and there is an ongoing search for local resources. Renewable energies will increase the needed amount of those “green” elements even further. Tailings from old mines are a possible source of those metals all over the EU.

Recent work has shown that gold and a subgroup of critical metals (hereafter referred to as precious metal associated critical metals or PMaCMs) can occur trapped within sulfide minerals often bound with the crystal lattice of e.g. pyrite (Reich et al. 2005; Gopon et al. 2019).

This study is part of a larger project, looking at different tailings piles in Styria, to evaluate their potential according to those PMaCMs. We will

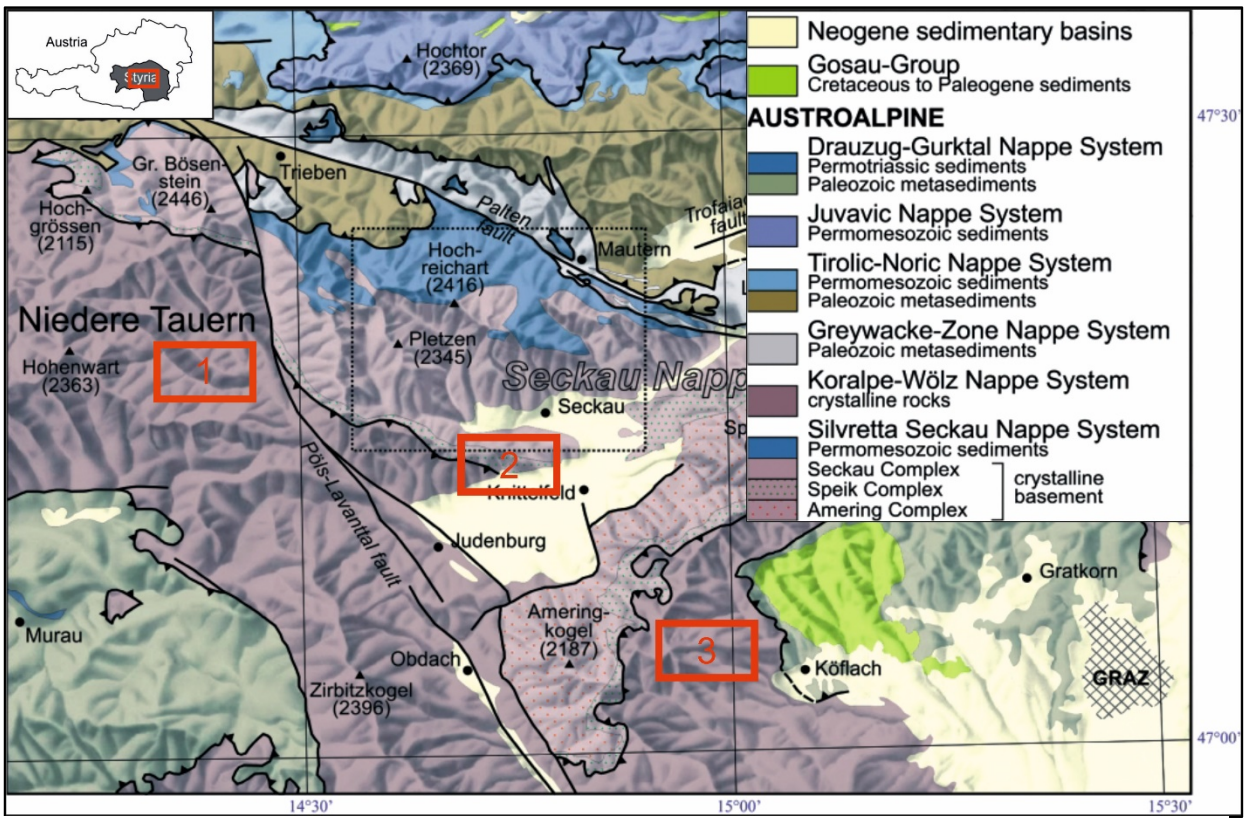

Figure 1. Geological map of Upper Styria with the former mining areas in red: 1= Pusterwald; 2= Flatschach; 3= Kothgraben. (modified after Gasser et al. 2009; Pfingstl et al. 2015)

present results from different tailings piles in three former gold mining districts, operated from the 15th up to the 20th century. These districts are located in Upper Styria and are Flatschach, Kothgraben and Pusterwald (Figure 1). The primary focus of our work is to determine in which quantities PMaCMs are found within these deposits (using whole rock geochemistry) and to characterize how they occur. Not all metals in these deposits are visible with the optical microscope or electron microscopes (i.e. electron probe micro-analyser (EPMA), scanning electron microscope (SEM)), and we report the occurrence of invisible gold within arsenic rich pyrite from at least one of the three deposits (Flatschach). Ongoing work is focusing on other sulfdes in these deposits potentially hosting gold and PMaCMs (using laser ablation inductively coupled plasma mass spectrometry (LA-ICP-MS) and EPMA).

2 Geological overview

The three districts are located in the Silvretta-Seckau and Koralpe- Wölz nappe of the upper lithology consists of medium to high grade metamorphic rocks (Neubauer 2002). The mined ore deposits are mesothermal vein type deposits.

3 Methods

45 samples were taken from different tailings piles in the three districts and 20 of them where send out for geochemical whole rock analysis. Polished sections, from our historic collection, as well as newly prepared ones where scanned with a Keyence VHX 6000 digital microscope. EPMA and SEM work was done with 10 selected samples. The main focus of the petrography was on the district Flatschach, as it seemed most suitable in terms of arsenic contents and existing minerals. The used EPMA was a JEOL JXA 8200 with an acceleration voltage of 15kV and a current of 15µA and the SEM work was done with a Zeiss Evo MA10 with a Bruker Quantax EDX detector. Pyrite as well as arsenopyrite grains where analysed, but major parts of the results are from pyrite analyses.

3.1 Atom probe tomography (APT)

APT is applied to characterize the atomic-scale link between gold, PMaCMs and arsenic (and other minor elements). Analysed were conducted on a CAMECA LEAP 4000 HR, located in the Department of Materials, Friedrich-Alexander-University, Erlangen. Because of the known link between arsenic and gold concentrations in pyrite (Reich et al. 2005), grains with a promising Au/As ratio where chosen. Two liftouts where done on the arsenic rich zones of the pyrites (one is shown in Figure 2).

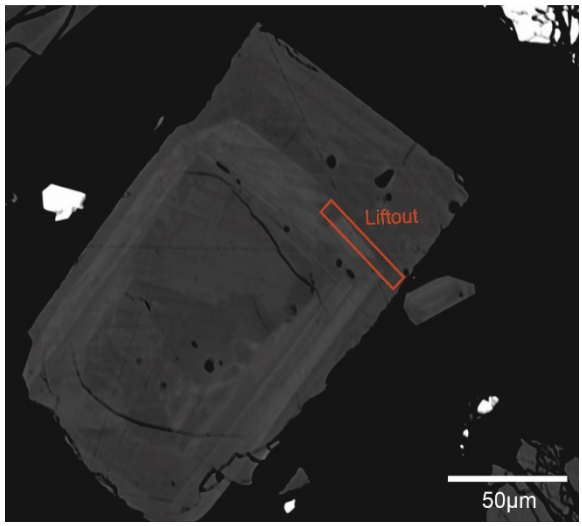

Figure 2. Back scatter image (BSE) image of one of the grains analysed with APT; red= liftout area.

4 Future work

The next step in this project will be the processing of the APT and LA-ICP-MS measurements to get an overall image of the trace element compositions of the grains and not only the selected APT areas. Additionally, we plan to constrain the timing of ore formation and to investigate the trace elemental signature of the ore minerals to determine if there is a geochemical and/or temporal link between these deposits that occur in comparable geological settings.

Acknowledgements

The work is financed by in part by the State of Styria (Green Transformations; ABT08-247901/2021), as well AUREX Biomining AG.

References

Gasser D, Gusterhuber J, Krische O, Puhr B, Scheuchter L, Wagner T, Stüwe K (2009) Geology of Styria: An overview. Mitteilungen des naturwissenschaftlichen Vereines für Steiermark 139:5-36

Gopon P, Douglas J O, Auger M A, Hansen L, Wade J, Cline J S, Robb L J, Moody MP (2019) A Nanoscale Investigation of Carlin-Type Gold Deposits: An Atom-Scale Elemental and Isotopic Perspective. Economic Geology 114:1123–1133

Neubauer F (2002) Evolution of late Neoproterozoic to early Paleozoic tectonic elements in Central and Southeast European Alpine mountain belts. Review and synthesis. Tectonophysics 352:87–103

Pfingstl S, Kurz W, Schuster R, Hauzenberger Ch (2015) Geochronological constraints on the exhumation of the Austroalpine Seckau Nappe (Eastern Alps). Austrian Journal of Earth Science 108/1:172–185

Reich M, Kesler S E, Utsunomiya Satoshi, Palenik C S, Chryssoulis S L, Ewig R C (2005) Solubility of gold in arsenian pyrite. Geochimica et Cosmochimica Acta, 69/11:2781-2796

Schmid S M, Fügenschuh B, Kissling E, Schuster R (2004) Tectonic map and overall architecture of the Alpine orogene. Eclogae geologicae Helvetiae 97:93–117

Comparison of the Wilson and Ivan monazite-bearing high-grade mineralization at Alces Lake, SK (Canada): Mineralogy, composition, and U-Pb chemical ages

Kateryna Poliakovska[1,2], Irvine R. Annesley[1,3,4], Olena Ivanik[2], Kahlen Branning[3]
[1]*GeoRessources, Université de Lorraine, Nancy, France*
[2]*Institute of Geology, Taras Shevchenko National University of Kyiv, Kyiv, Ukraine*
[3]*Appia Rare Earths & Uranium Corp., Toronto, Canada*
[4]*University of Saskatchewan, Saskatoon, Canada*

Abstract. This contribution presents part of an original study that combines field observations, petrography and geochronological constraints of the extremely high-grade REE-Th-U mineralization associated with the pegmatitic bodies of the Alces Lake deposit/prospect (SK, Canada). These pegmatites intrude the metasedimentary and meta-igneous rocks of the Murmac Bay Group with the mineralization hosted in monazite-(Ce) (within the studied Ivan and Wilson zones). The investigated samples display mostly peraluminous signatures and are dominated by the assemblage of quartz + K-feldspar + plagioclase + biotite +/- rutile at the Wilson zone +/- muscovite at the Ivan zone + monazite + zircon. Chemical U-Pb dating of monazite grains of 1.8-2.0 Ga for both studied zones confirm the relation to the Trans-Hudson Orogen metamorphism.

1 Introduction

Rare earth elements (REE) among the rare metals and other critical metals are of great economic interest and have become an irreplaceable part of our lives. However, their genesis often remains poorly defined. Sufficient understanding of the mineral systems of the rare metals is an essential part of discovering new prospects and thus reducing supply deficits, caused by increasing demand worldwide.

This paper focuses on studying and comparing zones of exceptional high-grade monazite (REE-Th-U) mineralization at Alces Lake (Northern Saskatchewan). The current study is a part of a larger research project (Poliakovska et al. 2022) focused on the genesis of the Alces Lake area mineralization (SK, Canada).

One of the key goals of the current research was to analyze the samples from 2 mineralized zones (Ivan and Wilson) of the deposit and ultimately suggest/determine the petrogenesis of the Alces Lake mineralization. This was carried out using field observations data, petrographic observations, and mineral chemistry.

2 Geological Setting

The Alces Lake REE mineralized area is located within the Rae Subprovince in the Churchill Province. Locally it is hosted by the Beaverlodge domain (northern Saskatchewan) at the junction of the Beaverlodge, Train, Zemlak and Ena Domains, approximately 28 km north of the Athabasca Basin
The rocks of the rocks of Alces Lake area (deposit/prospect) have a complex genesis, that is related to 4 major Paleoproterozoic tectonic events that highly deformed and metamorphosed (at mid- to high-pressure amphibolite- and granulite-facies conditions) the predominantly meta-sedimentary and meta-igneous rocks of Paleoproterozoic age (Ashton et al. 2013; Bethune et al. 2013; Regis et al. 2021).

Overall, the crystalline basement complex that comprises the geological suite of the area consists of: Archean to Paleoproterozoic granodioritic and mafic gneisses, amphibolites, granitic gneisses and paragneisses (Ashton et al. 2013) (Fig. 1).

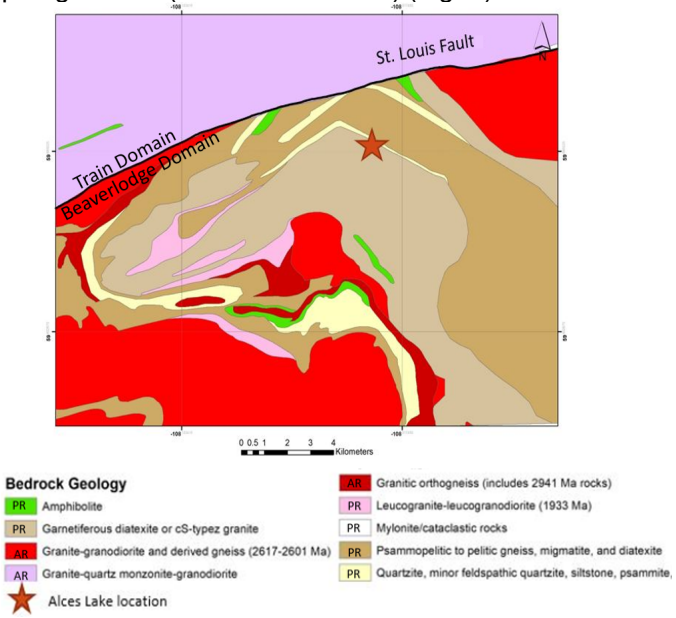

Fig. 1 Geological setting of Alces Lake in the Beaverlodge Domain (modified after the Saskatchewan Geological Atlas)

Alces Lake is ranked as the highest-grade REE occurrence in Canada (Sykes et al. 2018).

The REEs and associated Th, U, Ga, and Zr are hosted in monazite-rich (+/- zircon) granitic to residual melt/cumulate pegmatites, associated with biotite-rich (+/- sulfides) paragneisses. The mineralized pegmatitic bodies are found within/near the Archean/Paleoproterozoic transition zone and are interpreted to have formed under middle crustal P-T conditions (Annesley et al. 2019). At least 3 or 4 generations of pegmatites (biotite-rich mineralized and quartz-feldspar-rich non mineralized) have been identified at the Alces Lake area. The mineralization forms a complex system of pegmatite veins (lenses),

occurring in the form of individual grains, thin lenses from 1 to 3 cm thick, and massive augenitic clusters (i.e. boudins, up to a meter thick) of monazite grains 1 to 3 mm in size (on average).

3 Methodology

After an extensive petrographic study, two thin-sections were selected from a larger suite of thin sections from representative samples. Thus, one thin section was chosen for each study zone – for Wilson (thin-section "172") and for Ivan (thin-section "182"), located around 100 m from each other within the Alces Lake mineralization. The thin-sections were analysed using the micro-XRF – Bruker M4 Tornado µXRF. High-resolution imaging of individual monazite grains from monazite-bearing pegmatoids was performed by using a high-resolution scanning electron microscope (TESCAN VEGA3) in order to find and characterise any internal zoning or other heterogeneities in individual grains of monazite. As a result the backscattered electron (BSE) images have been recorded. Quantitative spot analyses of monazite, as well as X-ray element maps, were performed using the CAMECA SX100 electron microprobe at the SCMEM (Common Service of Electron Microscopy and X-ray Microanalysis) facilities at the GeoRessources laboratory. Monazite was analysed for a number of elements: Si, P, Ca, Y, La, Ce, Pr, Nd, Sm, Gd, Pb, Th, U, and O.

Thirty spot analyses were recorded for the monazite grains of the "182" thin-section and sixty three for the "172" thin-section (due to the larger heterogeneity of the grains within the Wilson zone). Consequently X-ray maps were created for representative monazite grains within the Ivan (5 grains) and Wilson (14 grains) zones.

4 Mineralogy

Petrographic observations have showed that the mineralized samples are composed mainly of feldspar, monazite, quartz, biotite, muscovite, rutile and zircon (Fig. 2, 3). Alteration has led to the chloritization of biotite and the sericitization/ kaolinization of feldspars.

Sample "172" – Wilson zone

In the studied sample, monazite grains are most commonly associated with biotite and feldspar. The monazite forms subhedral to fully rounded, corroded crystals that are variable in size (the grainsize of monazite commonly ranges from 0.1 to over 1 mm diameter) and characterized by extremely high REE, high Th and U contents. Some of the resorbed monazite grains show partial corrosion overgrowths of biotite or quartz. The most common inclusions in monazite are quartz and feldspar. Within the Wilson zone the monazite grains are either homogenous, or weakly to strongly zoned. When present, the chemical zoning can be characterized as: 1) concentric (oscillatory growth zoning), 2) patchy zoning.

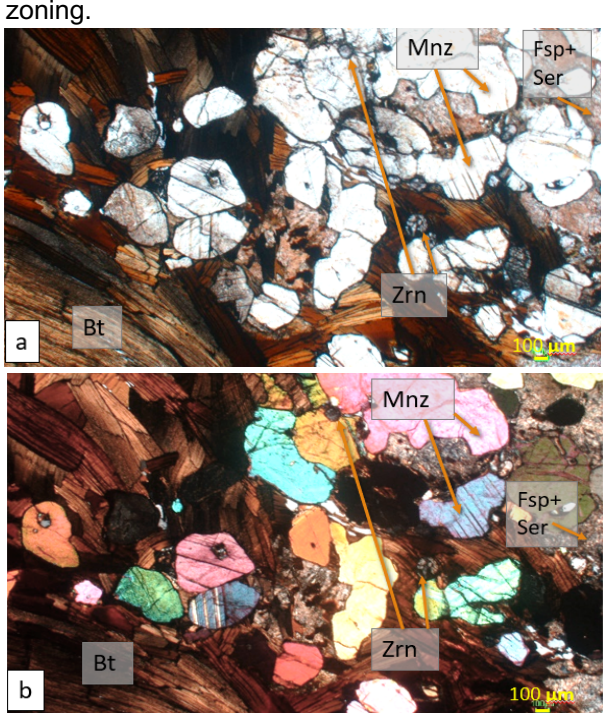

Fig. 2 Photomicrograph of high-grade monazite mineralization. **a** Plane light. **b** XPL image – from "172" – Wilson zone

Sample "182" – Ivan zone

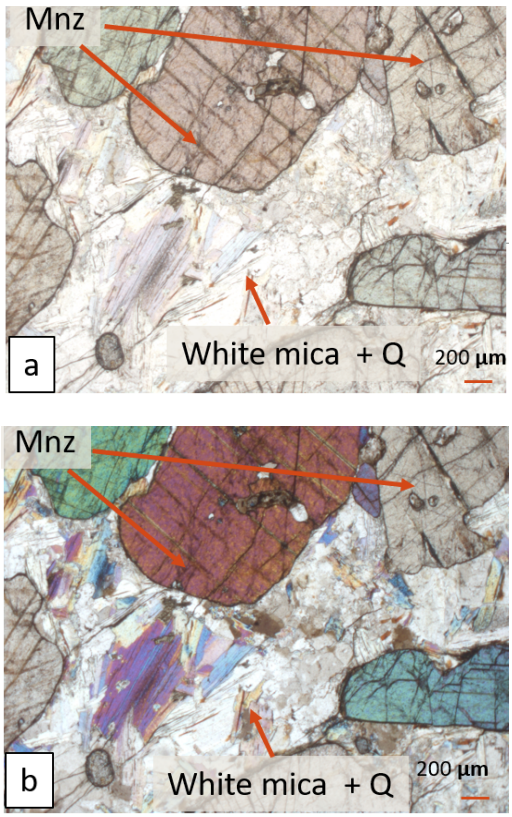

Fig. 3 Photomicrograph of high-grade monazite mineralization in muscovite-quartz matrix. **a** Plane light. **b** XPL image – "182" – Ivan zone

In this sample, monazite grains are associated mainly with biotite, muscovite and quartz. The monazite forms subhedral to fully rounded, corroded

crystals variable in size (the grainsize of monazite commonly ranges from 0.1 to over 1-3 mm diameter) characterized by extremely high REE, high Th and U contents. The most common inclusions in monazite are quartz, feldspar, and also fine-grained white mica. Within the Ivan zone, monazites are overall homogenous. EPMA X-ray mapping revealed slight sector zonation on some of the grains (SEM BSE images did not show any zonation).

EPMA quantifications

Data from 93 monazite spot analysis was compiled and analyzed to better characterize the REE mineralized zones. All the data plotted within the Ce-monazite zone (Fig. 4).

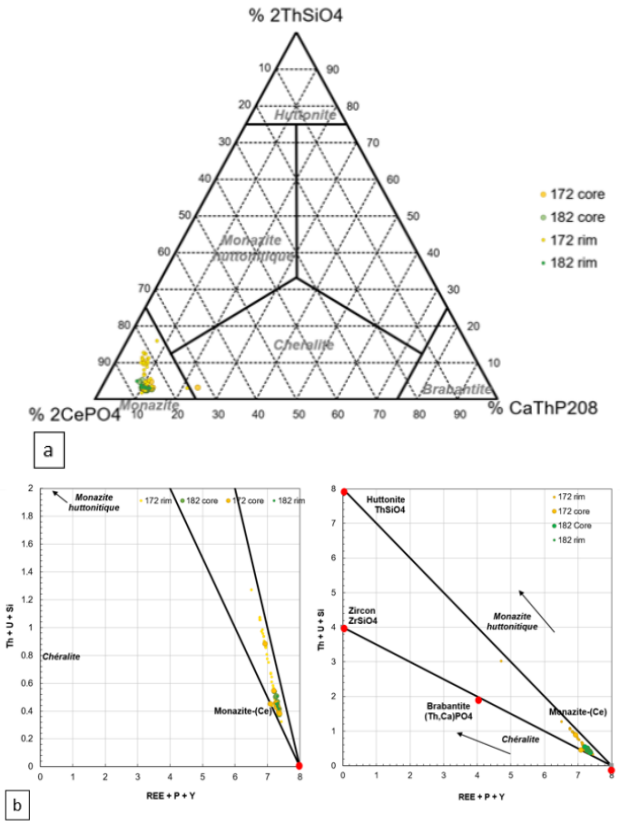

Fig. 4 a Ternary plot of the monazite compositions (in green – Ivan zone, in yellow – Wilson zone). **b** Th + U + Si vs REE + Y + P diagram. For the two identified zones, the monazite grains are dominated by monazite-(Ce) compositions

For sample “182” (Ivan zone), direct correlation between the following elements was observed: Ce and La, and Th and Pb; while inverse correlation was noted between Si and P; and Ce and Pb, Th. For sample “172” (Wilson zone) direct correlation between the following elements was observed P and Ca, Ce, Pr, Nd, Sm, Gd; and Th and Pb; and inverse correlation was noted between Si and P, Ce, Pr, Nd, Sm, Gd; and Ca and Th.

X-ray maps were created for a total of 19 monazite grains from both zones. It was observed that, for all the grains, the lighter colored grey zones (SEM BSE image – Fig. 5a) tend to be more U- and Th-rich and REE-poor (Fig. 5b, 5c) when compared to the darker grey matrix.

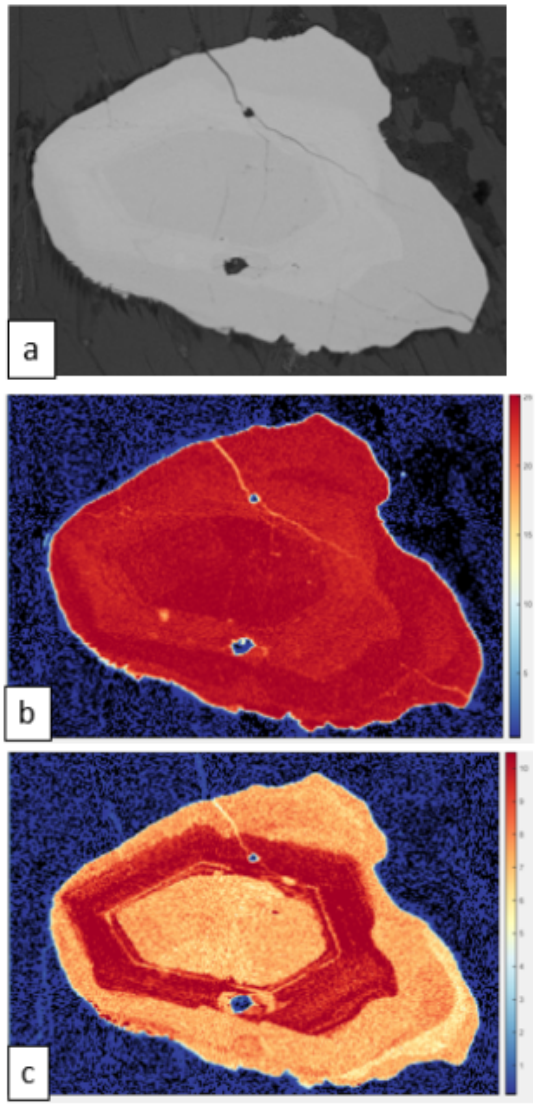

Fig. 5 a BSE SEM. **b** Ce. **c** Th (in weight %) of monazite grain from the Wilson zone of the Alces Lake deposit

U-Pb chemical ages

We attempted to calculate the chemical ages using the EPMA data and the procedures of Montel et. al. 1996. The graphs from the Fig. 6 show the obtained ages for both Wilson and Ivan zones. Most of chemical ages (U-Th-Pb) calculated from monazite EMPA analyses yield ages of 2.0 – 1.7 Ga. We can also observe slightly different age trends for these 2 selected zones where the age range for the Wilson zone is 1.4 – 2.1Ga (average=1.88 Ga, median=1.9 Ga) and for the Ivan one – 1.7 – 2 Ga (average=1.9 Ga, median =1.89 Ga).

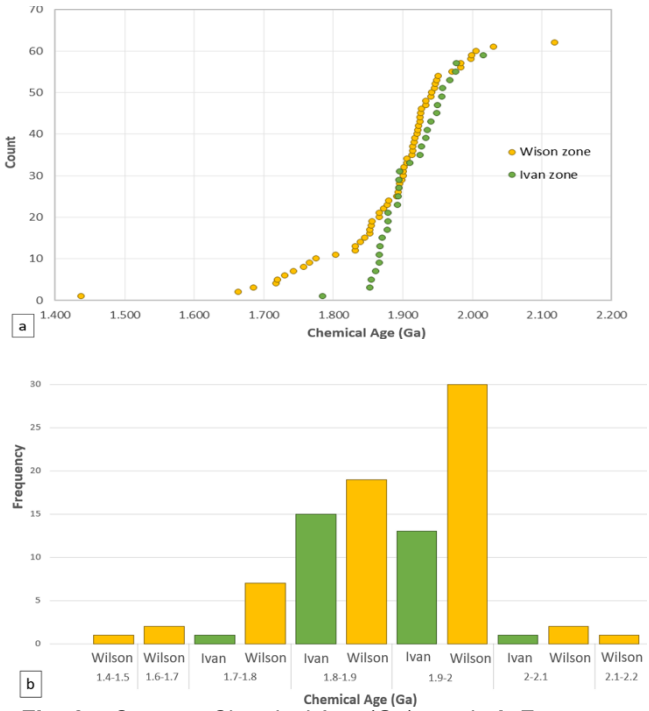

Fig. 6 a Count to Chemical Age (Ga) graph. **b** Frequency to Chemical Age graph

5 Discussions and Conclusions

In this study, we characterized the geological setting, ages, and mineral assemblages, as well as the composition of monazites of the pegmatitic mineralized zones at the Alces Lake deposit/prospect area. The results of this work show that the monazites, the main REE-Th-U bearing mineral identified in the studied samples from the Ivan and Wilson zones, have a complex history and most likely represent a combination of different origins. The studied pegmatites are LREE enriched and are composed of quartz + K-feldspar + plagioclase +/- rutile + biotite +/-muscovite + monazite and zircon.

Taking into account the mostly peraluminous nature of pegmatites along with other evidence they could have formed as a result of partial melting of the ortho and paragneisses (possibly the Murmac Bay Group rocks - a belt of Paleoproterozoic metasedimentary and meta-igneous rocks interleaved with Archean orthogneisses) during high-grade amphibolite to granulite-facies metamorphism related to the Trans-Hudson Orogen in a middle to lower crustal melt-transfer zone, with melt transport preferentially along shear zones and the Archean-Proterozoic transition zone.

Thus, from the field and mineralogical data presented here we interpret that the Alces Lake pegmatitic bodies are of anatectic origin (and not directly related to a parental granitic pluton and are representative of the abyssal REE-Th-U subclass of the Cerny and Ercit (2005) classification.

So, to date, the results of our investigation of the samples from the 2 chosen mineralized zones show that the REEs and associated Th, U, Ga, and Zr are hosted in monazite-rich (+/- zircon) granitic to residual melt/cumulate pegmatites, emplaced within/near the Archean/Paleoproterozoic transition zone under middle to lower crustal P-T conditions.

Both the Ivan and Wilson zones of the Alces Lake deposit/prospect have similar ranges of age (obtained from the chemical dating, thus need to be confirmed using more precise methods, e.g., LA-ICP-MS/ion microprobe dating to properly determine the age of the various stages of growth and recrystallization). The most prominent clusters for both zones are from 1.8 to 2 Ga, which can be interpreted initially as the age of the peak metamorphism, magmatic crystallization, and/or possible age of the source rock area.

We opine that this high-grade Th-rich monazite mineralization represents restitic material formed by disequilibrium melting, which then migrated as a restite-rich melt phase to / emplaced at the presently observed crustal level at Alces Lake (i.e. old middle crust at upper amphibolite/lower granulite facies).

Acknowledgements

This work was carried out thanks to the equipment of the SCMEM (Common Service of Electron Microscopy and X-ray Microanalysis) of the University of Lorraine.

References

Annesley IR, Poliakovska K, Sykes J, Pandur K (2019) The geology and mineralogy of high-grade rare earth element (REE-Th-U) mineralization at Alces Lake, Saskatchewan (Canada). Life With Ore Deposits on Earth, Proceedings of the 15th SGA Biennial Meeting, 2019, Glasgow, Scotland 1-4:1732–1735

Ashton KE, Hartlaub RP, Bethune KM, Heaman LM, Rayner N, Niebergall, GR (2013) New depositional age constraints for the Murmac Bay Group of the southern Rae craton, Canada. Precambrian Res 232:70–88

Bethune KM, Berman RG, Rayner N, Ashton KE (2013) Structural, petrological and U–Pb SHRIMP geochronological study of the western Beaverlodge domain: Implications for crustal architecture, multi-stage orogenesis and the extent of the Taltson orogen in the SW Rae craton, Canadian Shield. Precambrian Res 232:89–118

Černý P, Ercit TS (2005) The classification of granitic pegmatites revisited. Can Mineral 43:2005–2026

Montel J-M, Foret S, Veschambre M, Nicoll C, Provost A (1996) Electron microprobe dating of monazite. Chem. Geol. 131:37-53

Poliakovska K, Annesley IR, Ivanik O, Sykes J, Guest N, Otsuki A (2022) Geological setting, geochemistry and petrology of the granitic pegmatites hosting REE Th U mineralization at the Alces Lake area, Northern Saskatchewan, Canada. Proceedings of the 16th SGA Biennial Meeting, 28-31 March 2022, 1:325-328

Regis D, Pehrsson S, Martel E, Thiessen E, Peterson T, Kellett D (2021) Post-1.9 Ga evolution of the south Rae craton (Northwest Territories, Canada): A Paleoproterozoic orogenic collapse system. Precambrian Res 355(3):106105

Sykes J, Annesley IR, Pandur K (2018) The geological evolution of high-grade rare earth element mineralization on the Alces Lake Property, Northern Saskatchewan. Saskatchewan Geological Survey, Open House 2018 Abstract Volume, Misc Rep 2018-3: p 37

Forensic geometallurgy of Ni-Co laterites: Sustainable processing of Europe's low-grade ores and tailings into battery-grade metals

Fernando Prado Araujo[1], Philippe Muchez[1], Jens C.Ø. Andersen[2], Nívea Magalhães[2], Richard Crane[2], Hannah Hughes[2]
[1]KU Leuven, Department of Earth and Environmental Sciences, Belgium
[2]University of Exeter, Camborne School of Mines, United Kingdom

Abstract. The global nickel (Ni) and cobalt (Co) demand is expected to increase manyfold in the next decades. Both metals are essential components in rechargeable batteries, which are highly required for the energy transition away from fossil fuels. The current European production/refining landscape is not enough to cover such demand (even if recycling rates improve in the future). Additionally, the state-of-the-art processing routes can be energy intensive and not so environmental-friendly. The Horizon Europe-funded ENICON project offers an alternative HCl-based technology, with a lower eco-footprint, to process Europe's Ni-Co ore deposits and tailings into battery-grade metals. The full metal deportment in all products/by-products and valorised residues is done by combining several characterisation techniques into a mineral-focused geometallurgical protocol. This approach minimizes losses and allows the recovery of multiple valuable metals in the flowsheet, effectively improving the sustainability and viability of the European Ni/Co supply chain.

Introduction

Nickel (Ni) and cobalt (Co) are essential components of rechargeable batteries (Nickel Institute 2023). Hence, many studies forecast a sharp increase in their future demand (Campagnol et al. 2017; IEA 2021; Gregoir and van Acker 2022). However, European sources represent only a minor share of the extraction and refinement of battery-grade Ni and Co in the global market (Mudd and Jowitt 2022), leaving Europe mostly dependent on imports of these metals. Additionally, most of the current production practices are energy intensive and can pose environmental hazards (Bartzas et al. 2021). This poses a serious risk to Europe's plans of transitioning away from fossil fuels. Consequently, ensuring the sustainable supply of these critical raw materials is a key priority for Europe (European Commission 2008).

The Horizon Europe ENICON project (https://enicon-horizon.eu/) responds to this issue by enhancing the potential of Ni/Co resources within Europe – i.e. sulphidic ores and limonitic/saprolitic laterite ores – as well as by developing a more sustainable HCl-based processing route for these materials (Figure 4). The project consists of a multidisciplinary approach to (1) track the metals in the supply chain using forensic geometallurgy, (2) develop a new HCl leaching process to extract Ni and Co from ores and tailings, (3) ultra-refine the metals towards battery grade Ni/Co, and (4) provide solutions for the valorisation of residues. All those steps are further integrated into a Life Cycle-Techno Economic Assessment (LCA-TEA) to optimise the performance and decrease the environmental impact of the mining/refining operations (Figure 3). This contribution introduces the geometallurgical protocol for laterite ores (WP1) within the ENICON context.

Ni(/Co) laterites

Ni/Co-lateritic deposits are regoliths formed through weathering of ultramafic rocks and have low metal grades, commonly lower than 5% for Ni and less than 0.1% for Co (Elias 2002). The mineralisation is mainly hosted in two ore zones, saprolitic laterites and limonitic laterites (also known as oxide zone), with saprolite having a slightly higher grade than limonite (Elias 2002). These laterites are mineralogically and texturally complex materials with Ni and Co residing in several silicate and oxide minerals (Andersen et al. 2009). These features compound into a challenging process to release the metals from the mineral matrix.

Europe's two main laterite-processing companies, ENICON partners Larco and Euronickel, transform mixtures of saprolite and limonite laterite ores into an FeNi (Class-II Ni) product by a pyro-metallurgical route. Besides having a large carbon footprint (Bartzas and Komnitsas 2015) this process is unable to produce battery-grade Ni (Class-I Ni) and fails to recover sufficient Co, which largely ends up in the residues sent to landfills. In order to maximise the extraction efficiency of Ni, Co, and other valuable metals from these complex and heterogeneous deposits, it is crucial to understand the geological and mineralogical characteristics of the ore samples and apply a geometallurgical assessment of the processing flowsheet.

Forensic Geometallurgy

Geometallurgy is a multidisciplinary field that combines geology, mineralogy, and metallurgy to optimize mineral processing and increase the recovery of metals from ore deposits.

ENICON's forensic geometallurgy protocol (Figure 5) is a proactive approach that collects mineralogical, textural, and geochemical data of European Ni-Co deposits. It provides information

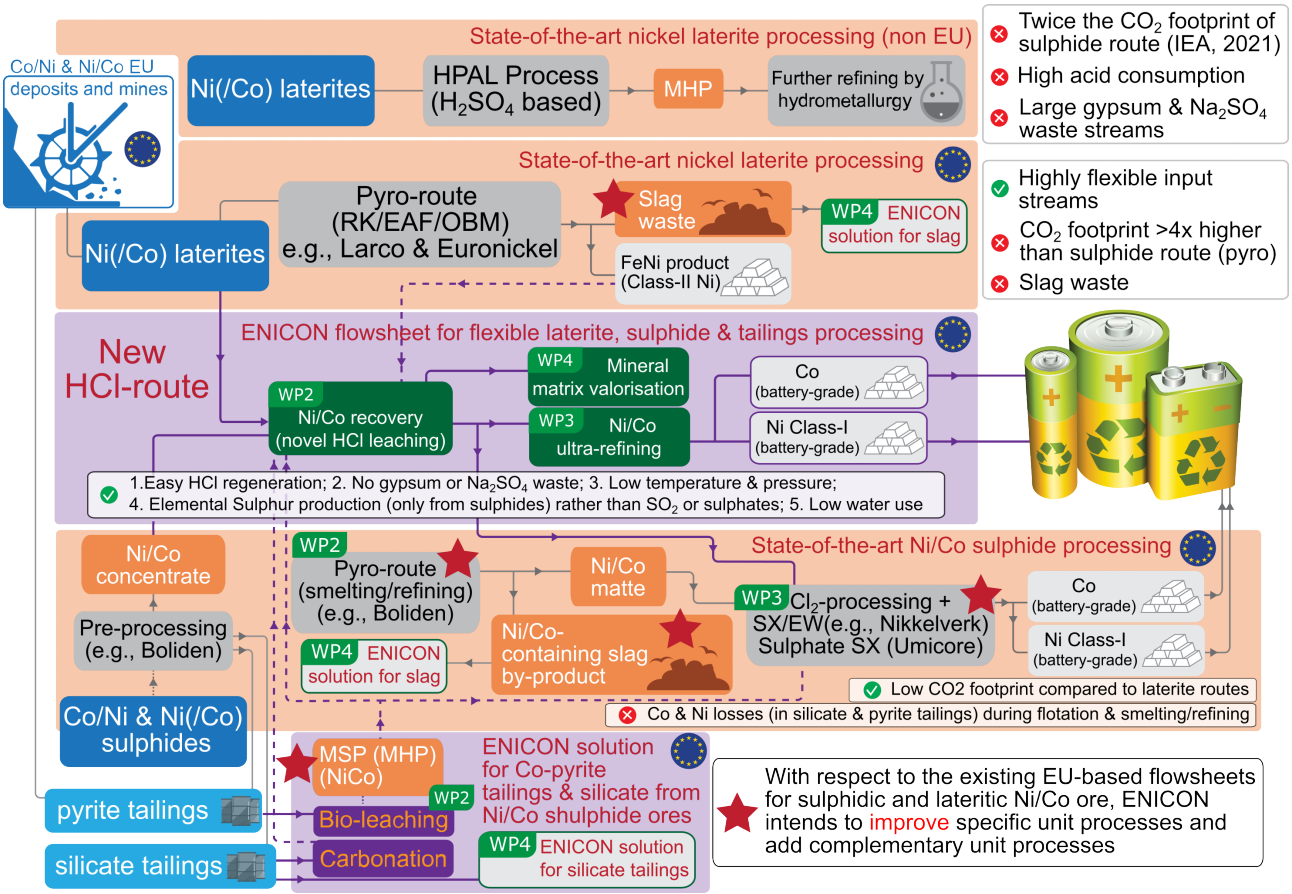

Figure 4. ENICON goes beyond the state-of-the-art for Ni/Co mining, recovery, and refining (orange boxes and grey arrows - source: IEA 2021). The new HCl route (upper purple box and purple arrows) is able to convert both laterite-based and sulphide-based materials into battery-grade Ni and Co, overcoming some of the issues associated with the state-of-the-art routes (green checks and red marks in white boxes near each specific flowsheet). A high-resolution version can be viewed at https://enicon-horizon.eu/.

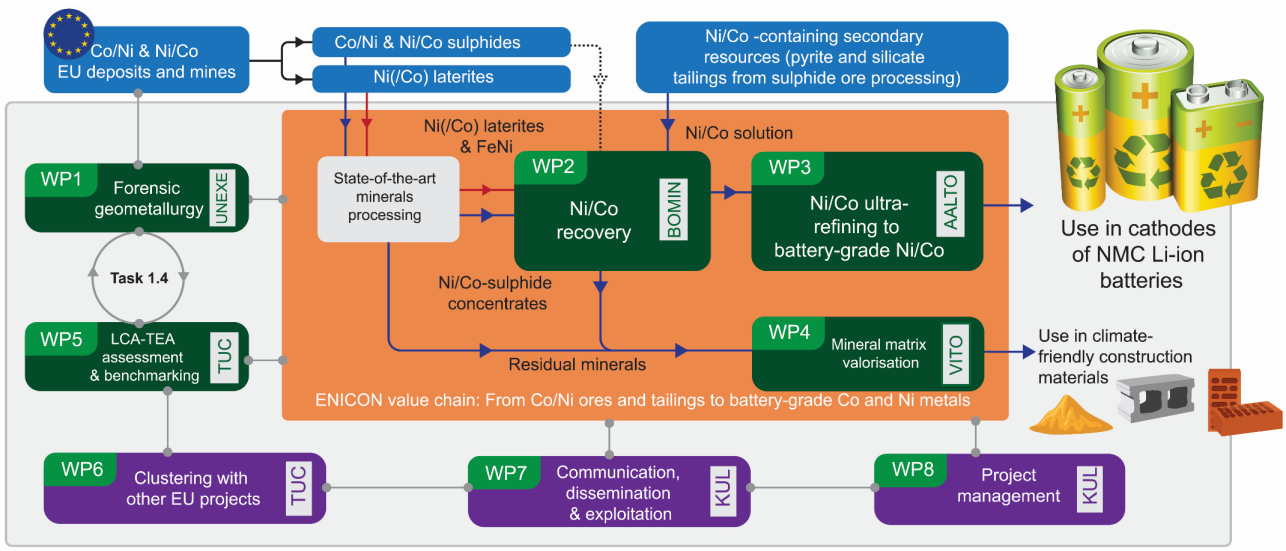

Figure 3. Division of the work package (WP green boxes) structure within the ENICON project. The link between raw material (EU Ni/Co deposits and tailings) to final product (battery-grade metals and climate-friendly construction materials) is monitored by the forensic geometallurgy protocol

about the metal pathways in all processing stages, aiming to track what happens to Ni, Co, potential by-products (e.g., platinum-group elements, Sc), penalty elements (e.g., As, Bi, Te, and Sb), active and passive gangue, and environmentally-deleterious products throughout the flowsheet from ore to battery-grade metal. This approach identifies the mineralogical and textural reasons for processing underperformance and mitigates losses in the Ni/Co mining, processing, and refining flowsheets and for the valorisation of waste materials. Additionally, the data will tell us how metals and minerals behave in the new HCl route compared to traditional stages of processing.

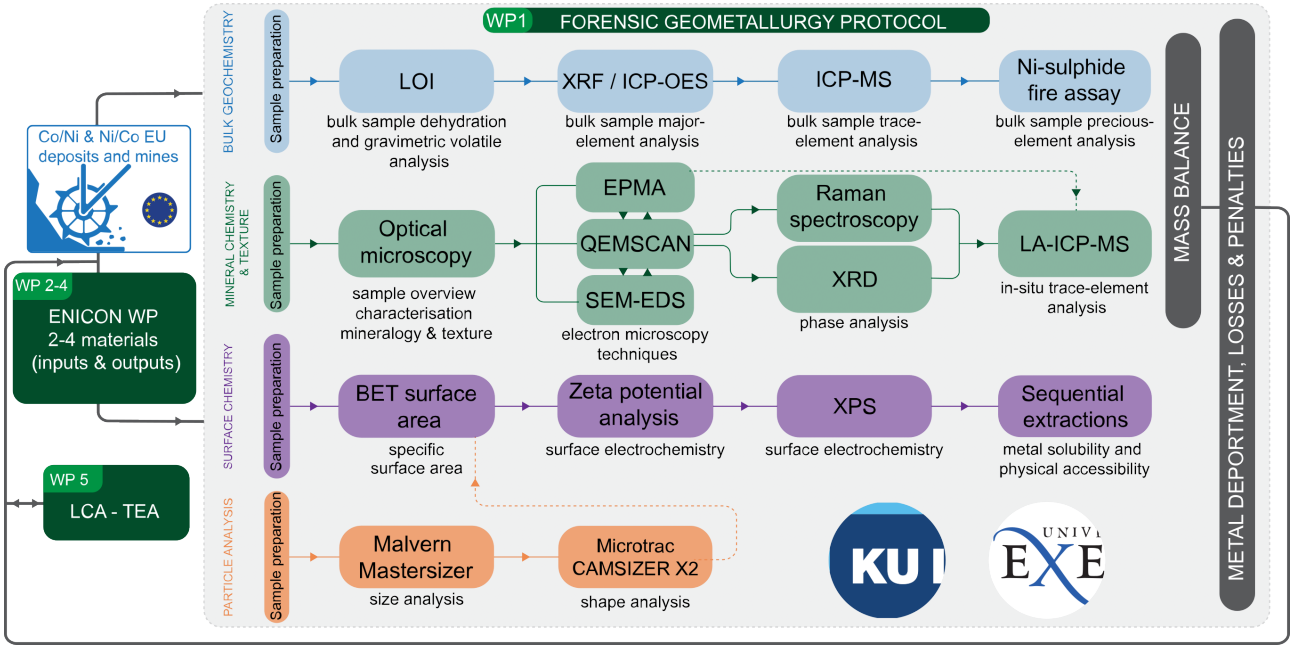

Figure 5. ENICON's forensic geometallurgy protocol & methodology (WP1) describing the main techniques that will be used in the project.

This advanced characterisation of materials involves a holistic investigation of their physical, chemical, and mineralogical parameters and characteristics. An array of techniques such as bulk geochemistry (loss on ignition, X-ray fluorescence, inductively coupled plasma (ICP)-optical emission spectroscopy, ICP-mass spectroscopy, and NiS fire assay), bulk and in situ mineralogy (optical microscopy, X-ray diffraction, scanning electron microscopy, electron microprobe, Raman spectroscopy, and laser ablation ICP-MS), and other analytical tools for particle size and shape distribution analyses are combined. This allows the definition of the metal deportment and losses from ore to battery-grade metal, and in all products/by-products, valorised waste, and residues.

Conclusions

The geometallurgy of nickel laterite deposits is a critical aspect to ensure effective mining and processing of these materials. By optimizing mineral processing and maximizing metal recovery, geometallurgical studies can play a vital role in improving the efficiency and sustainability of Ni and Co production from these ore deposits in Europe. The ENICON project targets to develop a competitive technology to treat the existing, newly exploited, and future low-grade Ni/Co European deposits to produce Class-I (battery-grade) Ni and Co with a lower eco-footprint. This will increase the effectiveness and sustainability of the Co/Ni supply chain in Europe, anticipating the increase in production required to meet Europe's electrification plan. The multi-metal mining approach and the residue valorisation strategies are needed to make the Co/Ni supply chain a near-zero-waste system in the future.

Acknowledgements

The ENICON project (https://enicon-horizon.eu/) has received funding from the European Union's Framework Programme for Research and Innovation Horizon Europe under Grant Agreement No. 101058124.

References

Andersen JCØ, Rollinson G, Snook B, et al (2009) Use of QEMSCAN® for the characterization of Ni-rich and Ni-poor goethite in laterite ores. Miner Eng 22:1119–1129. https://doi.org/10.1016/j.mineng.2009.03.012

Bartzas G, Komnitsas K (2015) Life cycle assessment of ferronickel production in Greece. Resour Conserv Recycl 105:113–122. https://doi.org/10.1016/j.resconrec.2015.10.016

Bartzas G, Tsakiridis PE, Komnitsas K (2021) Nickel industry: Heavy metal(loid)s contamination - sources, environmental impacts and recent advances on waste valorization. Curr Opin Environ Sci Health 21:100253. https://doi.org/10.1016/j.coesh.2021.100253

Campagnol N, Hoffman K, Lala A, Ramsbottom O (2017) The future of nickel: A class act. McKinsey&Company

Elias M (2002) Nickel laterite deposits – geological overview, resources and exploitation. CODES

European Commission (2008) The raw materials initiative — meeting our critical needs for growth and jobs in Europe

Gregoir L, van Acker K (2022) Metals for Clean Energy: Pathways to solving Europe's raw materials challenge. Eurometaux

IEA (2021) The Role of Critical Minerals in Clean Energy Transitions. OECD Publishing, Paris

Mudd GM, Jowitt SM (2022) The New Century for Nickel Resources, Reserves, and Mining: Reassessing the Sustainability of the Devil's Metal. Econ Geol 117:1961–1983. https://doi.org/10.5382/econgeo.4950

Nickel Institute (2023) Nickel in batteries. https://nickelinstitute.org/en/about-nickel-and-its-applications/nickel-in-batteries/. Accessed 9 Feb 2023

A mineralogical characterization of an antimony tailings dam: Implications for antimony recovery

Rembuluwani S. Ravele[1], Karel S. Viljoen[1], Derek H. Rose[1,2]
[1] Department of Geology, University of Johannesburg, P. O. Box 524, Auckland Park, 2006, South Africa
[2] Mintek, 200 Malibongwe Drive, Praegville, Randburg, 2194, South Africa

Abstract. Reprocessing of historical tailings storage facilities (TSFs) has gained momentum worldwide to address the demand for critical metals and minerals. Limited information about these repositories is available, hence the need to fill this knowledge gap. A tailings dam of the Murchison Greenstone Belt (MGB) was characterized to quantify the presence of economic antimony in terms of modal mineralogy, relative mineralogy and their associations (i.e. co-existing phases), and the deportment of antimony in various antimony-bearing minerals. Holes were drilled from the top to the bottom of the tailings dam to acquire samples for chemical and mineralogical characterization. A FEI 600F Mineral Liberation Analyzer (MLA) was used to characterize this tailings dam, accompanied by ICP-MS, XRF and LECO analyses. The MLA results, complemented by ICP-MS analyses revealed the occurrence of considerable amounts of Sb in this TSF. The TSF is mainly comprised of quartz, magnesite, chlorite and dolomite. Chapmanite and stibnite are the most abundant antimony-bearing minerals, along with other antimony minerals such as schafarzikite, senarmontite and berthierite. Significant antimony is mainly deported in stibnite, schafarzikite and senarmontite, with minor deportment into berthierite, cervantite, and other antimony phases.

1 Introduction

The Murchison Greenstone Belt (MGB) was the only antimony producer in South Africa, and produced about 18 % of the total world production by 1986, making it one of the biggest Sb producers in the world (Davis et al. 1986; Poujol and Robb 1999). A total historical estimation of 605 000 tonnes of antimony was mined from the MGB by 2015 (Pearton and Viljoen 2017). However, antimony production is now estimated to occur in a few countries, with China producing roughly 53 % of the world's production with no production from South Africa (Anderson 2019). The U.S. Department of the Interior has listed antimony as a critical mineral following the depletion of global resources and reserves while demand for antimony keeps growing (Anderson 2019).

The depletion of primary ore, coupled with the increase in commodity price and breakthroughs in extraction technology, has led to mine waste being considered as a secondary ore for critical metals and minerals (Lotternoser 2010).

Antimony has been mined along the antimony line (AL) of the east-north-trending MGB as a by-product of gold mining (Poujol and Robb 1999). The Weigel formation of the MGB hosts the prominent AL, where significant antimony mineralization occurs (Jaguin et al. 2012). The Weigel formation occupies the central part of the MGB, consisting of quartzite, quartz-chlorite-schist, quartz-muscovite-schist, minor banded iron formation and conglomerates (Davis et al. 1986; Jaguin et al. 2012). Mineralization along the AL is hosted by quartz-carbonate rocks, mainly quartz, dolomite and magnesite, with minor chlorite, talc and fuchsite. Antimony was mined in the form of stibnite and berthierite associated with pyrite and arsenopyrite from 18 mines (Poujol and Robb 1999).

The current study will only focus on the mineralogical characterization of the MGB antimony tailings dam to reprocess such tailings for antimony recovery. Major emphasis will be on antimony-bearing minerals.

2 Methodology

A total of five holes were drilled from the top to the bottom of the MGB Sb tailings dam with an automated auger drilling machine. Sampling holes were unevenly selected (R1 to R5 in Figure 1) based on accessibility and were selected to ensure representative sampling of the entire tailings repository. Samples were collected at 1.5 m intervals with depth and subsequently composited to produce three samples per hole (top, middle and bottom composite samples).

Each composite sample was split into two representative aliquots for chemical and mineralogical analyses. The first aliquot was sent to Intertek, Perth, Australia for geochemical analyses. Samples were analyzed by X-ray fluorescence spectrometry (XRF) for Al_2O_3, CaO, Cr_2O_3, Fe_2O_3, K_2O, MgO, MnO, Na_2O, SO_3 and SiO_2 (Intertek method FB1/XRF) with detection limits of 0.01 %. A combustion-infrared detection technique (Intertek method /CSA) was used to analyze C and S with detection limits of 0.01 %. Samples were also analyzed for Sb by ICP-MS (Intertek method 4A/MS) with a detection limit of 0.05 ppm. The second aliquot was used to prepare two transverse (90°) resin mounts from each composite sample for bulk modal mineralogical and relative modal mineralogical studies using a FEI 600F Mineral Liberation Analyser (MLA) (Gu, 2003; Fandrich et al. 2007). Bulk modal mineralogical composition was achieved through the XMOD mapping routine, whereas the SPL-GXMAP mapping routine was used for detailed assessment of antimony-bearing minerals. Analytical accuracy and precision of chemical data were monitored through duplicate analysis of selected samples and comparing the assay data to the MLA calculated assay data for quality assurance.

Figure 1. ArcGIS map showing the sampling points where samples were collected (marked R1 to R5).

3 Results

3.1 Tailings chemistry

Assay results of the antimony tailings dam samples from the MGB were combined and an average of the top, middle and bottom composites, are presented in Table 1. The table illustrates major and minor oxides encountered within this tailings dam, Sb, Au, total carbon and sulfur contents, and loss of ignition (LOI). The tailings dam under study contains SiO_2, MgO, Fe_2O_3, Al_2O_3, and CaO making up 78 % of the bulk composition of the samples while LOI makes up 20 %. Antimony was detected with an average value of 6955 ppm. Total C and S contents average 4.76 and 0.34 %, respectively. Minor oxides such as SO_3 (0.8 wt%), Na_2O (0.4 wt%), K_2O (0.2 wt%), Cr_2O_3 (0.2 wt%) and MnO (0.1 wt%) were also detected. Lesser gold was detected with an average of 0.6 ppm.

3.2 Tailings mineralogy

Mineralogical data is presented as a bulk composition of the top, middle and bottom following the observation that the modal mineralogy of the top, middle and bottom of each hole was identical. This study revealed that this tailings dam is primarily made up of quartz, followed by magnesite, chlorite and dolomite occurring at abundances ranging between 27 to 33 wt%, 16 to 22 wt%, 11 to 12 wt% and 8 to 9 wt%, respectively (Figure 2). Antimony-bearing minerals make up 1 to 3 wt% (abundance of each mineral to be discussed under relative modal mineralogy). Other minerals such as amphibole, pyroxene and feldspar were identified at abundances averaging 7 wt%, 5 wt% and 2 wt%, respectively.

Table 1. Analysis (assay data) of the top, middle and bottom composite samples from the MGB's tailings dam.

Elements	Top	Middle	Bottom	Average
Au (ppm)	0.4	0.4	0.9	0.6
Sb (ppm)	5754	6908	8202	6955
S (wt%)	0.2	0.3	0.5	0.3
C (wt%)	5.2	4.7	4.4	4.8
SiO_2 (%)	43.4	45.8	47.6	45.6
MgO (%)	18.1	17.2	15.1	16.8
Fe_2O_3 (%)	6.5	6.6	7.5	6.9
Al_2O_3 (%)	4.7	4.8	4.7	4.7
CaO (%)	4.0	3.9	4.2	4.0
SO_3 (%)	0.5	0.7	1.3	0.8
Na_2O (%)	0.4	0.4	0.4	0.4
K_2O (%)	0.3	0.2	0.2	0.2
Cr_2O3 (%)	0.2	0.2	0.2	0.2
MnO (%)	0.1	0.1	0.1	0.1
LOI (%)	20.1	18.4	17.1	18.5

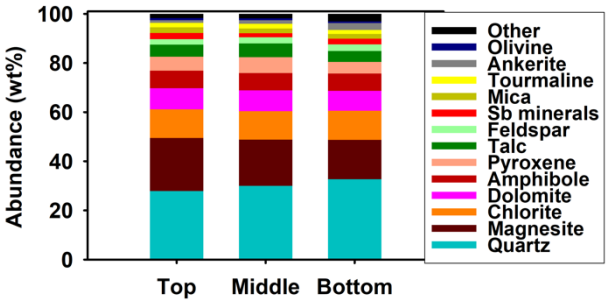

Figure 2. Stacked bar graphs depicting the MGB tailings dam's bulk modal mineralogy. Minerals were plotted in order of abundance with the most abundant mineral at the bottom of the stack and the least abundant mineral at the top.

3.3 Antimony-bearing minerals and their abundances

The MLA identified a total of 11 Sb-bearing minerals and the abundances of these are presented in Figure 3. This includes six Sb-bearing sulfide minerals (berthierite, gudmundite, Ottensite, stibnite, tetrahedrite and ullmannite), four secondary (oxide) Sb minerals (cervantite, schafarzikite, senarmontite and valentinite) and a silicate mineral (chapmanite). The data obtained from the MLA in wt% was normalized to the total Sb-bearing mineral population and presented as a relative percentage. Stibnite (Sb_2S_3) is the most abundant Sb-bearing mineral with values ranging between 28 to 46 % as observed at the top, middle and bottom of the tailings dam. Chapmanite ($Sb^{3+}Fe^{3+}{}_2(SiO_4)_2(OH)$), the only silicate Sb-bearing mineral identified in this study, is the second most abundant Sb-bearing mineral with an average value of 21 %. Gudmundite (FeSbS) and berthierite ($FeSb_2S_4$) form part of the most abundant Sb-bearing sulfide mineralisation with abundances of 7 to 12 %, and 3 to 9 %, respectively. Secondary

Sb-bearing minerals such as schafarzikite ($Fe^2Sb_2O_4$), senarmontite (Sb_2O_3) and valentinite (Sb_2O_3) were also identified with values ranging from 9 to 16 %, 5 to 9 % and <1 %, respectively. Figure 4 shows false colour images of some Sb-bearing minerals that the MLA encountered.

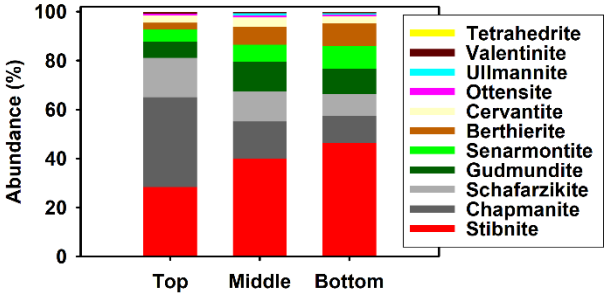

Figure 3. Stacked bar graphs depicting the abundance of antimony-bearing minerals with depth. Minerals were plotted in order of abundance with the most abundant mineral at the bottom of the stack and the least abundant mineral at the top.

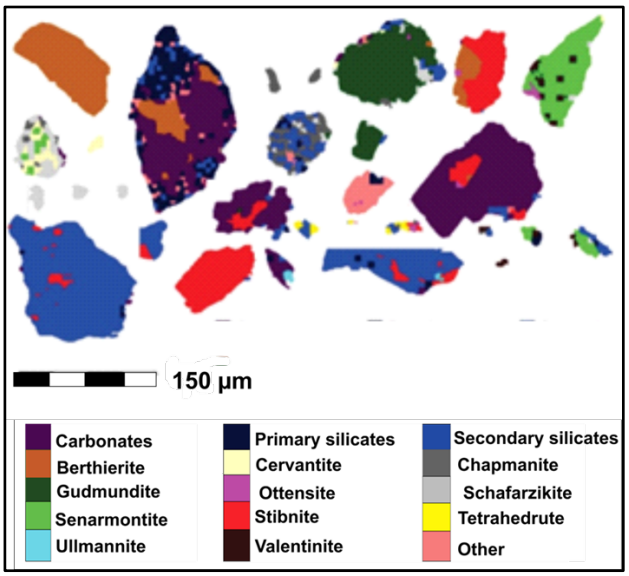

Figure 4. False color MLA images of some selected polished blocks showing antimony-bearing minerals and their association.

3.4 Antimony deportment

The bulk of the antimony from the MGB's tailings dam deports into stibnite (35 to 50 %), followed by schafarzikite (9 to 18 %) and senarmontite (7 to 12 %). Negligible amounts of antimony, 0.04 to 0.1 %, 0.3 to 0.9 and 0.6 to 0.9 %, deports in tetrahedrite, ullmannite and valentinite, respectively (see Figure 5).

3.5 Mineral association

Minerals that are not fully liberated are either associated with one mineral phase (binary) or two or more mineral phases (ternary). Figure 6 clearly illustrates Sb-bearing minerals being highly associated with secondary silicates, followed by primary silicates, carbonates and oxides. For simplicity when presenting the mineral association data, gangue minerals from the same mineral group were combined into four groups (i.e. carbonates, primary silicates, secondary silicates and other). As previously described the tailings consist mainly of quartz, magnesioferrite, chlorite and dolomite. These abundances are evidence of mineral associations as most of the Sb-bearing minerals are associated with these minerals.

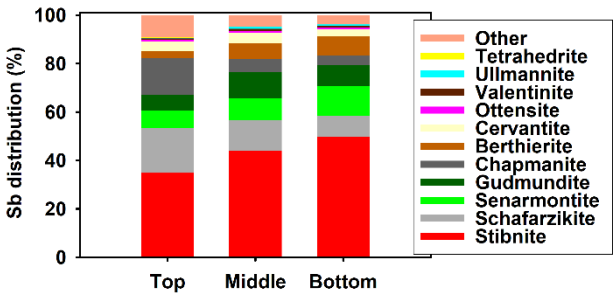

Figure 5. Stacked bar graphs showing the deportment of Sb in antimony-bearing minerals.

4 Discussion and conclusion

Based on the automated mineralogy results, the dominant gangue minerals are quartz, magnesite, chlorite and dolomite and minor amphiboles, pyroxene and feldspars. Antimony-bearing minerals mainly occur as sulfides, making up 56 % of the bulk Sb mineralisation (with stibnite as the main Sb-bearing sulfide), Sb oxides (23 %) and Sb silicates (21 %). Furthermore, about 45 % of Sb is deported into stibnite and approximately 25 % is deported into Sb oxides. The main Sb sulfides are primarily associated with secondary silicates (mostly quartz) and carbonate minerals (mostly magnesite) and have a minor association with primary silicate and other gangue minerals.

Antimony concentrations within the tailings dam under study generally increase with depth with the lowest (5754 ppm) and highest (8202 ppm) values occurring at the top and bottom parts of this tailings dam, respectively.

It was also noted that Sb-mineralisation in sulfide minerals (stibnite, gudmundite and berthierite) increases with depth. Stibnite and other Sb-sulfides oxidize rapidly (within days or weeks), under atmospheric conditions (Klimko et al. 2011; Álvarez-Ayuso et al. 2022) resulting in lower Sb-bearing sulfides at the top of the tailings pile compared to the bottom where oxidation rarely occurs. Secondary antimony-bearing minerals such as senamontite, valentinite and cervantite (the most common secondary antimony minerals) were most likely formed from the oxidation of stibnite and other antimony-bearing sulfides (Álvarez-Ayuso et al. 2022). This is evidence following the abundance of secondary minerals (Sb oxides) being abundant at the top of the tailings dam and less abundant at the bottom. It can be concluded from the deportment

results that bulk of Sb deports into Sb-sulfide mineralisation and less abundance occurs in secondary Sb-minerals. Antimony deportment in Sb-bearing sulfide minerals was less abundant at the top of the pile and more abundant at the bottom.

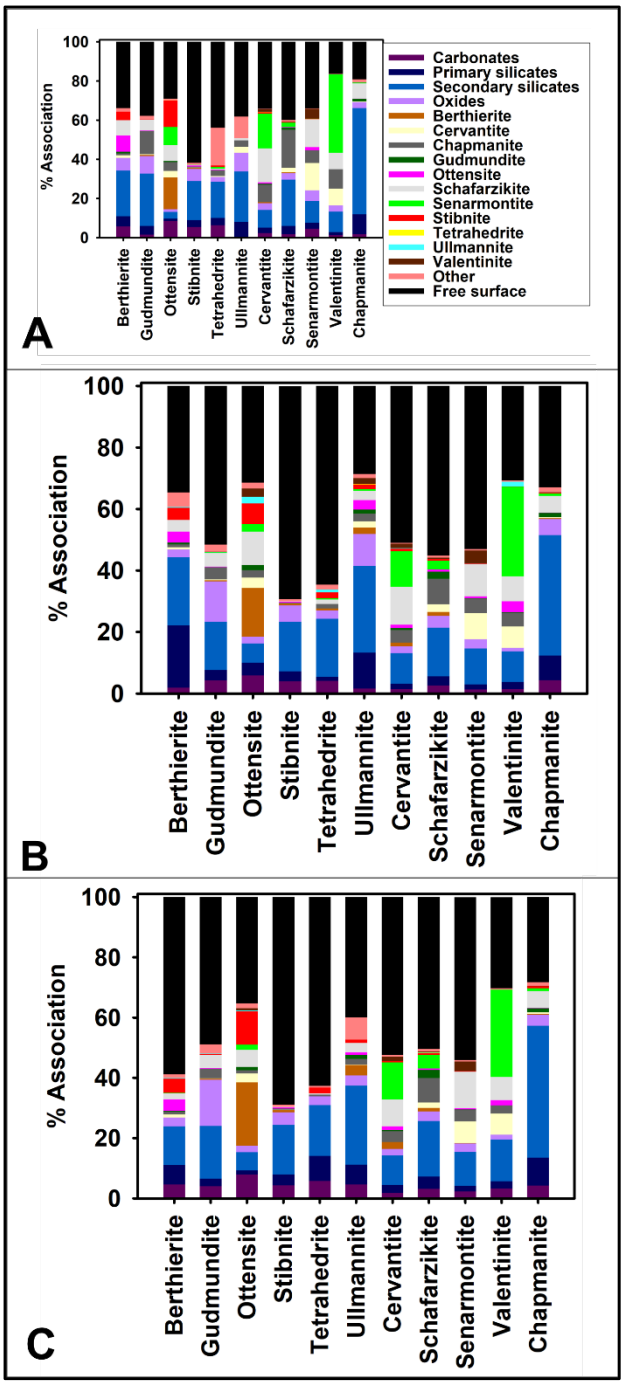

Figure 6. Stacked bar graphs depicting the mineral association of all antimony ore minerals with other minerals. (A) = Mineral association of antimony ore minerals for the top of the TSF. (B) = Mineral association of antimony ore minerals for the middle of the TSF. (C) = Mineral association of antimony ore minerals for the bottom for the TSF.

Since Sb in this TSF mostly deports into stibnite and other Sb-bearing sulfide minerals such as berthierite and gudmundite, alongside gangue minerals such as quartz, magnesite and other carbonate minerals, heavy medium separation and bulk sulfide flotation is recommended for antimony recovery (Anderson 2012). However, laboratory-scale metallurgical test work is recommended to deduce the possible antimony recovery before concluding the economic importance of this TSF.

Acknowledgments

Exceptional gratitude to the mine for granting permission to conduct this study and mine staff who assisted with acquiring samples and data. Prof. K.S. Viljoen acknowledges funding from the South African Department of Science and Innovation under their Research Chairs initiative, as administered by the National Research Foundation. Gabrielle van Heerden is thanked for her guidance on the Mineral Liberation Analyser.

References

Álvarez-Ayuso E, Murciego A, Rodríguez MA, Fernández-Pozo L, Cabezas J, Naranjo-Gómez JM, Mosser-Ruck R (2022) Antimony distribution and mobility in different types of waste derived from the exploitation of stibnite ore deposits. Science of The Total Environment 816: 151566.

Anderson CG (2012) The metallurgy of antimony. Geochemistry 72:3-8.

Anderson CG (2019) Antimony production and commodities. In: Kawatra K, Young CA (ed) SME mineral processing and extractive metallurgy handbook. Society for mining, metallurgy and exploration, Englewood, pp 1557-1568.

Davis DR, Paterson DB, Griffiths DHC (1986) Antimony in South Africa. Journal of the Southern African Institute of Mining and Metallurgy 86:173-193.

Fandrich R, Gu Y, Burrows D, Moeller K (2007) Modern SEM-based mineral liberation analysis. International Journal of Mineral Processing 84:310-320.

Gu Y (2003) Automated scanning electron microscope based mineral liberation analysis. Journal of Minerals and Materials Characterization and Engineering 2:33-41.

Jaguin J, Gapais D, Poujol M, Boulvais P, Moyen JF (2012) The Murchison greenstone belt (South Africa): a general tectonic framework. South African Journal of Geology 115:65-76.

Klimko T, Lalinsk B, Majzlan J, Chovan M, Kucerova G, Paul C (2011) Chemical composition of weathering products in neutral and acidic mine tailings from stibnite exploitation in Slovakia. Journal of Geosciences 56:327-340.

Lottermoser BG (2010) Tailings. In: Mine wastes: characterization, treatment and environmental impacts. Springer, Berlin, Germany, pp 205-241.

Pearton TN, Viljoen MJ (2017) Gold on the Kaapvaal Craton, outside the Witwatersrand Basin, South Africa. South African Journal of Geology 120:101-132.

Poujol M, Robb LJ (1999) New U-Pb zircon ages on gneisses and pegmatite from south of the Murchison greenstone belt, South Africa. South African Journal of Geology 102:93-97.

Distribution of critical elements in rocks and fluids, Taupo Volcanic Zone, New Zealand

Agnes G. Reyes[1]
[1]GNS-Science Lower Hutt, New Zealand

Abstract. Elements with the highest concentrations (>100kg/a) in the Taupo Volcanic Zone (TVZ) geothermal fluids, from lowest to highest, include Mo, Sb, Sr, W, Al, Cs, Rb, As, Li, Ca, B, Si and Na. Although discharge fluids produce only ~1-75 kg/a of Au, Ga, Tl, Ag, Ge, Rb and Cs, their high market prices warrant further study. Amongst gases of economic interest in the TVZ are CO_2 mainly for food processing, C_2H_6 and He. It is estimated that one producing geothermal system has ~NZ$850M/a worth of elements or ~NZ$19.5B/a for 23 systems. However, despite the presence of a wide range of critical elements in the TVZ fluids, only a few can be economically and technologically extracted at present.

1 Introduction

The terms “critical” or “endangered” elements refer to supply risks (https://www.acs.org) of ~90 economically significant natural elements (https://www.euchems.eu). Based on 2021 consumption levels, 12 elements from He to Ta are deemed to be in serious threat in the next 100 years. Another 12 are under rising threat and 19 are of limited availability and at future risk to supply from increasing use in rechargeable batteries and green energy devices, solar panels, aircraft engines, thermal imaging devices, GPS equipment, defense equipment and others (e.g., Geology.com). Supply is plentiful for more than 35 elements. Carbon in the form of gases such as CO_2 and CH_4 is generally plentiful although there is a shortage of CO_2 for food processing in New Zealand. Carbon in the form of oil and natural gas is under serious threat as known subterranean supplies diminish and because some of the most productive oil fields are in regions of political unrest.

There are remediation procedures to decrease the supply risk of elements e.g., recycling, substitution with more abundant materials, devising new ways of manufacturing equipment with an intent to recycle, finding new methods or revamping old methods to extract elements from unconventional sources more economically such as seawater (e.g., https://pubs.usgs.gov), geothermal fluids and precipitates, metal scrap, biological sources and others. Several studies aver, however, that mineral resources in the earth’s crust are by no means depleted, with the search for new resources improved by modern geophysical exploration methods (e.g. Best 2015) and the supply extended by exploitation of resources with lower concentrations.

The focus of this study is the Taupo Volcanic Zone (TVZ) where numerous studies demonstrate the propensity for precious, base, alkaline and alkaline earth metals and non-metals to be precipitated on the surface, in hot springs and geothermal installations (e.g., Weissberg et al. 1979; Hedenquist and Henley 1985; Reyes et al. 2002; Rowland and Simmons 2012; Pope and Brown 2014), subsurface rock formations (e.g. Simmons and Browne 2000) and entrained as solutes in discharge fluids (e.g. Hirner et al 1998; Wood 2003). Most chemical elements precipitate in the well and rock formations resulting to very low concentrations in surface fluid discharges and thus, downhole well samples have been analyzed by various workers (e.g. Simmons et al 2016).

The objectives of this paper are to examine the sources of critical elements (1) from volcanic contributions found in melt inclusions, leached from erupted volcanic ash or held in fresh volcanic rock, (2) contributed by greywacke and (3) enhanced by hydrothermal processes and water-rock interaction. This study also includes an evaluation of the mass (kg) of elements that can potentially be extracted from fluids discharged in TVZ geothermal systems.

2 Geological setting

The TVZ is a back arc rift developed from the oblique convergence of the Australian and Pacific plates along the Hikurangi margin east of the North Island (e.g. Acocella et al. 2003). The region is the locus of unusually voluminous rhyolite volcanism in the last 1.6 Ma and andesitic magmatism since 2.0 Ma with the volume of erupted rhyolites an order of magnitude higher than andesites (Wilson et al. 1995). Andesites occur only in the northernmost and southernmost regions of the TVZ (Rowland and Sibson 2004). There are at least 23 active hydrothermal systems with an estimated heat output of 4.2 GWt expelling at least 10^8 m^3/a (10^{11}kg/a) of aqueous fluids (Bibby et al. 1995). Six to eight of these systems are utilized for power production with an installed net capacity of more than 940 MWe (www.nzgeothermal.org.nz).

Except for magmatic-hydrothermal systems at Tongariro and White Island all other geothermal/hydrothermal systems in the TVZ are liquid-dominated. Two geochemically distinct source fluids were identified by Giggenbach (1995): subduction-related usually associated with andesitic volcanism, and rift-type associated with rhyolites and high-alumina basalts. Subduction-related or arc-type hydrothermal fluids, confined in the eastern side of the TVZ, are characterized by higher CO_2 contents, CO_2/Cl mole ratio, $CO_2/^3$He, N_2/Ar, B/Cl, Li/Cs and magmatic component than rift-type fluids. However, median Cl contents from well discharges are higher in rift-type (~1000 mg/kg) than in arc-type (~600

mg/kg) fluids. The annual mass flow of aqueous fluids and heat output of rift-type systems are 7x and 8x higher, respectively, than arc-type systems.

3 Results

An idealized cross-section of a typical TVZ hydrothermal system (Figure 1A) shows two major lithologies: the Mesozoic greywacke basement at depth overlain by igneous rocks. Sedimentary beds at shallower depths with tuffaceous intercalations are grouped under volcaniclastics due to similarities in chemical compositions.

3.1 Critical elements in greywacke, melt inclusions, fresh volcanic rocks and erupted ash

Concentrations of elements in the Mesozoic greywacke are either similar or less than in the earth's crust except for Au, B, As, Bi and S which are enhanced by 2x to 4x (this study). However, hot water-rock interaction experiments showed that volatile species such as As, Sb, Se and S can be extracted from greywacke in significant amounts (Ewers 1977).

Critical elements in volcanic fluids and rock are gleaned from melt inclusions and glass, and erupted lavas and tephras (2-4 in Figure 1A; e.g. Ewart et al. 1968; Reyes et al. 2012, Johnson et al. 2013; this study). Boron and Cl are more enriched in rhyolitic than andesitic melt inclusions. Melt inclusions show that pre-eruptive rhyolitic and andesitic magmatic fluids contain Fe, Ti, Co, Cu, V, Cr, Zn and Ni in various proportions but Mo, Hg, Pb and As appear to have a stronger affinity for rhyolite melts and Ge for andesite.

Erupted TVZ rhyolitic and andesitic lavas/tephra both show enrichment in Hg, As, B, and Ge relative to normal crustal abundances. However, Sb, Tl, Mo, Au, Cs, Li and Ba abundances are enhanced in rhyolite and I, Br, Se, Bi, Sc, Co and Cu in andesites, relative to the earth's crust (this study).

The volume of critical elements introduced to the surface by ash falls is illustrated by the 1995-1996 eruption of the andesitic Ruapehu volcano albeit mixed with materials from Crater Lake (this study). For a small eruptive episode of 0.04 km^3 of ash (Cronin et al. 1998), $\geq$1 kg each of Tl, Ag, Cd, Se, Cr, As, Li, Co, Ni, Pb, Cu, Zn, Mn, B and Fe together with F, Cl, and SO_4 was expelled from Ruapehu in less than a year.

Knowing that certain elements have a stronger affinity for rhyolite, andesite or greywacke in the TVZ may aide mining companies prospecting for critical elements in fluids. However, elemental affinities for specific rock compositions break down during hydrothermal or magmatic-hydrothermal water-rock interaction, evinced by leachate compositions from erupted ash at Ruapehu, that included materials from Crater Lake.

3.2 Water-rock interaction and critical elements in altered rock and fluid precipitates

Figure 1A shows some of the processes that enhance element deposition in the TVZ including (a) fluid mixing and neutralization of acid fluids, (b) phase separation and changes in redox conditions, (c) changes in temperature and pressure with depth or caused by hydrothermal brecciation and (d) water-rock interaction and rock dissolution.

Intensely altered rhyolite in surface hot springs, contain 2x to 200x, relative to fresh rhyolite, of most elements e.g., Cu, Zn, Sr, Ga, and Au and to 2x to >1000x of volatile elements (Tl, Hg, Sb and As). In contrast, moderately chloritized and silicified rhyolite altered at 270°C at depth is only enriched by 2x-50x, relative to fresh rock, in Cu, V, Cr, P, Mn, Ti, Mg, Ca and Fe (this study).

At least 24 mineral precipitates have been identified in hot springs, well casings and well surface installations in the TVZ (Figure 1B) containing Fe, As, S, Cu, Sb, Zn, Ag, Te, Pb, Ag and Au (e.g. Weissberg, 1969; Brown, 1986; Krupp and Seward, 1987; Reyes et al. 2002; Pope et al. 2005; Simmons et al. 2016; this study). The main mineral deposited in wells, well surface installations and hot springs is silica, a "sponge" for a several elements including Li, B, Cr, Ni, Cu, Zn, As, Ag, Hg, Sb, Au, Rb and Cs (Brown, 1986; Reyes et al. 2002). Other substrates to which elements preferentially adhere to include biogenic material for Hg, Ge, As, Sb and Te (Hirner et al. 1998) and possibly pyrite and fahlore (e.g. Makovicky and Karup-Moller, 2017). Rare earths have been reported in hot spring silica sinters and rock formations at depth, enhanced where acid waters circulate (e.g. Wood, 2003).

In summary, the chemical compositions of melt inclusions, rock, mineral precipitates and ash leachates in the TVZ show (1) enhanced abundance of a wide number of critical elements including Te, Zn, Ga, As, Ge, Ag, Y, Sr, U, Cu, Cd, Co, Cr, Dy, Li, B, Mg, P, Sc, V, Ni, Zr, Nb, Mo, Sn, Sb, W, Au, Hg, Tl, Pb, Bi and Nd, (2) affinity of various elements for rhyolite or andesite, and (3) variations in element abundances in the rock with alteration intensity/degree of water-rock interaction, type and process, and fluid pH.

3.3 Fluid discharges

Not all elements in the rock have been analyzed or detected in the fluids. Except for halides, concentrations of most "critical" elements in TVZ aqueous fluids are lower than in the rock or precipitates from hydrothermal fluids. But there has been increased interest in extracting "critical" elements from fluids in the TVZ in the past 5 years.

To assess the potential of mining fluids, the annual mass of various "critical" elements produced by a typical geothermal system in the TVZ was calculated assuming a median flowrate of $3x10^6$ m^3/a (340 m^3/h) and a gas:aqueous fluid ratio of 3:7. The highest yield of elements, at >100kg/a include

from lowest to highest: Mo, Sb, Sr, W, Al, Cs, Rb, As, Li, Ca, B, Si and Na. There are two sets of elements that warrant further study: (1) Au, Ga, Tl, Ag and Ge, despite low yields at only ~1-75 kg/a, because of high market prices and (2) Rb and Cs because of high yield from fluids and high market prices. Amongst gases of economic interest in the TVZ are CO_2 mainly for food processing, C_2H_6 and He.

4 Conclusions

Without considering costs of extraction from fluids and mineral substrates, production and research, cut-off concentrations for mining elements, and current technological capabilities to extract elements from aqueous solutions or silica precipitates, a typical TVZ geothermal system contains ~NZ$850M/a worth of elements or ~NZ$19.5B/a for 23 active systems. The estimated value of Mo, As, Ag and CO_2 in fluids from one TVZ system is $10k-100k/a per element; 100k-1M/a for Au, C_2H_6, He, Ge, Tl and B and >1M/a for Li, Na, Cs, Rb and Si. Despite the presence of a wide variety of "critical" elements in TVZ hydrothermal fluids, only a few can be economically and technologically extracted at present e.g., Li, Si, possibly CO_2, and as world-wide supplies rapidly diminish, perhaps He.

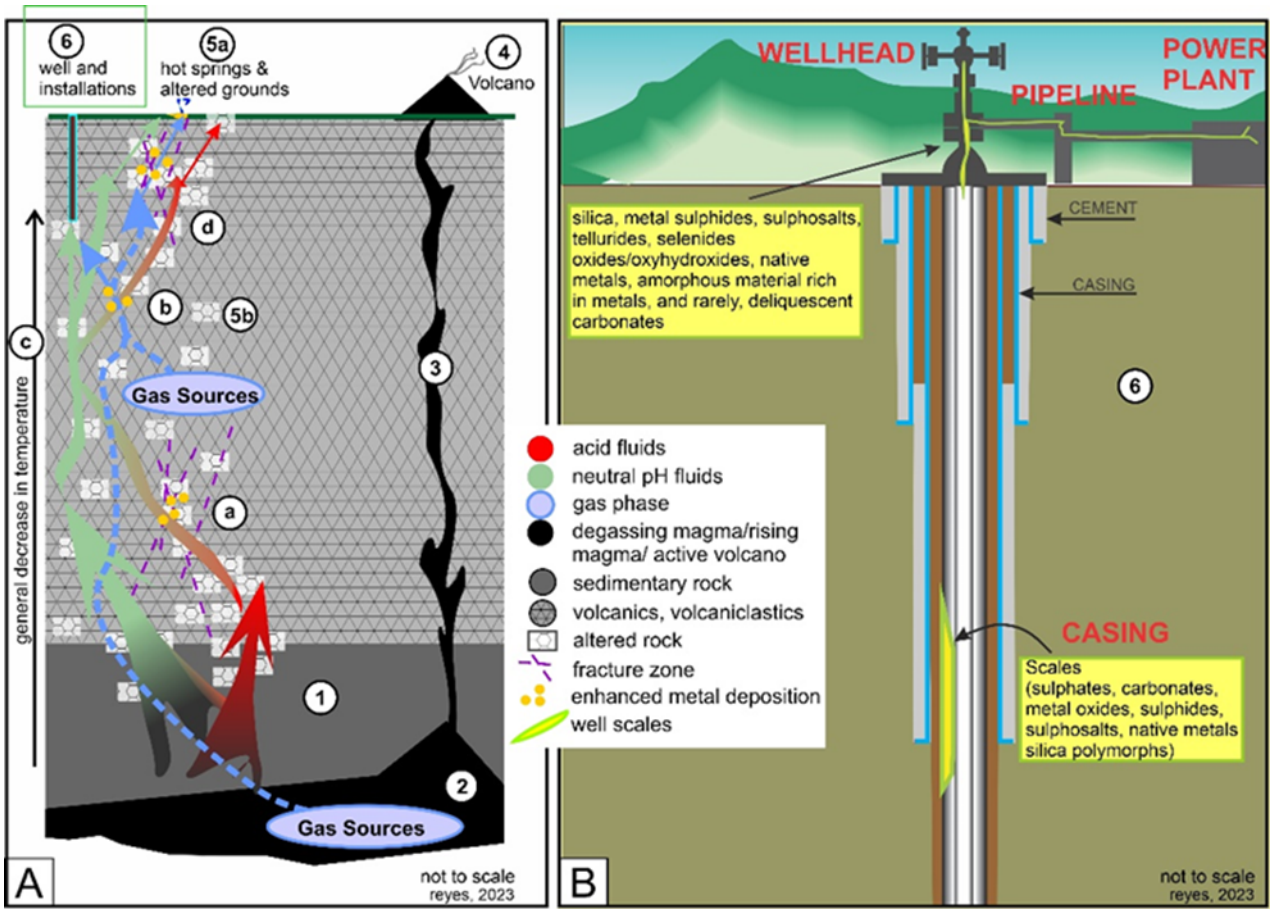

Figure 1. [A] Diagram showing major sources of critical elements in the TVZ marked by numbers and some sites of enhanced metal deposition in the rock formation (a, b, c and d), discussed in the text. Number 6 is shown in detail in [B] main sites and compositions of mineral deposition in a typical TVZ geothermal well and its surface installations (this study).

Acknowledgement

Part of this work was funded by the New Zealand Geothermal Future research programme.

References

Acocella V, Spinks, K, Cole, J, Nicol, A (2003) Oblique back arc rifting of Taupo Volcanic Zone, New Zealand Tectonics 22(4): 19-1 - 19-18

Best ME (2015) Mineral resources, Treatise on Geophysics. 11: 525-556

Bibby HM, Caldwell TG, Davey FJ, Webb TH (1995) Geophysical evidence on the structure of the Taupo Volcanic Zone and its hydrothermal circulation. JVGR, 68(1-3): 29-58.

Brown KL (1986) Gold deposition from geothermal discharges in New Zealand. Econ Geol 81: 979-983.

Cronin SJ, Hedley MJ, Neall VE, Smith RG (1998) Agronomic impact of tephra fallout from the 1995 and 1996 Ruapehu Volcano eruptions, New Zealand. Environ Geol 34(1): 21-30.

Ewart A, Taylor SR, Capp AC (1968) Trace and minor element geochemistry of the rhyolitic volcanic rocks, Central North Island, New Zealand, Contrib Min Petrol 18: 76-104.

Ewers, GR (1977) Experimental hot water-rock interaction and their significance to natural hydrothermal systems in New Zealand. Geochim Cosmochim Acta 41: 143-150.

Giggenbach WF (1995) Variations in the chemical and isotopic composition of fluids discharged over the Taupo Volcanic Zone. JVGR 68(1-3): 89-116.

Hedenquist JW, Henley RW (1985) The importance of CO2 on freezing point measurements of fluid inclusions:

evidence from active geothermal systems and implications for epithermal ore deposition. Econ Geol 80: 1379-1406.

Hirner AV, Feldman J, Krupp E, Grumping R, Goguel R, Cullen WR (1998) Metal(oid)organic compounds in geothermal gases and waters. Org Geochem 29(5-7): 1765-1778.

Johnson ER, Kamenetsky V, McPhie J (2013) The behaviour of metals (Pb, Zn, As, Mo, Cu) during crystallization and degassing of rhyolites from the Okataina Volcanic Centre, Taupo Volcanic Zone, New Zealand J Petrol 54(8): 1641-1659.

Krupp RE, Seward TM (1987) The Rotokawa geothermal system, New Zealand: an active epithermal gold-depositing environment, Econ Geol 82: 1109-1129.

Makovicky E, Karup-Moller, S (2017) Exploratory studies of substitutions in the tetrahedrite/tennantite-goldfieldite solid solution. Canadian Mineral 55: 233-244.

Pope JG, Brown KL (2014) Geochemistry of discharge at Waiotapu geothermal area, New Zealand- trace elements and temporal changes. Geothermics 51: 253-269.

Reyes AG, Trompetter WJ, Graham IJ (2012) Propensity for mineralization in volcanoes- evidence from melt inclusions. Intl J PIXE 22: 157−164.

Reyes AG, Trompetter WJ, Britten K, Searle J (2002) Mineral deposits in the Rotokawa geothermal pipelines, New Zealand. JVGR 119: 215-239.

Rowland JV, Sibson RH (2004) Structural controls on hydrothermal flow in a segmented rift system, Taupo Volcanic Zone, New Zealand. Geofluids4: 259-283.

Rowland JV, Simmons SF (2012) Hydrologic, magmatic, and tectonic controls on hydrothermal flow, Taupo Volcanic Zone, New Zealand: implications for the formation of epithermal vein deposits. Econ Geol 107: 427–457.

Simmons SF, Browne PRL (2000) Hydrothermal minerals and precious metals in the Broadlands-Ohaaki geothermal system: implications for understanding low-sulfidation epithermal environments Econ Geol 95: 971-999.

Simmons SF, Brown KL, Tutolo BM (2016) Hydrothermal transport of Ag, Au, Cu, Pb, Te, Zn, and other metals and metalloids in New Zealand geothermal systems: spatial patterns, fluid-mineral equilibria, and implications for epithermal mineralization, Econ Geol 111: 589-618.

Weissberg BG, Browne PRL, Seward TM (1979) Ore metals in active geothermal systems. In: Barnes HL (editor) Geochemistry of hydrothermal ore deposits, 738-780, John Wiley, New York.

Wilson CJN, Houghton BF, Pillans BJ, Weaver SD (1995) Taupo Volcanic Zone calc-alkaline tephras on the peralkaline Mayor Island volcano, New Zealand: identification and uses as marker horizons. JVGR 69(3-4): 303-311.

Wood SA (2003) The geochemistry of rare earth elements and yttrium in geothermal waters. In: Simmons SF, Graham I (editors) Volcanic, geothermal, and ore-forming fluids: rulers and witnesses of processes within the earth. SEG Special Publication 10: 133–158.

Ni-Co-As-Bi minerals in the Silius vein system, (SE Sardinia, Italy): The polymetallic evolution of a word-class fluorspar deposit

Ignazio Scano[1], Antonio Attardi[1], Fabrizio Cocco[1], Dario Fancello[1], Alessandro Murroni[2], Francesca Zara[1], Stefano Naitza[1]
[1]Università degli Studi di Cagliari, Dipartimento di Scienze Chimiche e Geologiche, Monserrato, Italy
[2]Mineraria Gerrei Srl, Silius, Italy

Abstract. The world-class Silius deposit (NE Sardinia, Italy), exploited for decades, represents a huge ENE-WSW to NE-SW directed vein system, characterized by abundant fluorite, minor barite, and Pb-(Zn-Cu-Fe) sulphides in quartz-carbonate gangue. This deposit shows many similarities to other European unconformity-related F-Ba districts linked to the regional-scale event of the breakup of Pangea, such as ore textures, low-temperature high-salinity fluids, and observed mineral assemblages. Besides fluorite, the mineralogy includes other critical raw materials (CRM) such as disseminated tiny LREE minerals and intergrowths of Ni-Co-Fe arsenides-sulpharsenides such as nickeline (NiAs), rammelsbergite ($NiAs_2$), gersdorffite (NiAsS), cobaltite (CoAsS) and arsenopyrite (FeAsS). Ni-Co assemblages, which were recently discovered in this deposit, were investigated by optical microscopy and SEM-EDS.

1 Introduction

In the last few years, the growing demand for critical raw materials, which are strategic and irreplaceable in many technological and industrial applications, led to a renewed interest in many deposits throughout Europe, even those that until recently were no longer considered worthy of exploitation. An example is the world-class Silius fluorspar deposit (Gerrei district, SE Sardinia, Italy), a hydrothermal vein system that was exploited for fluorite, galena, and barite for over 50 years and is currently on standby. The original size of the deposit was probably over 10 Mt of fluorspar ore; currently certified (proved) reserves consist of over 2.1 Mt at 32% CaF_2 and 3% Pb (Benz et al., 2001). Moreover, following the discovery of LREE minerals in the carbonate gangue, over 1200 tons of LREE are estimated to occur in the deposit (Mondillo et al. 2016, 2017). The reprise of mining led to the resumption of exploration activities, including new structural surveys and new studies on ore mineral associations, to improve the geological model of the deposit and the basic knowledge of its economic potential, particularly in the field of critical metals. This study initially focused on the less investigated sulphide portion of the ore, which led to the unexpected discovery of Ni-Co-Fe arsenide-sulpharsenide mineral associations in the lowest levels of the mine, at 400-500 m under the surface.

2 The Silius deposit

2.1 Geological and structural setting

The Silius mine is set in the External Nappe Zone of the Variscan basement of SE Sardinia. Country rocks are low-grade metamorphic rocks belonging to the Gerrei and Sàrrabus tectonic units, unconformably covered by Cenozoic sediments (Funedda et al. in press, Figure 1). Basement rocks consist of a strongly folded pre-Variscan succession, including a thick Cambrian-Lower Ordovician siliciclastic sequence, arc-related Middle Ordovician calc-alkaline felsic metavolcanics (the “Porfiroidi Auct.” Formation), Upper Ordovician siliciclastics., Silurian and Devonian black shales and meta-limestones.

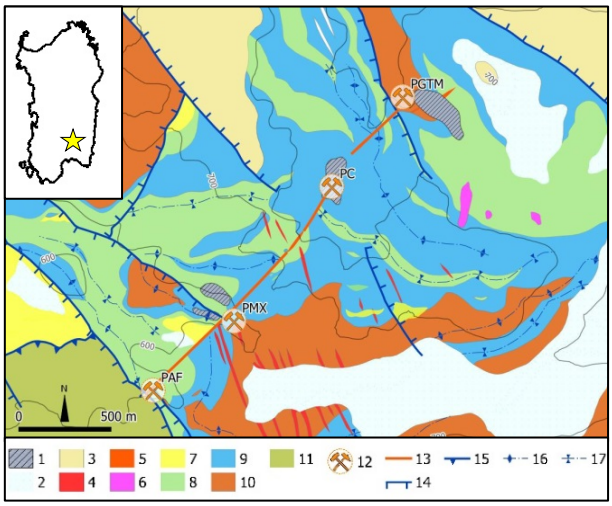

Figure 1. Geological sketch map of the Silius mine area. Legend: 1) Anthropic deposits. Hol.; 2) Recent sediments. Hol.; 3) Marine deposits. Low. Eoc.; 4) Granite porphyry dikes. Perm.; 5) Hydrothermal quartz veins Perm.; 6) Gabbro-diorites. Up. Carb.-Perm.; 7) Black shales and limestones. Sil.-Dev.; 8) Slates and metasandstones Up. Ord.; 9) Metarkose. Up. Ord.; 10) Porphyritic metarhyodacites. Mid. Ord.; 11) Metaquartzarenites. Cambr.-Ord.; 12) Mineshaft; 13) Silius mineralized vein; 14) Normal Fault; 15) Thrust; 16) Anticline fold; 17) Sincline fold

Late Variscan granitoids are poorly exposed in the area, being essentially represented by a large NW-SE swarm of Early Permian felsic dikes that crosses the basement detaching from the Sàrrabus pluton, which emerges more than 15 km further South. The Cenozoic sediments form a series of morphological plateaux resulting from an Eocene transgression over the Paleozoic basement.

The Variscan succession of the Gerrei Unit is located at the hanging wall of the regional "Villasalto Thrust", and it's organized in kilometres-scale recumbent folds verging towards the SW, with their parasitic folds occurring at any scale, producing an increase in the apparent thickness of the involved formations (particularly the Ordovician metavolcanics and metasandstones) and their repetition at depth. The Variscan post-collisional extension (late Carboniferous-Early Permian) resulted in the area as a widespread reactivation of thrust structures, with incremental development of low-angle to high-angle faults. A further reactivation of Paleozoic structures is documented by NW-SE, N-S and E-W directed faults associated with the Sardinian block rotation during Oligo-Miocene; these late structures determined the subdivision into blocks of the basement and the Eocene covers that currently mark the morphology of the area.

2.2 Geology of the deposit

The Silius vein system forms a pinch-and-swell structure, mainly hosted in the "*Porfiroidi Auct*." formation's felsic metavolcanics andOrdovician metasediments. The veins distinctly crosscut all the Variscan structures, including the Early Permian felsic dikes, defining a relative minimum age for the mineralizing event(s) (Natale 1969). The mineralised system consists of two principal parallel veins, namely the San Giorgio and San Giuseppe veins. They strike NE-SW to ENE-WSW, steeply dipping towards NW and coalescing at a depth of about 350 m (about 350m a.s.l.), where they reach 16 m in thickness against the medium thickness of 1 to 3.5 m of a single vein. The overall geometry of the veins, the structural context, and other kinematic features indicate a dextral sense of shearing, prevalent over the vertical component, which kinematic remains unclear, but presumably later reactivated as a high angle normal slip fault. The continuity of the vein system is interrupted to the NE and SW by two major NW-SE normal faults, which give the deposit a trapezoidal shape, with an extension of about 2km on the surface and almost 4km at the deepest exploitation level 100 (the name of the level refers to its location above sea level). Several minor normal faults with a strike-slip component crosscut the deposit at various angles, displacing it from null to about 2m.

The San Giorgio vein formed first and is characterised by alternating bands of chalcedony, pink fluorite, barite, and calcite. The San Giuseppe vein is also banded and shows several generations of fluorite, calcite, and galena (Boni et al. 2009, Mondillo et al. 2016). Both veins show early banded textures, followed by breccias and cockade textures. At the deposit scale, the mineralisation displays an evident vertical compositional evolution. In the shallower part of the deposit, the ore consists of an association of barite (prevalent) + fluorite + quartz ± calcite; the middle zone shows an increase in fluorite content (25% and more), along with calcite and sulphides, with the almost total disappearance of barite; at-depth, calcite is often dolomitised, fluorite is always > 30% and the ore shows a marked increase in sulphide content, mainly galena, observed as veins, aggregates and disseminations (Marino, 1996). Fluid inclusion studies on fluorite and calcite (Boni et al. 2009) indicate ore formation at temperatures in the range of 120–180 °C from fluids with salinities reaching up to ~18wt.% NaCl eq. In addition, Sr-Nd isotopic ratios and (REE + Y) contents in fluorite suggest a crustal origin of mineralising fluids likely from mixing in different proportions of evaporated seawater brines with fluids from the Paleozoic basement and Late Variscan magmatic rocks (Castorina et al. 2020). Moreover, Sm/Nd dating of carbonate gangue of the San Giuseppe vein by Castorina et al. (2020) provided an age of 294±40 Ma, but the Authors suggest as most likely an age around 270 Ma.

3 Methodology

New underground surveys and samplings were performed in three different sites at the 100 and 200 levels of the Silius mine (namely, from E to W, Pozzo Centrale, Muscadroxiu and S'Acqua Frida mineworks) mostly involving the Pb-Zn-Cu sulphide assemblages. The collected samples were studied both by optical microscopy (transmitted and reflected polarized light) and scanning electron microscopy (SEM-EDS), using a FEI Quanta 200 equipped with a ThermoFisher Ultradry EDS detector at CeSAR laboratories of Università di Cagliari (Italy) under high vacuum conditions, acceleration voltage 25–30 Kv, spot size 5 µm.

4. New observations on the Silius sulphide ore: the Ni-Co and Bi assemblages

The sulphide ore of Silius shows a simple mineralogy, mainly represented by galena, sphalerite, and chalcopyrite, followed by pyrite/marcasite (Table 1). Remarkably, no traces of fahlore, a mineral that is commonly associated with galena ores in E Sardinia fluorite-bearing deposits, has been found so far. Galena is the most abundant sulphide; sphalerite is subordinate, found in transparent (colourless to yellow/brown in transmitted light), sometimes idiomorphic individuals and zoned aggregates. Chalcopyrite is much less common and found either alone or intergrown with sphalerite. Marcasite is the last to crystallise and occurs in veinlets that crosscut all the precedent sulphide minerals. It is particularly abundant in the samples from the Pozzo Centrale mineworks sampling zone and contains some relics of pyrite.

In this study, striking evidence derived from optical microscopy work was the discovery of a Ni-Co arsenide/sulpharsenide assemblage, reported here for the first time. This peculiar assemblage was found in samples from every sampling site as

disseminated tiny and complex intergrowths of various Ni-Co-Fe-As-S phases (Figs. 2). They are mainly associated with sulphides (chalcopyrite and less frequently galena) or dispersed in quartz gangue (Figure 2). On SEM-EDS semiquantitative analyses Ni-Co-Fe phases display a large compositional variation (Figure 2): mono- and di-arsenides such as nickeline (NiAs) or rammelsbergite ($NiAs_2$) are overgrown by various mixtures and solid solutions of Ni-Co-Fe sulpharsenides such as gersdorffite (NiAsS), cobaltite (CoAsS) and arsenopyrite (FeAsS). Ni-Co-Fe sulpharsenides also occur in mono- and di-arsenide-free intergrowths, or partly replaced by sulphides.

Rare Bi minerals were found as inclusions in the Ni-Co-Fe arsenide/sulpharsenide assemblages or as complex intergrowths dispersed in fluorite gangue (Figure 3). They mainly consist of probable bismuthinite and of an unknown phase containing bismuth, lead, copper, sulphur and oxygen (possibly a sulphosalt). In the paragenetic succession of the Silius metallic ore, the Bi and Ni-Co arsenide/sulpharsenide assemblage comes first before the sulphides. In Table 1, a first attempt to summarize these observations is shown.

Ore minerals	
Bi minerals	
Ni-Co arsenides/sulfarsenides	
Sphalerite	
Chalcopyrite	
Galena	
Pyrite/marcasite	

Table 1. The schematic paragenetic sequence of the ore mineral assemblages of the Silius deposit.

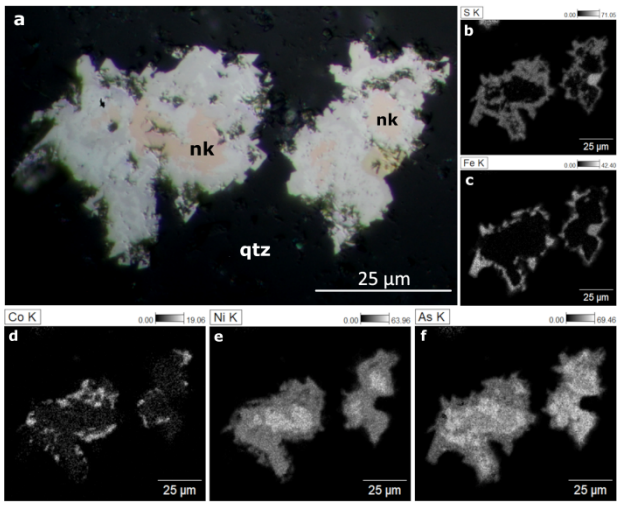

Figure 2. Reflected light photomicrograph (a) and SEM-EDS maps (b-f) showing a complex intergrowth of Ni-Co-Fe arsenides-sulpharsenides in quartz gangue. Nickeline (**nk:** pink) constitutes the core of the aggregate, rimmmed by rammelsbergite (pure white) overgrown by a complex mixture of Ni-Co-Fe sulpharsenides (gersdorffite, cobaltite, arsenopyryte).

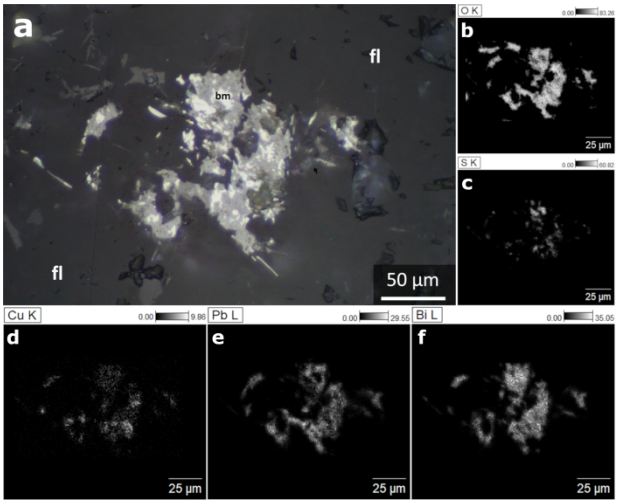

Figure 3. reflected light photomicrograph (a) and SEM-EDS maps (b-f) of an aggregate of Bi minerals (probable bismuthinite (bm) + a Bi-Pb-Cu sulphosalt) in fluorite gangue.

5 Discussion and Conclusions

5.1 Insights for future explorations: polymetallic evolution of the Silius deposit

The geological and mineralogical studies of this research confirm the high prospectivity of the Silius deposit. In detail, the study indicates that a) the ore composition presents an evident vertical variation, becoming progressively more complex with the deepening of the mineworks, and the deposit seems to acquire a true polymetallic character at depth; b) the CRM potential of the deposit, after the LREE phases (synchisite and xenotime-Y; Mondillo et al. 2016) is further expanded with the discovery of Ni-Co arsenides and Bi phases. Moreover, a comparison with the previous literature on fluorite-bearing polymetallic deposits in the Gerrei-Sàrrabus district (i.e., the so-called “Sàrrabus silver lode”; Cortecci et al. 1987 and references therein) in which Ni-Co sulpharsenides were found associated with abundant Ag sulphides and sulphosalts, suggest that this newly found Ni-Co mineral association could be considered as a predictive tool for future exploration in the deeper parts of the Silius deposit, as they may be indicative of the proximity of possible Ag-rich zones of the ore.

5.2 Metallogenic relevance of Ni-Co-Bi discovery: framing the Silius deposit at regional and European scale

Low-temperature (LT) hydrothermal veins are widely spread in the Paleozoic basement of Sardinia and are interpreted to have formed from circulating fluids during the Permian-Triassic time (Boni et al. 1992; 2002; 2009; Castorina et al. 2020). Recent studies on the Arburèse district of SW Sardinia

(Moroni et al. 2019a) allowed expanding this LT mineralisation dataset to the large Montevecchio vein system, whose southern branch has been fully included in the five-element (Ni-Co-As-Bi-Ag) class of hydrothermal deposits, hosting a rich Ni-Co arsenide-sulpharsenide mineral association (Moroni et al., 2019b). Although different in many compositional aspects (Montevecchio polymetallic sulphide ore has a quartz-carbonate gangue, with very rare fluorite), the new findings in the Silius deposit tend to bring these two types of mineralisation closer together, as also suggested by Boni et al. (2009) based on fluid inclusion studies. Thus, a wider metallogenic framework for the Permian-Triassic period in Sardinia, during which it is possible that multiple pulses of shallow crustal fluids mixed with seawater-derived brines (Cortecci et al., 1987; Castorina et al., 2020) is proposed. The reasons that explain the compositional differences between the different LT systems (i.e., Silius-type vs Montevecchio or five-element-type compositions) are speculative, but differences in basement rock geochemistry may have been a critical factor. The LT mineralising fluids that have led to the formation of the fluorite-rich Silius-type ores may have been derived from various F-bearing granite suites of the Sàrrabus pluton that intruded the Variscan basement in Early Permian (Secchi et al. 2021). The main features of the Silius deposit, including ore textures, mineral assemblages, and derivation from low-temperature and highly saline fluids resulting from the mixing of fluids of different origins, allow its comparison with the Mesozoic “unconformity-type” Ba-F and polymetallic deposits of Central Europe (Burisch et al. 2022). These latter were recently referred to late Permian to Cretaceous continental-scale metallogenic events related to the breakup of the Pangea supercontinent and the progressive opening of the Tethys and the North Atlantic Ocean (Burisch et al. 2022). In this large picture, and inside this complex family of deposits, the Silius vein system would therefore assume primary importance.

Acknowledgements

This work was supported by the RAS/FdS grant “Sustainable land management: the tools of geology for the environment” (F72F16003080002). The Authors acknowledge the Mineraria Gerrei Srl and G. Mura, Director of the Silius mine for IGEA SpA, for having allowed us to sample in the underground levels. Thanks are also due to Prof. G.B. De Giudici for SEM-EDS analyses, and equipment kindly provided by the CeSAR laboratory at the University of Cagliari.

References

Benz JP, Féraud J, Save M, Tréhin JL (2001) Expertise technico-économique de la mine de fluorine de Silius (Sardaigne) Rapport final: évaluation des réserves au 27.6.2001 et études de rentabilité. Rapport BRGM/RC-51042-FR

Boni M, Balassone G, Fedele L, Mondillo N (2009) Post-Variscan hydrothermal activity and ore deposits in southern Sardinia (Italy): selected examples from Gerrei (Silius Vein System) and the Iglesiente district. Per Mineral 78: 19–35

Boni M, Iannace A, Köppel V, Hansmann W, Früh-Green G (1992) Late- to post-Hercynian hydrothermal activity and mineralization in SW Sardinia. Econ Geol 87: 2113-2137

Boni M, Muchez P, Schneider J (2002) Permo-Mesozoic multiple fluid flow and ore deposits in Sardinia: a comparison with post-Variscan mineralization of Western Europe. Geol Soc Spec Pub 204: 199 – 211

Burisch M, Frenzel M, Seibel H, Gruber A, Oelze M, Pfänder JA, Sanchez-Garrido C, Gutzmer J (2021) Li-Co–Ni-Mn-(REE) veins of the Western Erzgebirge, Germany—a potential source of battery raw materials. Miner Deposita 56: 1223–1238

Burisch M, Markl G, Gutzmer J (2022) Breakup with benefits - hydrothermal mineral systems related to the disintegration of a supercontinent. Earth Planet Sci Lett 580: 117373

Castorina F, Masi, U, Gorello, I (2020) Rare earth element and Sr-Nd isotopic evidence for the origin of fluorite from the Silius vein deposit (southeastern Sardinia, Italy). J Geoch Explor 215: 106535

Cortecci G, Reyes E, Leone G, Turi, B (1987) Sulfur, Oxygen, Carbon, and Strontium Isotope Geochemistry of the Sarrabus-Gerrei Mining District, Southeastern Sardinia, Italy. Econ Geol 82: 1592–1610

Funedda A, Carmignani L, Pertusati PC, Forci A, Calzia P, Marongiu F, Pisanu G, Serra M (in print) Note illustrative Foglio 548 Senorbì. Note illustrative della Carta Geologica d’Italia 1:50000, ISPRA – RAS

Marino, A (1997) Il giacimento a fluorite e galena di Silius (Cagliari). C. Marini (Ed.): Le materie prime minerali sardi, problemi e prospettive, CUEC, Cagliari 258-268

Mondillo N, Boni M, Balassone G, Spoleto S, Stellato F, Marino A, Santoro L, Spratt J (2016) Rare earth elements (REE)—Minerals in the Silius fluorite vein system (Sardinia, Italy). Ore Geol Rev 74, 211–224

Mondillo N, Balassone G, Boni M, Marino A, Arfè G (2017) Evaluation of the amount of rare earth elements -REE in the Silius fluorite vein system (SE Sardinia, Italy). Per Mineral 86: 121-132

Moroni M, Naitza S, Ruggieri G, Aquino A, Costagliola P, De Giudici G, Caruso S, Ferrari E, Fiorentini M, Lattanzi P (2019a) The Pb-Zn-Ag vein system at Montevecchio-Ingurtosu, southwestern Sardinia, Italy: A summary of previous knowledge and new mineralogical, fluid inclusion, and isotopic data. Ore Geol Rev 115

Moroni M, Rossetti P, Naitza S, Magnani L, Ruggieri G, Aquino A, Tartarotti P, Franklin A, Ferrari E, Castelli D (2019b) Factors Controlling Hydrothermal Nickel and Cobalt Mineralization—Some Suggestions from Historical Ore Deposits in Italy. Minerals 9: 429

Natale P (1969) Il giacimento di Silius nel Gerrei. Boll Ass Miner Subalpina 6: 1–35

Secchi F, Naitza S, Oggiano G, Cuccuru S, Puccini A, Conte AM, Giovanardi T, Mazzucchelli M (2021) Geology of late-Variscan Sàrrabus pluton (south-eastern Sardinia, Italy). J Maps 17: 591-606

Critical Metal Resources Required for the Green Energy Transition

Adam C. Simon[1], Lawrence Cathles[2]
[1]Department of Earth & Environmental Sciences, University of Michigan, Michigan, U.S.A.
[2]Department of Earth & Atmospheric Sciences, Cornell University, New York, U.S.A.

Abstract. What does carbon neutrality mean? What does it require? Is it possible? In this presentation, I will discuss carbon neutrality through the lens of metal resources required to transition from a global energy infrastructure dependent on coal, natural gas, and oil, to one entirely reliant on a combination of photovoltaic solar, wind turbines, battery electric vehicles and grid-scale battery storage. Manufacturing and deploying those renewable energy resources requires dozens of metals, including cobalt, copper, graphite, lithium, manganese, nickel, rare earths, and many others. What types of mineral deposits do those metals come from? What are the geologic constraints on their availability? What are the economic constraints on their availability? What are the environmental permitting constraints on the timeframe for production and delivery to market? What are the political constraints on their availability? Analysis of the current mining supply of all metals required for the green energy transition, and the anticipated production from permitted mines at various stages of development, indicates that the demand for all critical metals required for the green energy transition will exceed supply by 2030. The green energy transition requires production of metals from new mineral deposits on an unprecedented scale.

1 Introduction

Our global society is electric, and copper is the backbone that delivers the electricity. Globally, society uses about 300% more copper every year than it did in 1960 (Figure 1) and demand for copper will increase significantly as renewable energy infrastructure is built (Figure 2).

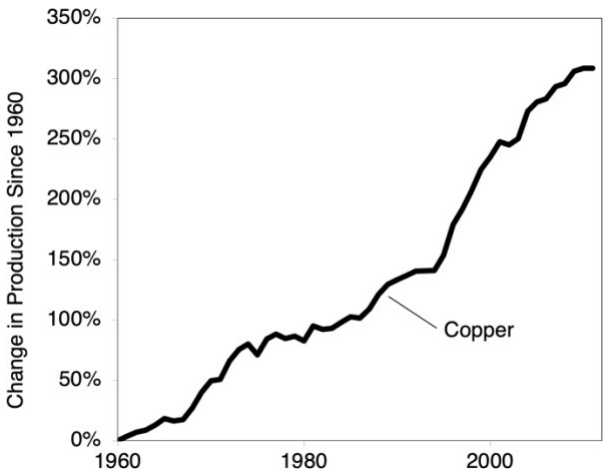

Figure 1. Change in global production (consumption) of copper relative to the year 1960 (Kesler and Simon, 2015).

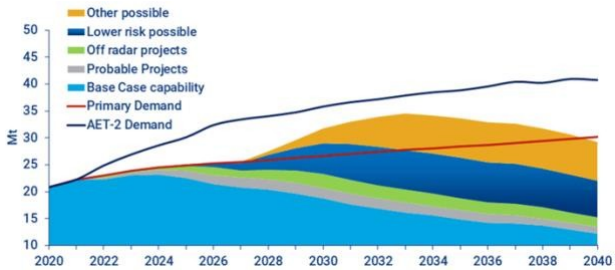

Figure 2. Global copper demand, copper production from operating mines and proposed new mines (Wood Mackenzie, 2023)

For example, using data for the United States, whichis 4% of the global population and consumes 15% ofglobal energy, achieving carbon neutrality by 2050 requires increasing the number of wind turbines andphotovoltaic solar by 5%/y over current levels. This requires 115,000 tonnes per year of copper for wind turbines and 685,000 tonnes per year more copper for photovoltaic solar panels. Sixteen million light duty vehicles are sold annually. Replacing these vehicles with battery electric vehicles requires 960,000 tonnes per year more copper. To put this in perspective, the Bingham Canyon porphyry copper mine in Utah produced 144,000 tonnes of copper in2022. Thus, to support just these modest stepstoward a green economy would require the U.S. put 12 new Bingham Canyon copper mines intoproduction each year for the next two decades. Thisseems a practical impossibility. Humans currently extract about 22 million tonnes of copper annually from 250 copper mines operating in 40 countries (Figure 3).

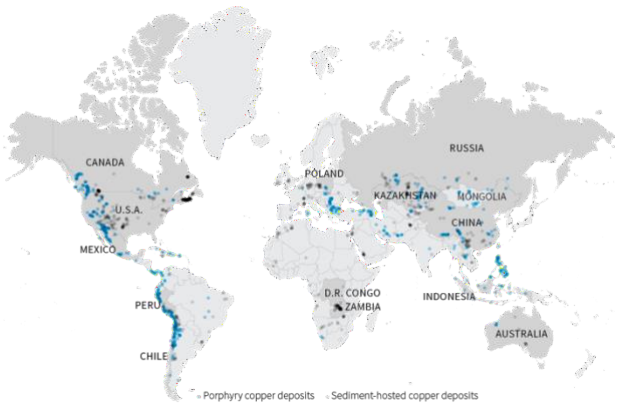

Figure 3. Global porphyry copper mines and sediment copper mines (Thomson Reuters 2023).

Replacing coal, oil, and natural gas, which together account for 85% of global primary energy supply, with a combination of photovoltaic solar, wind turbines, battery electric vehicles, grid-scale batterystorage and significantly expanded electrical grids, will require that annual production of copper increase by at least 50%. The magnitude of this challenge is illustrated in Figure 4 for all countries.

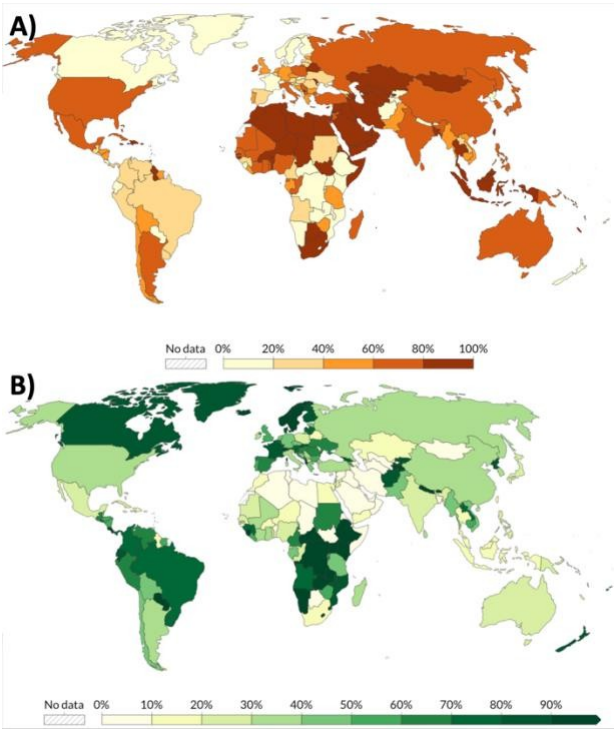

Figure 5. Current percent of total energy met by the sum of coal, oil and natural gas (A) and percent of electricity met by the sum of hydropower, solar, wind, biomass & waste, geothermal, wave, and tidal sources (Our World in Data 2023).

This is not possible from currently operating or planned mines and, considering that permitting and development of a new copper mine takes an average of 16 years, it is projected that there will be an annual global copper shortage of about 10 million tonnes by 2030. In fact, by 2030 there will be a global shortage of cobalt, copper, graphite, lithium, manganese, nickel, dysprosium, neodymium, praseodymium, terbium, and every other metal required for the green energy transition (Figure 5).

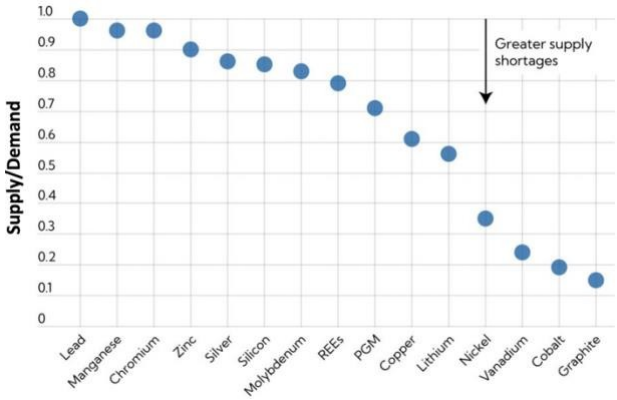

Figure 5. Ratio of supply to demand for energy critical metals required for the green energy transition (IMF, 2021).

These projections just consider the energy transition. They do not include the resources needed to bring the underdeveloped world up to developed world levels of energy use. This is illustrated in Figure 6.

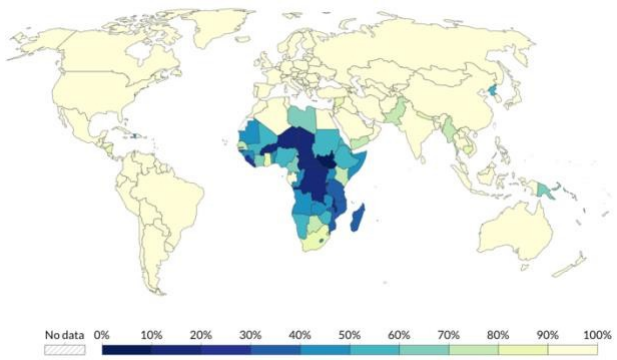

Figure 6. Access to electricity (Our World in Data 2023).

2 Conclusions

It will not be possible to achieve carbon neutrality by building photovoltaic solar and wind energy infrastructure on the timescale established by the International Panel on Climate Change (IPCC, 2023) enough to achieve the stated policy goals of for carbon neutrality. Further, for equity and feasibility, we must consider zero carbon strategies that take the pressure off resource supply.

References

IMF (2021) https://www.imf.org/en/Blogs/Articles/2021/12/08/metals demand-from-energy-transition-may-top-current-global supply. Accessed online 14 March 2023

IPCC (2023) AR6 Synthesis Report: Climate Change 2023. https://www.ipcc.ch/report/sixth-assessment-report cycle/. Accessed online 14 March 2023

Kesler, S.E., Simon, A.C. (2015) Mineral Resources, Economics, and the Environment. Cambridge Press.

Our World in Data based on BP Statistical Review of World Energy (2023); Our World in Data based on Ember's Yearly Electricity Data (2023); Our World in Data based on Ember's European Electricity Review (2022)

Thomson Reuters (2023) http://graphics.thomsonreuters.com/15/chile copper/index.html. Accessed online 14 March 2023

Wood Mackenzie (2021) https://www.woodmac.com/news/opinion/will-a-lack-of- supply-growth-come-back-to-bite-the-copper-industry/. Accessed online 14 March 2023

Hyperspectral cathodoluminescence of REE-bearing zirconosilicate minerals from Pajarito Mountain, USA

Paul Slezak[1], Siri L. Simonsen[2], Franziska D.H. Wilke[3], Dave Chew[4], Richard Wendlandt[5], Michael Berger[5], Murray W. Hitzman[1]
[1]Irish Centre for Research in Applied Geosciences, School of Earth Science, University College Dublin, Dublin 4, Ireland
[2]Department of Geosciences, University of Oslo, P.O. Box 1047, Blindern, N-0316 Oslo, Norway
[3]GFZ German Research Centre for Geosciences, Telegrafenberg, 14473 Potsdam, Germany
[4]Department of Geology, School of Natural Sciences, Trinity College Dublin, Dublin 2, Ireland
[5]Department of Geology and Geological Engineering, Colorado School of Mines, Golden, CO 80401 USA

Abstract. Agpaites are rare igneous rock types containing minerals abundant in high field strength elements (HFSE), rare earth elements (REE), and a variety of other critical metals, making them potentially important resources for critical raw materials. New Mexico (USA) hosts the layered Pajarito Mountain agpaitic complex (PMAC), which is prospective for Y and Zr hosted in abundant eudialyte as a primary cumulus phase. Hyperspectral cathodoluminescence (HyCL) shows that low luminescent minerals such as eudialyte have spectra in the infrared (e.g. 1.37 eV and 1.40 eV), suggesting the presence of Nd^{3+}. Eudialyte has been altered to Ca-zirconosilicate minerals, like gittinsite, which are highly luminescent and contains distinct light and dark CL zones. The lighter zones have much higher counts and peaks from ~2.0 eV to ~4.0 eV and may be related Eu^{3+}, Sm^{3+}, and/or Tb^{3+} to whereas the darker zones show an anomalous, prominent doublet at 1.25 eV and 1.26 eV. Hyperspectral CL imaging, spectral deconvolution, and activator identification provide valuable insights into zirconosilicate chemistry, elemental zonation, and potential element mobility related to alteration, especially regarding highly luminescent and critical metals such as the REE.

1 Introduction

Agpaites are rare, peralkaline igneous rocks — those defined as having a molar ratio of (Na + K)/Al > 1— that typically contain significant amounts of HFSE occurring in complex Na-Ca-HFSE minerals such as the eudialyte group minerals (EGM; Le Maitre et al. 2002; Marks and Markl 2017). Agpaitic rocks may also contain significant amounts of large ionic lithophile elements (LILE), halogens, and REE. Though they typically have lower REE grades than other alkaline igneous rocks such as carbonatites, they may contain higher REE tonnages overall and are also important sources of HFSE in addition to other important commodities including Li, Be, Sn, Ga, and Zn (Wall 2014; Marks and Markl 2017), making them potentially important sources of critical metals for technology items and green energy production (Weng et al 2015). Given the potential for a wide range in valuable elements in these rocks, many of which are critical raw materials (CRM), it is unsurprising that several agpaites have been delineated into mineral deposits such as Ilímaussaq (Greenland), Toongi (Australia), Nechalacho (Canada) and even mined, as is the case with Khibina and Lovozero (Russia; Marks and Markl 2015; Spandler et al. 2016; Möller and Williams-Jones 2016; Kalashnikov et al. 2016).

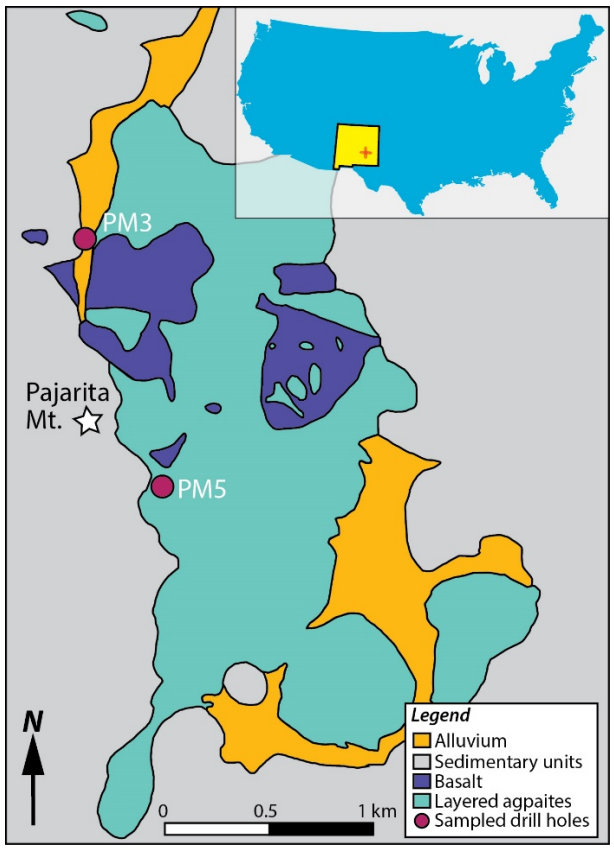

Figure 1. Location (inset) and simplified geologic map of the Pajarito Mountain agpaitic complex showing locations of drillholes PM3 and PM5 (from which the samples in this study were obtained) that intersected the layered intrusions (Modified from Jacobson, 1986; Berger, 2018).

The United States also hosts several agpaitic complexes, most of which are < 200 Ma in age (Marks and Markl 2017 and references therein). The PMAC is one of two Mesoproterozoic agpaitic complexes in the United States (Kelley 1968; Bauer and Pollock 1993). It is located in south-central New Mexico (Fig. 1) and was initially explored in the 1980s and 1990s by Molycorp for Y and Zr with more recent drilling and exploration conducted by the US Division of Energy and Mineral Development (DEMD) on behalf of the Mescalero Apache Tribe (Berger 2018). The drilling conducted by the DEMD and recent work by Berger (2018) indicated it is a layered complex and identified abundant eudialyte $[Na_{15}Ca_6Fe_3Zr_3Si(Si_{25}O_{73})(O,OH,H_2O)_3(Cl,OH)_2]$ as a rock-forming mineral in several layers. This study utilises a combination of petrographic techniques

and HyCL data to elucidate the evolution of the system and the origins of the eudialyte mineralisation, and its critical metal deportment within the eudialyte crystals. Since some critical metals, especially REE, are more desirable than others, identifying the location of specific elements at the mineral scale is important for processing and geometallurgy.

2 Geologic background

The PMAC consists of multiple layers of cumulate, peralkaline intrusions hosted in the southern region of a Grenvillian-aged A-type magmatic belt (see Bickford et al. 2000) and have an age range of 1155 ±25 to 1200 ±25 Ma obtained using K–Ar and Rb–Sr, respectively, on alkali amphiboles and feldspars (Kelley 1968; Bauer and Pollock 1993). The PMAC units are overlain and juxtaposed against younger Phanerozoic sedimentary units, all of which were uplifted during the Permian Pedernal uplift (Kottlowski 1985).

3 Methods

Samples were first analysed at University College Dublin (Ireland) using a Nikon Eclipse LV100NPol optical microscope. Backscattered electron images (BSE) and electron dispersive spectroscopy (EDS) were acquired using a JEOL Superprobe JXA-8230 at GFZ Potsdam (Germany).

Areas of interest were analysed using a Hitachi SU5000 FEG-SEM coupled to a Delmic Sparc HyCL unit at the University of Oslo (Norway). Operating conditions for eudialyte were set to 15 kV, a spot intensity of 50, and an exposure time of 200 ms. Other minerals were analysed at 10 kV, a spot intensity of 50, and an exposure time of 20 ms. Background spectra were obtained from both analytical settings (i.e. 15 kV at 200 ms and 10 kV at 20 ms) for spectral correction and processing. Images were processed and spectral data exported using Delmic's Odemis Viewer. The spectral data were deconvoluted using CSIRO's OpticalFit 21.x (Torpy and Wilson 2008).

4 Petrography

The different cumulate layered units comprising the PMAC have previously been divided into 4 groups by Berger (2018), which all consist of variable proportions of alkali feldspar, eudialyte, arfvedsonite, quartz with minor amounts of apatite and fluorite.

Here we examine PM5-257.25, which is an orthocumulate rock (Type II from Berger 2018) comprised of cumulus alkali feldspar and eudialyte with late cumulus to intercumulus arfvedsonite and intercumulus quartz. The other principal sample from this study is PM3-330.75, which is a mesocumulate rock (Type I from Berger 2018) made of cumulus eudialyte with lesser amounts of alkali feldspars and intercumulus quartz and arfvedsonite.

In all samples, the alkali feldspars are always an early cumulus phase comprised of euhedral albite crystal laths typically ranging in size from 350 µm up to 1000 µm (Fig. 2a) with occasional megacrysts up to 2500 µm. Eudialyte occurs in variable amounts (i.e. it is much more predominant in PM3-330.75) also as a cumulate phase and occasionally as oikocrysts (enveloping apatite). It is often found in higher abundances where quartz is also present. Eudialyte commonly occurs as euhedral, prismatic crystals ranging from 400 µm up to 1100 µm (Fig. 2a). Arfvedsonite is present as a late cumulus and as an early intercumulus phase (Fig. 2a,b). It is typically subhedral to anhedral an occasionally oikocrystic with respect to apatite. Arfvedsonite crystals range in size from 200 µm to 3000 µm. Quartz of variable sizes always occurs as an intercumulus phase (Fig. 2b,c). Apatite occurs as small (75 µm to 200 µm) ovoid crystals, commonly as chadacrysts in eudialyte and arfvedsonite. Fluorite is also present in trace amounts as prismatic, euhedral crystals up to 200 µm in diameter and is typically associated with the quartz-rich domains.

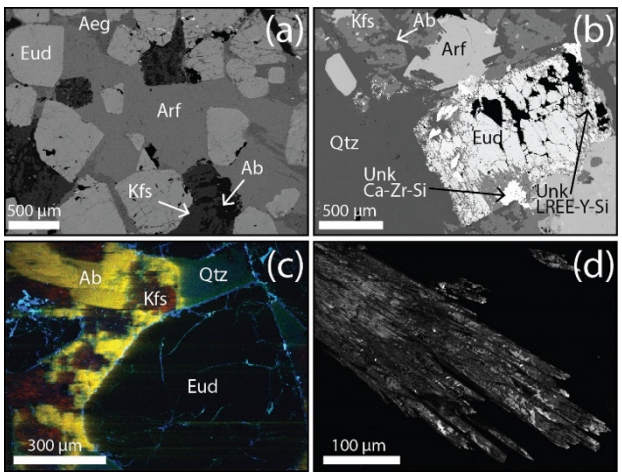

Figure 2. a BSE image from the mesocumulate sample PM3-330.75 (Type I) with cumulus eudialyte and alkali feldspar with intercumulus arfvedsonite displaying minor aegirine alteration. **b** BSE image of the orthocumulate sample PM5-257.25 (Type II) of eudialyte altered to unknown Ca-zirconosilicate and an unknown LREE-Y-silicate minerals. **c** HyCL image of PM3-330.75 with RGB overlay showing prominence of alkali feldspar luminescence compared to quartz and eudialyte. Blue areas are artifacts from cracks and crystal margins. **d** HyCL image of sample PM5-257.25 of an example Ca-zirconosilicate (likely gittinsite) mineral illustrating light and dark luminescent zones. Ab = albite, Aeg = aegirine, Arf = arfvedsonite, Eud = eudialyte, Kfs = potassium feldspar, Qtz = quartz.

Samples display consistent alteration with albite ubiquitously being replaced by patchy, tartan-twinned potassium feldspar (Fig. 2a-c). Arfvedsonite commonly displays minor alteration to aegirine along its crystal margins (Fig. 2a). Moderate to complete alteration to aegirine is present in some other samples but is less common. Eudialyte is occasionally altered (e.g. sample PM5-257.25; Fig.

2b) to a few unknown Ca-zirconosilicate minerals with 2nd order birefringence and crystal lath splays, some of which are likely gittinsite [$CaZrSi_2O_7$], as well as other hydrous and/or carbonated phases (Fig. 2b,d). Eudialyte also alters to an unknown LREE-Y-silicate mineral (Fig. 2b) and rarely, monazite.

5 Spectra results

Hyperspectral CL is a useful tool not only for identifying luminescent features (e.g. REE activators) in minerals outside the visible spectrum (i.e ultraviolet and infrared), but also for acquiring the mineral spectra on different luminescent zones (e.g. MacRae et al. 2012; 2013). Here we present the HyCL spectra on minerals that are not thought to traditionally luminesce, such as eudialyte. In addition we present spectral data on luminescent alteration minerals, like gittinsite, which display small, complex zonation under CL.

5.1 Eudialyte spectra

Compared to other minerals such as albite and potassium feldspar, eudialyte appears to not readily luminesce (Fig. 2c). However, HyCL scans show that eudialyte does have a spectrum (Fig. 3), albeit with count rates several orders of magnitude lower than the associated feldspars (e.g. 20,000 – 40,000 counts for feldspars compared to 80 counts for eudialyte under the same analytical conditions). By focusing on the eudialyte, we were able to obtain spectra (see Fig. 3) illustrating that eudialyte has several prominent peaks outside the visible range in the infrared at 1.27 eV, 1.37 eV, and 1.40 eV.

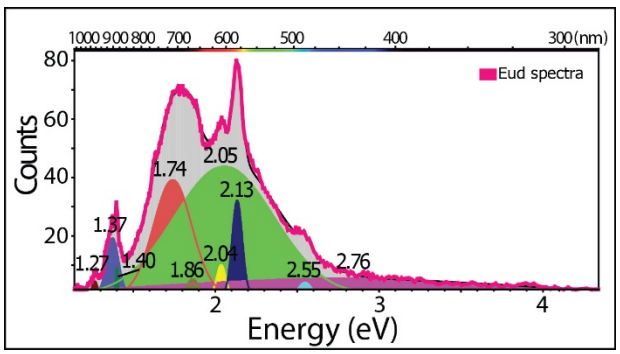

Figure 3. Example eudialyte spectra from PM3-330.75

5.2 Ca-zirconosilicate spectra

Though eudialyte is not the most luminescent mineral in the PMAC, some of its alteration assemblages display significant luminescence (see Fig. 2d), including an unknown Ca-zirconosilicate minerals (potentially gittinsite as determined by EDS). Figure 4a illustrates the difference in counts from the light and dark luminescent zones from Ca-zirconosilicates in Figure 2d. The light zones have significantly higher counts compared to the dark zones except near the 1.26 eV location, which is more prominent in the dark zones (Fig. 4a). This peak only appears as a small bump in the light zones (Fig. 4b), but in the dark zones consists of a distinct doublet at 1.25 eV and 1.25 eV (Fig. 4c). Both spectra show prominent peaks near 2.0 eV. When the spectra are deconvoluted, activators appear in the light and dark zones at or near 1.26 eV, 2.06 eV, 2.78 eV, 3.74 eV, and 4.12 eV (Fig. 4b,c), suggesting similar activators in both zones. However, the light zones have much more pronounced peaks near 3.74 and 4.12 eV (Fig. 4b).

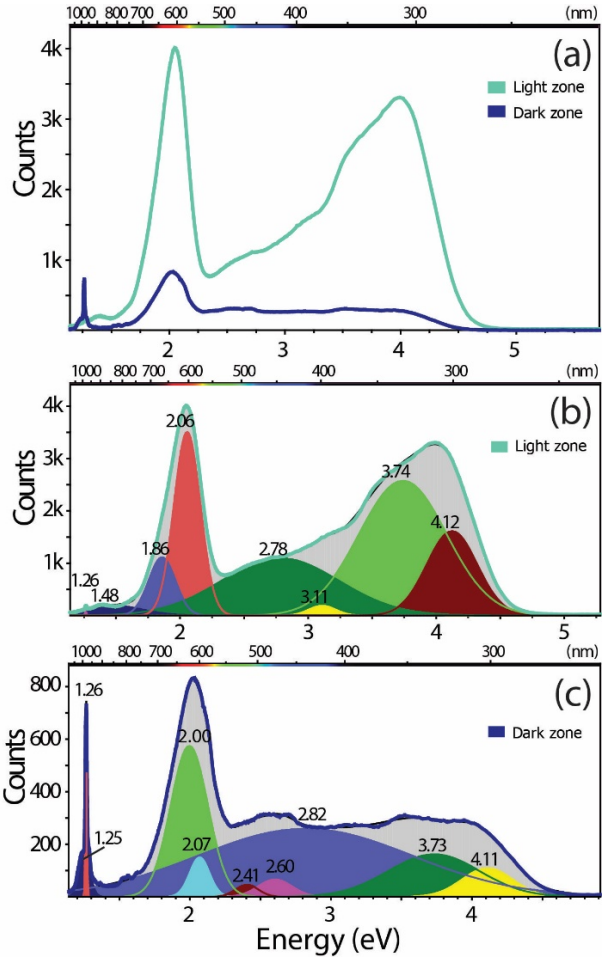

Figure 4. a Comparison of light and dark luminescent zones from the Ca-zirconosilicates in sample PM5-257.25. **b** deconvoluted light CL zone (see Fig. 2d for reference). **c** Deconvoluted dark CL zone (see Fig. 2d for reference)

6 Conclusions

Though eudialyte is typically not analysed for luminescence, many of the spectral peaks in this study are likely associated with REE activators since REE^{3+} activators tend to occur at similar wavelengths/energies in different host materials and minerals (Lenz et al. 2013). The doublet peak at 1.37 eV and 1.40 eV in eudialyte from PM3-330.75 may be attributed to Nd^{3+}. It also exhibits a potential low-level activator in the infrared (i.e. the broad peak centred at 2.76 eV), which may be associated with Y^{3+}(MacRae and Wilson 2008; Lenz et al. 2018).

Ca-zirconosilicate luminescence was first documented by Roelofsen and Veblen (1999) in samples from Strange Lake (Canada). They

described gittinsite as “orange to brownish-orange” under optical CL, but no spectra were captured in their study. Several studies on synthetic gittinsite crystals have been analysed for phosphorescent studies, suggesting that Eu^{3+} may be a potential activator (Bandi et al. 2010). In addition, other possible activators such as Sm^{3+} and Tb^{3+} have been found in similar energy ranges in doped REE^{3+} glasses (MacRae and Wilson 2008). The peak at 1.26 eV is anomalous as this occurs well within the infrared spectrum and outside the region of common CL activators, prompting further investigation.

Acknowledgements

This project has received funding from the European Union’s Horizon 2020 research and innovation programme under grant agreement No. 101005611 for Transnational Access (award code EXCITE_TNA_C2_2022_010) conducted at the SEM lab of the Department of Geosciences, University Oslo. It has also received support from Science Foundation Ireland (SFI) under Grant Number 16/RP/3849 and 13/RC/2092_P2. Lastly, We thank O. Appelt from GFZ Potsdam for their EPMA expertise as well as A. Gysi for their review, which greatly improved this manuscript.

References

Bandi VR, Jayasimhadri M, Jeong J, Jang K, Lee HS, Yi S-S, Jeong J-H (2010) Host sensitized novel red phosphor $CaZrS_2O_7$: Eu^{3+} for near UV and blue LED-based white LEDs. J Phys D Appl Phys 43:395103. doi: 10.1088/0022-3727/43/39/395103

Bandi VR, Grandhe BK, Jang K, Kim S-S, Shin D-S, Lee Y-I, Lim J-M, Song T (2011) Luminescent properties of a new green emitting Eu2+ doped CaZrSi2O7 phosphor for WLED applications. Journal of Luminescence 131:2414–2418. doi: 10.1016/j.jlumin.2011.06.004.

Bauer PW, Pollock TR (1993) Compilation of Precambrian Isotopic Ages in New Mexico. pp 128

Berger M (2018) Geology and mineralization of the Pajarita Mountain layered peralkaline syenitic pluton-hosted REE-Zr prospect, Mescalero Apache Reservation, New Mexico. Colorado School of Mines, USA, pp 84

Bickford ME, Soegaard K, Nielsen KC, McLelland JM (2000) Geology and geochronology of Grenville-age rocks in the Van Horn and Franklin Mountains area, west Texas: Implications for the tectonic evolution of Laurentia during the Grenville. Geol Soc Am Bull 112:1134–1148. doi: 10.1130/0016-7606(2000)112<1134:GAGOGR>2.0.CO2

Jacobson HS (1986) Pajarito Mountain Prospect, Mescalero Apache Indian Reservation, Otero County, New Mexico. Unocal Molycorp internal report, v. I & II

Kalashnikov AO, Konopleva NG, Pakhomovsky YA, Ivanyuk GY (2016) Rare Earth Deposits of the Murmansk Region, Russia—A Review. Econ Geol 111:1529–1559. doi: 10.2113/econgeo.111.7.1529

Kelley VC (1968) Geology of the Alkaline Precambrian Rocks at Pajarito Mountain, Otero County, New Mexico. Geol Soc Am Bull 79:1565–1572. doi: 10.1130/0016-7606(1968)79[1565:GOTAPR]2.0.CO2

Kottlowski FE (1985) Shoreline facies of the Yeso Formation in the northern Pedernal Hills, New Mexico In: Lucas SG, Zidek J (eds) New Mexico Geological Society 36th Annual Fall Field Conference Guidebook: Santa Rosa-Tucumcari Region. New Mexico Geological Society, Socorro, pp 167–169. doi: 10.56577/FFC-36.167

Le Maitre RW, Streckeisen A, Zanettin B, Le Bas MJ, Bonin B, Bateman P, Belleini G, Dukek A, Efremova S, Keller J, Lameyre J, Sabine PA, Schmid R, Sørensen H, Woolley AR (2002) Igneous Rocks A Classification and Glossary of Terms. Cambridge University Press, United Kingdom

Lenz C, Talla D, Ruschel K, Škoda R, Götze J, Nasdala L (2013) Factors affecting the Nd^{3+} (REE^{3+}) luminescence of minerals. Miner Petrol 107:415–428. doi: 10.1007/s00710-013-0286-2

MacRae CM, Wilson NC (2008) Luminescence database I - minerals and materials. Microsc Microanal. Cambridge University Press, Cambridge, U.K., pp 184–204.

MacRae C, Wilson NC, Torpy A, Davidson CJ (2012) Hyperspectral cathodoluminescence imaging and analysis extending from ultraviolet to near infrared. Microsc Microanal 18:1239–1245. doi: /10.1017/S1431927612013505

MacRae C, Wilson NC, Torpy A (2013) Hyperspectral cathodoluminescence. Miner Petrol 107:429-440. doi: /10.1007/s00710-013-0272-8

Marks MAW, Markl G (2015) The Ilímaussaq Alkaline Complex, South Greenland In: Charlier B, Namur O, Latypov R, Tegner C (eds) Layered Intrusions. Springer Netherlands, Dordrecht, pp 649–691. doi: 10.1007/978-94-017-9652-1_14

Marks MAW, Markl G (2017) A global review on agpaitic rocks. Earth-Sci Rev 173:229–258. doi: 10.1016/j.earscirev.2017.06.002

Möller V, Williams-Jones AE (2016) Petrogenesis of the Nechalacho Layered Suite, Canada: Magmatic Evolution of a REE–Nb-rich Nepheline Syenite Intrusion. J Petrol 57:229–276. doi: 10.1093/petrology/egw003

Roelofsen JN, Veblen DR (1999) Relationships among zirconosilicates: examination by cathodoluminescence and transmission electron microscopy. Mineralogy and Petrology 67:71–84. doi: 10.1007/BF01165117.

Spandler C, Morris C (2016) Geology and genesis of the Toongi rare metal (Zr, Hf, Nb, Ta, Y and REE) deposit, NSW, Australia, and implications for rare metal mineralization in peralkaline igneous rocks. CONTRIB MINERAL PETR Contrib Mineral Petr 171:104. doi: 10.1007/s00410-016-1316-y

Torpy A, Wilson NC (2008) OpticalFit Software by CSIRO Australia. http://www.csiro.au/luminescence/opticalfit/

Wall F (2014) Rare earth elements In: Gunn AG (ed) Critical Metals Handbook. John Wiley & Sons, pp 312–339

Weng Z, Jowitt SM, Mudd GM, Haque N (2015) A Detailed Assessment of Global Rare Earth Element Resources: Opportunities and Challenges. Econ Geol 110:1925–1952. doi: 10.2113/econgeo.110.8.1925

The typology of Czech graphite raw materials

Michal Poňavič[1], František Pticen[1], Bohdan Kříbek[1], Anna Vymazalová[1]
[1]Czech Geological Survey, Klárov 131/3, 118 21 Prague 1, Czech Republic

Abstract. Critical Raw Materials (CRM) in the Czech Republic have been studied under the framework of the project "Rock Environment and Natural Resource RENS" (SS02030023) with graphite being one of the CRMs. The purpose of this study is to investigate the processing of graphite raw material from Czech deposits and sources. The goal of this study is to determine the yield and quality of graphite concentrates after the 1st flotation. The different types of graphite raw materials were divided into three quality classes based on their technological treatability. Each class represents a different type of raw material and therefore different conditions for graphite formation.

1 Introduction

This study has been performed under the project "Rock Environment and Natural Resource RENS" (SS02030023), funded by the Technology Agency of the Czech Republic (TA ČR). The main goals of the project are research, monitoring, and evaluation of the state of the rock environment, natural resources, geological hazards, and geological information in the Czech Republic; and to make those findings available to government agencies, organizations within the field, and to the general public. The research is focusing on deposits of strategic mineral resources within the territory of the Czech Republic. The aim is the identification and evaluation of deposits, the study of refining and processing technologies, and evaluation of potential exploitation of these resources in the Czech Republic. One of the most important topics of the project is the detailed study of Czech graphite deposits.

Graphite deposits in the Czech Republic are located in several varied groups of crystalline rocks: In the Český Krumlov and Sušice-Votice Varied Groups (southern Bohemia) and in the Svratka Crystalline Unit (western Moravia) and in the Velké Vrbno Crystalline Unit (northern Moravia) (Fig. 1).

In the Bohemian Massif, graphite deposits were formed by thermal and pressure decomposition of the organic matter, mainly algae, cyanobacteria and bacteria. The products of their decomposition were deposited in shallow pools in the marine environment, probably at the boundary between the Upper Proterozoic and Lower Palaeozoic. In the course of subsequent geological processes (after the overlying of organic matter by sediments and subsequent metamorphism at temperatures of around 550–650 ^{0}C, and pressures of up to 25 kB), the organic matter was gradually decomposed into a mixture of gases, mainly carbon dioxide and methane (Kříbek 1997). Graphite then crystallized from this gas mixture as the rock complex cooled. In later low temperature processes, this crystalline graphite was affected in a number of places by mechanical processes (it was in fact ground up) to form microcrystalline graphite.

A fundamental problem of some South Bohemian graphite deposits is the processability of the raw material, which is adversely affected by its variable grain size composition and the coalescence and intergrowth of graphite flakes with rock-forming minerals, especially micas. Therefore, to release the graphite flake from the raw material by multi-stage flotation, very fine grinding of the raw material is required. However, such an approach degrades the grain size composition of the final product.

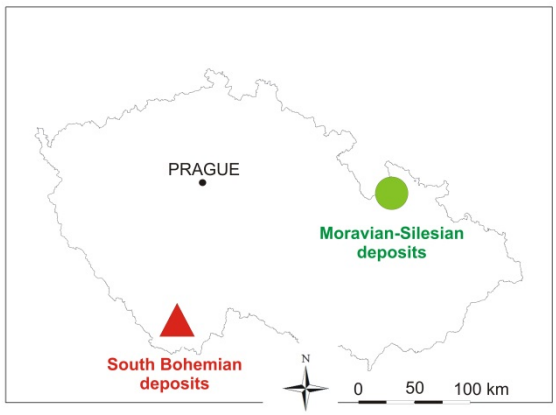

Figure 1. Schematic map of the Czech Republic with locations of the graphite deposits districts.

2 Samples and methods

Within the RENS project, not only archival samples of graphite raw material were studied, but new samples have been collected at available locations. After drying, the samples were crushed and milled to the required grain size (0.015 mm). The samples were further processed at the Central Laboratories of the Czech Geological Survey (CGS). Flotation experiments and detailed analyses of both concentrates and base (silicate analyses, C(tot), C(graph) and detailed trace element analyses) were performed. Graphite mineralogy and morphology were also studied in the CGS laboratories, using a scanning electron microscope. At the same time, rock-slides were made for detailed microscopic investigations.

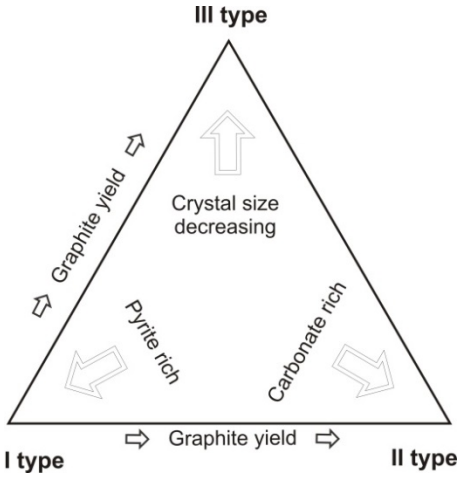

Figure 2. The typology of the Czech graphite raw material based on genetic type and yield of graphite concentrate.

3 Results and discussion

Based on a comparison of the obtained results, from (I) graphite concentration in the feedstock, (II) yield of concentrate after the first flotation, (III) graphite content in this concentrate, and (IV) graphite grain size and ballast mineral content, it is possible to divide the graphite raw materials into three basic groups (Fig. 2). Table 1 shows the average graphitic carbon contents in the raw material (milled to a grain size of 0.10–0.15 mm) and in individual concentrates after the first flotation.

Class I represents graphitic raw materials bound on gneisses. Sulphides (mainly pyrite) are common, and due to their decomposition, the pH of the raw material leachate ranges from 3.5 to 5.0. Graphite is present as small flakes of 0.05–0.15 mm in size. Often there is epitaxial overgrowth of graphite on micas, thus forming a graphite-mica composite (Fig. 3). Microcrystalline graphite (formed by tectonic damage to the gneisses) is also present in small quantities in the raw material. This type of raw material is by far the most common type and is present in the majority of deposits and resources in South Bohemia, with Český Krumlov-Městský vrch being the best known deposit.

Due to the low pH of the raw material, coagulation of particles occurs during flotation and it is therefore necessary to buffer the mixture, for example by adding $Ca(OH)_2$. However, the most important factor is the frequent coalescence of graphite with mica, which leads to low yields and poor quality graphite concentrate (Florena et al. 2016). To achieve acceptable yields it is therefore necessary to incorporate pre-treatment of the raw material, e.g. grinding by ultrasonic treatment (Kang and Li 2019). However, this results in higher energy requirements for the actual treatment.

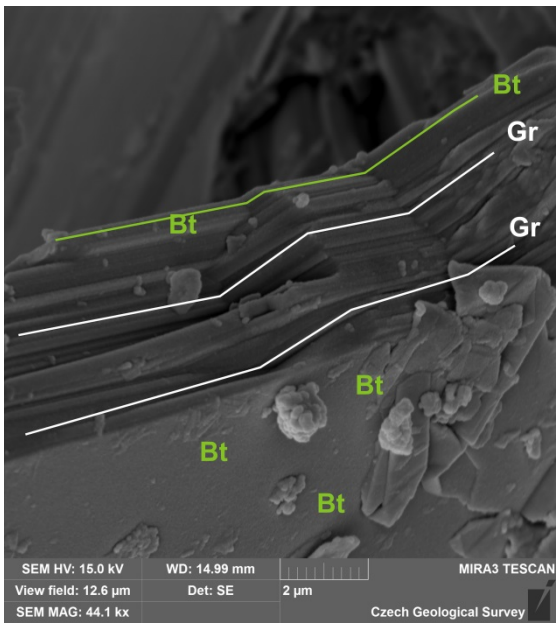

Figure 3. Secondary electron image of alternation between graphite (Gr) and biotite (Bt) in xxx, from the Český Krumlov-Městský vrch deposit.

Input concentrations of graphite are relatively low, ranging between 8–12% C(graph). Yields are also low, the amount of concentrate after the first flotation does not exceed 30 % with a graphitic carbon content of up to 20 % (Table 1).

Class II includes raw materials that may also be associated with gneisses but are predominantly associated with marbles. In this case, the pH of the leachate is between 6.0 and 7.0. Graphite is present as flakes of 0.1–0.25 mm and very often forms separate flakes, without other mineral phases (Fig. 4). This type of raw material is present only in a few deposits in southern Bohemia. The main representative is the Lazec-Křenov graphite deposit.

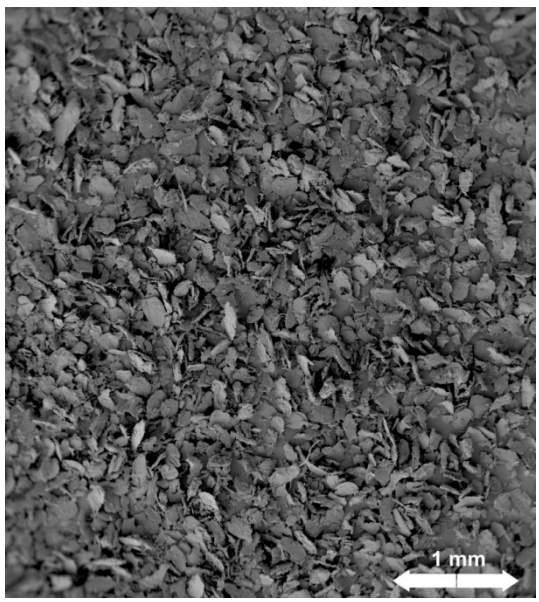

Figure 4. Secondary electron image of graphite flakes from a concentrate after 1st flotation, Lazec-Křenov deposit.

This type of raw material is relatively easy to process, obtaining high yields of high-quality graphite flakes concentrate. The three flotation cycles are sufficient to achieve maximum yields.

The graphite contents in this type of raw material ranges from 12 to 18 %. The yield of concentrate after the first flotation is around 30 % with a C(graph) content between 45 and 50 %.

Class III represents graphitic raw materials bound to gneisses, often tectonically affected. Pyrite may be present, the pH of the leachate ranges from 5.0 to 6.0. Graphite is present in microcrystalline (amorphous) form (Fig. 5). This type of raw material is present in most deposits and sources in the northern Moravia.

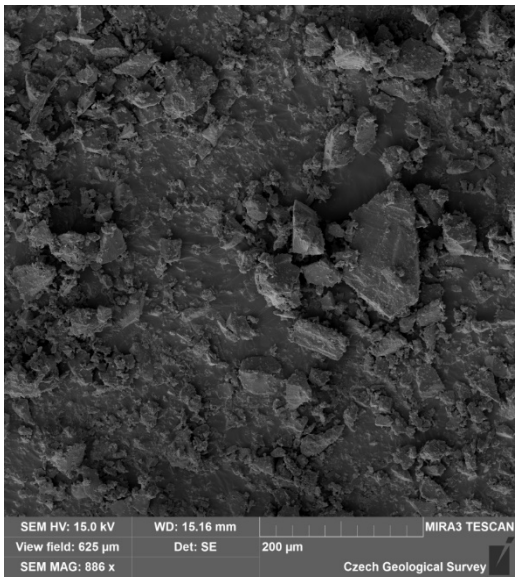

Figure 5. Secondary electron image of amorphous graphite from a concentrate after 1st flotation, Velké Vrbno Konstantin deposit.

This type of raw material is also easy to process, with significant yields of high-quality amorphous graphite concentrate. The graphite content in this type of raw material is very high, ranging from 25 to 30 %. The yield of concentrate after the first flotation is around 50 % with a C(graph) content between 50 and 60 %.

Table 1. Comparison of average graphitic carbon contents in raw materials (milled to a grain size of 0.10–0.15 mm) and in individual concentrates after the first flotation.

Raw material		Concentrate after 1st flotation	
	C(graph)(%)	Concentrate (%)	C(graph) (%)
I type	8–12	40	20–25
II type	18	30	45–50
III type	20–30	50	50–60

5 Conclusions

Samples of Czech graphite raw materials were studied in terms of their workability (yield and quality of graphite concentrate after the first flotation) and also in terms of their mineral association. Table 2 shows the studied graphite deposits. Based on the results so far, it was possible to divide the graphite raw material into three quality classes. They differ in terms of floatability and therefore graphite yield. Each type of graphite raw material thus requires different treatment.

Microcrystalline graphite (Clas III) and graphite associated with carbonates (Clas II) are well treatable and provide concentrates of relatively pure graphite (Jara et al. 2019). In contrast, graphite raw materials bound in gneisses with frequent sulphides requires good physical pre-treatment of the raw material.

This issue will be addressed in the next stages of the SS02030023 RENS project.

Table 2. Studied Czech graphite deposits, and their typology.

Deposit	Num. of samples	Raw material C(graph) average (%)	Category
Český Krumlov-Městský vrch	12	8	I type
Mokrá	8	11	
Chvalšiny	6	12	
Lazec-Křenov	15	18	II type
Velké Vrbno-Konstantin	10	30	III type
Malé Tresné	5	20	

Acknowledgements

Financial support through the project „Rock Environment and Natural Resource (RENS)", No SS02030023 from the state support of the Technological Agency of the Czech Republic (Environment for Life Programme) is gratefully acknowledged.

References

Florena FF, Syarifuddin F, Hanam ES, Trisko N, Kustiyanto E, Enilisiana Rianto A, Arinton G (2016) Floatability study of graphite ore from southeast Sulawesi (Indonesia). In AIP Conference Proceedings. AIP Publishing LLC. 1712, 1.

Jara AD, Betemariam A, Woldetinsae G, Kim JY (2019) Purification, application and current market trend of natural graphite: A review. Int J Min Sci Technol 29: 671–689.

Kang W, Li H (2019) Enhancement of flake graphite cleaning by ultrasonic treatment. R. Soc. open sci. 6191160191160http://doi.org/10.1098/rsos.191160

Kříbek B (1997) Carbonaceous formations of the Bohemian Massif and their mineralization. Czech Geological Survey, Prague, 120 p. (in Czech).

The Northern Copper Belt—a chance for a new giant copper district in Poland

Krzysztof Zieliński[1], Stanisław Speczik[1,2]
[1]Miedzi Copper Corp., Al. Jerozolimskie 96, 00-807 Warsaw, Poland
[2]University of Warsaw, Faculty of Geology, Żwirki i Wigury 93, 02-089 Warsaw, Poland

Abstract. The Northern Copper Belt has been identified recently in south-western Poland as a result of the exploration programme of Miedzi Copper Corp. This zone has great potential to become a new mining district for underground extraction of copper and silver ore. It is located entirely in a geological unit known as the Fore-Sudetic Monocline. The belt includes three newly discovered Cu-Ag ore deposits along with numerous prospective areas scattered around them. The deposits are situated relatively deeply, with an average depth of about 1900 m. The high probability of future extension of these deposits comes from the drillholes of Miedzi Copper Corp., and from the examinations of historical oil and gas exploration boreholes located nearby. Pre-feasibility studies prepared by mining experts confirm the profitability of future extraction of these deposits.
Keywords: Northern Copper Belt, stratiform copper mineralisation; Kupferschiefer-type deposits, deep copper and silver deposits

1 The Northern Copper Belt—an overview

The Northern Copper Belt (NCB) is located in south-western Poland, in the Fore-Sudetic Monocline which is a geological unit already known for its occurrences of stratiform copper and silver deposits. Ore mineralisation is present in the so-called Zechstein copper-bearing series, represented from bottom to top by marine sandstones, shales (the 'Kupferschiefer'), and limestones. The series overlies the barren Rotliegend unit, consisting of continental red bed sediments. The mineralisation occurs directly above the oxidised Rote Fäule zone, the vertical range of which shifts between reaching the sandstone, the Kupferschiefer, or even the limestone. The belt is situated north and east of the existing mines of the Lubin-Sieroszowice District (the so-called New Copper District), which extract ore from shallower parts of the same geological unit.

The NCB has been discovered as a result of an extensive exploration programme of the Miedzi Copper Corp. (MCC) initiated in 2011, which consisted of two stages (Speczik et al. 2021). The first stage involved reprocessing of historical geophysical data, as well as numerous detailed chemical analyses of historical drill core samples of the petroleum industry, irregularly scattered over the investigated area. For this part of the exploration, MCC cooperated with the University of Warsaw and the Polish Geological Institute, the latter of which had earlier performed limited examinations of selected oil and gas exploration boreholes which penetrated the mineralised horizon (Oszczepalski and Speczik 2011). The second stage involved drilling operations performed in areas considered the most promising based on the initial research. A total of 34 exploration boreholes were drilled, with the programme still continuing, and at least two more boreholes scheduled for 2023.

The work performed so far resulted in the discovery of three new Cu-Ag ore deposits (Nowa Sól, Sulmierzyce North, and Mozów) with resources already approved by the Polish government, as well as numerous prospective areas of ore mineralisation, both adjacent to the three deposits and independent therefrom. All these areas collectively form the Northern Copper Belt, which is a name suggested by MCC and already used in other publications on the subject (Speczik et al. 2022).

2 NCB Resources

The three deposits of the NCB have been documented based on MCC's exploration, including its drilling programme. General information about them is presented in Table 2.1.

Table 2.1. Basic characteristics of the Cu-Ag ore deposits of the Northern Copper Belt

Name	Surface area [km^2]	Depth [m b.g.l]	Type of resources (Polish category in brackets)	Cu resources [Mt]	Ag resources [kt]
Nowa Sól	119.2	1780–2160	inferred/ indicated (C_2)	10.96	35.32
Mozów	31.5	2370–2537	inferred/ (C_2)	4.59	6.49
Sulmierzyce North	61.0	1636–2060	inferred/ (C_2+D)	5.65	6.87
			TOTAL:	**21.20**	**48.68**

The resources of the Nowa Sól deposit are described as inferred/indicated, because their relative error of estimation is lower than 30%, which fulfils the requirements of Polish C_1 category, an equivalent of indicated resources according to CRIRSCO (Nieć 2010). The currently continuing exploration of this deposit will upgrade the resources to indicated. These three deposits have been entered into the registry of Polish mineral resources, updated annually by the Polish Geological Institute on commission from the Ministry of Climate and Environment.

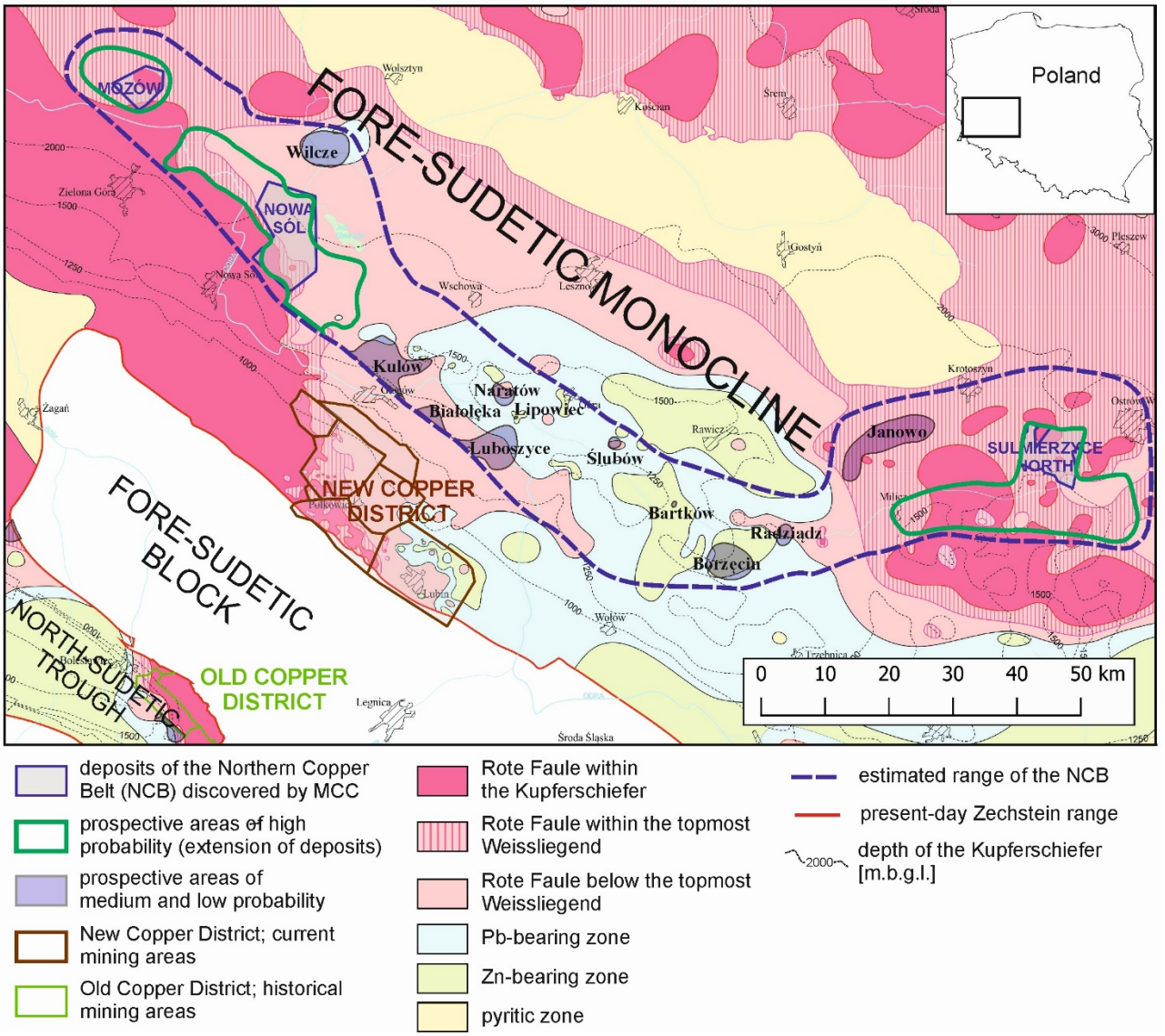

Figure 2.1. Location of the Northern Copper Belt, its ore deposits, and prospective areas.

The NCB also includes areas established as a result of MCC's analyses of old petroleum drill cores. The extent of the belt along with its deposits and prospects are presented in Figure 2.1.

Prospective areas in this part of the Fore-Sudetic Monocline were categorised differently over the years, based on their location with respect to the known deposits, and the degree of their exploration, e.g. as areas of hypothetical resources as well as speculative resources of low and high potential, each one with its own estimated resources (Oszczepalski et al. 2019). In a more recent paper, those among them which are adjacent to the Nowa Sól, Sulmierzyce North, and Mozów deposits were categorised separately as prospective areas allowing for the extension of these deposits (Speczik et al. 2022).

However, the present study uses a new approach, mainly due to the inclusion of additional areas demarcated by historical boreholes, which had been analysed but were not taken into account in previous research. This was because they were represented by incomplete or damaged cores, which could not be used for any official calculations of resources due to their subpar quality. The fragments of intervals with high-grade mineralisation observed in some of those cores make those areas appealing targets for future exploration.

The classification of prospective areas used in the present study is shown in Table 2.2.

Table 2.2. The criteria used to categorise the prospective areas of Cu-Ag ore mineralisation in the Northern Copper Belt.

Type of resources	Description
Prospective of high probability (extension of known deposits)	Adjacent to NCB deposits, identified by historical boreholes with complete core intervals; supplementary boreholes with incomplete cores are allowed
Prospective of medium probability	Distant from NCB deposits, identified by several historical boreholes with complete core intervals; supplementary boreholes with incomplete cores are allowed
Prospective of low probability	Distant from NCB deposits, identified by a single historical borehole with a complete core interval, or only by boreholes with incomplete cores

The prospective areas of the NCB established based on the abovementioned criteria are listed in Table 2.3.

Table 2.3. Basic characteristics of the prospective areas of Cu-Ag ore mineralisation in the Northern Copper Belt.

Type of resources	Name	Surface area [km^2]	Depth [m b.g.l]	Estimated Cu resources [Mt]	Estimated Ag resources [kt]
Prospective of high probability	Nowa Sól (extended)	320*	1600–2200	34.75*	148.26*
	Mozów (extended)	105*	2300–2600	15.27*	23.58*
	Sulmierzyce North (extended)	375*	1400–2100	21.17*	25.71*
Total prospective of high probability:				71.19*	197.55*
Prospective of medium probability	Kulów	50	1500–1800	6.20	16.98
	Białołęka	7	1500–1600	0.33	1.56
	Luboszyce	38	1400–1600	1.21	7.23
	Janowo	56	1700–1800	2.55	5.59
Total prospective of medium probability:				10.29	31.36
Prospective of low probability	Wilcze	36	2400–2500	1.66	18.88
	Naratów	8	1400–1500	0.22	0.91
	Lipowiec	0.2	1400–1500	0.01	0.02
	Ślubów	3	1300–1400	0.11	0.21
	Bartków	0.5	1300–1400	0.02	0.03
	Borzęcin	32	1400–1600	2.01	no data
	Radziądz	6	1600–1800	0.25	0.19
Total prospective of low probability:				4.28	20.24
Total estimated NCB resources:				85.76*	249.15*

*including the deposit(s) from Table 2.1

As seen in Table 2.3, the extensions of the three known deposits (prospective areas of high probability) suggest a considerable increase in their resources, therefore making their future exploration justified and highly appealing.

3 Major ore characteristics

Genetic studies indicate that the richest mineralisation in Fore-Sudetic Monocline is associated with palaeo-elevations like the Wolsztyn High and the Fore-Sudetic Block, and faults, which attracted the flow of mineralising fluids towards those structures and through them. The ore grade is related to the time of the activity of open conduits for mineralising fluids, and on the composition of basement rocks, which also affects the concentrations of accompanying elements, e.g. lead (Borg et al. 2012, Speczik et al. 2021).

The three deposits of the NCB are highly dissimilar from those of the active Lubin-Sieroszowice District. The sole exception is Nowa Sól, which is somewhat comparable to the Polkowice, Sieroszowice, and Rudna deposits of the New Copper District in terms of ore mineralogy (Speczik 2022). This deposit is characterised by eastward dipping of the top of the Rote Fäule horizon. Therefore, the main orebodies of Nowa Sól are located in limestones in its western part; further east they also include shales, and near the eastern edge the ore reaches a few metres deep into the sandstone.

The Mozów deposit is characterised by the prevalence of carbonate ore, related to its close proximity to the vast Zielona Góra oxidised field and the continuously high position of Rote Fäule. Shale ore is present but accounts for only 25% of copper resources, and the underlying sandstones are barren (Speczik 2022).

The Sulmierzyce deposit is peculiar due to its large thickness of the copper-bearing shale, up to 1.5 m, which makes it stand out among both the NCB deposits and the New Copper District Deposits. In fact, the shale resembles the so-called copper-bearing marls (Kupfermergel) of the Old Copper District, currently abandoned and also shown in Figure 2.1. The close proximity of this area to two large oxidised fields resulted in its patchy structure as well as in the mixing of mineralising fluids, which caused the lack of metal zonality. This zonality is typical of the other deposits of the Fore-Sudetic Monocline, and involves the succession of Cu, Pb, and Zn zones in the vertical profile (Borg 2012). Its absence from Sulmierzyce North is another distinguishing feature of this deposit (Speczik 2022).

4 Chances for a new mining district

Even at the current stage of exploration, the Nowa Sol deposit is the largest copper deposit in Poland (Speczik et al. 2022). It also ranks 19th in the world in terms of resources (see Table 4.1), while also occupying the 3rd or 4th place globally with respect to ore grade. The resources of Sulmierzyce North and Mozów are similar to those of the deposits currently mined in the New Copper District.

In 2017, technical reports constituting pre-feasibility studies were prepared for MCC by the Runge Pincock Minarco company—currently RPMGlobal (Bohnet et al. 2017, Goodell et al. 2017). Those documents only considered the resources known at the time, which were lower and less explored. According to them, economically profitable extraction of these deposits is possible, but it would necessitate the application of modern mining technologies, which have not yet been employed in Poland. They include underground flotation performed selectively in order to recover a larger number of valuable elements, the paste backfill technology, cooling of mining headings with ice, and automation of mining machinery (Oszczepalski et al. 2019). These new methods can make the extraction of ore from the NCB deposits more profitable than the mining operations currently continuing in the New Copper District.

Table 4.1. The Nowa Sól deposit among the world's largest copper deposits

No.	Name	Country	Cu resources/ reserves [Mt]	Status
1	Kamoa Kakula	Congo	43.6	in development
2	Escondida	Chile	43.2	active
3	Pebble	USA	37.0	in development
4	Collahuasi	Chile	28.1	active
5	Resolution	USA	27.3	in development
6	Morenci	USA	27.0	active
7	Buenavista	Mexico	26.7	active
8	La Granja	Peru	22.0	in development
9	Andina	Chile	18.8	active
10	Cerro Verde	Peru	18.1	active
11	Toquepala	Peru	17.7	active
12	Tampakan	Phillipines	15.2	in development
13	El Pachon	Argentina	15.0	in development
14	Grasberg	Indonesia	14.6	active
15	Taca Taca	Argentina	12.9	in development
16	Radomiro Tomic	Chile	12.1	active
17	El Teniente	Chile	11.1	active
18	Los Bronces	Chile	11.1	active
19	Nowa Sól	Poland	11.0	in development
20	Cascabel	Ecuador	10.9	in development
21	Baimskaya	Russia	9.5	in development
22	Chuquicamata	Chile	9.4	active
23	Vizcachitas	Chile	7.7	in development
24	Michiquillay	Peru	7.3	in development

The pre-feasibility studies of 2017 estimated the operating costs of future mines at about US $2400–2800 per 1 t of copper, depending on the depth (Bohnet et al. 2017, Goodell et al. 2017). Accounting for inflation, the authors of the present paper believe that these costs should be updated to about $3500. This is still low, considering the current copper prices are about US $9000 per tonne, and according to the predictions of Bank of America and Goldman Sachs, they should reach about $10000–11000 in 2023, and $12000 in 2024 (Christensen 2022).

Another major advantage of the NCB deposits is their continuity. They form relatively uniform orebodies, which may be only locally disrupted by Rote Fäule zones. All three deposits have been identified by regular drilling grids, and new boreholes are currently drilled in the Nowa Sól area. The history of documenting copper and silver ore deposits in the Fore-Sudetic Monocline shows that adding new holes inside the drilling grids of exiting deposits always ends in a slight increase in resources, due to their homogeneity on a macroscale (Speczik et al. 2020).

Further drilling operations are necessary to upgrade the categories of documentation of these deposits to C_1 according to the Polish system, which is an equivalent of indicated resources (Nieć 2010). Pursuant to Polish regulations, this category allows an investor to submit an application for a mining licence. The Nowa Sól deposit is currently at the most advanced stage of exploration, with the largest number of boreholes already drilled, and with a relative error of estimation of resources below 30%, fulfilling the criteria of the C_1 category.

5 Summary

The Northern Copper Belt is a region in south-western Poland, demarcated as a result of the exploration programme of Miedzi Copper Corp. The resources of its three copper and silver ore deposits are already approved by the Polish government, and constitute a major contribution to the country's rich Cu and Ag resources. All three deposits have great potential for growth, and their profitable extraction is already possible, under the condition of utilising modern mining technologies due to their considerable depths.

The NCB also includes numerous prospective areas, with resources estimated at various levels of probability. Further investigation of these areas could lead to the identification of new deposits, some of them shallower than those already documented in the belt. However, already at the current stage of exploration, the NCB presents a proven chance for the development of a new giant mining district for the world's copper industry.

Acknowledgements

The authors would like to thank Prof. Sławomir Oszczepalski of the Polish Geological Institute.

References

Bohnet E, Goodell T, Jorgensen M (2017) Technical Report on Miedzi Copper's Sulmierzyce Project, Poland (Unpublished). RungePincockMinarco, Lakewood

Borg G, Piestrzyński A, Bachmann GH, Püttmann W, Walther S, Fiedler M (2012) An overview of the European Kupferschiefer deposits. Society of Economic Geologists Special Publication 16:455–486

Christensen N (2022) Copper prices to find their groove in the second half of 2023. https://www.kitco.com/news/2022-12-21/Copper-prices-to-find-their-groove-in-the-second-half-of-2023.html (Accessed 28 February 2023)

Goodell T, Jorgensen M, Bohnet E (2017) Technical Report of the Miedzi Copper Project, Poland (Unpublished). RungePincockMinarco, Lakewood

Nieć M (2010) Międzynarodowe klasyfikacje zasobów złóż kopalin. Górnictwo i Geoinżynieria 34(3):33–49 (in Polish)

Oszczepalski S, Speczik S (2011) Rudy miedzi i srebra. In: Wołkowicz S, Smakowski T, Speczik S (eds) Bilans perspektywicznych zasobów kopalin Polski wg stanu na 31 XII 2009 r. Polish Geological Institute, Warsaw, p 76–93 (in Polish)

Oszczepalski S, Speczik S, Zieliński K, Chmielewski A (2019) The Kupferschiefer Deposits and Prospects in SW Poland: Past, Present and Future. Minerals 9. https://doi.org/10.3390/min9100592

Speczik S, Bieńko T, Pietrzela A, Zieliński K (2020) Documenting deep copper and silver deposits—investor's criteria. Górnictwo Odkrywkowe 1:43–54 (in Polish with English abstract)

Speczik S, Zieliński K, Bieńko T, Pietrzela A (2021) The prospecting strategy for a deep Cu-Ag ore deposit in Poland – An anatomy of success. Ore Geol Rev 131. https://doi.org/10.1016/j.oregeorev.2021.104053

Speczik S, Szamałek S, Wierchowiec J, Zieliński K, Pietrzela A, Bieńko T (2022) The new Northern Copper Belt of south-western Poland: a summary. Acta Geol Pol 72(4):469–477

